Stochastic crack growth simulation in reinforced concrete structures by means of coupled finite element and meshless methods

(Stochastische Rissfortschrittsberechnung in bewehrten Betonstrukturen unter Kopplung der Finiten Elemente Methode mit netzfreien Verfahren)

DISSERTATION

Zur Erlangung des akademischen Grades
Doktor-Ingenieur (Dr.-Ing.)
an der Fakultät Bauingenieurwesen
der
Bauhaus-Universität Weimar

vorgelegt von
Dipl.-Ing. Thomas Most
geb. am 15. Juni 1975 in Bad Salzungen

Weimar, Juni 2005

Gutachter:

1. Prof. Dr. techn. Christian Bucher, Bauhaus-Universität Weimar

2. Prof. Dr. techn. Günter Hofstetter, Universität Innsbruck

3. Prof. Dr. habil. Ulrich Häussler-Combe, Techn. Universität Dresden

Disputation am 28. November 2005

Für Yvonne, Olivia, Magnus und meine Eltern

Vorwort

Die vorliegende Arbeit entstand während meiner Tätigkeit als wissenschaftlicher Mitarbeiter am Institut für Strukturmechanik innerhalb des Sonderforschungsbereiches 524 "Werkstoffe und Konstruktionen für die Revitalisierung von Bauwerken" an der Bauhaus-Universität Weimar.

Mein besonderer Dank gilt Herrn Professor Christian Bucher für die Anregung und Förderung dieser Arbeit sowie für die hervorragende Betreuung. Besonders wertvoll waren dabei die Vielzahl fachlicher Diskussionen, sein Vertrauen und seine Offenheit, welche den idealen Rahmen für diese Arbeit bildeten.

Herr Professor Günter Hofstetter und Herr Professor Ulrich Häussler-Combe danke ich für die Übernahme der Gutachten und für die Gespräche innerhalb verschiedener wissenschaftlicher Veranstaltungen.

Weiterhin möchte ich mich bei allen Mitarbeitern des Instituts für Strukturmechanik für die Unterstützung und die angenehme Arbeitsatmosphäre bedanken. Besonders hervorheben möchte ich dabei Herr Jörg F. Unger und Herr Dr. Michael Macke. Einen wichtigen Beitrag zum Gelingen dieser Arbeit leisteten weiterhin die fachlichen Diskussionen mit Herrn Professor Carsten Könke, mit Herrn Stefan Eckardt und mit Herrn Kai Schrader.

Ganz besonders möchte ich mich bei meiner lieben Yvonne und unseren Kindern für ihre Motivation und auch für ihr Verständnis in schwierigen Phasen bedanken. Dieser Rückhalt ist zur Realisierung dieser Arbeit eine unverzichtbare Basis gewesen.

Abschließend danke ich meinen Eltern für die Unterstützung in den vergangenen Jahren insbesondere jedoch für die frühe Förderung meiner Interessen an den Naturwissenschaften, die die wesentlichliche Grundlage dieser Arbeit darstellen.

Abstract

The complex failure process of concrete structures can not be described in detail by standard engineering design formulas. The numerical analysis of crack development in concrete is essential for several problems. In the last decades a large number of research groups have dealt with this topic and several models and algorithms were developed. However, most of these methods show some difficulties and are limited to special cases. The goal of this study was to develop an automatic algorithm for the efficient simulation of multiple cracking in plain and reinforced concrete structures of medium size. For this purpose meshless methods were used to describe the growth of crack surfaces. Two meshless interpolation schemes were improved for a simple application. The cracking process of concrete has been modeled using a stable criterion for crack growth in combination with an improved cohesive crack model which can represent the failure process under combined crack opening and crack sliding very well. This crack growth algorithm was extended in order to represent the fluctuations of the concrete properties by enlarging the single-parameter random field concept for multiple correlated material parameters.

Kurzfassung

Das komplexe Versagensverhalten von Betonstrukturen kann in der Regel nicht mit Standardbemessungsformeln beschrieben werden. Eine detaillierte numerische Analyse der Rissentwicklung in Beton ist für einige Problemstellungen unverzichtbar. In den letzten Jahrzehnten haben sich eine Vielzahl von Forschergruppen mit dieser Thematik auseinandergesetzt. Dabei wurden verschiedene Modelle und Algorithmen entwickelt. Die meisten dieser Verfahren weisen jedoch verschiedene Probleme auf oder sind nur für Spezialfälle anwendbar. Das Ziel dieser Arbeit war die Entwicklung eines automatischen Algorithmus zur effizienten Simulation von mehrfacher Rissentwicklung in Beton- und Stahlbetonstrukturen mittlerer Größe. Dabei wurden netzfreie Verfahren angewendet, um die Änderung der Rissoberflächen abzubilden. Zwei netzfreie Interpolationstypen wurden im Hinblick auf eine unkomplizierte Anwendung angepaßt. Der Versagensprozess des Betons wurde mit Hilfe eines stabilen Risskriteriums in Kombination mit einem erweiterten kohäsiven Rissmodell abgebildet. Dieses erweiterte Modell kann die Zusammenhänge bei kombinierter Rissöffnung und -gleitung sehr gut wiedergeben. Der entwickelte Algorithmus zur Risssimulation wurde in Hinblick auf eine stochastische Modellierung erweitert. Zu diesem Zweck wurde das Zufallsfeldkonzept für die Abbildung mehrerer untereinander korrelierter Materialparameter ergänzt.

Contents

Symbols and abbreviations

General notations

$\delta(\cdot)$	Variation of $\cdot$
$\lvert \cdot \rvert$	Absolute value of $\cdot$
$\lVert \cdot \rVert$	Norm of $\cdot$
$[\cdot]^T$	Transpose of $\cdot$
$\mathrm{div}(\cdot)$	Divergence of $\cdot$
$\mathrm{tr}(\cdot)$	Trace of $\cdot$
$\det(\cdot)$	Determinant of $\cdot$
$\ln(\cdot)$	Natural logarithm of $\cdot$
$\exp(\cdot)$	Exponential function of $\cdot$
$x,\ y,\ z$	Global coordinates
$r,\ s,\ t$	Local coordinates
$r,\ \theta$	Polar coordinates
δ_{ij}	Kronecker symbol
$\eta,\ \mu$	Lamé constants
E	Young's modulus
ν	Poisson's ratio
Π	Total potential energy
Ω	Domain
Γ^f	Neumann boundary
Γ^u	Dirichlet boundary
$\mathbf{f}^S$	Natural boundary conditions
$\mathbf{u}^S$	Essential boundary conditions
$\mathbf{f}^B$	Body forces

$\mathbf{x}$	Position vector $\mathbf{x} = [x, y, z]^T$
$\mathbf{u}$	Displacement vector $\mathbf{u} = [u, v, w]^T$
$\mathbf{u}^h$	Interpolated displacement vector
$\boldsymbol{\epsilon}$	Linearized strain tensor
$\boldsymbol{\sigma}$	Linearized stress tensor
$\mathbf{C}$	Elastic constitutive matrix
$\mathbf{D}$	Tangential constitutive matrix
$\mathbf{K}$	Tangential global stiffness matrix
$\mathbf{d}$	Global displacement vector
$\mathbf{f}^{ext}$	Global external force vector
$\mathbf{f}^{int}$	Global internal force vector

Mechanical fundamentals

$\mathbf{X}$	Position vector in the reference configuration
$\mathbf{x}$	Position vector in the actual configuration
$\boldsymbol{\varphi}$	Transformation from $\mathbf{X}$ to $\mathbf{x}$
$\mathbf{F}$	Deformation gradient
$\mathbf{C}$	Right Cauchy-Green strain tensor
$\mathbf{E}$	Green-Lagrangian strain tensor
$\mathbf{T}$	Cauchy stress tensor
$\mathbf{P}$	First Piola-Kirchhoff stress tensor
$\mathbf{S}$	Second Piola-Kirchhoff stress tensor
$\mathbb{C}$	Elasticity tensor
$\partial_{\boldsymbol{\epsilon}}$	Linear gradient operator
$\tilde{\mathbf{u}}_e$	Finite element nodal displacement vector
$\mathbf{H}_e$	Finite element shape function matrix
$\mathbf{B}_e$	Finite element strain-displacement matrix
$\mathbf{K}_e$	Finite element stiffness matrix
$\mathbf{f}_e^{ext}$	Finite element external force vector
$\mathbf{f}_e^{int}$	Finite element internal force vector
$\mathbf{J}$	Jacobian matrix

Meshless methods

$\mathbf{p}$	Vector of polynomial basis
$\mathbf{a}$	Vector of polynomial coefficients
$\mathbf{P}$	Matrix of polynomial basis values
$\mathbf{W}$	Matrix of weighting function values
w	Weighting function
d_i	Distance to node i
s_i	Standardized distance to node i
D	Influence radius
$\mathbf{B}$	Auxiliary matrix $\mathbf{B} = \mathbf{PW}$
$\mathbf{A}$	Auxiliary matrix $\mathbf{A} = \mathbf{PWP}^T$
Φ^{MLS}	Moving Least Squares shape function
α	Shape parameter for exponential weighting function
ϵ	Regularization parameter for regularized weighting function
f_B	Blending function
T_i	First order Voronoi cell belonging to node i
T_{ij}	Second order Voronoi cell belonging to node i and j
Φ^{NEM}	Natural Neighbor shape function
$\mathbf{B}_m$	Meshless strain-displacement matrix
$\mathbf{K}_m$	Meshless stiffness matrix
$\mathbf{f}_m^{ext}$	Meshless external load vector

Discrete crack modeling

$\mathcal{G}, \mathcal{G}_I, \mathcal{G}_{II}$	Elastic energy release rates
G_f, G_f^I, G_f^{IIa}	Specific fracture energies
t	Thickness of a plane structure
$K_{I,II,III}$	Stress intensity factors
$\bar{x}, \bar{y}$	Local crack coordinates
κ	Kolosov constant
δa	Virtual crack extension
δA	Area of virtual crack extension
Δa	Discrete crack extension
ΔA	Area of Discrete crack extension
θ_c	Crack propagation angle

$\sigma_N,\ \sigma_T$	Stresses in normal and tangential direction to the crack surface
$\mathbf{\Delta u}$	Relative displacements in the crack surface $\mathbf{\Delta u} = \begin{bmatrix} \Delta u_N, & \Delta u_T \end{bmatrix}^T$
$\mathbf{\Delta u}^{el}$	Elastic relative displacements in the crack surface
$\mathbf{\Delta u}^{cr}$	Plastic (crack) relative displacements in the crack surface
$f_t,\ \chi$	Tensile strength
c	Shear strength
$\tan\phi$	Friction coefficient
$k_N,\ k_T$	Penalty stiffnesses in the crack surface
F	Yield surface
Q	Plastic potential
W^{cr}	Work spent on the fracture process
$\psi\left(\xi, \alpha\right)$	Scaling function
α_χ	Shape parameter for tensile softening
α_c	Shape parameter for shear softening
$f_c^{dil},\ f_\sigma^{dil}$	Scaling functions for dilatancy
$\alpha_c^{dil},\ \alpha_\sigma^{dil}$	Shape parameters for dilatancy
σ^{dil}	Stress for vanishing dilatancy
R	Nonlocal interaction radius
$\mathbf{f}^{coh}$	Global vector of cohesive forces
L_{CT}	Length of crack tip interface element
σ_τ	Shear stress in the bond surface
$\Delta u\tau$	Relative displacement in the bond surface
$\Delta\bar{u}\tau$	Relative displacement for maximum shear stress
$\Delta\tilde{u}\tau$	Relative displacement for vanishing shear stress

Modeling of uncertainties

X	Single random variable
F_X	Distribution function of X
f_X	Probability density function of X
Φ	Standard normal distribution function
ϕ	Standard normal probability density function
$\bar{X}$	Mean value of X
σ_X	Standard deviation of X
V_X	Coefficient of variation X
$E[\cdot]$	Expected value of $\cdot$
$\Gamma(\cdot)$	Gamma function of $\cdot$
C_{XX}	Covariance function
ρ_{ij}	Coefficient of correlation
$\mathbf{X}$	Random variable vector $\mathbf{X} = [X_1, X_2, \ldots, X_n]^T$
$\mathbf{C_{XX}}$	Covariance matrix
F	Nataf coefficient
$f_{X_1 \ldots X_n}$	Joint probability density function of $\mathbf{X}$
ϕ_n	Joint standard normal probability density function
H	Random field
$\bar{H}$	Mean value of a random field
σ_H	Standard deviation of a random field
V_H	Coefficient of variation of a random field
R_{HH}	Auto correlation function
$\mathbf{C_{YY}}$	Matrix containing variances of uncorrelated Gaussian variables
$\mathbf{\Psi}$	Eigenvectors of Gaussian covariance matrix $\mathbf{\Psi} = [\mathbf{\Psi}_1, \mathbf{\Psi}_2, \ldots, \mathbf{\Psi}_n]$
Q	Representation quality of a random field
$\mathbf{C_{PP}}$	Parameter correlation matrix
$\mathbf{C_{HH}}$	Random field covariance matrix
$\mathbf{C_{HH}^*}$	Extended random field covariance matrix
$\mathbf{P}$	Permutation matrix for Latin Hypercube Sampling
$\mathbf{R}$	Simulation matrix for Latin Hypercube Sampling
$\mathbf{S}$	Sampling matrix for Latin Hypercube Sampling

Abbreviations

FEM	Finite Element Method
CST	Constant Strain Triangle, three-node 2D solid element
Q4	Quad 4, four-node 2D solid element
Q8	Quad 8, singular eight-node 2D solid element
Q9	Quad 9, nine-node 2D solid element
MLS	Moving Least Squares
MLS (G)	MLS with Gaussian weighting type
MLS (R)	MLS with regularized weighting type
MLS (RS)	MLS with regularized spline weighting type
MLS (SI)	MLS with singular weighting type
EFG	Element-free Galerkin
NEM	Natural Element Method (=Natural Neighbor Galerkin Method)
LEFM	Linear Elastic Fracture Mechanics
VCE	Virtual Crack Extension
CCM	Cohesive Crack Model
PDF	Probability Density Function
COV	Coefficient Of Variation
MCS	Monte Carlo Simulation
LHS	Latin Hypercube Sampling

Chapter 1

Introduction

1.1 Motivation

Numerical simulation has become an important alternative to experimental investigations in applied and engineering science in recent decades. The development of numerical tools has been accelerated due to the very fast development of computer technology, which enables a large group of researchers and users to access powerful hardware. Today several simulation methods are available in a large number of commercial software applications and an even larger number of research programs have been developed in the university and industrial environment.

Today the Finite Element Method is an established tool for numerical simulations in civil and mechanical engineering. This method was permanently further developed in a huge number of research groups in order to simulate sophisticated material behavior and complex structures efficiently.

The development of numerical tools for the simulation of damage processing due to crack formation and crack growth is still mainly an academic research field. The frequent publication of new methods and algorithms shows the importance of this topic in the international research environment. But numerical simulations of crack processing are done only rarely in industrial practice.

The simulation of crack development in a base material requires adapting the discretization in order to represent the moving domain boundary. Two different approaches in the context of the Finite Element Method have been developed for this purpose, the smeared crack approach and the discrete crack approach. In the smeared method the crack surface is represented as a reduced strength at the integration point level, which is smeared over the whole element by the standard element formulation. This approach is in general relatively expensive, since the size of incremental steps is strongly limited to avoid numerical problems. The application of the discrete approach is more robust, but due to the explicit representation of the crack surface a permanent update of the finite element discretization is necessary. The traditional way for this update is local remesh-

ing of the finite element structure, which is very complex in three dimensions and may cause several problems due to the mapping between the original and the new meshes. For this reason some improved finite element formulations without remeshing have been developed in recent years which represent the crack surface by additional shape functions. These shape functions are handled either as local modes in embedded formulations or as global enhancements in an extended formulation.

As an alternative to finite element formulations the development of meshless or mesh-free methods was accelerated since the middle of the nineties. With these methods the shape function formulation is very flexible and can be adapted in a simple way. Furthermore these methods use a continuous interpolation, which leads to smooth strains and stresses in contrast to the Finite Element Method. Many of the meshless methods can represent growing crack surfaces without a discretization update and without additional formulations. But generally these methods do not satisfy the interpolation property, which leads to huge problems by imposing boundary conditions. Most of the meshless approaches are based on the definition of influence domains by introducing additional numerical parameters. These parameters generally have a strong influence on the numerical results, although they do not have a physical meaning.

Apart from the discretization of the crack development, the principles of crack growth in metals can be described very well using available fracture mechanical concepts. The material concrete has a much more complex fracture process as compared to metals due to its inhomogeneity. For modeling concrete cracking on the macro scale the fictitious crack model is a simple and efficient approach. This model is based on a homogenized material, and its formulation does not consider the dilatancy effect and the interlocking for crack sliding. A more detailed description is a meso scale approach where the aggregates and the cement matrix are modeled explicitly, but at present this procedure is limited to small specimen sizes and cannot no be applied to complex structures due to the huge numerical effort. A further field of current research activity in modeling concrete cracking is the question of the criteria for crack growth and crack direction. Mostly a stress-based formulation is used, which depends strongly on the discretization.

Due to the already mentioned inhomogeneity and varying conditions during the construction process the material properties of concrete show significant fluctuations as compared to other materials. The consideration of such uncertainties in a numerical crack growth analysis has been considered only in very few studies, where one material parameter of a single structural member is mainly modeled as a random variable. A more detailed spatial distribution has been represented only in some individual cases.

The mentioned arguments show that an enormous need for research activities exists in developing and improving numerical models for the simulation of cracking in concrete structures.

1.2   Aims of the present work

The goal of this work is the development of an automatic algorithm for the efficient simulation of cracking in plain and reinforced concrete structures of medium size. For this purpose meshless methods will be applied such that adaptive coupling with finite elements is realized, where the meshless discretization is used only in regions with developing cracks. For this purpose a meshless interpolation scheme for modeling discrete cracks will be developed, which solves the problems of existing approaches in imposing the boundary conditions and enabling an easy coupling with finite elements.

Furthermore the concrete cracking will be modeled on the macroscopic scale where the applied cohesive crack model represents the complex behavior in the fictitious crack surfaces for combined crack opening and sliding, the so-called mixed mode cracking. This concept will be implemented in a crack criterion which gives very stable results even for coarse discretization.

The mentioned spatial fluctuations of the concrete properties will be represented using random fields. For this purpose the single parameter random field concept will be extended to an arbitrary number of random material parameters, which are correlated among each other. Thus the reduction of the random variables will have an important significance in order to enable the application of the developed concept to approximation methods.

To achieve these goals, the following assumptions will be made:

- The implementation will be done for the two-dimensional case and an extension to three dimensions will be discussed.

- The modeling of concrete failure will be limited to cracking due to tensile loading. This implies that the base material remains linear elastic in the discrete crack approach.

- The parameters of the cohesive crack model will be assumed to be constant material properties. A variation due to not fully developed or overlapping fracture process zones will be neglected.

- Quasi-static behavior will be assumed, which implies that no kinetic energy will be released during the cracking process.

- Creep and shrinkage effects of the concrete will not be considered.

- The bond behavior between concrete and reinforcement will be modeled using existing shear stress-slip relations.

- Uncertainties in the reinforcement, in the external loading, and in the geometrical and boundary conditions will not be represented.

- The stochastic analysis will be limited to estimating the statistical properties of the structural response. An application of the probabilistic model to reliability analyses will be discussed.

1.3   Outline

This work is organized as follows: After this introduction, the second chapter presents the mechanical fundamentals which are necessary for understanding the further chapters. The basic ideas of the Finite Element Method are shown and the extension to nonlinear material behavior with some solution procedures is given.

The third chapter gives a survey on existing meshless methods. Two methods, the Element-free Galerkin Method and the Natural Neighbor Galerkin Method are improved and adapted to the intended application. The effects of the developed enhancements is shown by means of several simple examples.

The fourth chapter starts with an introduction to Linear Elastic Fracture Mechanics. Then the presented concepts are used in modified form to develop a criterion for crack growth and crack direction. The standard and an improved cohesive crack model are described and analyzed in combination with this criterion. An investigation of some plain concrete structures and a reinforced concrete beam rounds off this chapter.

The fifth chapter introduces the random variable and random field theory and illustrates the extension to multi-parameter random fields. After presented some sampling strategies the probabilistic model is verified using several numerical examples.

Finally the sixth chapter summerizes and assesses the presented results and gives impulses for further research activities.

Chapter 2

Mechanical fundamentals

In this chapter the mechanical formulations are presented, which are necessary for the understanding of this work. Based on the continuum description of an elastic domain a derivation of the Finite Element Method is given, which is the basis of the following chapters. Furthermore this chapter contains the extension for nonlinear material behavior and a survey of approaches to the solution of such nonlinear problems.

2.1   Continuum formulation

2.1.1   Kinematics

In the undeformed reference configuration of a body B, the position vector of an arbitrary point is defined as

$$\mathbf{X} = X_1\mathbf{e}_1 + X_2\mathbf{e}_2 + X_3\mathbf{e}_3 = X_i\mathbf{e}_i \tag{2.1}$$

where X_i are called Lagrangian coordinates. The position vector in the actual configuration reads analogously

$$\mathbf{x} = x_1\mathbf{e}_1 + x_2\mathbf{e}_2 + x_3\mathbf{e}_3 = x_i\mathbf{e}_i \tag{2.2}$$

with the Eulerian coordinates x_i. The transformation of a point from the reference to the actual configuration is described by

$$\mathbf{x}(\mathbf{X}) = \boldsymbol{\varphi}(\mathbf{X}). \tag{2.3}$$

In Fig. 2.1, the principle of this transformation is shown. The change of position from $\mathbf{X}$ to $\mathbf{x}$ can be characterized by the displacement vector

$$\mathbf{u}(\mathbf{X}) = \mathbf{x}(\mathbf{X}) - \mathbf{X}. \tag{2.4}$$
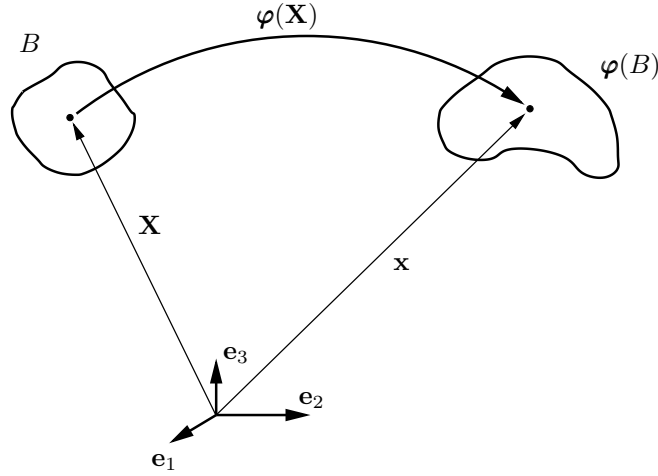
Figure 2.1. Movement of a single point from the reference to the actual configuration

The transformation of a differential line element

$$d\mathbf{x} = \mathbf{F}d\mathbf{X} \tag{2.5}$$

is described by the deformation gradient $\mathbf{F}$

$$\mathbf{F} = \frac{\partial \boldsymbol{\varphi}(\mathbf{X})}{\partial \mathbf{X}} = \frac{\partial \mathbf{x}}{\partial \mathbf{X}} \tag{2.6}$$

which is in general an asymmetric tensor. The differential line element by using Eq. (2.5) reads

$$ds^2 = d\mathbf{x}^T d\mathbf{x} = d\mathbf{X}^T \mathbf{F}^T \mathbf{F} d\mathbf{X} = d\mathbf{X}^T \mathbf{C} d\mathbf{X} \tag{2.7}$$

where $\mathbf{C}$ is the right Cauchy-Green tensor defined as

$$\mathbf{C} = \mathbf{F}^T \mathbf{F}. \tag{2.8}$$

Based on a right-polar decomposition of the deformation gradient

$$\mathbf{F} = \mathbf{R}\mathbf{U} \tag{2.9}$$

into a rotational part $\mathbf{R}$ and a symmetric deformational part $\mathbf{U}$, $\mathbf{C}$ can be expressed as

$$\mathbf{C} = \mathbf{F}^T \mathbf{F} = \mathbf{U}^T \mathbf{R}^T \mathbf{R} \mathbf{U} = \mathbf{U}^T \mathbf{U}. \tag{2.10}$$

The absolute elongation finally reads

$$ds^2 - dS^2 = d\mathbf{X}^T \mathbf{C} d\mathbf{X} - d\mathbf{X}^T d\mathbf{X} = d\mathbf{X}^T (\mathbf{C} - \mathbf{1}) d\mathbf{X} = d\mathbf{X}^T 2\mathbf{E} d\mathbf{X} \tag{2.11}$$

by introducing the Green-Lagrangian strain tensor as

$$\mathbf{E} = \frac{1}{2}\left(\mathbf{C} - \mathbf{1}\right).$$

(2.12)

This tensor can be written as

$$E_{ij} = \frac{1}{2}\left(\frac{\partial u_i}{\partial X_j} + \frac{\partial u_j}{\partial X_i} + \frac{\partial u_k}{\partial X_i}\frac{\partial u_k}{\partial X_j}\right).$$

(2.13)

2.1.2 Equilibrium

Let $\mathbf{t}$ be the real stress vector in a point of a body

$$\mathbf{t} = \lim_{\Delta S \to 0}\frac{\Delta \mathbf{f}}{\Delta S} = \frac{d\mathbf{f}}{dS}$$

(2.14)

where $\Delta \mathbf{f}$ are the section forces affecting the section surface area ΔS. The stress $\mathbf{t}$ can be obtained from the symmetric Cauchy stress tensor $\mathbf{T}$ as

$$\mathbf{t} = \mathbf{T}\mathbf{n}$$

(2.15)

where $\mathbf{n}$ is the normal to the section surface. The acting body and surface forces for an arbitrary domain fulfill the equilibrium condition

$$\int_V p_i dV + \int_S t_i dS = 0.$$

(2.16)

The second part of Eq. (2.16) can be transformed to a volume integral by using Eq. (2.15), which leads to the equation

$$\int_V p_i dV + \int_V \frac{\partial T_{ij}}{\partial x_j} dV = 0.$$

(2.17)

Considering volume elements we obtain the well-known equilibrium equation

$$p_i + \frac{\partial T_{ij}}{\partial x_j} = 0$$

(2.18)

or

$$\mathbf{p} + \mathrm{div}\mathbf{T} = \mathbf{0}.$$

(2.19)

The stress tensor which is the energetic conjugate of the deformation gradient $\mathbf{F}$ is the first Piola-Kirchhoff stress tensor $\mathbf{P}$. This tensor is obtained by transforming the resulting

force acting on an infinitesimal section surface area ds in the actual configuration

$$\mathbf{F_t} = \int_{ds} \mathbf{T}\mathbf{n}ds \tag{2.20}$$

to the reference configuration by using the transformation equation

$$ds = \det(\mathbf{F})\mathbf{F}^{-T}dS. \tag{2.21}$$

This leads to the formulation

$$\mathbf{F_t} = \int_{dS} \det(\mathbf{F})\mathbf{T}\mathbf{F}^{-T}\mathbf{N}dS \tag{2.22}$$

where the first Piola-Kirchhoff stress tensor is defined as

$$\mathbf{P} = \det(\mathbf{F})\mathbf{T}\mathbf{F}^{-T}. \tag{2.23}$$

Due to the asymmetric $\mathbf{P}$ the second Piola-Kirchhoff stress tensor was introduced

$$\mathbf{S} = \mathbf{F}^{-1}\mathbf{P} \tag{2.24}$$

which is the energetic conjugate of the Green-Lagrangian strain tensor $\mathbf{E}$.

2.1.3   Constitutive law

For linear elastic materials Hooke's law can be given in the form

$$\mathbf{S} = \mathbb{C}\mathbf{E} \tag{2.25}$$

where $\mathbb{C}$ is the four-dimensional elasticity tensor containing 81 components. In the case of the restriction to isotropic materials this tensor can be represented by the Lamé constants η and μ

$$C_{ijkl} = \eta\delta_{ij}\delta_{kl} + \mu\left(\delta_{ik}\delta_{jl} + \delta_{il}\delta_{jk}\right) \tag{2.26}$$

where δ_{ij} is the Kronecker symbol

$$\delta_{ij} = \begin{cases} 1 & i = j \\ 0 & i \neq j \end{cases}. \tag{2.27}$$

The relations between the Lamé constants and the commonly used Young's modulus E and Poisson's ratio ν are given as

$$\eta = \frac{E\nu}{(1+\nu)(1-2\nu)} \tag{2.28}$$

and

$$\mu = \frac{E}{2(1+\nu)}. \tag{2.29}$$

Using Eq. (2.26), Eq. (2.28) and Eq. (2.29) in Eq. (2.25) yields the relation

$$\mathbf{S} = \eta \operatorname{tr}(\mathbf{E})\mathbf{1} + 2\mu\mathbf{E} = \frac{E\nu}{(1+\nu)(1-2\nu)} \operatorname{tr}(\mathbf{E})\mathbf{1} + \frac{E}{(1+\nu)}\mathbf{E}. \tag{2.30}$$

If only small strains are considered, which means that a geometrically linear analysis is performed, the linearized strain tensor can be obtained from the Green-Lagrangian strain tensor by neglecting higher order terms. It reads

$$\epsilon_{ij} = \frac{1}{2}\left(\frac{\partial u_i}{\partial X_j} + \frac{\partial u_j}{\partial X_i}\right). \tag{2.31}$$

The conjugated stress tensor $\boldsymbol{\sigma}$ is called the linearized stress tensor. The linearized stress-strain relation is then given as

$$\boldsymbol{\sigma} = \mathbb{C}\boldsymbol{\epsilon}. \tag{2.32}$$

Introducing the three-dimensional displacement degrees of freedom u_x, u_y and u_z and the linear gradient operator $\boldsymbol{\partial_\epsilon}$, the kinematic relation in Eq. (2.31) reads in matrix-vector form

$$\boldsymbol{\epsilon} = \boldsymbol{\partial_\epsilon}\mathbf{u}$$

$$\begin{bmatrix} \epsilon_{xx} \\ \epsilon_{yy} \\ \epsilon_{zz} \\ 2\epsilon_{xy} \\ 2\epsilon_{xz} \\ 2\epsilon_{yz} \end{bmatrix} = \begin{bmatrix} \epsilon_{xx} \\ \epsilon_{yy} \\ \epsilon_{zz} \\ \gamma_{xy} \\ \gamma_{xz} \\ \gamma_{yz} \end{bmatrix} = \begin{bmatrix} \frac{\partial}{\partial x} & 0 & 0 \\ 0 & \frac{\partial}{\partial y} & 0 \\ 0 & 0 & \frac{\partial}{\partial z} \\ \frac{\partial}{\partial y} & \frac{\partial}{\partial x} & 0 \\ \frac{\partial}{\partial z} & 0 & \frac{\partial}{\partial x} \\ 0 & \frac{\partial}{\partial z} & \frac{\partial}{\partial y} \end{bmatrix} \begin{bmatrix} u_x \\ u_y \\ u_z \end{bmatrix}. \tag{2.33}$$

The constitutive law in Eq. (2.32) can be written as

$$
\begin{bmatrix}
\sigma_{xx} \\
\sigma_{yy} \\
\sigma_{zz} \\
\sigma_{xy} \\
\sigma_{xz} \\
\sigma_{yz}
\end{bmatrix}
= \mathbf{C}
\begin{bmatrix}
\epsilon_{xx} \\
\epsilon_{yy} \\
\epsilon_{zz} \\
\gamma_{xy} \\
\gamma_{xz} \\
\gamma_{yz}
\end{bmatrix}
\tag{2.34}
$$

with the constitutive matrix $\mathbf{C}$ for linear elastic materials

$$
\mathbf{C} = \frac{E}{(1+\nu)(1-2\nu)}
\begin{bmatrix}
1-\nu & \nu & \nu & 0 & 0 & 0 \\
\nu & 1-\nu & \nu & 0 & 0 & 0 \\
\nu & \nu & 1-\nu & 0 & 0 & 0 \\
0 & 0 & 0 & \frac{1-2\nu}{2} & 0 & 0 \\
0 & 0 & 0 & 0 & \frac{1-2\nu}{2} & 0 \\
0 & 0 & 0 & 0 & 0 & \frac{1-2\nu}{2}
\end{bmatrix}.
\tag{2.35}
$$

If a plane stress state is assumed, Eq. (2.33) and Eq. (2.34) read

$$
\begin{bmatrix}
\epsilon_{xx} \\
\epsilon_{yy} \\
\gamma_{xy}
\end{bmatrix}
=
\begin{bmatrix}
\frac{\partial}{\partial x} & 0 \\
0 & \frac{\partial}{\partial y} \\
\frac{\partial}{\partial y} & \frac{\partial}{\partial x}
\end{bmatrix}
\begin{bmatrix}
u_x \\
u_y
\end{bmatrix}
\tag{2.36}
$$

and

$$
\begin{bmatrix}
\sigma_{xx} \\
\sigma_{yy} \\
\sigma_{xy}
\end{bmatrix}
=
\frac{E}{1-\nu^2}
\begin{bmatrix}
1 & \nu & 0 \\
\nu & 1 & 0 \\
0 & 0 & \frac{1-\nu}{2}
\end{bmatrix}
\begin{bmatrix}
\epsilon_{xx} \\
\epsilon_{yy} \\
\gamma_{xy}
\end{bmatrix}.
\tag{2.37}
$$

2.2 Finite Element Method

The system of governing differential equations and boundary conditions for a linear elastic continuum $\Omega \in R^3$ with the domain boundary Γ can be written as

$$
\begin{aligned}
\partial_{\epsilon}{}^T \boldsymbol{\sigma} + \mathbf{f}^B &= \mathbf{0} &&\text{in } \Omega \\
\boldsymbol{\epsilon} &= \partial_{\epsilon} \mathbf{u} &&\text{in } \Omega \\
\boldsymbol{\sigma} &= \mathbf{C}\boldsymbol{\epsilon} &&\text{in } \Omega \\
\mathbf{n}\boldsymbol{\sigma} &= \mathbf{f}^S &&\text{on } \Gamma^f \\
\mathbf{u} &= \mathbf{u}^S &&\text{on } \Gamma^u \\
\Gamma &= \Gamma^u \cup \Gamma^f \\
\Gamma^u &\cap \Gamma^f = \emptyset
\end{aligned}
\tag{2.38}
$$

where $\mathbf{f}^S$ is the prescribed traction vector on the Neumann boundary Γ^f, the so-called natural or static boundary conditions

$$
\mathbf{f}^S = \begin{bmatrix} f_x^S & f_y^S & f_z^S \end{bmatrix}^T ,
\tag{2.39}
$$

$\mathbf{u}^S$ is the vector of prescribed displacements on the Dirichlet boundary Γ^u, known as essential or kinematic boundary conditions

$$
\mathbf{u}^S = \begin{bmatrix} u_x^S & u_y^S & u_z^S \end{bmatrix}^T ,
\tag{2.40}
$$

$\mathbf{f}^B$ is the body force vector, and $\mathbf{n}$ is the matrix of direction cosine components of a unit normal to the domain boundary (positive outwards)

$$
\mathbf{n} = \begin{bmatrix}
n_x & 0 & 0 & n_y & n_z & 0 \\
0 & n_y & 0 & n_x & 0 & n_z \\
0 & 0 & n_z & 0 & n_x & n_y
\end{bmatrix} .
\tag{2.41}
$$

In (Argyris and Kelsey 1954) a concept was developed where the above system of differential equations is solved only in a given set of discrete points and the solution is mapped onto the domain Ω by using element-wise defined interpolation functions. Today this *Finite Element Method* presents an essential tool for the numerical solution of differential equations in different fields of engineering science.

2.2.1 Method of Galerkin

The Ritz method is a very well-known procedure for the solution of differential equations, where linearly independent uniform base functions ϕ_k are used to approximate an

unknown function $u(x, y, z)$ which is chosen here in a three-dimensional domain Ω as

$$u = \phi_0(x, y, z) + \sum_{k=1}^{m} c_k \phi_k(x, y, z). \tag{2.42}$$

Since only the fulfillment of kinematic boundary conditions is postulated for the base functions ϕ_k, an error occurs by the insertion of Eq. (2.42) into the differential equation. This error, which is called the residue

$$R(x, y, z) = \Delta \phi_0 + \sum_{k=1}^{m} c_k \Delta \phi_k - u(x, y, z), \tag{2.43}$$

can be minimized in Ω by weighting Eq. (2.42) with an arbitrary linearly independent function set $\psi_1(x, y, z), ..., \psi_m(x, y, z)$. This approach is known as the method of weighted residues. In the method of Galerkin (Galerkin 1915) the weighting functions ψ_k are chosen according to the function set ϕ_k. This leads to an orthogonal function subspace, which presents the best approximation in the space of ϕ_k. By postulating a vanishing error in the domain Ω in integral sense the formulation

$$\int_{\Omega} R \phi_j d\Omega = 0; \quad j = 1, ..., m \tag{2.44}$$

is obtained. Thus the method of Galerkin is a special form of the method of weighted residues.

2.2.2 Variational formulation

Considering the total potential (Bathe 1996)

$$\Pi(\mathbf{u}) = \frac{1}{2} \int_{\Omega} \boldsymbol{\epsilon}^T(\mathbf{u}) \mathbf{C} \boldsymbol{\epsilon}(\mathbf{u}) d\Omega - \int_{\Omega} \mathbf{u}^T \mathbf{f}^B d\Omega - \int_{\Gamma^f} \mathbf{u}^T \mathbf{f}^S d\Gamma \tag{2.45}$$

and invoking the stationarity of Π yields the weak form of the equilibrium

$$\delta \Pi(\mathbf{u}) = 0 = \int_{\Omega} \delta \boldsymbol{\epsilon}^T(\mathbf{u}) \mathbf{C} \boldsymbol{\epsilon}(\mathbf{u}) d\Omega - \int_{\Omega} \delta \mathbf{u}^T \mathbf{f}^B d\Omega - \int_{\Gamma^f} \delta \mathbf{u}^T \mathbf{f}^S d\Gamma. \tag{2.46}$$

This weak form is called the *principle of virtual work* and has the advantage that the only varying terms are the displacements whose boundary conditions can be easily considered. In a Galerkin approach the virtual displacements $\delta \mathbf{u}$, called test functions, and the unknown displacements $\mathbf{u}$, called trial functions, are assumed to exist in the same function space.
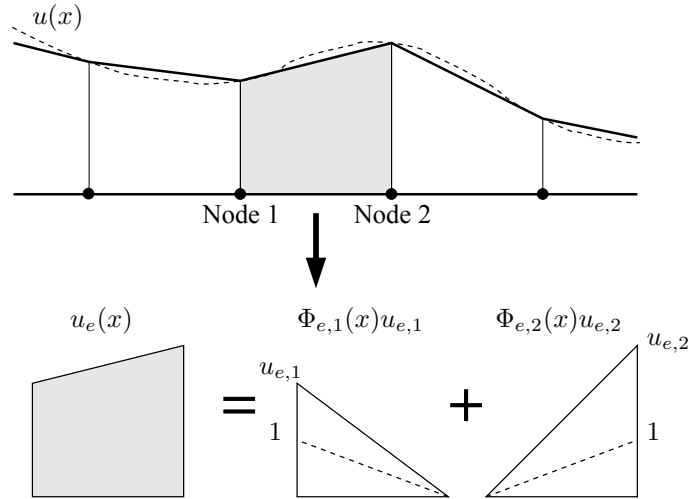
Figure 2.2. One-dimensional linear finite element interpolation

2.2.3 Discretization by finite elements

By introducing the finite element shape functions $\Phi_{e,i}(\mathbf{x})$, the interpolated displacements in an element are given as

$$\mathbf{u}_e^h(\mathbf{x}) = \mathbf{H}_e(\mathbf{x})\tilde{\mathbf{u}}_e \tag{2.47}$$

where the matrix $\mathbf{H}_e$ contains the nodal shape function values of this element depending on the position $\mathbf{x}$,

$$\mathbf{H}_e(\mathbf{x}) = \begin{bmatrix} \Phi_{e,1}(\mathbf{x}) & 0 & 0 & \dots & \Phi_{e,m}(\mathbf{x}) & 0 & 0 \\ 0 & \Phi_{e,1}(\mathbf{x}) & 0 & \dots & 0 & \Phi_{e,m}(\mathbf{x}) & 0 \\ 0 & 0 & \Phi_{e,1}(\mathbf{x}) & \dots & 0 & 0 & \Phi_{e,m}(\mathbf{x}) \end{bmatrix}, \tag{2.48}$$

and $\tilde{\mathbf{u}}_e$ is the local node displacement vector. The finite element shape functions fulfill the interpolation conditions exactly,

$$\Phi_{e,i}(\mathbf{x})_j = \delta_{ij}. \tag{2.49}$$

Fig. 2.2 shows the example of a one-dimensional finite element interpolation. The strains within the element can be obtained from Eq. (2.33) by defining a strain-displacement-matrix

$$\mathbf{B}_e(\mathbf{x}) = \partial_{\boldsymbol{\epsilon}} \mathbf{H}_e(\mathbf{x}) \tag{2.50}$$

in the form

$$\boldsymbol{\epsilon}_e(\mathbf{x}) = \mathbf{B}_e(\mathbf{x})\tilde{\mathbf{u}}_e. \tag{2.51}$$

The discrete formulation of Eq. (2.46) by using Eq. (2.47) and Eq. (2.51) reads for one single element

$$0 = \int_{\Omega_e} \delta\tilde{\mathbf{u}}_e^T \mathbf{B}_e^T \mathbf{C} \mathbf{B}_e \tilde{\mathbf{u}}_e d\Omega - \int_{\Omega_e} \delta\tilde{\mathbf{u}}_e^T \mathbf{H}_e^T \mathbf{f}^B d\Omega - \int_{\Gamma_e^f} \delta\tilde{\mathbf{u}}_e^T \mathbf{H}_e^T \mathbf{f}^S d\Gamma \tag{2.52}$$

which has to be valid for every variation $\delta\tilde{\mathbf{u}}_e$. This implies

$$0 = \int_{\Omega_e} \mathbf{B}_e^T \mathbf{C} \mathbf{B}_e d\Omega \tilde{\mathbf{u}}_e - \int_{\Omega_e} \mathbf{H}_e^T \mathbf{f}^B d\Omega - \int_{\Gamma_e^f} \mathbf{H}_e^T \mathbf{f}^S d\Gamma. \tag{2.53}$$

Eq. (2.53) is the well-known element-stiffness relation and can be written as

$$\mathbf{K}_e \tilde{\mathbf{u}}_e = \mathbf{f}_e^{ext} \tag{2.54}$$

with

$$\begin{aligned} \mathbf{K}_e &= \int_{\Omega_e} \mathbf{B}_e^T \mathbf{C} \mathbf{B}_e d\Omega, \\ \mathbf{f}_e^{ext} &= \int_{\Omega_e} \mathbf{H}_e^T \mathbf{f}^B d\Omega + \int_{\Gamma_e^f} \mathbf{H}_e^T \mathbf{f}^S d\Gamma. \end{aligned} \tag{2.55}$$

Eq. (2.55) clarifies a very important advantage of the Galerkin method: by choosing equal test and trial functions a symmetric stiffness matrix is obtained, which enables efficient solution procedures.

By using the relation between nodes and elements, which are usually stored in the incidence table, the global stiffness matrix $\mathbf{K}$ and the external load vector $\mathbf{f}^{ext}$ are assembled and the unknown global displacement vector $\mathbf{d}$ can be determined by solving

$$\mathbf{K}\mathbf{d} = \mathbf{f}^{ext}. \tag{2.56}$$

Due to the compact support of the finite element shape functions, the global stiffness matrix has sparse character. Thus in an implementation of the Finite Element Method only the small number of nonzero values of the global stiffness matrix has to be stored. This can be done for example using the Compressed Storage Format (Karypis and Kumar 1998). Furthermore this sparse character enables the application of special solvers for the system of linear equations, which are much more efficient for this special matrix type than using standard algorithms for dense matrices. Chapter 2.3.1 describes different types of such sparse matrix solvers. This work shows how to accelerate assembling of the element and the global stiffness matrices for multiprocessor computer systems with shared
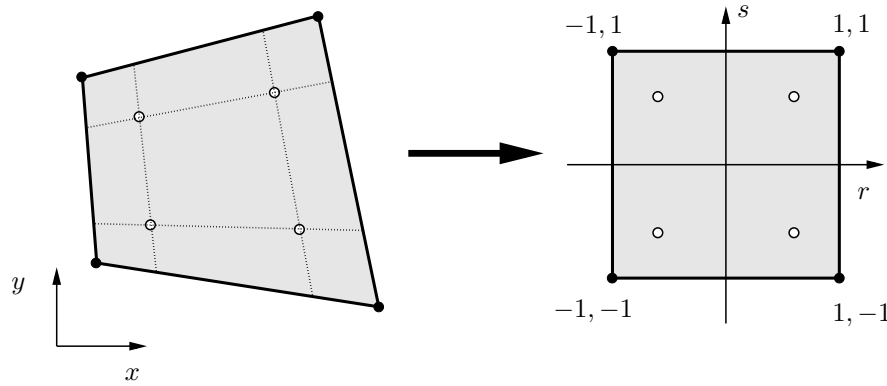
Figure 2.3. Projection of a distorted four-node element with belonging Gaussian integration points into local coordinates

memory with the parallelization environment OpenMP (OpenMP Architecture Review Board 2002). In appendix A.1 more detailed information about this topic can be found.

2.2.4 Numerical integration

The integration required in Eq. (2.55) can be done analytically only in some special cases, e.g. for three-node triangular elements in 2D and for four-node tetrahedral elements in 3D. For higher order elements a Gaussian numerical integration is most commonly used with the Finite Element Method. This approach obtains the exact solution for a polynomial of degree $2n - 1$ with n supporting points. The shape functions have to be defined locally as

$$\mathbf{u}_e(\mathbf{x}) = \mathbf{H}_e(\mathbf{r})\tilde{\mathbf{u}}_e \tag{2.57}$$

where

$$\mathbf{r} = \begin{bmatrix} r & s & t \end{bmatrix}^T \tag{2.58}$$

and a projection onto the unit square or triangle (in 2D) is necessary. This is shown in Fig. 2.3 for a linear two-dimensional four-node element with the required 2×2 Gaussian integration points. This projection, which is given as

$$dx\, dy\, dz = \det\mathbf{J}\, dr\, ds\, dt, \tag{2.59}$$

is realized by defining the Jacobian matrix

$$\mathbf{J} = \frac{\partial \mathbf{x}}{\partial \mathbf{r}} = \begin{bmatrix} \frac{\partial x}{\partial r} & \frac{\partial y}{\partial r} & \frac{\partial z}{\partial r} \\ \frac{\partial x}{\partial s} & \frac{\partial y}{\partial s} & \frac{\partial z}{\partial s} \\ \frac{\partial x}{\partial t} & \frac{\partial y}{\partial t} & \frac{\partial z}{\partial t} \end{bmatrix}. \tag{2.60}$$

The Jacobian determinant has to be positive to ensure the reversibility of Eq. (2.59), which is fulfilled for convex element geometries. In (Bathe 1996) the required weighting factors and the positions of the integration points are given for different polynomial orders. The integration scheme for determining the stiffness matrix in Eq. (2.55) for a three-dimensional element reads

$$\mathbf{K}_e = \int_{\Omega_e} \mathbf{B}_e^T \mathbf{C} \mathbf{B}_e d\Omega = \sum_{i=1}^{l} \sum_{j=1}^{m} \sum_{k=1}^{n} w_i w_j w_k \mathbf{B}_e^T \mathbf{C} \mathbf{B}_e \det \mathbf{J}. \tag{2.61}$$

The strain-displacement matrix is obtained from the shape functions defined in local coordinates as

$$\mathbf{B}_e(\mathbf{x}) = \partial_{\boldsymbol{\epsilon}} \mathbf{H}_e(\mathbf{x}) = \partial_{\boldsymbol{\epsilon}} \mathbf{J}^{-1} \begin{bmatrix} \frac{\partial}{\partial r} \\ \frac{\partial}{\partial s} \\ \frac{\partial}{\partial t} \end{bmatrix} \mathbf{H}_e(\mathbf{r}). \tag{2.62}$$

2.2.5 Material nonlinearity

The derivation in section 2.2.2 and 2.2.3 can be extended for materials which are not linear elastic. A nonlinear constitutive equation is introduced,

$$\boldsymbol{\sigma} = \tilde{\boldsymbol{\sigma}}(\boldsymbol{\epsilon}, \boldsymbol{\alpha}_{int}), \tag{2.63}$$

where $\tilde{\boldsymbol{\sigma}}$ denotes the nonlinear constitutive operator and $\boldsymbol{\alpha}_{int}$ contains the internal variables

$$\boldsymbol{\alpha}_{int} = \begin{bmatrix} \alpha_{int} & \beta_{int} & \dots \end{bmatrix}^T \tag{2.64}$$

which describe the state of an inelastic material. In general the internal variables are path dependent and influenced by the strain history. For the discretized case we obtain

$$\boldsymbol{\sigma}_e = \tilde{\boldsymbol{\sigma}}(\mathbf{B}_e \tilde{\mathbf{u}}_e, \boldsymbol{\alpha}_{int}). \tag{2.65}$$

The discretized weak form given in Eq. (2.52) now reads

$$\int_{\Omega_e} \delta \tilde{\mathbf{u}}_e^T \mathbf{B}_e^T \tilde{\boldsymbol{\sigma}}(\mathbf{B}_e \tilde{\mathbf{u}}_e, \boldsymbol{\alpha}_{int}) d\Omega = \int_{\Omega_e} \delta \tilde{\mathbf{u}}_e^T \mathbf{H}_e^T \mathbf{f}^B d\Omega + \int_{\Gamma_e^f} \delta \tilde{\mathbf{u}}_e^T \mathbf{H}_e^T \mathbf{f}^S d\Gamma, \tag{2.66}$$

which leads to the abbreviated equation

$$\mathbf{f}_e^{int}(\tilde{\mathbf{u}}_e) = \mathbf{f}_e^{ext} \tag{2.67}$$

where

$$\mathbf{f}_e^{int}(\tilde{\mathbf{u}}_e) = \int_{\Omega_e} \mathbf{B}_e^T \tilde{\boldsymbol{\sigma}}(\mathbf{B}_e \tilde{\mathbf{u}}_e, \boldsymbol{\alpha}_{int}) d\Omega \tag{2.68}$$

is the vector of the equivalent internal forces depending on the nodal displacements $\tilde{\mathbf{u}}^e$ in a nonlinear way. Eq. (2.55), where linear elasticity is assumed, is a special case of Eq. (2.67). The internal forces are given for this case $\mathbf{f}_e^{int}(\tilde{\mathbf{u}}_e) = \mathbf{K}_e \tilde{\mathbf{u}}_e$.

To solve the system of nonlinear equations given in Eq. (2.67), the concept of linearization can be applied. Then a given strain state $\bar{\boldsymbol{\epsilon}}$ with corresponding stress state $\bar{\boldsymbol{\sigma}} = \tilde{\boldsymbol{\sigma}}(\bar{\boldsymbol{\epsilon}})$ is assumed to be known and the constitutive function $\tilde{\boldsymbol{\sigma}}$ can be expressed in the vicinity of $\bar{\boldsymbol{\epsilon}}$ by a Taylor series

$$\tilde{\boldsymbol{\sigma}}(\bar{\boldsymbol{\epsilon}} + \Delta\boldsymbol{\epsilon}) = \tilde{\boldsymbol{\sigma}}(\bar{\boldsymbol{\epsilon}}) + \left.\frac{\partial\tilde{\boldsymbol{\sigma}}}{\partial\boldsymbol{\epsilon}}\right|_{\boldsymbol{\epsilon}=\bar{\boldsymbol{\epsilon}}} \Delta\boldsymbol{\epsilon} + \dots. \tag{2.69}$$

For small increments $\Delta\boldsymbol{\epsilon}$ the linearized equation

$$\boldsymbol{\sigma}(\bar{\boldsymbol{\epsilon}} + \Delta\boldsymbol{\epsilon}) \approx \tilde{\boldsymbol{\sigma}}(\bar{\boldsymbol{\epsilon}}) + \mathbf{D}(\bar{\boldsymbol{\epsilon}})\Delta\boldsymbol{\epsilon} \tag{2.70}$$

can be obtained where $\mathbf{D} = \partial\tilde{\boldsymbol{\sigma}}/\partial\boldsymbol{\epsilon}$ is the tangential material stiffness matrix depending on the actual strain state $\bar{\boldsymbol{\epsilon}}$. By linearizing Eq. (2.68) at a given nodal displacement state $\bar{\mathbf{u}}_e$ we obtain a similar formulation

$$\mathbf{f}_e^{int}(\bar{\mathbf{u}}_e + \Delta\mathbf{u}_e) \approx \mathbf{f}_e^{int}(\bar{\mathbf{u}}_e) + \mathbf{K}_e(\bar{\mathbf{u}}_e)\Delta\mathbf{u}_e, \tag{2.71}$$

where $\mathbf{K}_e = \partial\mathbf{f}_e^{int}/\partial\tilde{\mathbf{u}}_e$ is the tangential stiffness matrix at $\bar{\mathbf{u}}_e$ which reads, according to Eq. (2.55),

$$\mathbf{K}_e(\bar{\mathbf{u}}_e) = \int_{\Omega_e} \mathbf{B}_e^T \mathbf{D}(\bar{\boldsymbol{\epsilon}})\mathbf{B}_e d\Omega = \int_{\Omega_e} \mathbf{B}_e^T \mathbf{D}(\mathbf{B}_e\bar{\mathbf{u}}_e)\mathbf{B}_e d\Omega. \tag{2.72}$$

Again linear elasticity is a special case of Eq. (2.70) and Eq. (2.72), where the tangential material stiffness matrix is equivalent to the constant constitutive matrix in Eq. (2.35): $\mathbf{D} \equiv \mathbf{C}$ and the tangential stiffness matrix corresponds to the initial stiffness matrix and remains constant with increasing displacements: $\mathbf{K}_e = \text{const}$.

For anisotropic materials the symmetry of the tangential stiffness matrix can break and a special handling is necessary for the solution of the global system of equations. Furthermore the application of the Gaussian integration scheme presented in section 2.2.4 is, for most nonlinear constitutive laws, only an approximation which necessitates the refinement of the element integration scheme or of the finite element discretization depending on the required accuracy.

2.3   Solution strategies

2.3.1   Linear analysis

To solve a system of linear equations

$$\mathbf{Ab} = \mathbf{c} \tag{2.73}$$

the Gaussian elimination algorithm can be applied (Bronstein and Semendjajew 1979). The high-performance linear algebra library LAPACK (Linear Algebra PACKage) (Anderson, E. et al. 1995) contains a very efficient implementation of this algorithm to solve the above equation. This library, which uses internally the BLAS package (Basic Linear Algebra Subprograms) (Hanson et al. 1973), has already been adapted to parallel computer architectures in the ScaLAPACK library (Blackford, L. S. et al. 1997). ScaLA-PACK can be used on shared and distributed memory systems with the PVM (Parallel Virtual Machine) (Geist, A. et al. 1994) or MPI (Message Passing Interface) (M.P.I. Forum 1994), (Snir et al. 1996) parallel environments. Communication between the processors is arranged by the BLACS package (Basic Linear Algebra Communication Subprograms) (Dongarra and van de Geijn 1991). Both the LAPACK and the ScaLAPACK library contain a large number of further algebraic routines, for example an eigenvalue and eigenvector decomposition of a quadratic matrix.

Within a Galerkin method the unknown displacements $\mathbf{d}$ can be determined directly for a linear elastic problem by solving the equation

$$\mathbf{Kd} = \mathbf{f}^{ext} \tag{2.74}$$

where the stiffness matrix $\mathbf{K}$ has, in general, sparse character due to the compact support of the shape functions. The solution of Eq. (2.74) can only be found if $\mathbf{K}$ is not singular. Furthermore the discretization of the differential equation presented in section 2.2.3 leads to a symmetric matrix $\mathbf{K}$. The standard procedure for solving Eq. (2.74) with a symmetric and non-singular matrix $\mathbf{K}$ is the $\bar{\mathbf{L}}\bar{\mathbf{D}}\bar{\mathbf{L}}^T$ factorization (Bathe 1996)

$$\mathbf{K} = \bar{\mathbf{L}}\bar{\mathbf{D}}\bar{\mathbf{L}}^T \tag{2.75}$$

where $\bar{\mathbf{L}}$ is a triangular matrix and $\bar{\mathbf{D}}$ has diagonal form. The unknown displacement vector $\mathbf{d}$ is then obtained by using the backward substitution

$$\begin{aligned} \bar{\mathbf{L}}\mathbf{v} &= \mathbf{f}^{ext} \\ \bar{\mathbf{D}}\bar{\mathbf{L}}^T\mathbf{d} &= \mathbf{v}. \end{aligned} \tag{2.76}$$

Another solution procedure is the Cholesky factorization scheme (Bathe 1996)

$$\mathbf{K} = \tilde{\mathbf{L}}\tilde{\mathbf{L}}^T$$
$$\tilde{\mathbf{L}} = \bar{\mathbf{L}}\bar{\mathbf{D}}^{\frac{1}{2}},$$
$$(2.77)$$

which needs slightly more operations than the $\bar{\mathbf{L}}\bar{\mathbf{D}}\bar{\mathbf{L}}^T$ factorization and is limited to systems with a positive definite matrix $\mathbf{K}$. Both methods are direct solution procedures. Iterative solution procedures are a second group, for example the conjugate gradient or the Gauss-Seidel method (Bathe 1996). In this section only direct solvers are discussed as they are independent of a start vector and have higher accuracy.

For an efficient and fast implementation of a factorization scheme the number of arising additional nonzero entries of the matrix $\mathbf{K}$ should be limited. This can be realized by reducing the band-width of $\mathbf{K}$. Several algorithms have been developed for this purpose, for example the Cuthill-McKee-algorithm (Cuthill and McKee 1969), a spectral reduction technique (Barnand et al. 1993) or a geometrical ordering approach (Bucher, C. et al. 2002). Due to the limitation of the band-width reduction algorithms a new group of methods has become popular in the recent years. It reduces the fill-in during the factorization process. With these methods the number of additional nonzero entries can be reduced more significantly for systems with higher band-width. One of the first algorithms of this group was the Approximate Minimum Degree (AMD) ordering (Davis et al. 1994). Today the METIS package (Karypis and Kumar 1998) is one of the most efficient fill-reducing orderings of sparse matrices.

In the course of this work different sequential and parallel direct solver libraries for sparse matrices have been investigated and implemented in the software package SLang. These solvers are a sequential sparse direct solver developed at the Czech University in Prague (Vondráček 2003) with Approximate Minimum Degree ordering, the MUltifrontal Massively Parallel Solver (MUMPS) (Amestoy et al. 2003), which uses MPI, and the OpenMP based PARallel DIrect SOlver (PARDISO) (Schenk and Gärtner 2004). The MUMPS package offers several built-in ordering algorithms, like an Approximate Minimum Degree and an Approximate Minimum Fill ordering, and furthermore an interface to the external ordering packages PORD (Schulze 2001) and METIS. PARDISO contains an Approximate Minimum Degree ordering and a METIS interface. The performance of these solvers is investigated and compared to the performance of the SLang implementation of the $\bar{\mathbf{L}}\bar{\mathbf{D}}\bar{\mathbf{L}}^T$ factorization solver with band-width reduction in section 2.4.1. Detailed information of the implementation of the MUMPS library in SLang using an external MPI-application are given in (Schrader 2004a).

2.3.2 Load controlled nonlinear analysis

Nonlinear finite element simulations determine the response of a structural model subject to a given loading history. This is usually done by applying the external load in several incremental steps. The response after each step is obtained by solving the global form of Eq. (2.67)

$$\mathbf{f}^{int}(\mathbf{d}) = \mathbf{f}^{ext} \tag{2.78}$$

in an iterative way. One of the most commonly used iterative methods for this purpose is the standard or modified Newton-Raphson procedure (Bathe 1996), which will be explained in this section.

In a load controlled analysis the external nodal force vector is given by a sequence $\mathbf{f}^{ext,(1)}, \mathbf{f}^{ext,(2)}, \mathbf{f}^{ext,(3)}, ...$, which was evaluated by using Eq. (2.55). The goal of this analysis is to find the corresponding nodal displacement vectors $\mathbf{d}^{(1)}, \mathbf{d}^{(2)}, \mathbf{d}^{(2)}, ...$ such that each couple $(\mathbf{d}^{(n)}, \mathbf{f}^{ext,(n)})$ fulfills Eq. (2.78). By starting with the known displacements of the previous load increment $\mathbf{d}^{(n)}$ the unknown displacement increment $\Delta\mathbf{d}^{(n+1)} = \mathbf{d}^{(n+1)} - \mathbf{d}^{(n)}$ has to be found by solving

$$\mathbf{f}^{int}(\mathbf{d}^{(n)} + \Delta\mathbf{d}^{(n+1)}) = \mathbf{f}^{ext,(n+1)}. \tag{2.79}$$

Eq. (2.79) can by linearized in the first iteration step according to Eq. (2.71) as

$$\mathbf{K}(\mathbf{d}^{(n)})\Delta\mathbf{d}^{(n+1,1)} = \mathbf{f}^{ext,(n+1)} - \mathbf{f}^{int}(\mathbf{d}^{(n)}) \tag{2.80}$$

where $\Delta\mathbf{d}^{(n+1,1)}$ is the first approximation of the unknown displacement increment assuming the initial displacement values to be $\mathbf{d}^{(n+1,0)} = \mathbf{d}^{(n)}$. Eq. (2.80) can be solved by using the linear solvers for sparse matrices mentioned in section 2.3.1 in the same manner as for Eq. (2.74).

The following iteration procedure reads for $i = 1, 2, 3, ...$

$$\begin{aligned} \mathbf{K}(\mathbf{d}^{(n+1,i-1)})\delta\mathbf{d}^{(n+1,i)} &= \mathbf{f}^{ext,(n+1)} - \mathbf{f}^{int}(\mathbf{d}^{(n+1,i-1)}) \\ \mathbf{d}^{(n+1,i)} &= \mathbf{d}^{(n+1,i-1)} + \delta\mathbf{d}^{(n+1,i)} \end{aligned} \tag{2.81}$$

where $\mathbf{d}^{(n+1,i)}$ is the displacement approximation after the i-th iteration in the load step $n+1$ and $\delta\mathbf{d}^{(n+1,i)}$ is the displacement correction applied in the i-th iteration. The accumulated displacement corrections during the iteration converge to the unknown displacement increment

$$\Delta\mathbf{d}^{(n+1)} = \lim_{i \to \infty} \Delta\mathbf{d}^{(n+1,i)} \tag{2.82}$$

with

$$\Delta \mathbf{d}^{(n+1,i)} = \sum_{k=1}^{i} \delta \mathbf{d}^{(n+1,i)}. \tag{2.83}$$

In a numerical implementation of this method the algorithm is stopped after a finite number of cycles i if the convergence criteria are satisfied. The last approximation is used as the new equilibrium state

$$\Delta \mathbf{d}^{(n+1)} \approx \Delta \mathbf{d}^{(n+1,i)}. \tag{2.84}$$

Three common criteria for the convergence of an iteration process are described in this section according to (Bathe 1996). The first one analyzes the displacement increment after each iteration step

$$\frac{\|\delta \mathbf{d}^{(n+1,i)}\|}{\|\mathbf{d}^{(n+1,i)}\|} \leq \epsilon_D. \tag{2.85}$$

The second criterion is fulfilled if the normalized imbalance forces are less than a given tolerance

$$\frac{\|\mathbf{f}^{ext,(n+1)} - \mathbf{f}^{int}(\mathbf{d}^{(n+1,i)})\|}{\|\mathbf{f}^{ext,(n+1)} - \mathbf{f}^{int}(\mathbf{d}^{(n)})\|} \leq \epsilon_F. \tag{2.86}$$

Another criterion investigates the increment of the global energy

$$\frac{\left[\mathbf{f}^{ext,(n+1)} - \mathbf{f}^{int}(\mathbf{d}^{(n+1,i-1)})\right]^T \delta \mathbf{d}^{(n+1,i)}}{\left[\mathbf{f}^{ext,(n+1)} - \mathbf{f}^{int}(\mathbf{d}^{(n)})\right]^T \Delta \mathbf{d}^{(n+1,1)}} \leq \epsilon_E. \tag{2.87}$$

These criteria can be used individually or combined for all iterative solution procedures presented in this section.

In the modified Newton-Raphson method the stiffness matrix in Eq. (2.81) is not evaluated in the iteration steps but is taken from the last equilibrium state $\mathbf{K}(\mathbf{d}^{(n+1,i-1)}) = \mathbf{K}(\mathbf{d}^{(n)})$. Thus the rate of convergence slows down, but the most time consuming processes in one iteration step, the evaluation and the factorization of the stiffness matrix, has to be done only once for each load increment, which leads to a more efficient solution procedure for weakly nonlinear problems. A further simplification is the initial stiffness method, where the stiffness matrix is taken from the initial state of the structure $\mathbf{K}(\mathbf{d}^{(n+1,i-1)}) = \mathbf{K}(\mathbf{d}^{(0)})$. For strongly nonlinear problems such as those investigated in this work, the application of the modified Newton-Raphson or the initial stiffness method may lead to convergence problems, thus the full Newton-Raphson method is more promising for such investigations.

2.3.3   Displacement control

Structures consisting of materials with ideal-plastic or softening behavior have in general a certain load-carrying capacity. If load controlled algorithms are used for the analysis, the post-peak behavior cannot be investigated. For this reason displacement controlled methods have been developed. In this section the direct displacement control is presented according to the details in (Jirásek and Bažant 2002).

In the direct displacement control approach the nodal displacements are divided into two groups $\mathbf{d} = [\mathbf{d}_1, \mathbf{d}_2]^T$, where the first one contains the unknown displacements $\mathbf{d}_1$ and the second one the prescribed displacements $\mathbf{d}_2$ at the controlled degrees of freedom. According to this assumption the external and internal force vectors are partitioned in the same manner, $\mathbf{f}^{ext} = [\mathbf{f}_1^{ext}, \mathbf{f}_2^{ext}]^T$ and $\mathbf{f}^{int} = [\mathbf{f}_1^{int}, \mathbf{f}_2^{int}]^T$, respectively. For simplicity (Jirásek and Bažant 2002) assumed the external forces $\mathbf{f}_1^{ext}$ corresponding to the unknown displacements $\mathbf{d}_1$ to be equal to zero. Thus all external forces acting on the structure are represented by the reactions $\mathbf{f}_2^{ext}$ at the supports. The global equilibrium equation given in Eq. (2.78) reads

$$
\begin{aligned}
\mathbf{f}_1^{int}(\mathbf{d}_1, \mathbf{d}_2) &= \mathbf{0}, \\
\mathbf{f}_2^{int}(\mathbf{d}_1, \mathbf{d}_2) &= \mathbf{f}_2^{ext}.
\end{aligned}
\tag{2.88}
$$

The second part of Eq. (2.88) can be obtained directly after solving the first part, which is done iteratively. Introducing the partitioned stiffness matrix

$$
\mathbf{K} = \frac{\partial \mathbf{f}^{int}}{\partial \mathbf{d}} = \left[\begin{array}{cc} \dfrac{\partial \mathbf{f}_1^{int}}{\partial \mathbf{d}_1} & \dfrac{\partial \mathbf{f}_1^{int}}{\partial \mathbf{d}_2} \\[2ex] \dfrac{\partial \mathbf{f}_2^{int}}{\partial \mathbf{d}_1} & \dfrac{\partial \mathbf{f}_2^{int}}{\partial \mathbf{d}_2} \end{array} \right] = \left[\begin{array}{cc} \mathbf{K}_{11} & \mathbf{K}_{12} \\ \mathbf{K}_{21} & \mathbf{K}_{22} \end{array} \right]
\tag{2.89}
$$

obtains the linearized equation

$$
\mathbf{f}_1^{int,(n)} + \mathbf{K}_{11}^{(n)} \Delta \mathbf{d}_1^{(n+1,1)} + \mathbf{K}_{12}^{(n)} \Delta \mathbf{d}_2^{(n+1,1)} = \mathbf{0}.
\tag{2.90}
$$

Due to the known displacement increment $\Delta \mathbf{d}_2^{(n+1)} = \mathbf{d}_2^{(n+1)} - \mathbf{d}_2^{(n)}$, Eq. (2.90) can be rewritten as

$$
\mathbf{K}_{11}^{(n)} \Delta \mathbf{d}_1^{(n+1,1)} = -\mathbf{f}_1^{int,(n)} - \mathbf{K}_{12}^{(n)} \Delta \mathbf{d}_2^{(n+1)}.
\tag{2.91}
$$

The iteration process is performed for $i = 1, 2, 3, \ldots$ in the form

$$
\begin{aligned}
\mathbf{K}_{11}^{(n+1,i-1)} \delta \mathbf{d}_1^{(n+1,i)} &= -\mathbf{f}_1^{int,(n+1,i-1)} - \mathbf{K}_{12}^{(n+1,i-1)} \delta \mathbf{d}_2^{(n+1,i)} \\
\mathbf{d}^{(n+1,i)} &= \mathbf{d}^{(n+1,i-1)} + \delta \mathbf{d}^{(n+1,i)}
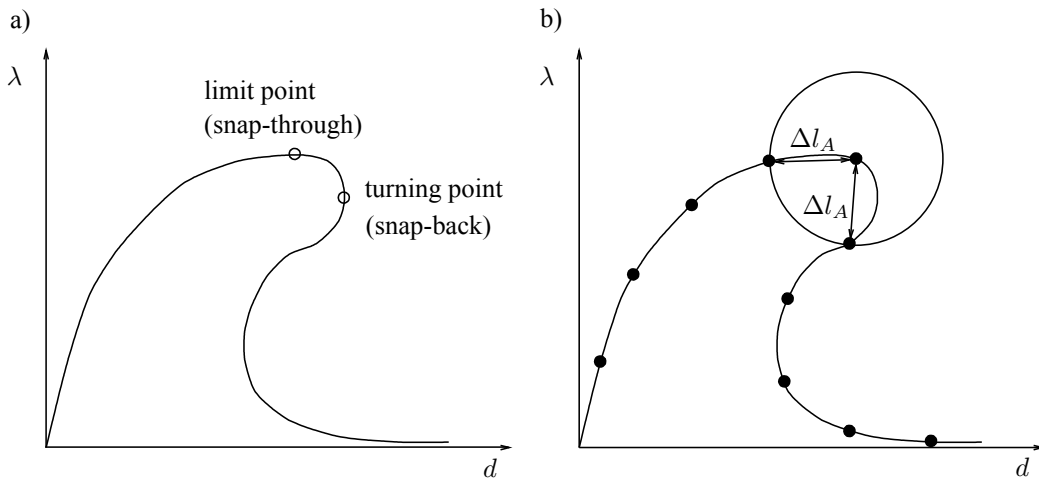\end{aligned}
\tag{2.92}
$$

Figure 2.4. a) Load displacement diagram for a single degree of freedom system with snap-back, b) arc-length method with equilibrium states (Jirásek and Bažant 2002)

where

$$
\begin{aligned}
\mathbf{d}_1^{(n+1,0)} &= \mathbf{d}_1^{(n)} \\
\mathbf{d}_2^{(n+1,0)} &= \mathbf{d}_2^{(n)} \\
\delta\mathbf{d}_2^{(n+1,1)} &= \mathbf{d}_2^{(n+1)} - \mathbf{d}_2^{(n)} \\
\delta\mathbf{d}_2^{(n+1,i)} &= \mathbf{0} \quad \text{for} \quad i = 2, 3, ...
\end{aligned}
\tag{2.93}
$$

until the convergence criteria are satisfied.

2.3.4 Arc-length method

Direct displacement control can not be applied, if structures are investigated where several different points or surfaces are loaded and the relation between the displacements of the belonging nodes can not be formulated in advance. Furthermore this displacement control approach can not represent the load-displacement curve including a turning or snap-back point as shown in Fig. 2.4. This snap-back effect can occur if a localized softening takes place in a mainly elastically deformed structure. In section 2.4.2, a simple snap-back problem is presented. The arc-length method can handle such snap-back behavior and can obtain the post-peak load-displacement relation by using a defined external loading vector. In general, linear loading

$$
\mathbf{f}^{ext}(\lambda) = \bar{\mathbf{f}}_0 + \lambda\bar{\mathbf{f}}
\tag{2.94}
$$

is assumed with a constant component $\bar{\mathbf{f}}_0$ and proportionally increasing component $\lambda\bar{\mathbf{f}}$, where λ is the scalar loading factor. In (Crisfield 1981) a spherical arc-length

$$
\Delta l_A = \sqrt{\Delta\mathbf{d}^T\Delta\mathbf{d} + (c\Delta\lambda)^2}
\tag{2.95}
$$

is introduced where $\Delta\mathbf{d}$ is the unknown displacement increment and $\Delta\lambda$ is the unknown load factor increment in one solution step. The scaling factor c defines the relation between displacements and load increments and can be obtained for example from the assumption that the contributions of load and displacements should be equal as long as the structure remains linear elastic (Jirásek and Bažant 2002). This leads to

$$c = \sqrt{\mathbf{d}_{elast}^T \mathbf{d}_{elast}} \tag{2.96}$$

where $\mathbf{d}_{elast}$ is the solution of

$$\mathbf{K}_{elast}\mathbf{d}_{elast} = \bar{\mathbf{f}}. \tag{2.97}$$

The equations of equilibrium

$$\mathbf{f}^{int}(\mathbf{d}) = \bar{\mathbf{f}}_0 + \lambda\bar{\mathbf{f}} \tag{2.98}$$

and the definition of the arc-length in Eq. (2.95) gives a set of $N_{DOF} + 1$ nonlinear equations, where N_{DOF} is the number of nodal degrees of freedom, which is solved iteratively. Eq. (2.98) can be linearized in the i-iteration as

$$\mathbf{K}^{(n+1,i-1)}\delta\mathbf{d}^{(n+1,i)} = \bar{\mathbf{f}}_0 + \lambda^{(n+1,i-1)}\bar{\mathbf{f}} - \mathbf{f}^{int,(n+1,i-1)} + \delta\lambda^{(n+1,i)}\bar{\mathbf{f}} \tag{2.99}$$

with the unknown displacement correction $\delta\mathbf{d}^{(n+1,i)}$ and the unknown load factor correction $\delta\lambda^{(n+1,i)}$. By solving the separated equations

$$\begin{aligned}
\mathbf{K}^{(n+1,i-1)}\delta\mathbf{d}_0 &= \bar{\mathbf{f}}_0 + \lambda^{(n+1,i-1)}\bar{\mathbf{f}} - \mathbf{f}^{int,(n+1,i-1)} \\
\mathbf{K}^{(n+1,i-1)}\delta\mathbf{d}_{\mathbf{f}} &= \bar{\mathbf{f}}
\end{aligned} \tag{2.100}$$

the displacement correction is obtained as

$$\delta\mathbf{d}^{(n+1,i)} = \delta\mathbf{d}_0 + \delta\lambda^{(n+1,i)}\delta\mathbf{d}_{\mathbf{f}}. \tag{2.101}$$

By substituting this expression in the modified formulation of Eq. (2.95)

$$\begin{aligned}
\left(\Delta\mathbf{d}^{(n+1,i-1)} + \delta\mathbf{d}^{(n+1,i)}\right)^T &\left(\Delta\mathbf{d}^{(n+1,i-1)} + \delta\mathbf{d}^{(n+1,i)}\right) \\
&+ c^2\left(\Delta\lambda^{(n+1,i-1)} + \delta\lambda^{(n+1,i)}\right)^2 = \left(\Delta l_A\right)^2,
\end{aligned} \tag{2.102}$$

with

$$\Delta\mathbf{d}^{(n+1,i)} = \sum_{k=1}^{i} \delta\mathbf{d}^{(n+1,i)},$$

$$\Delta\lambda^{(n+1,i)} = \sum_{k=1}^{i} \delta\lambda^{(n+1,i)},$$

(2.103)

a quadratic equation for the unknown load factor correction $\delta\lambda^{(n+1,i)}$ is obtained. The correct root for this solution, which is very important to avoid doubling back, is chosen in general such that the corresponding incremental displacements $\Delta\mathbf{d}_1^{(n+1,i)}$ or $\Delta\mathbf{d}_2^{(n+1,i)}$ encircle the smaller angle with the displacement increments of the last iteration step (Crisfield 1981)

$$\angle(\Delta\mathbf{d}_{1,2}^{(n+1,i)}\Delta\mathbf{d}^{(n+1,i-1)}) = \min.$$

(2.104)

If sharp snap-backs are investigated with the spherical arc-length method, convergence problems may occur at the turning point. Then the application of the cylindrical arc-length method, where the scaling factor c is taken as zero, is more promising (Crisfield 1983). In this work a further stabilized technique, the cylindrical arc-length method with minimal residues (Hellweg and Crisfield 1998) is applied. There the solution is taken from this value of $\delta\lambda_{1,2}^{(n+1,i)}$ where the corresponding internal force vector has the minimal difference from the external forces

$$\|\bar{\mathbf{f}}_0 + (\lambda^{(n)} + \Delta\lambda_{1,2}^{(n+1,i)})\bar{\mathbf{f}} - \mathbf{f}^{int}(\mathbf{d}^{(n)} + \Delta\mathbf{d}_{1,2}^{(n+1,i)})\| = \min.$$

(2.105)

2.3.5   Acceleration of convergence using the line search method

The line search method is an iterative technique to accelerate the convergence of nonlinear solution algorithms. This method can be applied to load and displacement controlled analyses in the same manner as for the arc-length method. If the standard Newton-Raphson iteration does not converge, which can be caused by several reasons e.g. if the nonlinear function contains inflection points, the line search method may achieve convergence in most cases.

In this section the line search approach is presented according to (Reich 1993). This method automatically under- or over-relaxes the obtained displacement correction $\delta\mathbf{d}^{(n+1,i)}$ of the actual global iteration step i. The displacement correction is multiplied by a scalar value s^k, which defines the amount of under- or over-relaxing. Thus the update of the total displacements reads

$$\mathbf{d}^{(n+1,i+1,k)} = \mathbf{d}^{(n+1,i)} + s^k\delta\mathbf{d}^{(n+1,i)}. \tag{2.106}$$

For $k = 0$ and $k = 1$ the values of s^k are 0 and 1, respectively. Therefore

$$\begin{aligned}
\mathbf{d}^{(n+1,i+1,0)} &= \mathbf{d}^{(n+1,i)}, \\
\mathbf{d}^{(n+1,i+1,1)} &= \mathbf{d}^{(n+1,i+1)}.
\end{aligned} \tag{2.107}$$

The amount of under- or over-relaxing is determined by enforcing an orthogonality condition between the displacement corrections $\delta\mathbf{d}^{(n+1,i)}$ and the unbalanced forces $\mathbf{R}^{(i+1)}$. This is realized by defining a scalar value g^k representing the iterative change in energy as

$$g^k = \delta\mathbf{d}^{(n+1,i)}\mathbf{R}^{(i+1,k)} \tag{2.108}$$

with

$$\mathbf{R}^{(i+1,k)} = \mathbf{f}^{ext} - \mathbf{f}^{int}(\mathbf{d}^{(n+1,i+1,k)}). \tag{2.109}$$

The object of the line search method is to find s^k such that g^k is zero. An estimate of s^{k+1} is determined using an extrapolation procedure

$$s^{k+1} = s^k\frac{g^0}{g^0 - g^k}. \tag{2.110}$$

After s^{k+1} has been obtained $\mathbf{d}^{(n+1,i+1,k+1)}$, $\mathbf{f}^{int}(\mathbf{d}^{(n+1,i+1,k+1)})$ and $\mathbf{R}^{(i+1,k+1)}$ are computed for the next line search iteration step. The iteration terminates if

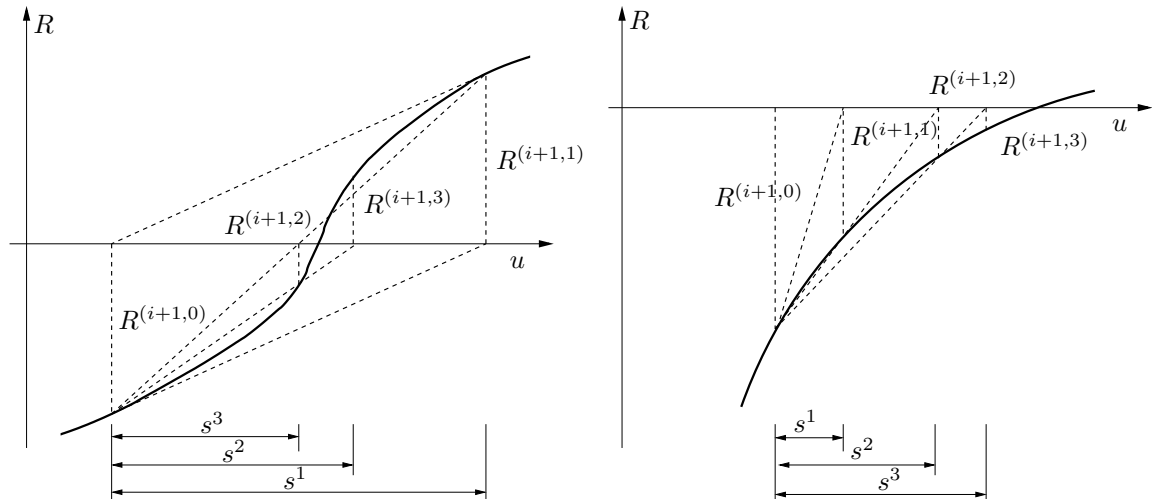$$\frac{|g^k|}{|g^0|} < TOL \tag{2.111}$$

Figure 2.5. Line search method for a SDOF system a) improves standard Newton-Raphson method near an inflection point and b) accelerates modified Newton-Raphson method

where the tolerance TOL is generally chosen between 0.5 and 0.8. If Eq. (2.111) is not fulfilled after three steps, the iteration is canceled and the value of s^k, where $|g^k/g^0|$ was minimal, is used to obtain the final displacement vector $\mathbf{d}^{(n+1,i+1,k)}$.

In Fig. 2.5a the line search algorithm is shown for a single-degree-of-freedom (SDOF) system near an inflection point where the standard Newton-Raphson procedure does not converge. In Fig. 2.5b the principle of the acceleration of the modified Newton-Raphson method is presented. In this work the line search method was used for the investigated problems in combination with the standard Newton-Raphson method.

2.4   Examples

The numerical examples in this section have been chosen to demonstrate the differences of the described direct solvers for sparse matrices with respect to their efficiency. Furthermore the reason for the appearance of the snap-back effect is shown on a simplified example.

2.4.1   Performance of direct sparse matrix solvers
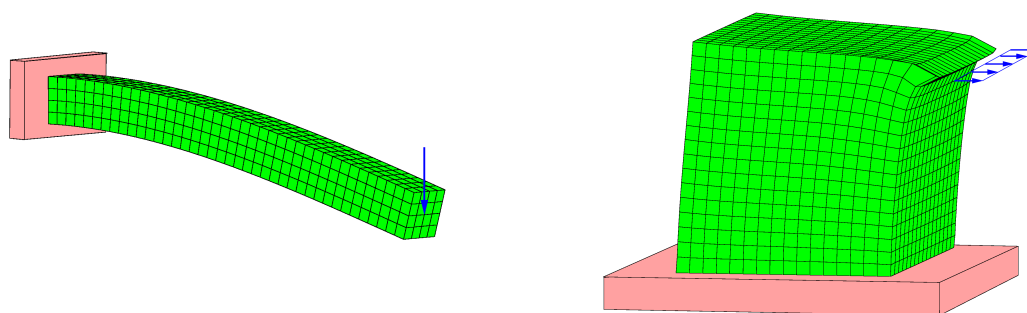

Figure 2.6. Investigated cantilever and compact block with load and boundary conditions

In this section the performance of the different direct sparse matrix solvers mentioned in section 2.3.1 will be investigated on two simple structures. The first system is a cantilever with a length of $1m$ and a quadratic cross section of $0.1m \times 0.1m$, which is loaded by a single load of $1N$ as shown in Fig. 2.6. The second investigated structure is a compact block with $1m$ edge length. The assumed load and boundary conditions for this system are shown additionally in Fig. 2.6. The linearly distributed load is taken with $16N/m$. Both systems have been analyzed using 27-node hexahedral finite elements with quadratic shape functions. For each structure two different discretization levels have been investigated: the cantilever was modeled with 640 elements and 6561 nodes, resulting in 19612 degrees of freedom (DOFs) and with 5120 finite elements, 46529 nodes and 139516 DOFs and the compact block was discretized with 512 elements, 4913 nodes and 13872 DOFs and 4096 elements, 35937 nodes and 106928 DOFs. The material has been assumed to be linear-elastic and the properties are taken as $E = 10^3 N/m^2$ for Young's modulus and $\nu = 0.3$ for Poisson's ratio.

These two structures were chosen to clarify the differences of the solver performance for a system with small and a system with high band-width. In Fig. 2.7 the assignment of the lower symmetric part of the stiffness matrices optimized using the spectral reduction algorithm are displayed.

In Table 2.1 the required computational times for one factorization and solution step with initial ordering are listed. The calculations have been carried out using the SLang implementations of the $\bar{\mathbf{L}}\bar{\mathbf{D}}\bar{\mathbf{L}}^T$ solver with geometrical, spectral and Cuthill-McKee band-
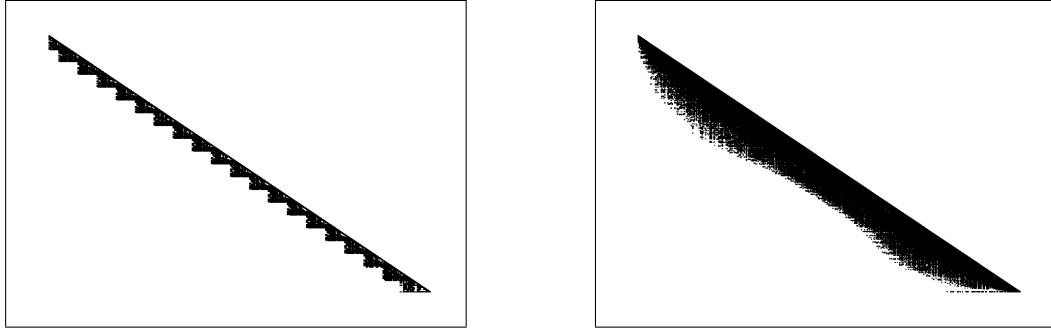
Figure 2.7. Optimized stiffness matrix assignments for the cantilever and the compact block model using spectral reduction

width reduction, the Vondráček solver with AMD ordering and the MUMPS and PAR-DISO solvers with METIS ordering. The values have been obtained on an AMD Opteron computer with 2.2 GHz using one processor and Linux. The missing values (-) indicate

DOFs	Geom. red.	Spectral red.	Cuthill	Vondráček	MUMPS	PARDISO
Cantilever						
19612 a)	7.87s	6.96s	11.03s	3.33s	1.99s	1.69s
19612 b)	0.05s	1.64s	2.88s	0.74s	1.73s	1.71s
139516 a)	656.38s	-	1322.11s	450.83s	70.76s	71.24s
139516 b)	0.10s	-	162.9s	12.16s	17.25s	17.20s
Compact block						
13872 a)	55.37s	41.72s	408.82s	8.66s	2.84s	2.44s
13872 b)	0.04s	0.77s	0.58s	0.79s	1.17s	1.15s
106944 a)	-	-	-	1671.96s	136.22s	141.18s
106944 b)	-	-	-	8.16s	12.10s	13.25s

Table 2.1. Comparison of computational time for the different matrix solvers (a: factorization and solution, b: ordering)

the unsuccessful factorization of the solver caused by memory problems. The table clearly indicates that the solvers which use a fill-in reducing ordering (Vondráček, MUMPS and PARDISO) have much better performance compared to the solvers with band-width reduction, especially for the compact block example, where a very high band-width exists. Furthermore the METIS ordering leads to an even faster factorization than using the AMD algorithm. Both solvers with METIS ordering (MUMPS and PARDISO) have a similar performance for the investigated examples. Their performance data have been obtained by using the LAPACK and BLAS implementation of the Intel Math Kernel Library (MKL) (Intel Corporation 2004). These routines are mainly used by the MUMPS and PARDISO solvers, thus the efficiency of these solvers is much higher with the MKL than using self-compiled LAPACK and BLAS libraries.

By means of the structures presented above the scalability of the parallel solvers, MUMPS and PARDISO, was investigated on a shared memory system, the SGI Altix 3000 super computer with 40 Itanium II processors with 900 Mhz by using 64-bit Linux.
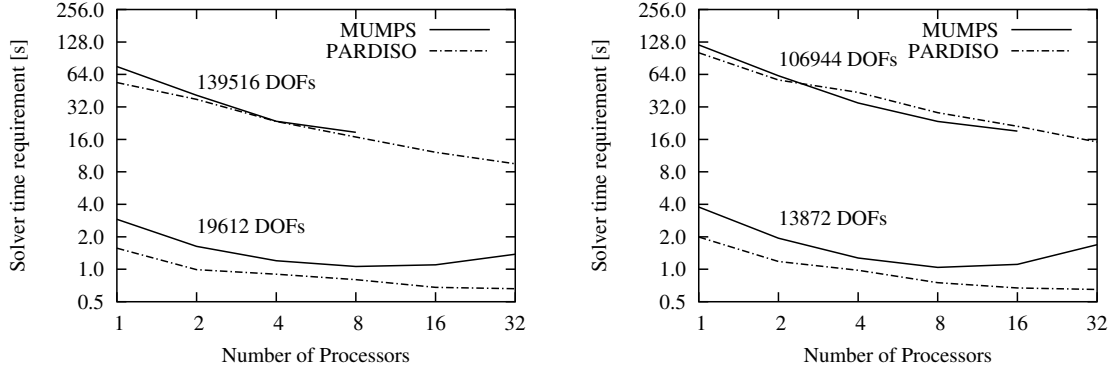
Figure 2.8. Required computational time for one factorization and solution step of the cantilever and the compact block model

Both solvers use the sequential ordering package METIS on the master processor and do the factorization and solution distributed on all involved processors. In Fig. 2.8 the obtained computational time for one factorization and solution step is shown depending on the number of processor for both structures. The figure indicates that both solvers scale very well for the larger models even for higher numbers of processors. The OpenMP-based PARDISO solver shows a better scaling behavior above 8 processors than the MPI-based MUMPS solver, especially for the smaller models. More investigations with the presented sequential and parallel solvers can be found in (Most and Eckardt 2004) and (Schrader 2004a).

Furthermore a parallel MPI-based implementation of the METIS package, ParMETIS, can be used to reduce the computational time required for the ordering on parallel computers. In (Schrader 2004b) an interface to connect the ParMETIS package with the MUMPS solver within SI$^{\mathrm{ang}}$ was developed. The application of ParMETIS reduces the required time for ordering on the one hand, but the scaling of the MUMPS factorization is reduced on the other hand. Thus no significant overall performance profit could be observed for most investigated systems.

2.4.2   Simulation of a snap-back problem using the arc-length method

In this example the formation of a snap-back effect is presented on a simple tensile bar. The tensile bar, as shown in Fig. 2.9, has a cross section of $0.1m \times 0.1m$ and a localization zone orthogonal to the loading axis, which is modeled by a single two-dimensional four-node interface element (Appendix A.2). The continuum is modeled linear elastically with standard four-node 2D solid elements by assuming $E = 2.5 \cdot 10^{10} N/m^2$ for Young's modulus and $\nu = 0.2$ for Poisson's ratio. In the interface surface a simple linear softening model is used for the relation between the normal stress σ_N and the relative displacement Δu_N, which is shown in Fig. 2.9. For this model the elastic tangent modulus is taken with $k_{N,elast} = 10^{11} N/m^3$, the maximum stress with $\sigma_{N,max} = 2 \cdot 10^6 N/m^2$ and the softening modulus with $k_{N,soft} = -2.5 \cdot 10^{10} N/m^3$. The relation between the applied load F and
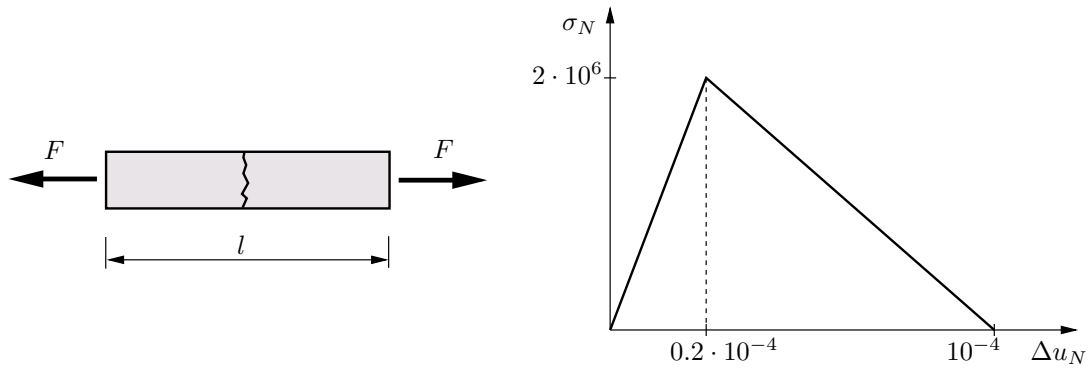
Figure 2.9. Tensile bar with localization zone and belonging interface softening model
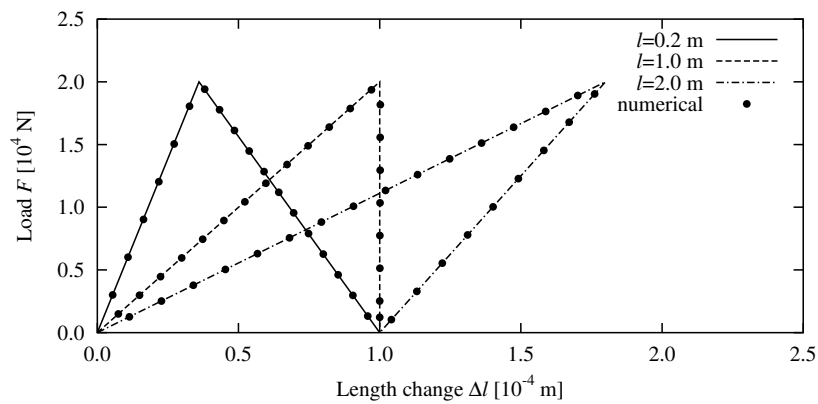

Figure 2.10. Numerically (dots) and analytically (lines) obtained relations between the load F and the length change Δl of the bar depending on the increasing length l

the corresponding change of the bar length Δl is investigated depending on the increasing bar length l, by using the cylindrical arc-length method with a constant arc-length of $\Delta l_A = 5 \cdot 10^{-5} m$. Fig. 2.10 shows the analytical and numerical values for different bar lengths. The figure indicates that with increasing l the elastic energy of the bar at the limit point increases, but the total inelastic energy, which is released in the interface zone in this process, remains constant. This is the reason for the snap-back effect, where the maximum elastic energy in the system, which is reversible, exceeds the inelastic energy released in the interface zone.

Chapter 3

Meshless methods

Conventional numerical methods, like the Finite Element Method, need a predefinition of the node connectivity, since they rely on a mesh. During the last two decades a new class of numerical methods was developed, which approximates partial differential equations based only on a set of nodes without the need for an additional mesh. Today a huge number of different meshless methods are available, but here only a brief overview is given of the most common methods. Several state-of-the-art-reports, e.g. (Duarte 1995), (Belytschko et al. 1996), (Li and Liu 2002) and (Fries and Matthies 2003), give more detailed access to this field.

The most important feature of meshless methods compared to mesh-based approaches is the absence of a mesh, so they are not alignment sensitive. Furthermore the connectivity of the nodes is determined at run-time, which leads to a much simpler implementation of adaptive schemes. No initial mesh generation is necessary at the beginning of the calculation, which is still not a fully automatic process in mesh-based methods, especially for complex three-dimensional structures. For problems with large deformations or moving boundaries meshless methods show several advantages since no remeshing is necessary, which degrades the accuracy of the numerical method due to the required projection between the meshes. Another important advantage is that the meshless shape functions can easily be constructed to have any desired order of continuity, thus no post-processing is necessary to obtain smooth strains etc.

In practice meshless methods are often more time-consuming than mesh-based methods, caused by the more complex shape functions which require a larger number of integration points. For every integration point the neighboring nodes have to be determined and several operations are necessary to calculate the shape function values. The global system of equations has in general a larger band-width than for comparable mesh-based methods. Another problem of most meshless methods is the imposition of essential boundary conditions, which is not straight-forward as the interpolation property is not fulfilled, and additional numerical effort is necessary to solve this problem.

In (Fries and Matthies 2003) a good classification of meshless and mesh-based meth-
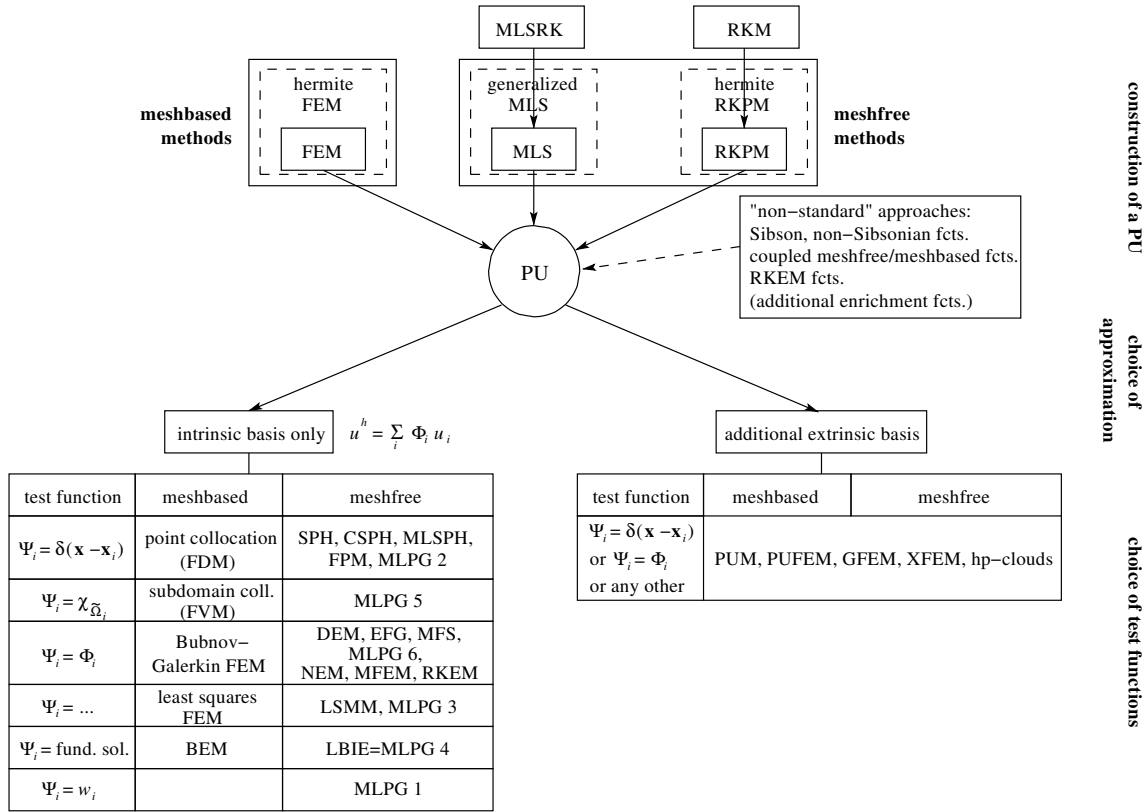
Figure 3.1. Classification of meshless and mesh-based methods (Fries and Matthies 2003)

ods is given, which is shown in Fig. 3.1. All mentioned methods in Fig. 3.1 construct a Partition of Unity (PU) of order n with different approximations. If in a weighted residual method a function u is approximated by a set of functions Φ_i as

$$u \approx u^h = \sum_i \Phi_i \tilde{u}_i, \tag{3.1}$$

and Φ_i builds a Partition of Unity of order n, it is possible to find an exact polynomial solution of a partial differential equation up to this order. Most of the meshless and mesh-based methods have a Partition of Unity of order 0 or 1, thus they can exactly represent a constant displacement field (better known as rigid body modes) or a linear displacement field. In Fig. 3.1 the methods are classified according to their choice of approximation, which can use the intrinsic basis only or add an extrinsic basis and the choice of test functions. The construction of the PU is mainly done using the Moving Least Squares (MLS) concept introduced by (Lancaster and Salkauskas 1981) and the Reproducing Kernel Method (RKM) (Liu et al. 1995). The MLS approach uses a local least squares approximation around a fixed point. Reproducing Kernel Methods are in general a class of operators that reproduce the function itself through integration over the domain. From the continuous form of the RKM approximation a discretized form, the Reproducing Kernel Particle Method (RKPM), was derived. One of the first and the simplest meshless meth-

ods was the Smooth Particle Hydrodynamics (SPH) method (Lucy 1977), which is similar to the RKPM concept. The SPH method was originally introduced for unbounded problems in astrophysics. Its application to bounded problems leads to major problems such as the "spurious boundary effect" and a tension instability, caused by the not fulfilled PU of the SPH shape functions. In the Corrected Smoothed Particle Hydrodynamics (CSPH) these problems have been solved partially by additional correction terms for the kernel functions and in the Moving Least Squares Particle Hydrodynamics (MLSPH) the MLS interpolation is used instead of the traditional kernel functions.

The most common meshless method is the Element-free Galerkin Method (EFG) (Belytschko et al. 1994), which uses the MLS interpolation to construct the trial and test functions. This method is similar to the Diffuse Element Method (DEM) proposed in (Nayroles et al. 1992), but some improvements have been realized. In the DEM the derivatives of the interpolant are computed be considering only the polynomial terms, where the coefficients, which depend on the position of the interpolation point, are assumed to be constant. In the EFG method the complete derivatives have been used in order to avoid problems caused by this incorrectness. Furthermore a much larger number of integration points was used in the EFG method, which are arranged in a background cell structure, in order to obtain more accurate results. Another improvement is the enforcement of the essential boundary conditions with special methods. This was not realized in the DEM and the boundary conditions were fulfilled only approximately.

In the Meshfree Local Petrov-Galerkin (MLPG) method (Atluri and Zhu 1998) a local weak form is used instead of the global form of a standard Galerkin approach. The local weak form is formulated over all local sub-domains and the integration is performed over these domains. Thus this method is called "truly meshless" in (Atluri and Zhu 1998), since no background mesh is required. Several special cases have been derived for the MLPG concept depending on the choice of the test functions. If the MLS interpolation is used as test functions the method is similar to EFG and DEM but with local weak form. The Method of Finite Spheres (MFS) proposed in (De and Bathe 2000) uses this approach in a modified form, whereby the so-called Shepard interpolation (Shepard 1968) instead of the MLS interpolation is applied. The choice of other test functions in the MLPG approach leads to the Least Squares Meshfree Method (LSMM) proposed by (Park and Youn 2001) or to the Local Boundary Integral Equation (LBIE), which is the meshless and local equivalent to the well-known Boundary Element Method (BEM).

The class of Partition of Unity Methods (PUM) contains meshless and mesh-based approaches, like the Partition of Unity FEM (PUFEM) proposed in (Melenk and Babuška 1996), which is regarded as a meshless method, and the Extended Finite Element Method (XFEM) (Moës et al. 1999), which is a local enrichment of the standard FEM. All of these methods are essentially identical, since a lower order PU is enriched to a higher order approximation. The shape functions are a product of the PU functions and higher order

local approximation functions. Thus more unknowns per node are needed as opposed to the MLS and RPKM approaches. Essential boundary conditions can be implemented by choosing an appropriate local approximation space as shown in (Babuška et al. 2002). In the Method of Finite Spheres the concept of Partition of Unity Methods was included to obtain a higher order approximation than the used Shepard interpolation.

A further meshless approach is the so-called hp-Clouds method (Duarte and Oden 1996). This method considers the h and p enrichment of the approximation space from the beginning. In this method the p-enrichment, which increases the polynomial degree of the functions used for the shape function computation, does not introduce discontinuities in contrast to the MLS and RKPM approaches. This is the main advantage of this method, which enables an individual enrichment of the approximation function for each node. The h-refinement is realized by adding more clouds of smaller size while keeping the shape function degree unchanged.

Alternative "non-standard" approaches to construct the partition of unity are the Sibsonian (Sibson 1980) and Non-Sibsonian interpolation (Belikov et al. 1997), which are used in the Natural Neighbor Galerkin Method (Sukumar et al. 1998) also called Natural Element Method (NEM). In this method a Voronoi diagram of the nodal domain is used to determine the neighbor nodes of an interpolation point. Since this Voronoi diagram is directly defined by the nodal positions, and no predefined mesh is necessary, and the obtained interpolation is smooth except at the nodes, this method is interpreted as a meshless method. A very important advantage compared to many other meshless methods is the fulfillment of the interpolation property, which enables the direct imposition of essential boundary conditions.

A kind of a coupled method is the Meshless Finite Element Method (MFEM) proposed in (Idelsohn et al. 2002), where the domain is uniquely divided into polyhedra which are handled as finite elements such that in each polyhedron the Non-Sibsonian interpolation is used. This concept destroys the smoothness of the interpolation which is one main advantage of meshless methods. Meshless ideas are only considered to find the shape functions of arbitrary elements. Some further methods have been developed by employing RKPM ideas to combine meshless and finite element methods, e.g. the Reproducing Kernel Element Method (RKEM) proposed by (Liu et al. 2004) and the Moving Particle Finite Element Method introduced by (Hao et al. 2002).

Due to the higher numerical effort of meshless methods compared to mesh-based approaches, in this work the use of meshless methods is limited to some parts of the domain, where their advantages, interpolation without a mesh, good accuracy, smooth derivatives and trivial adaptivity, are sufficient. These parts are sub-domains where cracks develop. Thus an adaptive coupling of meshless methods with the standard FEM in an automatic crack growth algorithm was one aim of this work. Because of this reason only approaches with intrinsic basis have been investigated. Two meshless methods were analyzed and en-

hanced for the crack growth simulation in this work. The first one is the Element-free Galerkin Method, which was chosen because of its widely successful application to mechanical problems. One of the biggest problems of this approach, the lack of the interpolation property, is solved in this work by a new weighting function type. As second method the Natural Neighbor Galerkin Method is favored, since in this method the interpolation property is automatically fulfilled and the shape function computation is in general simpler than in the EFG method. This method was not yet applied to automatic crack growth, thus its adaptation for this purpose, especially the modeling of non-convex domains, was necessary in this work.

In this chapter both enhanced methods will be presented in detail and their advantages and disadvantages will be discussed. The application in the framework of the developed crack growth algorithm will be shown in the next chapter.

3.1   Element-free Galerkin Method

3.1.1   Moving Least Squares interpolation

An arbitrary function u is interpolated at a point $\mathbf{x}$ by a polynomial as

$$u^h(\mathbf{x}) = \begin{bmatrix} 1 & x & y & x^2 & xy & y^2 & ... \end{bmatrix} \begin{bmatrix} a_1 \\ : \\ a_n \end{bmatrix} = \mathbf{p}^T(\mathbf{x})\mathbf{a} \qquad (3.2)$$

where $\mathbf{p}(\mathbf{x})$ is the base vector and $\mathbf{a}$ contains the coefficients of the polynomial. These coefficients are constant in the interpolation domain and can be determined directly if the number of supporting points m used for the interpolation is equivalent to the number of coefficients n. This principle is applied for example in the Finite Element Method, where an element-wise interpolation is realized. There the coefficients are simply given as

$$\mathbf{a} = \mathbf{P}^{T^{-1}}\tilde{\mathbf{u}} \qquad (3.3)$$

where $\tilde{\mathbf{u}}$ contains the function values at the supporting points

$$\tilde{\mathbf{u}} = \begin{bmatrix} \tilde{u}_1 & ... & \tilde{u}_m \end{bmatrix}^T \qquad (3.4)$$

and $\mathbf{P}$ consists of the values of the polynomial basis calculated at the supporting points

$$\mathbf{P} = \begin{bmatrix} P_1(\mathbf{x}_1) & P_1(\mathbf{x}_2) & ... & P_1(\mathbf{x}_m) \\ P_2(\mathbf{x}_1) & P_2(\mathbf{x}_2) & ... & P_2(\mathbf{x}_m) \\ \vdots & \vdots & \ddots & \vdots \\ P_n(\mathbf{x}_1) & P_n(\mathbf{x}_2) & ... & P_n(\mathbf{x}_m) \end{bmatrix}. \qquad (3.5)$$

The matrix $\mathbf{P}$ is not invertible for some configurations of the supporting points. In (Häussler-Combe 2001) this problem is investigated in detail and the requirements for a regular $\mathbf{P}$ are derived.

Within the "Moving Least Squares" (MLS) interpolation method (Lancaster and Salkauskas 1981) the number of supporting points m exceeds the number of coefficients n, which leads to an overdetermined system of equations. This kind of optimization problem can be solved by using a least squares approach

$$\mathbf{P}\tilde{\mathbf{u}} = \mathbf{P}\mathbf{P}^T\mathbf{a}(\mathbf{x}) \qquad (3.6)$$

with changing ("moving") coefficients $\mathbf{a}(\mathbf{x})$. If an interpolation technique should by used in a numerical method the compact support of the interpolation is essential for an efficient implementation. This was realized for the MLS-interpolation by introducing a distance
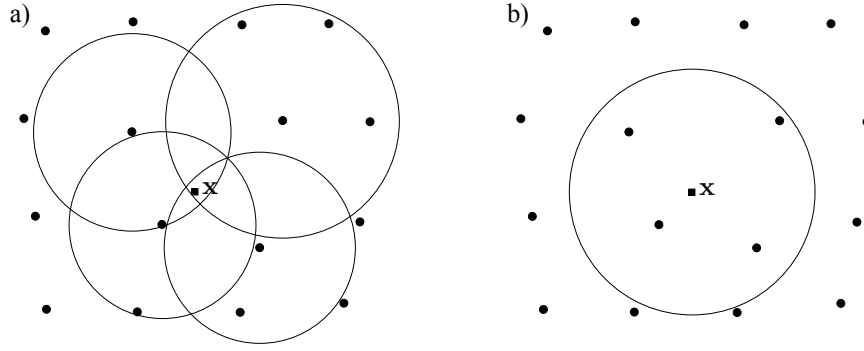
Figure 3.2. Neighbor search a) from the nodal positions with varying D and b) from the interpolation point with unique D

depending weighting function $w = w(s)$, where s is the standardized distance between the interpolation point and the considered supporting point

$$s_i = \frac{\|\mathbf{x} - \mathbf{x}_i\|}{D} \tag{3.7}$$

and D is the influence radius, which is defined as a numerical parameter. All types of functions can be used as weighting function $w(s)$ which have their maximum in $s = 0$ and vanish outside of the influence domain specified by $s = 1$. This distance depending weighting function type leads to circular and spherical influence domains in two and three dimensions, respectively. Alternatively to this type, rectangular or other shaped influence domains have been applied (Dolbow and Belytschko 1999), but the distance depending type is more general and mostly realized in efficient implementations. In the following section some common and new distance depending weighting functions will be presented and discussed. The nodes whose weighting function values do not vanish at the interpolation point are the influencing nodes of the interpolation point. The determination of these nodes is the most time consuming process in the Moving Least Squares interpolation. If the influence radius D is assumed to be equal for all nodes, the influencing nodes can be determined more efficient directly from the interpolation point, which is shown in Fig. 3.2. This procedure can be accelerated if additional neighbor information resulting from the integration cells are considered (see section 3.3.1).

Using the introduced weighting function, Eq. (3.6) is expanded to

$$\mathbf{B}(\mathbf{x})\tilde{\mathbf{u}} = \mathbf{A}(\mathbf{x})\mathbf{a}(\mathbf{x}), \tag{3.8}$$

where $\mathbf{A}(\mathbf{x})$ and $\mathbf{B}(\mathbf{x})$ are given as

$$\mathbf{A}(\mathbf{x}) = \mathbf{PW}(\mathbf{x})\mathbf{P}^T,$$
$$\mathbf{B}(\mathbf{x}) = \mathbf{PW}(\mathbf{x}), \tag{3.9}$$

and the diagonal matrix $\mathbf{W}(\mathbf{x})$ can be determined as

$$
\mathbf{W}(\mathbf{x}) = \begin{bmatrix} w(\mathbf{x} - \mathbf{x}_1) & 0 & \ldots & 0 \\ 0 & w(\mathbf{x} - \mathbf{x}_2) & \ldots & 0 \\ \vdots & \vdots & \ddots & \vdots \\ 0 & 0 & \ldots & w(\mathbf{x} - \mathbf{x}_m) \end{bmatrix}.
\tag{3.10}
$$

The interpolated value of the function u at $\mathbf{x}$ can be obtained by introducing the MLS shape functions

$$
u^h(\mathbf{x}) = \boldsymbol{\Phi}^{MLS}(\mathbf{x})\tilde{\mathbf{u}}, \quad \boldsymbol{\Phi}^{MLS}(\mathbf{x}) = \mathbf{p}^T(\mathbf{x})\mathbf{A}(\mathbf{x})^{-1}\mathbf{B}(\mathbf{x}).
\tag{3.11}
$$

Similar to Eq. (3.3) the invertibility of the matrix $\mathbf{A}(\mathbf{x})$ has to be assured, which is not automatically given if the interpolation point is in the influence domain of at least m nodes. This is fulfilled for a linear or quadratic polynomial basis in 2D if these nodes span two or three linear independent vectors, respectively, as derived in (Häussler-Combe 2001).

In contrast to the Finite Element Method the MLS interpolation does not pass through the nodal values caused by the applied least squares approach. This implies that the interpolation condition is not fulfilled,

$$
\Phi_i^{MLS}(\mathbf{x}_j) \neq \delta_{ij}.
\tag{3.12}
$$

Eq. (3.12) holds if regular weighting functions are used. In (Lancaster and Salkauskas 1981) it was pointed out that the interpolation property can be recovered by using weighting functions which are singular at the nodes. But this leads to many problems, e.g. if an interpolation point is too close to the singularity. In (Kaljevic and Saigal 1997) this problem was solved by additional basis functions, which leads to an additional numerical effort. Thus this technique was not applied in further studies.

The properties of the MLS interpolation depend mainly on the polynomial basis and on the weighting function. This means that every function of polynomial type can be reproduced exactly if the polynomial basis has the same order as the interpolated function, but the number of polynomial basis terms is limited for efficiency reasons because of the increasing numerical effort in inverting the matrix $\mathbf{A}(\mathbf{x})$ and the higher number of required supporting points in the influence domain of an interpolation point. The most simple polynomial basis is a constant function $\mathbf{p} = [1]$ which leads to the so-called Shepard interpolation (Shepard 1968)

$$
\Phi_i^{MLS,const}(\mathbf{x}) = \frac{w(\mathbf{x} - \mathbf{x}_i)}{\displaystyle\sum_{j=1}^{m} w(\mathbf{x} - \mathbf{x}_j)}.
\tag{3.13}
$$

This interpolation function represents the rigid body modes exactly, thus the following equation, which is known as Partition of Unity condition, is fulfilled for every interpolation point of the domain Ω if the polynomial basis contains the constant term

$$\sum_{i=1}^{m} \Phi_i^{MLS}(\mathbf{x}) = 1 \qquad \forall \mathbf{x} \in \Omega. \tag{3.14}$$

Furthermore, Linear Completeness, which means that a linear function can be represented and which is necessary for the convergence of a Galerkin method, can be obtained by using a linear polynomial basis. The smoothness of the MLS interpolation is directly related to the smoothness of the weighting function. If the weighting function has C^k continuity the interpolation has C^k continuity as well if the basis polynomial is also at least continuous as the weighting function (Duarte 1995).

The derivatives of the shape functions, which are necessary to compute the strain-displacement matrix, can be obtained from Eq. (3.11) as

$$\frac{\Phi_i}{\partial x_j} = \frac{\partial \mathbf{p}^T}{\partial x_j} \mathbf{A}^{-1} \mathbf{B} + \mathbf{p}^T \frac{\partial \mathbf{A}^{-1}}{\partial x_j} \mathbf{B} + \mathbf{p}^T \mathbf{A}^{-1} \frac{\partial \mathbf{B}}{\partial x_j} \tag{3.15}$$

where

$$\begin{aligned} \frac{\partial \mathbf{A}^{-1}}{\partial x_j} &= -\mathbf{A}^{-1} \frac{\partial \mathbf{A}}{\partial x_j} \mathbf{A}^{-1}, \\ \frac{\partial \mathbf{A}}{\partial x_j} &= \mathbf{P} \frac{\partial \mathbf{W}}{\partial x_j} \mathbf{P}^T, \\ \frac{\partial \mathbf{B}}{\partial x_j} &= \mathbf{P} \frac{\partial \mathbf{W}}{\partial x_j}. \end{aligned} \tag{3.16}$$

Higher order derivatives can be computed in closed form as well. The second derivatives, which might be necessary for adaptive algorithms by using strain gradients, can be derived as

$$\begin{aligned} \frac{\partial^2 \Phi_i}{\partial x_j \partial x_k} ={}& \frac{\partial^2 \mathbf{p}^T}{\partial x_i \partial x_j} \mathbf{A}^{-1} \mathbf{B} \\ &+ \frac{\partial \mathbf{p}^T}{\partial x_i} \left(\frac{\partial \mathbf{A}^{-1}}{\partial x_j} \mathbf{B} + \mathbf{A}^{-1} \frac{\partial \mathbf{B}}{\partial x_j} \right) + \frac{\partial \mathbf{p}^T}{\partial x_j} \left(\frac{\partial \mathbf{A}^{-1}}{\partial x_i} \mathbf{B} + \mathbf{A}^{-1} \frac{\partial \mathbf{B}}{\partial x_i} \right) \\ &+ \mathbf{p}^T \left(\frac{\partial^2 \mathbf{A}^{-1}}{\partial x_i \partial x_j} \mathbf{B} + \mathbf{A}^{-1} \frac{\partial^2 \mathbf{B}}{\partial x_i \partial x_j} + \frac{\partial \mathbf{A}^{-1}}{\partial x_i} \frac{\partial \mathbf{B}}{\partial x_j} + \frac{\partial \mathbf{A}^{-1}}{\partial x_j} \frac{\partial \mathbf{B}}{\partial x_i} \right) \end{aligned}$$
$$\tag{3.17}$$

where

$$\frac{\partial^2 \mathbf{A}^{-1}}{\partial x_j \partial x_k} = -\frac{\partial \mathbf{A}^{-1}}{\partial x_j}\frac{\partial \mathbf{A}}{\partial x_k}\mathbf{A}^{-1} - \mathbf{A}^{-1}\frac{\partial^2 \mathbf{A}}{\partial x_j \partial x_k}\mathbf{A}^{-1} - \mathbf{A}^{-1}\frac{\partial \mathbf{A}}{\partial x_j}\frac{\partial \mathbf{A}^{-1}}{\partial x_k},$$

$$\frac{\partial^2 \mathbf{A}}{\partial x_j \partial x_k} = \mathbf{P}\frac{\partial^2 \mathbf{W}}{\partial x_j \partial x_k}\mathbf{P}^T, \tag{3.18}$$

$$\frac{\partial^2 \mathbf{B}}{\partial x_j \partial x_k} = \mathbf{P}\frac{\partial^2 \mathbf{W}}{\partial x_j \partial x_k}.$$
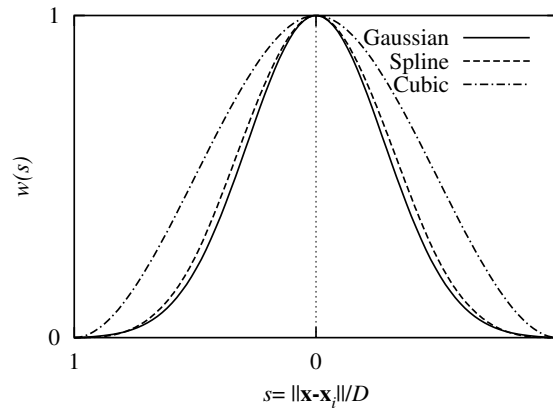
3.1.2 Weighting functions

Figure 3.3. Gaussian, cubic spline and cubic weighting functions

A large number of different weighting functions for the Moving Least Squares interpolation can be found in the literature. In (Fries and Matthies 2003) a good overview is given. In this section the most common weighting function types are discussed, which are the Gaussian weighting function, the cubic weighting function and a cubic spline weighting function. In Fig. 3.3 these function types are displayed depending on the standardized distance s. This section gives only a brief overview of these weighting types. More detailed information including the first and second derivatives can be found in the appendix.

The Gaussian weighting function is of exponential type and is given as (Häussler-Combe 2001)

$$w_G(s) = \begin{cases} \dfrac{e^{-\frac{s^2}{\alpha^2}} - e^{-\frac{1}{\alpha^2}}}{1 - e^{-\frac{1}{\alpha^2}}} & s \leq 1 \\ 0 & s > 1 \end{cases}. \tag{3.19}$$

The shape parameter α is often taken to be 0.4 (Karutz 2000). The first and second derivatives of this function at the boundary of the influence domain $s = 1$ are not exactly zero, thus C^1 and C^2 continuity can only be reached approximately using this weighting type. In (Levin 1998) a MLS interpolation with C^∞ continuity is presented. There the weighting function is of the same exponential type, but defined for the whole domain. Thus
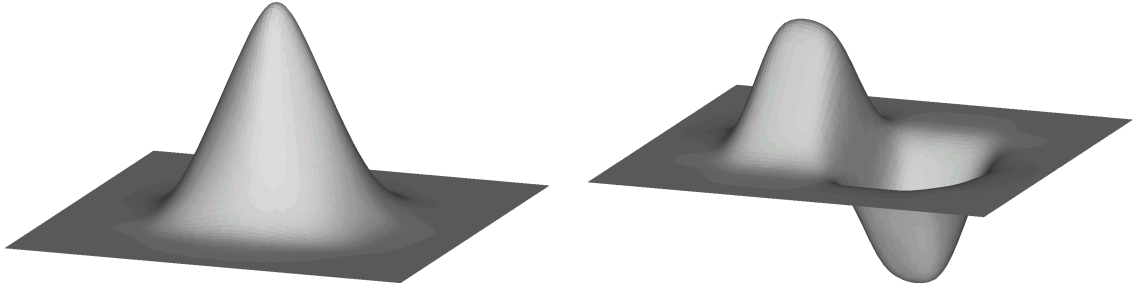
Figure 3.4. MLS shape function and first derivative for a regular set of nodes using the Gaussian weighting function

the shape functions do not have compact support and the interpolation is not applicable efficiently in a Galerkin approach. For data interpolation and response surface application it seems to be more attractive.

In Fig. 3.4 an MLS shape function with belonging first derivative obtained with the Gaussian weighting type is shown for a regular set of nodes.

The weighting function based on a cubic polynomial is given in (Karutz 2000) as

$$
w_C(s) = \begin{cases} 1 - 3s^2 + 2s^3 & s \leq 1 \\ 0 & s > 1 \end{cases}.
$$
(3.20)

With this type only C^1 continuity can be reached, the second derivative for $s = 1$ is not equal to zero.

In (De and Bathe 2001a) an improved weighting function type using a cubic spline is introduced, which leads to exact C^2 continuity

$$
w_S(s) = \begin{cases} 1 - 6s^2 + 6s^3 & s \leq \frac{1}{2} \\ 2 - 6s + 6s^2 - 2s^3 & \frac{1}{2} < s \leq 1 \\ 0 & s > 1 \end{cases}.
$$
(3.21)

Due to the applied least square approach explained in the previous section, the obtained nodal shape functions by using one of the presented weighting types have a strong dependence on the size of the influence radius D. In Fig. 3.5 a single nodal shape function of the middle node of a regular one-dimensional set of nodes is shown for increasing D. As weighting function the above described Gaussian type and a linear polynomial basis $\mathbf{p} = \begin{bmatrix} 1 & x \end{bmatrix}$ are used. The figure indicates that with increasing influence radius, the shape function error at each support point, caused by the approximative character of the MLS approach, increases dramatically. This problem is even more significant for irregular nodal setups. As a result the application of geometrical boundary conditions is difficult and additional numerical effort is necessary to fulfill these conditions. Different methods to impose the boundary conditions have been developed in recent years and will
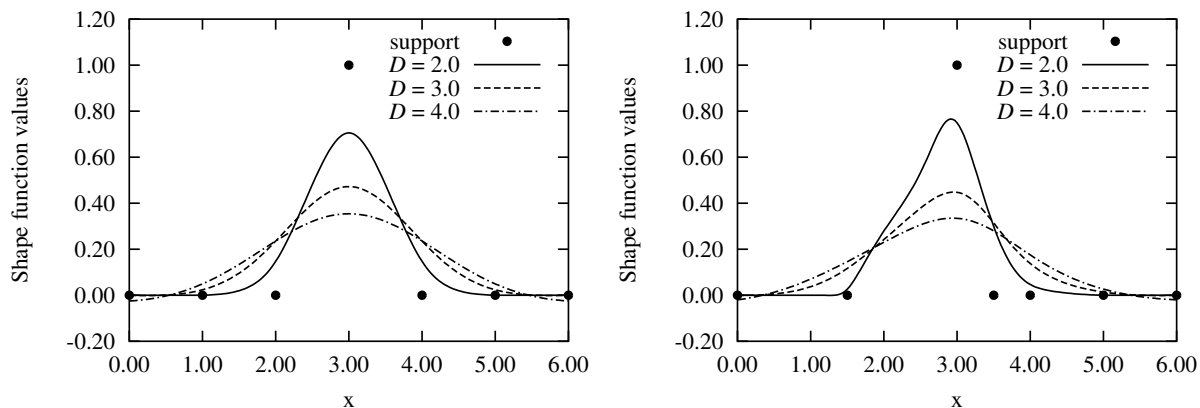
Figure 3.5. Nodal shape function of the MLS interpolation using Gaussian weighting and linear polynomial basis for regular and irregular sets of nodes

be explained in section 3.1.4.

Because of the presented problems using existing weighting function types, in this work a new weighting function was developed which enables the fulfillment of the MLS interpolation condition with very high accuracy without any additional numerical effort

$$\Phi_i^{MLS}\left(\mathbf{x}_j\right) \approx \delta_{ij}. \tag{3.22}$$

This can only be reached if Eq. (3.23) holds,

$$w_i\left(\mathbf{x}_j\right) \approx \delta_{ij}. \tag{3.23}$$

The weighting function value of a node i at an interpolation point $\mathbf{x}$ is introduced by the following regularized formulation

$$w_R(s_i) = \frac{\tilde{w}_R(s_i)}{\displaystyle\sum_{j=1}^{m} \tilde{w}_R(s_j)} \tag{3.24}$$

with

$$\tilde{w}_R(s) = \frac{\left(s^2 + \epsilon\right)^{-2} - \left(1 + \epsilon\right)^{-2}}{\epsilon^{-2} - \left(1 + \epsilon\right)^{-2}}; \quad \epsilon \ll 1. \tag{3.25}$$

This weighting function has a singularity at $s = 0$ if $\epsilon = 0$, which leads to an exact fulfillment of the interpolation conditions as already mentioned in the previous section. In this work this singular function is regularized by a regularization parameter ϵ, which has to be chosen small enough to fulfill Eq. (3.23) with high accuracy, but large enough to obtain a regular, differentiable function at $s = 0$ within the machine precision. In this
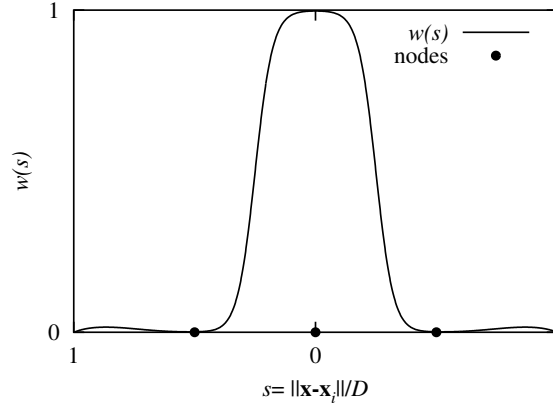
Figure 3.6. Regularized weighting function for a single node with two neighbor nodes

work it is recommended to use the value

$$\epsilon = 10^{-5}. \tag{3.26}$$

In Fig. 3.6 the regularized weighting function is displayed as a function of the standard-ized distance s and the position of the supporting points. The maximum weighting function error at these points in the interpolation domain Ω can be approximated by assuming

$$s_{min}^2 = \frac{\|\mathbf{x}_i - \mathbf{x}_j\|_{min}^2}{D^2} \gg \epsilon \tag{3.27}$$

as

$$|w_i(\mathbf{x}_j) - \delta_{ij}|_{max} \approx \left((s_{min})^{-4} - 1\right) \cdot \epsilon^2 \tag{3.28}$$

where $\|\mathbf{x}_i - \mathbf{x}_j\|_{min}$ specifies the minimal distance between two nodes. The detailed derivation is given in the appendix.

In order to reduce the numerical effort of the shape function computation a simplification of Eq. (3.24) in combination with Eq. (3.11) can be made as

$$\begin{aligned}
\mathbf{\Phi}^{MLS}(\mathbf{x}) &= \mathbf{p}^T(\mathbf{x})\mathbf{A}(\mathbf{x})^{-1}\mathbf{B}(\mathbf{x}) \\
&= \mathbf{p}^T(\mathbf{x})\left[\mathbf{PW}(\mathbf{x})\mathbf{P}^T\right]^{-1}\mathbf{PW}(\mathbf{x}) \\
&= \mathbf{p}^T(\mathbf{x})\left[\frac{1}{\displaystyle\sum_{j=1}^{m}\tilde{w}_R(s_j)}\mathbf{P\tilde{W}}(\mathbf{x})\mathbf{P}^T\right]^{-1}\frac{1}{\displaystyle\sum_{j=1}^{m}\tilde{w}_R(s_j)}\mathbf{P\tilde{W}}(\mathbf{x}) \\
&= \mathbf{p}^T(\mathbf{x})\left[\mathbf{P\tilde{W}}(\mathbf{x})\mathbf{P}^T\right]^{-1}\mathbf{P\tilde{W}}(\mathbf{x}).
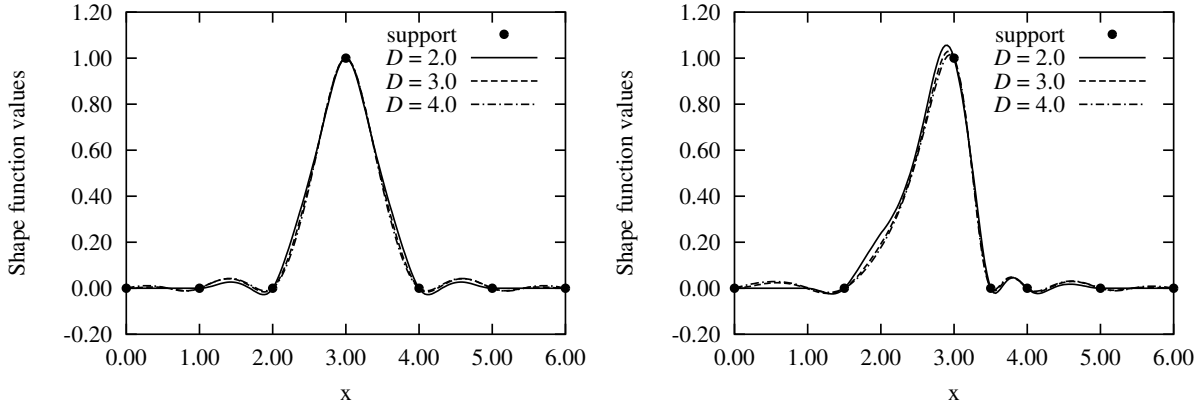\end{aligned} \tag{3.29}$$

Figure 3.7. Nodal shape function of the MLS interpolation with regularized weighting function and linear polynomial basis for regular and irregular sets of nodes
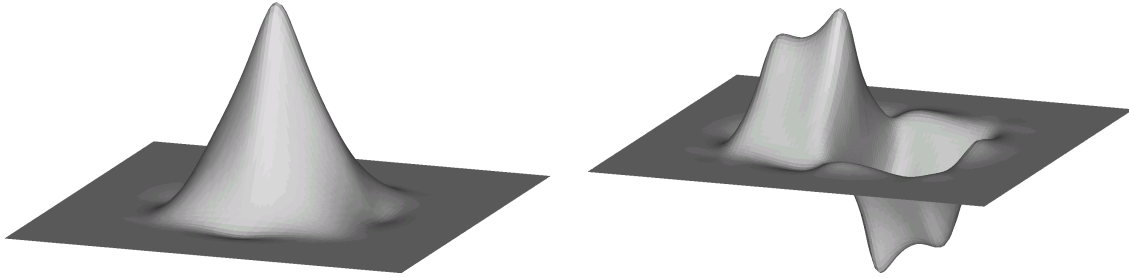

Figure 3.8. MLS shape function and first derivative for a regular set of nodes using the regularized spline weighting function

This means that instead of the complex weighting function from Eq. (3.24) the much simpler formulation in Eq. (3.25) can be used as weighting function by obtaining exactly the same shape function values.

In Fig. 3.7 a single nodal shape function obtained by using the regularized weighting function type is shown for different values of the influence radius D.

Fig. 3.7 and Eq. (3.28) clearly point out that the interpolation condition is fulfilled with very high accuracy even for irregular sets of nodes with grading node density. In clear contrast to the shape functions obtained with the Gaussian weighting function the influence radius D influences the regularized shape function characteristics marginally if a certain value of D is reached.

The first and the second derivative of the regularized weighting function at the boundary of the influence domain $d = D$ are not exactly zero, similar to the Gaussian weighting function, thus C^1 and C^2 continuity are not reached exactly.

Exact C^2 continuity can be achieved if the weighting function is multiplied by the cubic spline from Eq. (3.21)

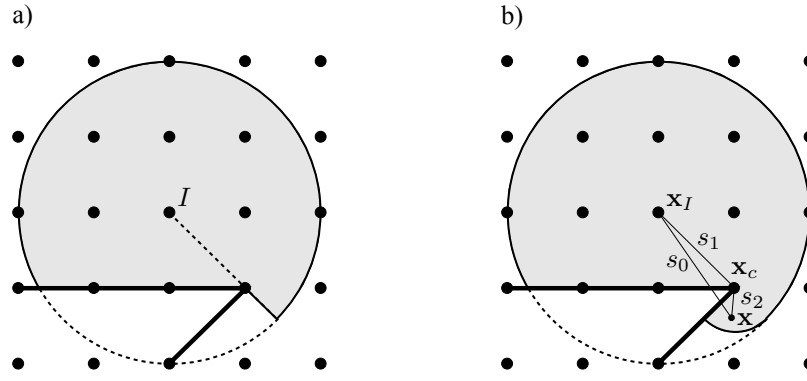$$w_{RS}(s) = w_S(s) \cdot w_R(s). \tag{3.30}$$

Figure 3.9. Modified influence domain of a node close to a non-convex corner using a) the visibility and b) the diffraction approach

More accurate results can be obtained for this combined function type if a slightly modified regularized weighting function is used,

$$w_{RS}(s) = w_S(s) \cdot \frac{(s + \epsilon)^{-2} - (1 + \epsilon)^{-2}}{\epsilon^{-2} - (1 + \epsilon)^{-2}}; \quad \epsilon = 10^{-3}. \tag{3.31}$$

In Fig. 3.8 a MLS shape function with corresponding first derivative obtained by using this combined regularized spline weighting function is shown for a regular set of nodes.

3.1.3 Representation of non-convex domains

With the Moving Least Squares interpolation non-convex domains, bodies with for example internal holes, curved external boundaries, or sharp discontinuity lines, can be modeled by modifying the weighting function. The first approach doing so was the so-called visibility criterion (Belytschko et al. 1994), which defines an influencing node of a single interpolation point only if the node can be "seen" by the interpolation point, which means that the connecting line is not cut by a boundary or discontinuity. Fig. 3.9 shows the influence domain of a node I close to a non-convex corner. Due to the resulting jump in the weighting function, the interpolation function gets an artificial displacement discontinuity inside the domain.

An improved technique, the diffraction method, models a diffraction around a concave corner, similar to light propagation (Belytschko et al. 1996). The modified influence domain is shown additionally in Fig. 3.9. The standardized distance from an interpolation point with the coordinates $\mathbf{x}$ in the diffraction area to the node I is defined as

$$s_I = \left(\frac{s_1 + s_2(\mathbf{x})}{s_0(\mathbf{x})} \right)^{\lambda_D} s_0(\mathbf{x}), \tag{3.32}$$

where the distances $s_1 = \|\mathbf{x}_I - \mathbf{x}_c\|/D$, $s_2 = \|\mathbf{x} - \mathbf{x}_c\|/D$ and $s_0 = \|\mathbf{x} - \mathbf{x}_I\|/D$ are indicated in the figure and λ_D is the diffraction parameter and describes the shape of the diffraction area.

A further approach is the transparency method, which defines a linearly decreasing transparency for the visibility (Belytschko et al. 1996). This method was developed for sharp corners, like crack tips. Because of the fact that both sharp and non-sharp concave corners have to be modeled for complex structures, the transparency method is not applied in this work. Further details about this method can be found in (Karutz 2000).

3.1.4 Fulfillment of geometrical boundary conditions

By using the standard Moving Least Squares interpolation in a Galerkin method, the essential or geometrical boundary conditions are not fulfilled automatically because of the approximative character of the shape functions

$$\Phi_i^{MLS}\left(\mathbf{x}_j\right) \neq \delta_{ij}. \tag{3.33}$$

Several methods have been developed during the recent years to overcome this problem. The most common approaches will be presented in this section briefly. A complete overview is given in (Fries and Matthies 2003).

One of the first approaches was the introduction of Lagrange multipliers (Belytschko et al. 1994). The principle of virtual work in Eq. (2.46) reads in modified form

$$\int_\Omega \delta\boldsymbol{\epsilon}^T(\mathbf{u})\mathbf{C}\boldsymbol{\epsilon}(\mathbf{u})d\Omega - \int_\Omega \delta\mathbf{u}^T\mathbf{f}^B d\Omega - \int_{\Gamma^f} \delta\mathbf{u}^T\mathbf{f}^S d\Gamma$$
$$- \int_{\Gamma^u} \delta\boldsymbol{\lambda}^T(\mathbf{u} - \mathbf{u}^S)d\Gamma + \int_{\Gamma^u} \delta\mathbf{u}^T\boldsymbol{\lambda}d\Gamma = 0 \tag{3.34}$$

where $\boldsymbol{\lambda}$ is a vector containing the Lagrange multipliers at one point of the Dirichlet boundary

$$\boldsymbol{\lambda} = \left[\begin{array}{ccc} \lambda_x & \lambda_y & \lambda_z \end{array}\right]^T. \tag{3.35}$$

The fulfillment of the essential boundary conditions is included as constrained condition

$$\mathbf{K}_u\mathbf{d} = \mathbf{q}_u, \tag{3.36}$$

and the global system of equations given in Eq. (2.56) is extended to the relation

$$\left[\begin{array}{cc} \mathbf{K} & \mathbf{K}_u \\ \mathbf{K}_u & \mathbf{0} \end{array}\right]\left[\begin{array}{c} \mathbf{d} \\ \bar{\boldsymbol{\lambda}} \end{array}\right] = \left[\begin{array}{c} \mathbf{f}^{ext} \\ \mathbf{q}_u \end{array}\right] \tag{3.37}$$

which requires special solvers due to the singular coefficient matrix. Further details about the calculation of the symmetric matrix $\mathbf{K}_u$ and the equivalent vector on the geometrical boundary $\mathbf{q}_u$ are given in (Häussler-Combe 2001).

In (Lu et al. 1994), Eq. (3.34) was rewritten to obtain the constrained equation

$$\boldsymbol{\lambda} = \mathbf{f}^u \quad \text{on } \Gamma^u \tag{3.38}$$

where $\mathbf{f}^u$ is the traction vector on the Dirichlet boundary and can be expressed as

$$\mathbf{f}^u = \mathbf{n}\boldsymbol{\sigma} \quad \text{on } \Gamma^u. \tag{3.39}$$

This leads to the standard equation

$$\mathbf{K}\mathbf{d} = \mathbf{f}, \tag{3.40}$$

but the construction of the coefficient matrix $\mathbf{K}$ and the load vector $\mathbf{f}$ is more expensive due to the additional constrained equation.

A further possibility to apply geometrical boundary conditions is the definition of a penalty term β as presented in (Häussler-Combe 2001),

$$\beta \gg \|\mathbf{K}\|. \tag{3.41}$$

The boundary conditions can be enforced by

$$\int_\Omega \delta\boldsymbol{\epsilon}^T(\mathbf{u})\mathbf{C}\boldsymbol{\epsilon}(\mathbf{u})d\Omega - \int_\Omega \delta\mathbf{u}^T\mathbf{f}^B d\Omega - \int_{\Gamma^f} \delta\mathbf{u}^T\mathbf{f}^S d\Gamma$$
$$-\beta \int_{\Gamma^u} \|\mathbf{u} - \mathbf{u}^S\|^2 d\Gamma = 0, \tag{3.42}$$

but the correct choice of β is uncertain and the global system of equations can be ill-conditioned.

All three approaches assume clearly defined, static boundary conditions. If compatibility conditions have to be considered, for example for the coupling with finite elements, where the displacements in coupling points are unknown, these procedures become much more complex as shown in (Häussler-Combe 2001). For this reason another method was developed in (Krongauz 1996) where the boundary of the meshless domain Ω_{MLS} is modeled with a transition zone Ω_{trans}, which is discretized by transition elements as shown in Fig. 3.10. In these elements the meshless shape functions are modified by blending functions $R(\mathbf{x})$ to obtain finite element interpolation conditions on the boundary,

$$\tilde{\Phi}_i^{MLS}(\mathbf{x}) = \begin{cases} [1 - R(\mathbf{x})]\Phi_i^{FEM}(\mathbf{x}) + R(\mathbf{x})\Phi_i^{MLS}(\mathbf{x}) & \mathbf{x}_i \in \Omega_{trans} \\ \Phi_i^{MLS}(\mathbf{x}) & \mathbf{x}_i \in \Omega_{MLS} \end{cases} . \tag{3.43}$$

Linear or cubic function types are used as blending functions, whereby the latter type enables a continuous blending of the strains. In (Karutz 2000) this concept was realized
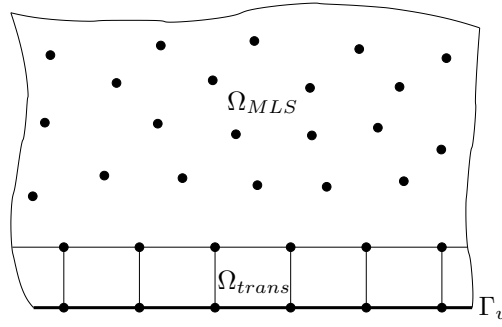
Figure 3.10. Application of essential boundary conditions using transition elements

in an automatic algorithm with adaptive coupling between meshless and finite element domains in 2D. An extension to the three-dimensional case is relatively difficult due to the complexity of the changing coupling interface and the belonging update of the transition elements.

If the new regularized weighting function is applied in the MLS interpolation the essential boundary conditions are fulfilled with high accuracy,

$$\mathbf{u} \approx \mathbf{u}^S \quad \text{on } \Gamma^u. \tag{3.44}$$

Thus no special method is necessary and the numerical implementation is straight-forward. Furthermore the application of the above methods does not decrease the interpolation error of the standard MLS interpolation inside the domain, which may lead to problems by the evaluation of crack criteria. These problems do not occur with the presented regularized weighting type.

3.1.5 Application of boundary forces

The external forces acting on the Neumann boundary of a meshless domain can be formulated analogous to Eq. (2.55) as

$$\mathbf{f}_{\Gamma^f}^{ext} = \int_{\Gamma^f} \mathbf{\Phi}^T \mathbf{f}^S d\Gamma. \tag{3.45}$$

In the Finite Element Method this external force vector can be obtained very easily because of the linear or quadratic precision on the domain boundary. The shape functions of internal nodes are zero at the boundary lines, thus they have no contribution to the nodal force vector.

In the Moving Least Squares interpolation the nodal domain is only specified by the influence radius. This leads to arbitrary intersections of the domain of internal nodes with the domain boundary Γ as shown in Fig. 3.11 for node I. In general, internal nodes contribute to the nodal force vector if their influence domain overlaps the Neumann boundary
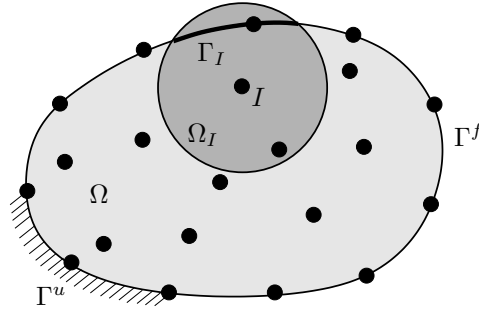
Figure 3.11. Intercept of the domain of an internal node with the boundary

$$\mathbf{f}_I^{ext} = \int_{\Gamma_I^f} \mathbf{\Phi}_I^T \mathbf{f}^S d\Gamma \neq 0. \tag{3.46}$$

This problem complicates the assembling of the external force vector and does not allow a coupling with finite elements with compatible displacements along the coupling boundary. The application of the transition elements explained in the previous section does solve this problem automatically, the internal meshless shape functions are blended out in boundary elements and linear precision is obtained on the boundary. Because of the complex handling of the transition elements, if an adaptive coupling with finite elements is used, the application of this method is not straight-forward.

In this work an easier blending concept is developed. The weighting function of the internal nodes are blended out in a blending domain around the boundary, by multiplying the values of the weighting function with a blending value. The blending domain is simply defined by a blending length l_B, thus the required blending value can be obtained very easily from the position of the interpolation point and the boundary description. The resulting blending region is shown in Fig. 3.12 for a two-dimensional discretization. As the figure indicates, three different blending types have to be considered for 2D, which are marked in the figure by A, B and C. The first type in region A is valid if an interpolated point $\mathbf{x}$ is not located in the area of a convex (region B) or concave corner (region C). Then the blending value is simply given as

$$w_B(\mathbf{x}) = f_B \left(\frac{d_B(\mathbf{x})}{l_B} \right) \tag{3.47}$$

where $f_B(s)$ is the blending function which has to be zero for $s = 0$ and one for $s = 1$, and d_B is the shortest distance of $\mathbf{x}$ to the boundary. As blending function the cubic function
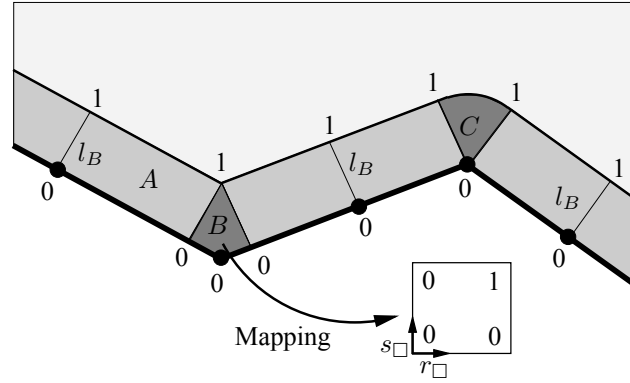
Figure 3.12. Blending region of an internal node with convex and concave boundary corner

from Eq. (3.20) is adapted,

$$f_B(s) = \begin{cases} 3s^2 - 2s^3 & s \le 1 \\ 1 & s > 1 \end{cases}. \tag{3.48}$$

This function has the useful property

$$f_B(s) = 1 - f_B(1 - s) \tag{3.49}$$

which leads to a smooth blending over the whole blending region. Due to the C^1 continuity of f_B the resulting blended weighting function has C^1 continuity, if the original weighting function has at least C^1 continuity.

The second blending type has to be applied to convex corners (region B), where a bilinear blending is used. This is realized by mapping the coordinates of the point $\mathbf{x}$ in the convex boundary area into a unit square as shown in Fig. 3.12. The blending value in a convex corner is defined in the form

$$w_{B,convex}(\mathbf{x}) = f_B(r_\square(\mathbf{x}))f_B(s_\square(\mathbf{x})). \tag{3.50}$$

This formulation preserves the C^1 continuity of the blending function in rectangular convex corners, where the domain which has to be mapped onto the unit square is not distorted. If the convex angle is not equal to ninety degrees, this mapping leads to weak discontinuities of the blending function derivative along the connection lines between region B and region A. Thus the obtained blending function has only approximative C^1 continuity in such cases.

In a concave corner (region C) a radial blending is realized

$$w_{B,concave}(\mathbf{x}) = f_B\left(\frac{d_{N_{concave}}(\mathbf{x})}{l_B}\right), \tag{3.51}$$
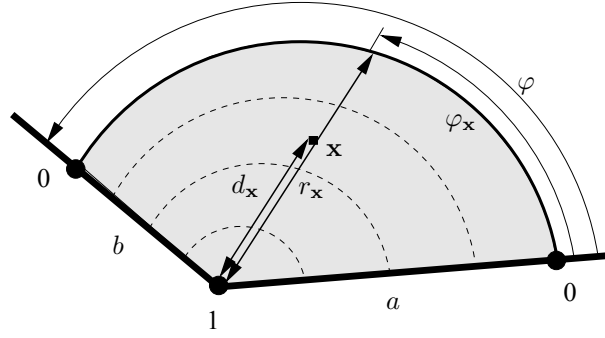
Figure 3.13. Blending function of a boundary node

where $d_{N_{concave}}$ is the distance to the node located at the concave corner. This radial blending preserves the C^1 continuity inside the concave region as well as on the crossover to the region of type A. With the presented blending technique the weighting functions of internal nodes are modified such that their values are exactly zero along the boundary. This blending does not destroy the property of the MLS interpolation that the polynomial basis can be represented exactly inside the domain.

For the imposition of a linear interpolation between the boundary nodes directly at the boundary polygon, a mapped radial blending of the boundary node weighting function is performed, which is illustrated in Fig. 3.13. The resulting blending value is defined as

$$w_{B,boundary}(\mathbf{x}) = f_B \left(1 - \frac{d_\mathbf{x}}{r_\mathbf{x}} \right) \tag{3.52}$$

where $d_\mathbf{x}$ is the distance of the interpolation point to the boundary node and $r_\mathbf{x}$ is the mapped radius, which is simply defined as

$$r_\mathbf{x} = a + (b - a)\frac{\varphi_\mathbf{x}}{\varphi}. \tag{3.53}$$

The lengths of the boundary segments a and b and the angles $\varphi_\mathbf{x}$ and φ spanned by the interpolation point and the boundary segment a and by both boundary segments, respectively, are indicated in the figure. The blending of the boundary nodes is independent of the blending length l_B and depends only on the position of the neighbor boundary nodes. Inside the domain, the obtained blending function has C^1 continuity. For a stable application of this boundary blending it is necessary that at least one internal node is located inside the blending region of each boundary node.

3.2   Natural Neighbor Galerkin Method

3.2.1   Voronoi diagram and Delaunay tesselation

The Natural Neighbor Interpolation is based on the Voronoi diagram and its dual Delaunay tesselation of the domain. Both can be defined for an arbitrary set of nodes in the m-dimensional space. The Voronoi diagram is a subdivision of the nodal domain into subregions T_i, which are either closed and convex or unbounded. Each region T_i is associated with a node N_i such that any point $\mathbf{x}$ in T_i is closer to the natural neighbor node N_i than to any other node in the domain (Green and Sibson 1978),

$$T_i = \{\mathbf{x} \in \mathbb{R}^m : d(\mathbf{x}, \mathbf{x}_i) < d(\mathbf{x}, \mathbf{x}_j) \quad \forall \quad i \neq j\} \tag{3.54}$$

where $d(\mathbf{x}, \mathbf{x}_i)$ is the distance between the point $\mathbf{x}$ and the node N_i. An example of a Voronoi diagram for a two-dimensional set of nodes is shown in Fig. 3.14. The figure indicates that for all nodes inside the convex hull the Voronoi cells are closed and bounded and for all nodes on the boundary of the convex hull the cells are unbounded.
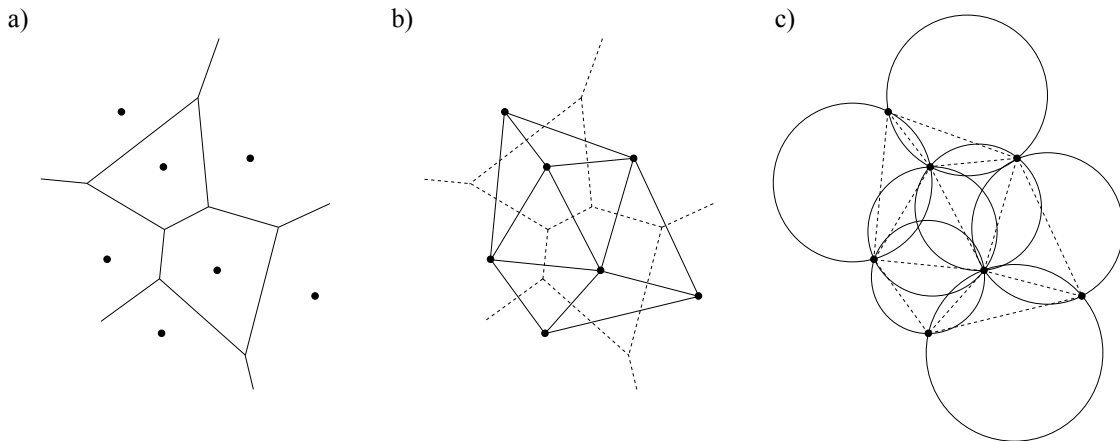

Figure 3.14. a) Voronoi diagram, b) Delaunay triangulation and c) Natural neighbor circumcircles

The Delaunay triangulation, which is the dual of the Voronoi diagram, is constructed by connecting the nodes with common Voronoi edges. This defines the Delaunay edges only between nodes which are natural neighbors. All Delaunay triangles fulfill the empty circumcircle criterion (Lawson 1977), thus the circumcircle of every Delaunay triangle contains no other nodes. In Fig. 3.14 the Delaunay triangulation and the belonging Delaunay or natural neighbor circumcircles are shown. In the case that more than three nodes are on the circumcircle of a Delaunay triangle, the triangulation is not unique and different Delaunay triangulations are possible for the same nodal set, but the corresponding Voronoi diagram is always unique.

Several algorithms have been developed to determine the Delaunay triangulation or the Voronoi diagram. An overview can be found in (Fortune 1995). In this work the

package Triangle (Shewchuk 1996) is used in a two-dimensional framework.

3.2.2 Natural Neighbor Interpolation

(Sibson 1980) introduced the natural neighbor coordinates by defining second order Voronoi cells. This second order diagram is a subdivision into cells T_{ij}, where each region is associated with a nodal neighbor pair, N_i and N_j, such that N_i is the nearest neighbor and N_j is the second nearest neighbor. A second order Voronoi cell is defined (Sibson 1980) as

$$T_{ij} = \{\mathbf{x} \in \mathbb{R}^m : d(\mathbf{x}, \mathbf{x}_i) < d(\mathbf{x}, \mathbf{x}_j < d(\mathbf{x}, \mathbf{x}_k) \quad \forall \quad k \neq i, j\}. \tag{3.55}$$

T_{ij} is non-empty only if N_i and N_j are natural neighbors. This leads to the result that for an arbitrary point $\mathbf{x}$ located in the circumcircle of a Delaunay triangle $\triangle N_i N_j N_k$ the nodes spanning the triangle N_i, N_j and N_k are natural neighbors of $\mathbf{x}$. In Fig. 3.15 the insertion of the point $\mathbf{x}$ into the original Voronoi diagram and the belonging first and second order Voronoi cells, $T_{\mathbf{x}}$ and $T_{\mathbf{x}i}$, are shown. In the example indicated in the figure
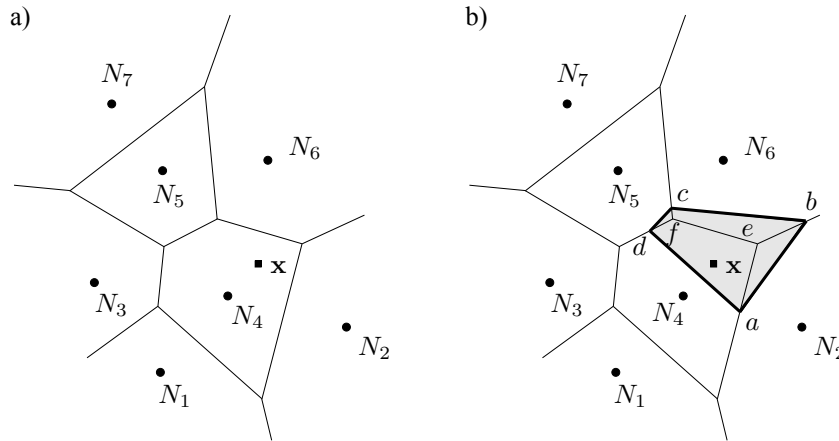

Figure 3.15. a) Insertion of a point $\mathbf{x}$ into the Voronoi diagram, b) First and second order Voronoi cells concerning $\mathbf{x}$

$\mathbf{x}$ has four natural neighbors, N_2, N_4, N_5 and N_6. The natural neighbor coordinates of $\mathbf{x}$ with respect to the node i are defined in 2D as the ratio of the area or in 3D as the ratio of the volume of $T_{\mathbf{x}i}$ and $T_{\mathbf{x}}$

$$\Phi_i(\mathbf{x}) = \frac{A_i(\mathbf{x})}{A(\mathbf{x})} \tag{3.56}$$

where

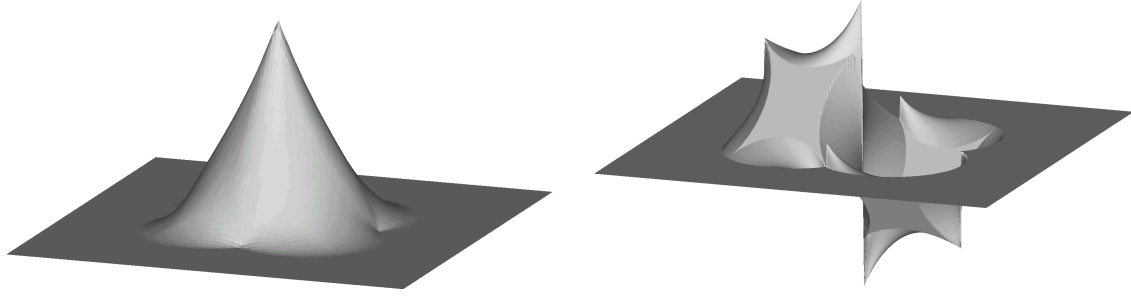$$A(\mathbf{x}) = \sum_{j=1}^{n} A_j(\mathbf{x}) \tag{3.57}$$

Figure 3.16. NEM shape function and first derivative for a regular set of nodes

and n is the number of natural neighbors. The four regions in Fig. 3.15, which are the closed polygons $aefd$, abe, $bcfe$, cdf, are the second order Voronoi cells and their union, the closed polygon $abcd$, is the first order Voronoi cell of $\mathbf{x}$.

The Natural Neighbor Interpolation or Sibsonian interpolation of a function $u(\mathbf{x})$ is carried out by using the natural neighbor coordinates in Eq. (3.56) as interpolation shape functions

$$u^h(\mathbf{x}) = \sum_{i=1}^{n} \Phi_i(\mathbf{x})\tilde{u}_i \tag{3.58}$$

where $\tilde{u}_i = u^h(\mathbf{x}_i)$ are the nodal values at the n natural neighbors. The application of this interpolation scheme in a Galerkin approach is called Natural Neighbor Galerkin Method or Natural Element Method (NEM) (Sukumar et al. 1998). In Fig. 3.16 a NEM shape function and its first derivative are shown for a regular set of nodes.

The natural neighbor shape functions have compact support, their values are only non-zero in the neighborhood of the belonging node. The Natural Neighbor Interpolation passes exactly through the nodal values,

$$\Phi_i^{NEM}(\mathbf{x}_j) = \delta_{ij}, \tag{3.59}$$

which implies that essential boundary conditions are fulfilled automatically. Furthermore the interpolated function depends only on the nodal positions and no additional parameter is necessary. Thus the nodal influence domain is automatically adjusted for varying node densities. The interpolation fulfills the partition of unity condition

$$\sum_{i=1}^{n} \Phi_i^{NEM}(\mathbf{x}) = 1 \quad \forall \quad \mathbf{x} \in \Omega \tag{3.60}$$

and linear completeness is satisfied (Sukumar et al. 1998). Along boundary lines the interpolation has linear precision, which enables an easy application of boundary forces and a compatible coupling with linear finite elements. Natural neighbor shape functions have C^1 continuity, except at the nodes, where we find C^0 continuity (Sibson 1980). The

first derivatives of the shape functions are obtained by differentiation of Eq. (3.56),

$$\frac{\partial \Phi_i(\mathbf{x})}{\partial x_j} = \frac{1}{A(\mathbf{x})} \left[\frac{\partial A_i(\mathbf{x})}{\partial x_j} - \Phi_i(\mathbf{x}) \frac{\partial A(\mathbf{x})}{\partial x_j} \right]. \tag{3.61}$$

Further differentiation yields

$$\frac{\partial^2 \Phi_i(\mathbf{x})}{\partial x_j \partial x_k} = \frac{1}{A(\mathbf{x})} \frac{\partial^2 A_i(\mathbf{x})}{\partial x_j \partial x_k} + \frac{2A_i}{A^3(\mathbf{x})} \frac{\partial A(\mathbf{x})}{\partial x_j} \frac{\partial A(\mathbf{x})}{\partial x_k}$$
$$- \frac{1}{A^2(\mathbf{x})} \left[\frac{\partial A_i(\mathbf{x})}{\partial x_j} \frac{\partial A(\mathbf{x})}{\partial x_k} + \frac{\partial A(\mathbf{x})}{\partial x_j} \frac{\partial A_i(\mathbf{x})}{\partial x_k} + A_i(\mathbf{x}) \frac{\partial^2 A(\mathbf{x})}{\partial x_j \partial x_k} \right]. \tag{3.62}$$

The natural neighbors of an interpolation point are determined according to (Unger 2003), where it is assumed that the Delaunay triangle in which the point is located is known. Starting from one of the nodes of the triangle it is checked whether the circumcenter corresponding to the adjacent triangle in counterclockwise order contains this node. If the first triangle circumcircle is found the node is not located in, this procedure is stopped. Then the next node is chosen in clockwise order within the last triangle having the last node inside its circumcircle. This is repeated until the second node of the triangle edge is reached. The described procedure is repeated for all three initial triangle edges.

For the sake of completeness of this section, another natural neighbor based interpolation, the Laplacian or Non-Sibsonian interpolation (Belikov et al. 1997), is presented briefly here. Within this method the shape functions are not defined as the ratio of the area of a second order Voronoi cell belonging to a node and the area of the first order Voronoi cell of the interpolation point $\mathbf{x}$ as given in Eq. (3.56). The two-dimensional Non-Sibsonian shape functions are introduced as the ratio of the length of the Voronoi edge $s_i(\mathbf{x})$ associated with node N_i, and the perpendicular distance $h_i(\mathbf{x})$ between the Voronoi edge of N_i and the point $\mathbf{x}$ as

$$\Phi_i(\mathbf{x}) = \frac{\alpha_i(\mathbf{x})}{\sum_{j=1}^{n} \alpha_j(\mathbf{x})}, \quad \alpha_j(\mathbf{x}) = \frac{s_j(\mathbf{x})}{h_j(\mathbf{x})}. \tag{3.63}$$

Fig. 3.17 shows the required distances for a simple set of nodes. The Non-Sibsonian interpolation has similar properties as the Sibsonian interpolation: the partition of unity criterion is fulfilled, linear completeness is satisfied and linear precision is obtained on the boundary (Sukumar et al. 2001). This method is computationally easier, because in 2D only distances have to be calculated instead of areas, but the C^1 continuity of the Sibsonian interpolation between the nodes can not be preserved. For this reason the method is not applied in this work.
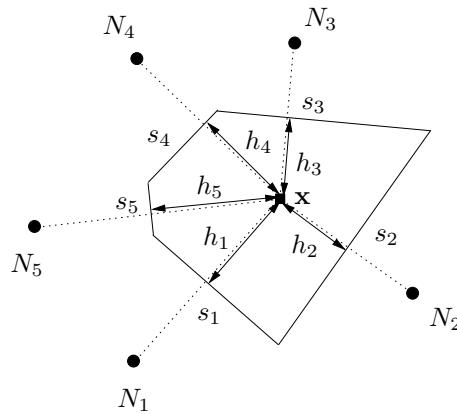
Figure 3.17. Non-Sibsonian interpolation

3.2.3   Shape function computation

Different algorithms have been developed for the automatic computation of the natural neighbor shape functions. In this work the algorithms of (Watson 1994) and (Lasserre 1983) are used, which are presented in this section according to (Unger 2003).

Watson's algorithm calculates the areas of the second order Voronoi cells as the sum of the signed areas of triangles. This algorithm can be applied only in 2D and only to points located inside of triangles. First the neighbor triangles for a given Point X are determined. They are those triangles in whose circumcircle X is located. In Fig. 3.18 the principle of the algorithm is shown. There the neighbor triangles of X are $\triangle BAG$ and $\triangle AFG$. The
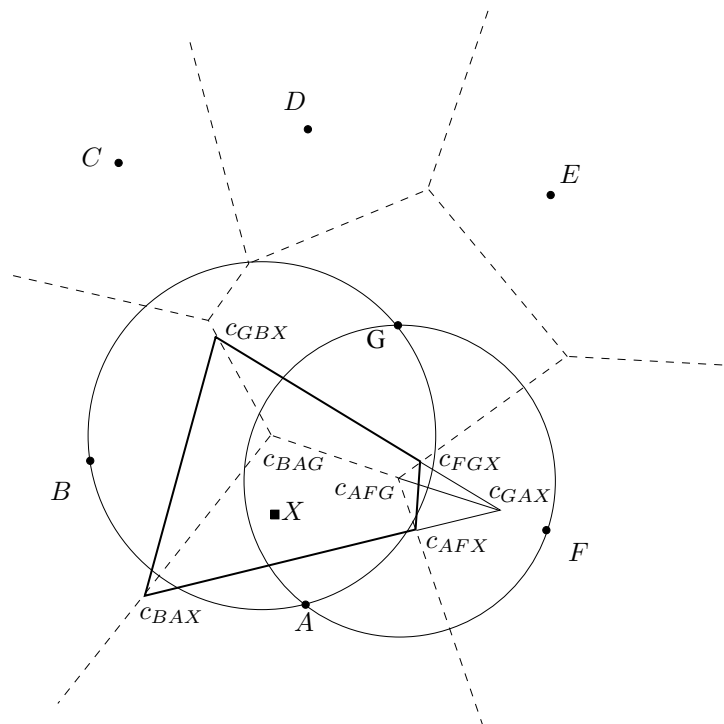

Figure 3.18. Shape function computation using Watson's algorithm (Unger 2003)

sign of the area is determined automatically by using a counterclockwise enumeration for all triangles. Each neighbor triangle t_n is decomposed into three sub-triangles t_1, t_2 and t_3 spanned by X and two vertices of t_n, for example $\triangle BAG$ is subdivided in $\triangle BAX$, $\triangle AGX$ and $\triangle GBX$. Then the circumcenter c_{ijx} of each sub-triangle, where i and j are the vertices of the neighbor triangle, are calculated as a function of X. The signed area of a second order Voronoi cell belonging to a node I is calculated by considering all neighbor triangles of X which have I as vertex. The sum over all of these neighbor triangles t_n of the signed area of the triangle $\triangle c_{IJX}, c_{IKX}, c_{IJK}$ gives the area of a second order Voronoi cell, where c_{IJX} and c_{IKX} are the two circumcenters of the sub-triangles of t_n. c_{IJK} is the circumcenter of t_n, and J and K the other two vertices belonging to t_n. In Fig. 3.18 the area of the second order Voronoi cell of X belonging to node A is obtained as the sum of the triangles areas of $\triangle c_{BAX}, c_{GAX}, c_{BAG}$ and $\triangle c_{GAX}, c_{AFX}, c_{AFG}$, where the second one has a negative area. The total area of the first order Voronoi cell of X is the sum of all areas of the second order Voronoi cells. A detailed description of the scheme used for calculating the area of the triangles and the circumcenter of a triangle is given in (Sukumar 1998) and (Unger 2003).

The algorithm of (Lasserre 1983) can be applied in 2D and 3D and has no restriction about the position of the interpolation point. The first step of the algorithm tests whether the point is located on a boundary segment. If this is the case, linear interpolation between the nodes of the belonging segment is performed. Otherwise a bounding box is constructed which contains all neighbor nodes and natural neighbor circumcircles. In 2D a polygon p belonging to each neighbor node I is assembled separately, which contains the circumcenters of all neighbor triangles of X spanned by I. This polygon defines the intersection of the Voronoi cell belonging to node I and the bounding box. If two successive triangles of I do not share a triangle edge, two additional points are inserted on the boundary, where the median lines of both edges cut the bounding box. In Fig. 3.19a this is illustrated for node A: the points Q and R are added and since they are not on the same edge of the bounding box, the additional point S is inserted into p. The area of the closed polygon containing n points $\mathbf{p}^i$ is then calculated by

$$A_p = \frac{1}{2} \sum_{i=1}^{n} p_x^i p_y^{i+1} - p_y^i p_x^{i+1}, \tag{3.64}$$

where $\mathbf{p}^{n+1} = \mathbf{p}^1$. The calculated area is positive if the points $\mathbf{p}^i$ are ordered in counterclockwise order. The polygon obtained for node A in Fig. 3.19a contains Q, S, R and the circumcenter of $\triangle ABE$.

In the second step the sub-triangles spanned by the neighbor nodes of X and by X itself are calculated. Each neighbor node is part of two sub-triangles. The calculated polygon p and the circumcenters of the two sub-triangles belonging to node I form another polygon $\hat{p}$. In Fig. 3.19b this second polygon contains Q, S, R and the circumcenters
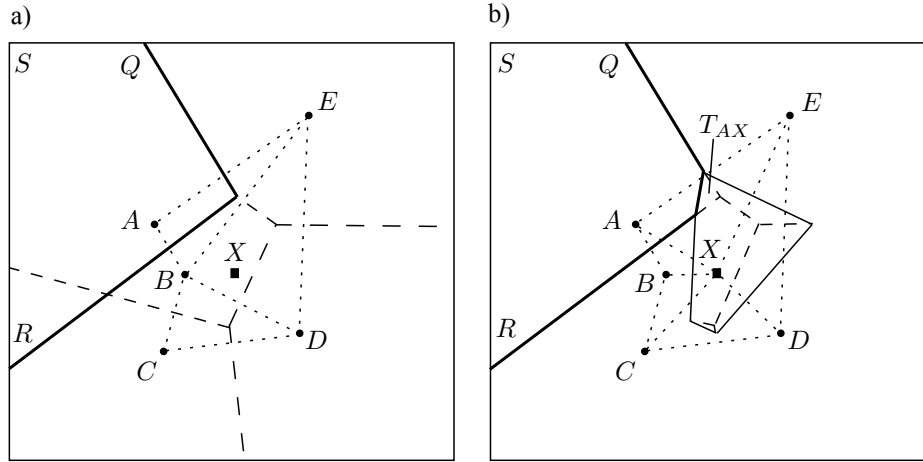
Figure 3.19. Shape function computation using Lasserre's algorithm, a) Neighbor triangles of interpolation point, b) Sub-triangles of neighbor nodes and interpolation point (Unger 2003)

of $\triangle ABX$ and $\triangle EAX$. The area of the second order Voronoi cell T_{IX} of the point X belonging to node I is then simply given by the difference of the areas of the polygons $\hat{p}$ and p. The total area of the first order Voronoi cell of X can be calculated again as the sum of the second order Voronoi cell areas.

Compared to Watson's algorithm this approach is more complex and requires a higher numerical effort. Thus in this work Watson's algorithm is used for all points inside a triangle and Lasserre's method only for points on triangle edges.

3.2.4 Adaptation for non-convex domains

The standard Delaunay triangulation can only be applied to convex domains, where the boundary of the body is always the convex hull of the domain. Non-convex domains, where the convex hull does not correspond to the external boundary, can be modeled by using either conforming or constrained triangulation (Lo 1989). The boundary of a non-convex domain can be represented by using a Planar Straight Line Graph (PSLG), which is a set of boundary segments, each spanned by two boundary nodes. In a conforming Delaunay triangulation the empty circumcircle criterion is preserved and the triangulation is still the strict dual of the Voronoi diagram. This is achieved by subdividing each PSLG segment whose belonging triangle does not initially fulfill the empty circumcircle criterion. The additional points on these segments are called Steiner points. For the application in a hybrid discretization containing a NEM domain coupled with finite elements, these additional Steiner points have to be considered by refining the finite element mesh, which leads to additional numerical effort.

In a constrained Delaunay triangulation the duality property does not hold and the empty circumcircle criterion may not be fulfilled for some triangles. For convex bodies the convex hull containing all boundary segments can be defined as PSLG and the belonging constrained triangulation fulfills the Delaunay criterion. If only the bound-
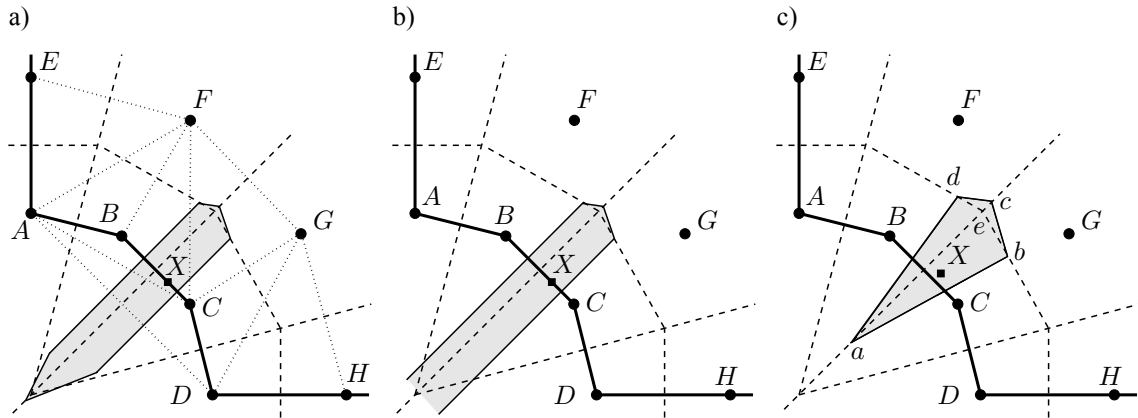
Figure 3.20. Interpolation on the boundary of a non-convex body, a) Bounded 2nd order Voronoi cells of X, b) Modified unbounded cells, c) 2nd order cells for a point close to the boundary

ary of non-convex bodies is included in the PSLG the corresponding triangulation is a true Delaunay triangulation as well, if the triangles outside of the boundary are deleted (Unger 2003). The obtained triangulation does not need additional points, which enables a straight-forward coupling with finite elements. Thus this approach is applied in this work to model non-convex domains.

In Fig. 3.20a a piece of a two-dimensional non-convex body is shown with the belonging Voronoi diagram and the constrained Delaunay triangulation. The interpolation value of a point X on the boundary segment spanned by the nodes B and C is not a linear function between B and C because the nodes A and D are additional natural neighbors of X and the second order Voronoi cells of X belonging to B and C are not unbounded, as shown in the figure. If the external triangles $\triangle ACB$ and $\triangle ADC$ are deleted, the nodes A and D are not the natural neighbors of X anymore. The resulting second order Voronoi cells of X belonging to B and C become unbounded as shown in Fig. 3.20b, thus linear interpolation on the boundary segments is obtained. Watson's algorithm can be applied to the calculation of the area of the second order Voronoi cells without any modification in this case. If X is close to the boundary as shown in Fig. 3.20c, the area of the belonging second order cells corresponding to the nodes B and C, namely the triangles $\triangle aed$ and $\triangle abe$, increases with decreasing distance of X to the boundary. In the limit, the area of both cells is infinite, while the area of the second order cells of the other neighbor nodes remains finite, which leads to a linear interpolation between B and C.

The presented concept is not complete, because for non-convex domains with sharp concave corners, like crack tips, the circumcircles of one side of an internal boundary may overlap the domain on the opposite side of the boundary as shown in Fig. 3.21a. The resulting interpolation on the boundary segment is again not linear between the two belonging nodes. The second order Voronoi cells of these nodes are bounded because of the irregular neighbor nodes on the opposite side. In this work the concept of visibility, introduced for the Moving Least Squares interpolation, is adapted such that the
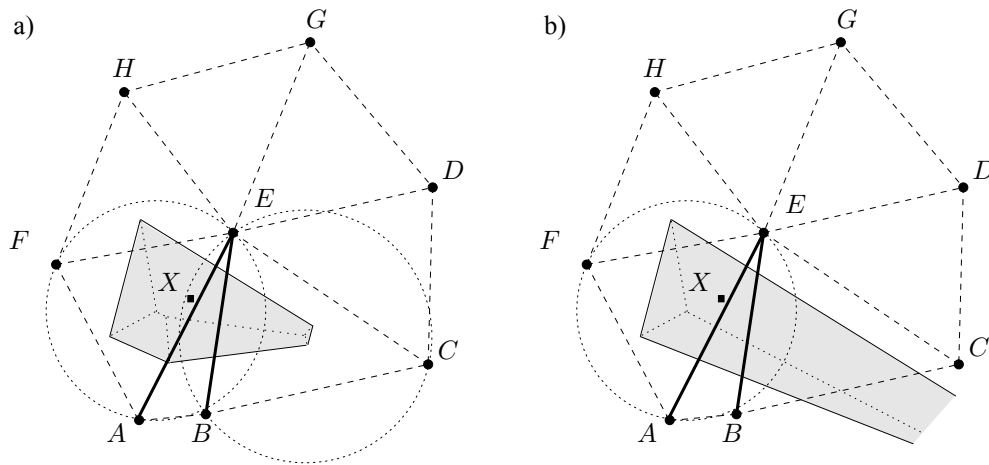
Figure 3.21. a) Irregular neighborhood relations across a non-convex boundary, b) Modified interpolation using the visibility criterion

visibility criterion is checked for all determined neighbor nodes of X. Those nodes which do not fulfill this criterion are not handled as natural neighbors of X, thus the required linear precision on the boundary segment is preserved. In Fig. 3.21 the original and the modified second order Voronoi cells are shown for a point close to the boundary. The figure indicates that by using the visibility criterion, the area of the cells belonging to the boundary nodes increases by decreasing the distance of X to the boundary. In contrast to the MLS-interpolation the shape functions obtained by using the visibility criterion are continuous.

The presented concept requires the initial definition of the boundary segments as PSLG. This is very simple in 2D but more complex in 3D. In (Cueto et al. 2000) the concept of α-shapes, which are widely used in scientific visualization, was introduced to impose a linear interpolation condition on the boundary. By using this concept the domain boundary need not to be defined in advance. Thus it can be easily applied to two- or three-dimensional non-convex domains whose geometry is only defined by a set of points. This method checks the neighborhood of nodal tuples and deletes the neighbor relations
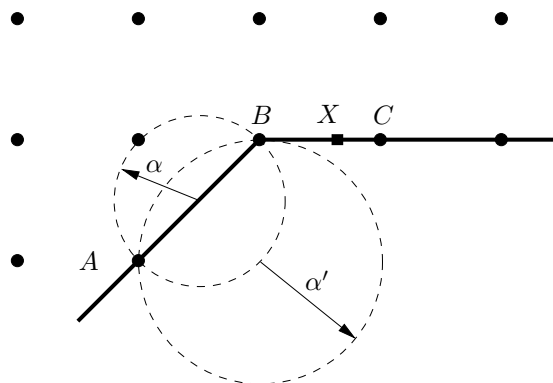
Figure 3.22. Neighborhood in the context of α-complexes (Cueto et al. 2000)

of these nodes, which are not located in the domain of the α-complex. In Fig. 3.22 the node A is not in the neighborhood of the point X, thus it is not considered as a neighbor node in the shape function computation. This method fails for sharp concave corners, like crack tips, thus in this work the concept of the PSLG-defined boundary including the visibility criterion is used in a 2D implementation, where it can be applied much easier than the concept of α-shapes.

3.3   Numerical integration

In meshless methods the discretization of the weak form in Eq. (2.46) can be done similarly to the Finite Element Method, where the meshless domain can be assumed to be a hyper-element with flexible node number. The stiffness relation of such a meshless zone Ω_m reads in analogy to Eq. (2.55)

$$
\begin{aligned}
\mathbf{K}_m &= \int_{\Omega_m} \mathbf{B}_m^T \mathbf{C} \mathbf{B}_m d\Omega \\
\mathbf{f}_m^{ext} &= \int_{\Omega_m} \mathbf{\Phi}_m^T \mathbf{f}^B d\Omega + \int_{\Gamma_m^f} \mathbf{\Phi}_m^T \mathbf{f}^S d\Gamma.
\end{aligned}
\tag{3.65}
$$

Thus a coupling of several meshless zones with finite elements can be easily represented in the global stiffness relation in Eq. (2.56), but this requires a compatible coupling which is achieved in this work as presented in the sections 3.1.4, 3.1.5 and 3.2.4. In this section different approaches for the numerical integration of Eq. (3.65) will be explained.

3.3.1   Gauss integration

In the Element-free Galerkin Method a Gauss quadrature over background meshes is generally performed (Belytschko et al. 1996). Two different approaches have been developed for this purpose, the usage of integration cells which cover the whole body exactly, and the integration over a background cell structure which includes the whole domain where the edges do not coincide with the domain boundary. The required integration order is uncertain for these approaches since the interpolant is a rational function and the integration cells do not coincide with the support of the shape functions. In (Belytschko et al. 1994) the integration order n_Q is approximated in 2D depending on the number of nodes m per integration cell in the form

$$
n_Q = \sqrt{m} + 2.
\tag{3.66}
$$

In (Most and Bucher 2003) the authors used a triangle background mesh spanned by all nodes, which leads to an adapted integration scheme for varying node densities and an exact reproduction of the boundary lines. The triangles are computed using a modified Advancing Front Method based on (Peraire et al. 1987). In (Beissel and Belytschko 1996) a quadrature scheme without a background mesh is presented, but this nodal integration approach is much more complex and does not lead to any better numerical results.

Within the Natural Neighbor Galerkin Method the Delaunay triangles needed for the shape function computation are generally taken as integration cells to avoid an additional background mesh (Sukumar et al. 1998). The same accuracy problems as in the EFG occur, caused by rational interpolant and the fact that integration cells and shape function supports do not coincide. In this work the Delaunay triangulation is used for both meth-

ods, NEM and EFG, as background mesh for the Gauss integration because the Delaunay triangulation gives the best triangle shapes by maximizing the minimum angle in all triangles (Lawson 1977). The weighting factors and the positions of the integration points in a Gauss quadrature over triangles are given for example in (Dunavant 1985).

The influencing nodes needed in the MLS interpolation are determined by using the neighborhood relations of the triangles. The applied algorithm works similar to that described for the NEM in section 3.2.2 by starting with the triangle in which the integration point is located.

3.3.2 Support decomposition of the domain

In (Gonzáles et al. 2004) a method with a decomposition of the domain into subregions is proposed for the Natural Neighbor Galerkin Method. This method was developed to overcome accuracy problems due to integration cells that differ from the shape function support. In the Natural Neighbor Interpolation the area of influence of a node is the union of all circumcircles, corresponding to the triangles in the Delaunay triangulation having this node as a vertex. Thus this is a natural decomposition into subregions that are bounded by segments of all circumcircles of the Delaunay triangulation. Using this decomposition the whole domain is split into triangles and segments of circles. In order to perform the integration over the segments of circles, a mapping from a unit square onto the segment is used (De and Bathe 2001b). Since this transformation his highly nonlinear, and a Gauss point quadrature is used within the unit square, the integration is again only an approximation. Furthermore this procedure is inefficient from a computational point of view, since subregions with a constant number of influencing nodes can be bounded by many circular or straight segments. Thus many further decompositions are required. This approach is applied similarly in the Method of Finite Spheres in (De and Bathe 2001a), where the spherical nodal influence domains are sub-divided in regions with a constant number of influencing nodes.

3.3.3 Stabilized conforming nodal integration

The Stabilized Conforming Nodal Integration scheme (Chen et al. 2001) was developed to enable the exact representation of a linear displacement field within the Element-free Galerkin Method. This method was adapted for the Natural Element Method in (Gonzáles et al. 2004).

If a linear displacement field is assumed, the strain and the stresses in a linear elastic domain are constant. The equilibrium of internal and external forces at node I can be formulated as

$$\mathbf{f}_I^{int} = \mathbf{f}_I^{ext}, \tag{3.67}$$

with

$$
\mathbf{f}_I^{int} = \int_{\Omega_I} \mathbf{B}_I^T \boldsymbol{\sigma} \Omega
$$
$$
\mathbf{f}_I^{ext} = \int_{\Gamma_I^f} \boldsymbol{\Phi}_I^T \boldsymbol{\sigma} d\Gamma. \tag{3.68}
$$

The body forces have to be zero to enable a constant stress field. The constant stress $\boldsymbol{\sigma}$ can be moved outside of the integral and the following relation is obtained

$$
\int_{\Omega_I} \mathbf{B}_I^T \Omega = \int_{\Gamma_I^f} \boldsymbol{\Phi}_I^T d\Gamma, \tag{3.69}
$$

which is the integration constraint condition that has to be fulfilled for every node to enable the exact representation of a linear displacement field. This condition is not fulfilled by using the Gauss integration in the Natural Element Method or in the Element-free Galerkin Method, although the basic interpolations can represent a linear displacement field.

In (Chen et al. 2001) an assumed strain is introduced at the node I

$$
\tilde{\epsilon}_{ij}(\mathbf{x}_I) = \frac{1}{A_I} \int_{\Omega_I} \epsilon_{ij} d\Omega, \quad A_I = \int_{\Omega_I} d\Omega, \tag{3.70}
$$

where ϵ_{ij} are the strains obtained from the kinematic relation

$$
\epsilon_{ij} = \frac{1}{2}\left(\frac{\partial u_i}{\partial x_j} + \frac{\partial u_j}{\partial x_i}\right), \tag{3.71}
$$

and Ω_I is the representative domain of node I, which is assumed to be the first order Voronoi cell of I. By applying the divergence theorem the following equation is obtained

$$
\tilde{\epsilon}_{ij}(\mathbf{x}_I) = \frac{1}{2A_I} \int_{\Gamma_I} (u_i n_j + u_j n_i) d\Gamma, \tag{3.72}
$$

where n_i are the direction cosine components of a unit normal to the nodal domain boundary Γ_I. By introducing the meshless shape function the discrete form of Eq. (3.72) reads

$$
\tilde{\boldsymbol{\epsilon}}(\mathbf{x}_I) = \sum_{L \in G_I} \tilde{\mathbf{B}}_L(\mathbf{x}_I) \tilde{\mathbf{u}}_L, \tag{3.73}
$$

where G_I is the group of the nodes in which their associated shape function supports cover

the domain Ω_I. The modified strain-displacement matrix $\tilde{\mathbf{B}}$ is given in two dimensions

$$\tilde{\mathbf{B}}_L(\mathbf{x}_I) = \frac{1}{A_I} \int_{\Gamma_I} \begin{pmatrix} \Phi_L(\mathbf{x})n_y(\mathbf{x}) & 0 \\ 0 & \Phi_L(\mathbf{x})n_x(\mathbf{x}) \\ \Phi_L(\mathbf{x})n_x & \Phi_L(\mathbf{x})n_y(\mathbf{x}) \end{pmatrix} d\Gamma. \tag{3.74}$$

In (Chen et al. 2001) in was shown, that the assumed strain exactly satisfies the integration constraint for a linear displacement field given in Eq. (3.69). For the implementation of the strain smoothing formulation in a Galerkin approach the mixed variational principle based on an assumed strain method (Simo and Hughes 1986) is considered

$$\delta\Pi(\mathbf{u}, \tilde{\boldsymbol{\epsilon}}) = \int_\Omega \delta\tilde{\boldsymbol{\epsilon}}^T \mathbf{C}\tilde{\boldsymbol{\epsilon}} d\Omega - \int_\Omega \delta\mathbf{u}^T \mathbf{f}^B d\Omega - \int_{\Gamma^f} \delta\mathbf{u}^T \mathbf{f}^S d\Gamma. \tag{3.75}$$

By introducing the discrete formulation for the displacements and the assumed strains and performing nodal integration this variational equation reads

$$\begin{aligned} \mathbf{K}\tilde{\mathbf{u}} &= \mathbf{f}^{ext} \\ \mathbf{K}_{KL} &= \sum_{I=1}^{N_P} \tilde{\mathbf{B}}_L^T(\mathbf{x}_I)\mathbf{C}\tilde{\mathbf{B}}_K(\mathbf{x}_I)A_I \\ \mathbf{f}_L^{ext} &= \sum_{I=1}^{N_P} \boldsymbol{\Phi}_L^T(\mathbf{x}_I)\mathbf{f}^B(\mathbf{x}_I)A_I + \sum_{I=1}^{N_{PB}} \boldsymbol{\Phi}_L^T(\mathbf{x}_I)\mathbf{f}^S(\mathbf{x}_I)s_I, \end{aligned} \tag{3.76}$$

where $\mathbf{K}_{KL}$ is a submatrix associated with node K and node L, N_P is the number of points in G_I, N_{PB} is the number of points on the natural boundary and s_I are the associated weights.

In (Unger 2003) and (Unger et al. 2004) it was shown, that this method fails for systems with load or geometry induced singularity points, like crack tips, which can be observed from an artificial oscillation of the displacements. Furthermore this approach destroys the continuous stress function, which is the main advantage of a meshless interpolation. This can lead to problems especially when evaluating a crack criterion. In (Gonzáles et al. 2004) several systems have been investigated, for nonlinear displacement fields the application of this method did not lead to better results compared to the Gauss integration. For these reasons this nodal integration approach is only applied for comparison in this work.

3.3.4   Adaptive integration

Because of the presented problems of existing integration procedures in (Unger 2003) an adaptive Gauss integration method was developed. These procedures uses the triangle integration cells with a variable Gauss integration order. Starting with a uniform low order the number of Gauss points is increased in these triangles, where the integration

constraints for a linear displacement field in Eq. (3.69) are exceeded most significantly. This constraint equation reads for an internal node I in discretized form

$$\mathbf{0} = \int_{\Omega_I} \mathbf{B}_I^T(\mathbf{x}) \, d\Omega \approx \sum_{L=1}^{N_{IP}} \mathbf{B}_I^T(\mathbf{x}_L)\omega_L, \tag{3.77}$$

where B_I contains the derivatives of the shape functions $\partial\Phi_I(\mathbf{x})/\partial x$ and $\partial\Phi_I(\mathbf{x})/\partial y$, N_{IP} belongs to the number of integration points in the nodal influence domain Ω_I and ω_L are the integration point weights. The normalized integration error at the node is determined as

$$\Delta e_{I,tot} = \frac{1}{A_I} \left[\left(\sum_{L=1}^{N_{IP}} \frac{\partial\Phi_I(\mathbf{x}_L)}{\partial x}\omega_L\right)^2 + \left(\sum_{L=1}^{N_{IP}} \frac{\partial\Phi_I(\mathbf{x}_L)}{\partial y}\omega_L\right)^2 \right]. \tag{3.78}$$

This leads to the error density for a single Delaunay triangle $\triangle_i$

$$\rho_{\triangle_i} = \frac{1}{A_{\triangle i}} \int_{\Omega_{\triangle_i}} \sum_{I=1}^{N} \Delta e_{I,tot}\Phi_I(\mathbf{x}) \, d\Omega, \tag{3.79}$$

where N is the number of nodes with shape function support in $\triangle_i$. Depending on a given error tolerance the integration order in the triangles will be increased until the integration constraints are fulfilled for all triangle integration zones with the required accuracy. This method was verified for different simple examples, but the choice of the error tolerance was done only empirically and the applicability to more complex examples was not yet realized. Therefore more research activities are necessary before this method can be applied to automatic crack growth simulations.

3.4 Examples

The following simple examples will demonstrate the effect of the presented improvements of the MLS and Natural Neighbor Interpolation. There the robustness of the interpolation procedures with respect to strong distortions of the discretization are investigated and compared to finite element simulations.

3.4.1 MLS-shape functions for regular and irregular sets of nodes

Within this example the interpolation errors are calculated for a regular and a irregular set of 5×5 nodes with a distance of $a = 0.25m$ by using the Gaussian, the regularized and the regularized spline weighting function. In Fig. 3.23 both investigated nodal sets are displayed.
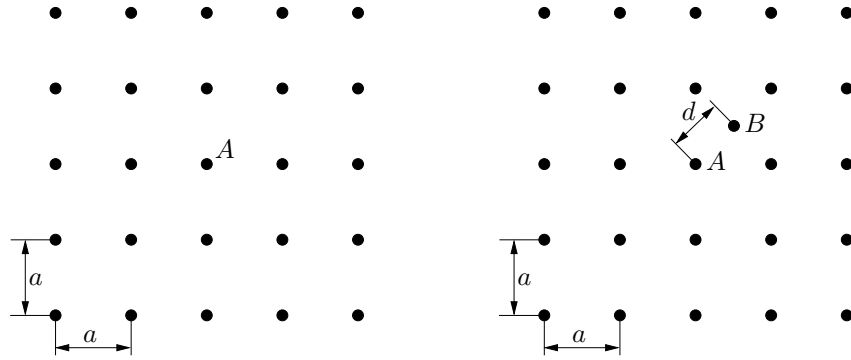

Figure 3.23. Investigated regular and irregular set of nodes

First the interpolation error according to Eq. (3.22) at the supporting points for the shape function of node A is analyzed for a varying influence radius D using the regular nodal set. The regularization term is assumed to be $\epsilon = 10^{-5}$ for the regularized weighting function and $\epsilon = 10^{-3}$ for the regularized spline weighting function. The Gaussian shape parameter is taken with $\alpha = 0.3295$. In Table 3.1 the obtained maximum error is given for

D	$\left\|\Phi_{i,G}^{MLS}\left(\mathbf{x}_j\right) - \delta_{ij}\right\|_{max}$	$\left\|\Phi_{i,R}^{MLS}\left(\mathbf{x}_j\right) - \delta_{ij}\right\|_{max}$	$\left\|\Phi_{i,RS}^{MLS}\left(\mathbf{x}_j\right) - \delta_{ij}\right\|_{max}$
0.3 m	0.6 %	$3.84 \cdot 10^{-4}$ %	$2.50 \cdot 10^{-4}$ %
0.4 m	10.1 %	$2.30 \cdot 10^{-5}$ %	$4.82 \cdot 10^{-5}$ %
0.5 m	30.5 %	$2.66 \cdot 10^{-5}$ %	$7.19 \cdot 10^{-6}$ %
0.6 m	49.5 %	$1.27 \cdot 10^{-5}$ %	$8.88 \cdot 10^{-6}$ %
1.0 m	81.5 %	$1.50 \cdot 10^{-5}$ %	$6.39 \cdot 10^{-5}$ %

Table 3.1. Maximum interpolation error at the nodes as a function of the influence radius using Gaussian (G), regularized (R) and regularized spline (RS) weighting types

all investigated weighting types. It can be seen, that with increasing influence radius the error using the Gaussian weighting function increases but the error from the regularized

types remains very small. This means that Eq. (3.22) is fulfilled with extremely high accuracy if the regularized weighting function is used.

The influence of the minimum nodal distance on the interpolation accuracy is investigated on the irregular set of nodes shown in Fig. 3.23 by decreasing the distance between node A and B. The influence radius is kept constant with $D = 0.5m$. In Table 3.2 the obtained interpolation errors are shown. The table clearly indicates that the interpolation

d_{AB}/D	$\left|\Phi_{i,G}^{MLS}\left(\mathbf{x}_j\right) - \delta_{ij}\right|_{max}$	$\left|\Phi_{i,R}^{MLS}\left(\mathbf{x}_j\right) - \delta_{ij}\right|_{max}$	$\left|w_{i,R}\left(\mathbf{x}_j\right) - \delta_{ij}\right|_{max}$	
			numerical	approximation
0.4	36.8 %	$1.19 \cdot 10^{-5}$ %	$3.81 \cdot 10^{-9}$	$3.81 \cdot 10^{-9}$
0.2	47.7 %	$2.34 \cdot 10^{-6}$ %	$6.24 \cdot 10^{-8}$	$6.24 \cdot 10^{-8}$
0.1	55.2 %	$1.02 \cdot 10^{-5}$ %	$9.97 \cdot 10^{-7}$	$1.00 \cdot 10^{-6}$
0.01	59.0 %	$1.05 \cdot 10^{-3}$ %	$8.26 \cdot 10^{-3}$	$1.00 \cdot 10^{-2}$
0.001	59.0 %	$1.05 \cdot 10^{-1}$ %	$8.26 \cdot 10^{-1}$	–

Table 3.2. Maximum numerical error as a function of the minimum nodal distance

error by using the regularized weighting function is very small even if the nodal arrangement is strongly irregular. Additionally the maximum weighting function error at the supporting points and the approximated values by using Eq. (3.28) are shown in the table. It can be seen, that the approximated values agree very well with the numerical values. For $d_{AB}/D = 0.001$ the assumption in Eq. (3.27) is not valid and the approximation in Eq. (3.28) can not be used.

The application of a weighting function of singular type, which was realized for this example using the function in Eq. (3.25) with $\epsilon = 0$, leads to a exactly fulfilled interpolation condition for all investigated configurations.

3.4.2   Patch test with irregular node distribution

The representation of a linear displacement field depending on the integration type is analyzed in this example. For the investigations a system according to (Unger 2003) is chosen, which is shown with load and boundary conditions in Fig. 3.24. The thickness of the panel is taken as $d = 1m$ and the material properties are assumed to be $E = 10^5 N/m^2$ for the Young's modulus and $\nu = 0.2$ for the Poisson's ratio.

If the MLS interpolation with the regularized spline (RS) weighting function is used, the analytical solution can not be represented because of the nonzero boundary intercepts of the internal nodes. This is shown additionally in Fig. 3.24, where the calculated strains are displayed by using 2500 equally weighted integration points per integration cell. By applying the presented blending technique a behavior similar to the Natural Neighbor Interpolation is obtained, which is shown in Fig. 3.25. The blending length is taken as $l_B = 2.0m$. Similar results can be observed by using the Gaussian (G) weighting type. The deviation from the analytical solution decreases with increasing integration order for
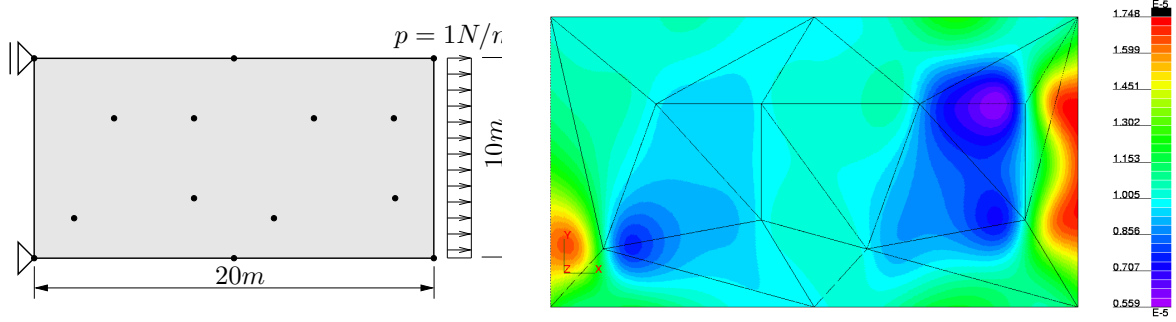
Figure 3.24. Patch test system with loading and boundary conditions and obtained MLS-strains in load direction using regularized weighting and no blending

all three interpolation types. If the singular (SI) weighting type is used, the results are similar only for a smaller number of integration points. If this number increases and some integration points are located too close to the nodes, this error increases.

In Fig. 3.26 the influence of the blending length on the maximum nodal displacement error using the regularized spline weighting function is shown. The figure indicates, that if a certain blending length is reached, the error value converges. If internal nodes are inside of the blending region, which is valid for this example for $l_B = 2.0m$, the results are not influenced negatively. In Table 3.3 the obtained maximum displacement errors by using Gauss integration are given depending on the number of integration points per integration cell. The table indicates, that the displacement errors using NEM and MLS

	Maximum displacement error				Maximum strain error			
N_{IP}	NEM	MLS (G)	MLS (RS)	MLS (SI)	NEM	MLS (G)	MLS (RS)	MLS (SI)
1	2.44 %	33.33 %	10.90 %	11.45 %	20.99 %	48.30 %	80.85 %	77.33 %
4	1.49 %	6.36 %	6.98 %	85.11 %	5.67 %	21.03 %	18.94 %	3984 %
7	0.65 %	1.34 %	0.40 %	0.93 %	3.38 %	11.43 %	6.37 %	11.82 %
12	0.19 %	0.33 %	0.11 %	0.72 %	1.86 %	3.98 %	1.85 %	5.16 %

Table 3.3. Maximum displacement and strain errors for Gauss integration using blended MLS interpolation with Gaussian (G) and regularized spline (RS) weighting and NEM interpolation

interpolation are in the same range. For the practical use in a numerical simulation a displacement error of about 0.2% seems to be acceptable. For higher order displacement fields, the error which occurs by an interpolation of lower order is more significant, thus similar results can be obtained with the presented meshless methods than with comparable finite elements, which will be shown in section 3.4.4. Furthermore this table shows, that the singular weighting function may lead to very bad results, if some of the integration points have a position close to a nodal singularity. Thus this weighting type should not be applied in a Galerkin approach.

By using the Natural Neighbor Interpolation with the Stabilized Conforming Nodal Integration approach, the linear displacement field can be represented exactly. The obtained maximum nodal displacement error for this example by using two Gauss points
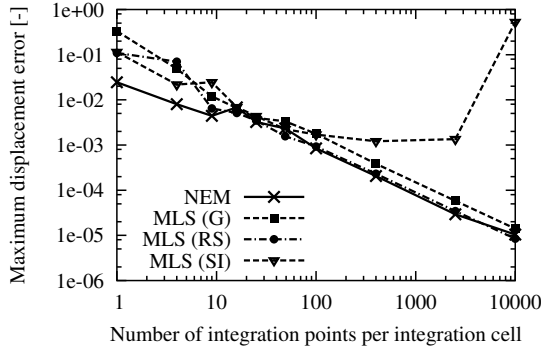
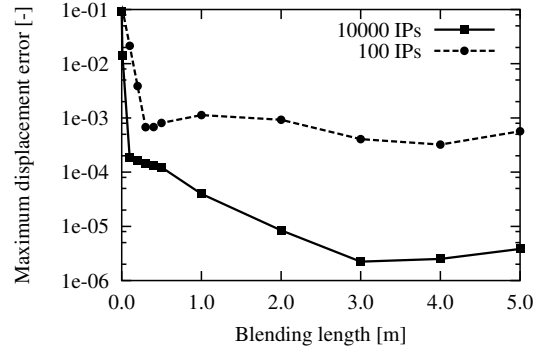**Figure 3.25.** Displacement error vs. integration order using NEM and blended MLS

Figure 3.26. Influence of blending length l_B on the maximum nodal displacement error

per Voronoi segment is $3.02 \cdot 10^{-15}$, which is in the range of the machine precision.

3.4.3 Interpolation along a non-convex boundary

The imposition of a linear boundary interpolation for non-convex domains, presented in section 3.2.4 for the Natural Neighbor Interpolation and in section 3.1.5 for the Moving Least Squares interpolation will be verified in this example. For this purpose the non-convex system shown in Fig. 3.27 is investigated. The properties for the linear elastic material have been taken with $1000 N/m^2$ for the Young's modulus and $\nu = 0.1$ for the Poisson's ratio. The thickness was assumed to be $1.0m$.

The deviations from the function, obtained by using a linear interpolation between the nodal displacement values along the boundary $ABCD$, and the values of the meshless interpolations in several points inside the domain with equal distance from the non-convex boundary are analyzed. In Fig. 3.27 these interpolation errors are shown depending on the distance. The figure indicates, that the application of the Natural Neighbor Interpolation
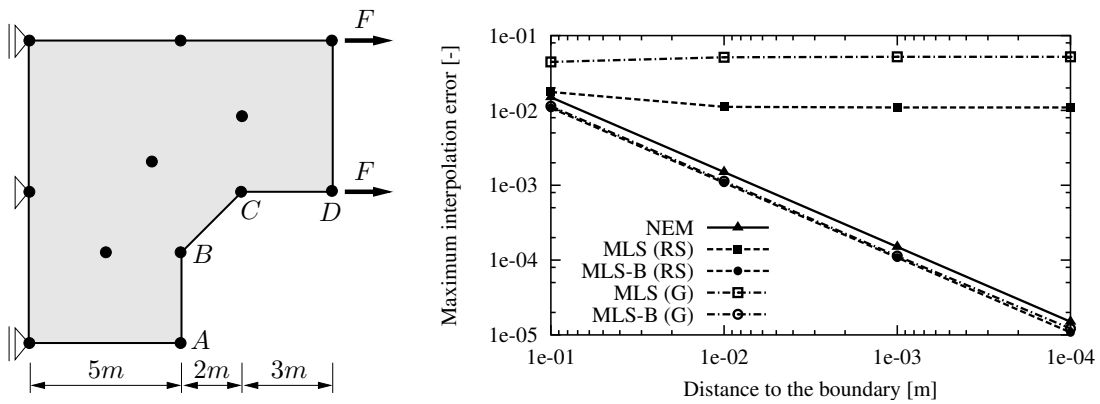

Figure 3.27. Non-convex system with loading and boundary conditions and obtained deviations from an assumed linear boundary interpolation using NEM and MLS interpolation with blending (MLS-B) and without blending and Gaussian (G) and regularized spline (RS) weighting types

leads to a vanishing error for a very small distance, thus the linear precision is fulfilled

asymptotically. By using the MLS interpolation without the presented blending technique the interpolation errors do not converge to zero, therefore the interpolation is not linear along the boundary. If the blending technique is applied, a behavior similar to the Natural Neighbor Interpolation is obtained and linear precision is imposed on the non-convex boundary.

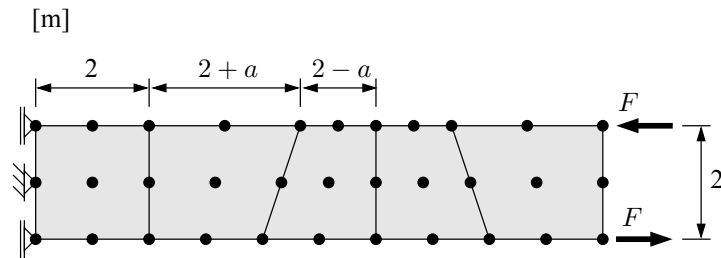### 3.4.4 Cantilever with increasing distortion

Figure 3.28. Investigated distorted cantilever with Q9 mesh

Within this example the accuracy of the meshless interpolation embedded in a Galerkin method is investigated for a quadratic displacement field as a function of increasing distortion of the nodal arrangement. In Fig. 3.28 the system with geometrical properties and boundary conditions is shown. For comparison the investigated beam was discretized with three-node (CST), four-node (Q4) and nine-node (Q9) iso-parametric finite elements. In Fig. 3.28 the Q9 discretization is shown exemplarily. The material was assumed to be linear elastic and the properties are taken as $3000 N/m^2$ for the Young's modulus and $\nu = 0.0$ for the Poisson's ratio and the thickness was defined to be $0.1 m$.

In Fig. 3.29 the obtained maximum nodal displacement errors using the Natural Neighbor Interpolation are displayed as a function of increasing distortion a. The numerical in-
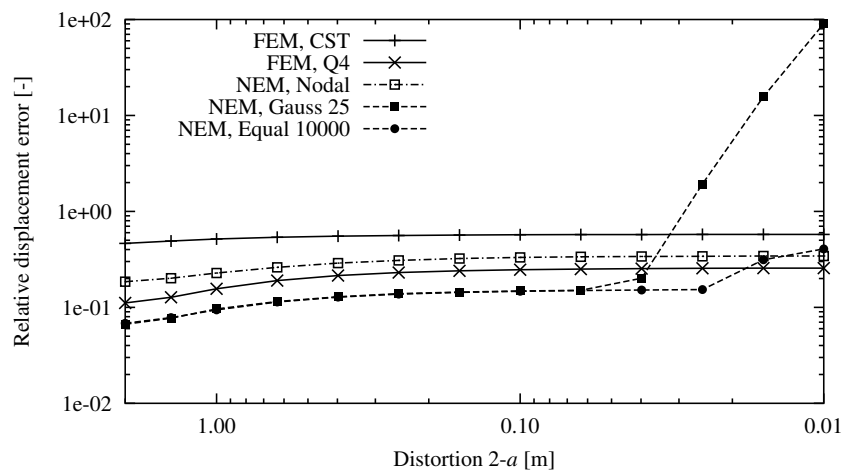

Figure 3.29. Maximum nodal errors for a quadratic displacement field under increasing distortion obtained by using Natural Neighbor Interpolation with Gauss and stabilized nodal integration
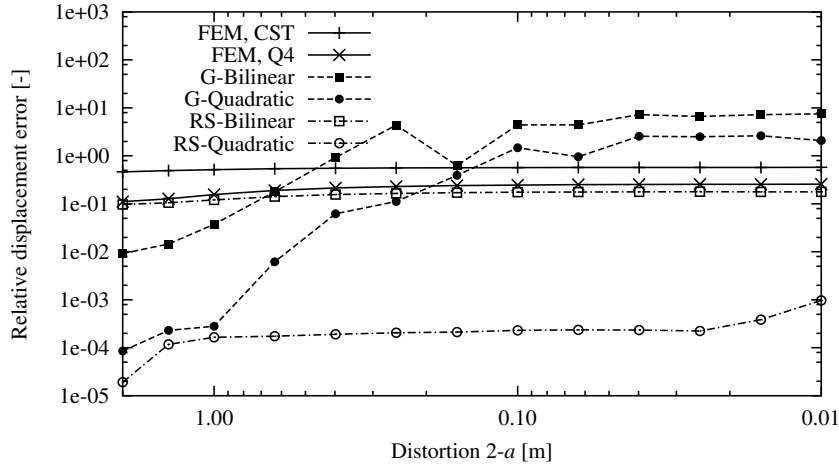
Figure 3.30. Maximum nodal errors obtained by using MLS interpolation with Gaussian (G) and regularized spline (RS) weighting functions and bilinear and quadratic base polynomials

tegration is carried out via a Gauss quadrature over 25 integration points and using 10000 equally weighted integration points per triangular background cell and via stabilized nodal integration with 3 integration points per Voronoi segment. The figure clearly indicates, that the Gauss integrated NEM interpolation gives significantly better results than using the CST and Q4 finite element discretization. By using the Q9 finite elements the analytical solution was obtained within the machine precision for every distorted system. For a very high distortion the obtained error using the Gauss integrated NEM interpolation increases dramatically, which is caused by the integration error. This error is reduced if the integration order is increased, but if highly distorted triangles are avoided during the simulation, the integration error is negligible even for a smaller number of integration points. The application of the nodal integration scheme leads to results, which are very robust against the applied distortion, but the deviations from the analytical solution are much higher than using the Gauss integration.

The obtained numerical errors using the Moving Least Squares interpolation with the common Gaussian weighting and the new regularized spline weighting are shown in Fig. 3.30. The integration is done again using Gauss quadrature over 25 integration points and bilinear and quadratic base polynomials are investigated. The meshless calculations with the quadratic base polynomial led to a very good agreement for the undistorted structure. The remaining deviations from the analytical solution are a result of the integration error. With increasing distortion the usage of the Gaussian weighting function results in an increasing error, whereby the application of the regularized spline type gives very good results even for stronger distortions. For the calculations using the bilinear base polynomial the same trend was observed, there the results from the regularized weighting function are slightly better than these obtained with the Q4 finite elements. The meshless simulations have been carried out by taken the influence radius as $D = 2.5m$ for the bilinear base polynomial and as $D = 3.0m$ for the quadratic base polynomial.
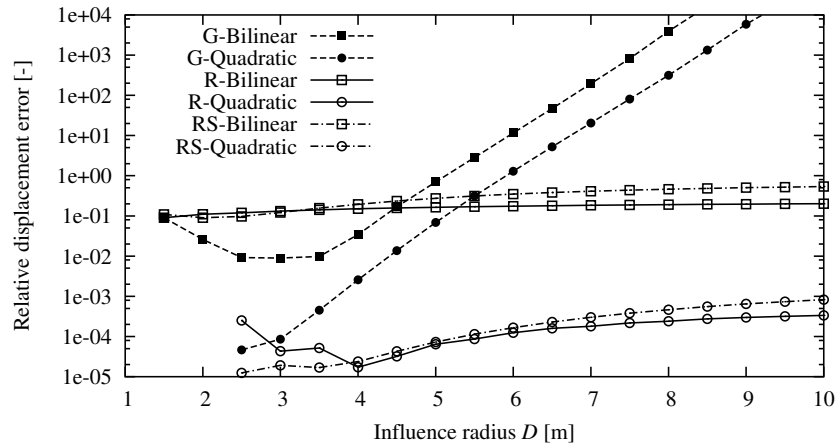
Figure 3.31. Maximum nodal error depending on the influence radius D using Gaussian (G), regularized (R) and regularized spline (RS) weighting types

Furthermore the influence of the size of the influence radius D on the displacement errors is investigated for MLS interpolation. In Fig. 3.31 the obtained errors using the Gaussian, the regularized and the regularized spline weighting functions are shown for an undistorted structure depending on the influence radius D. The figure indicates that the results obtained with the regularized weighting type are almost independent of the influence radius size in strong contrast to these from the Gaussian weighting function. The multiplication of the regularized weighting function with the cubic spline, presented in Eq. (3.30), increases the dependence on D slightly, but compared to the Gaussian weighting function this dependence is negligible.

Chapter 4

Discrete crack modeling

The simulation of crack growth at the macro scale is traditionally done by using two different approaches, the smeared crack model and the discrete crack model. The fracture process is represented within the smeared approach by a number of parallel cracks of small opening smeared over the finite element (Bažant and Planas 1998). The finite element mesh is kept unchanged during the calculation and the crack evolution is represented by a stiffness and strength decrease of the material. The crack behavior is included into the stress-strain relation of the constitutive laws. Two different assumptions of the crack behavior lead to the fixed crack (Červenka 1970) and the rotating crack model (Gupta and Akbar 1984). Some difficulties in the numerical analysis can appear due to the strain softening in the constitutive formulation , such as an ill-posed system of equations, instabilities through localization, and stress-locking caused by mesh sensitivities. A nonlocal approach (Bažant and Pijaudier-Cabot 1988) has been developed to overcome these problems, but they could not be solved in general.

The second group are discrete crack models. They were developed first mainly for the investigation of the fracture behavior of metals by using Linear Elastic Fracture Mechanics (LEFM). One of the first discrete methods was the nodal release approach, where crack growth is possible only along predefined element edges by splitting existing nodes. Due to the strong mesh dependence this method could not be applied to the general case and further techniques were developed. These methods are split-element-methods (Saouma 1981) and approaches using a local remeshing procedure, called the delete-and-refill method. A famous simulation tool for crack growth is the program Franc (Wawrzynek 1991), which uses this adaptive update of the initial finite element mesh to represent an arbitrary geometry of an evolving crack. The main advantages of discrete approaches compared to smeared models are the reduced mesh dependency and the linear-elastic base material, which avoids several problems in the global solution procedure.

Due to the adaptation of the finite element arrangement around a moving crack tip a transfer of the integration point state variables is necessary when investigating nonlinear material behavior. Since the stresses are discontinuous across the element edges this is

not straight-forward. Another problem is the automatic remeshing procedure, which is simple in 2D but very complex and numerically expensive in 3D. Because of this reason the development of meshless discretization techniques has been accelerated in the nineties to overcome this problem. By using meshless methods for crack growth simulations no complex mesh generators are necessary and a state variable transfer, if it is required, is straight-forward due to the continuous stress functions. An adaptive coupling of mesh-less zones in the growing fracture area with traditional finite elements in the undamaged domain, as presented in (Karutz 2000), seems to be necessary to obtain an efficient algorithm. This is because meshless methods require larger numerical effort to determine the shape function values. Another development for modeling discrete cracks is the enrichment of standard finite elements with additional shape functions to represent a line of discontinuity inside the elements in order to avoid any discretization update of the domain. In (Jirásek and Belytschko 2002) two very famous methods are discussed and compared. These are finite elements with embedded discontinuities (Belytschko et al. 1988), which are based on the Enhanced Assumed Strain method (Simo and Rifai 1990), and the Extended Finite Element Method (Moës et al. 1999) which is a Partition of Unity Method. The difference between the two methods is the handling of additional shape functions representing the discontinuity. In elements with embedded discontinuities these additional modes are condensed out and the number of global degrees of freedom remains unchanged. This leads to a discontinuous crack path which is in general adjusted using tracking algorithms. In the Extended Finite Element Method the additional modes are handled as global degrees of freedom, which leads to a continuous crack geometry. In both methods a state variable transfer analog to adaptive finite elements is still necessary for nonlinear materials due to the integration point rearrangement in cracked elements. Furthermore there remain some problems, which have to be solved in the future, e.g. the initiation of a new crack within only one element. Many published applications of these methods still need a fine discretization of the domain to represent curved cracks accurately (Moës and Belytschko 2002). Today several meshless and enriched finite element methods are used by different research groups, since all methods have advantages and disadvantages and an ultimate method can not be defined.

The concepts of Linear Elastic Fracture Mechanics can be used for discrete crack growth only if the fracture process zone at a crack tip is small compared to the system size (Bažant and Planas 1998). When analyzing fracture behavior the size of the fracture process zone is larger for concrete than for metals because of the inhomogeneous character of the material which leads to a widespread aggregate interlock and material de-bonding with developing micro cracks before a macro crack occurs. In (Hillerborg et al. 1976) the fictitious or cohesive crack model was introduced. It merges the number of micro cracks in the fracture process zone in front of a real crack tip to a single fictitious crack with cohesive force transmission over the crack surfaces numerically. Today this

concept is widely used for the crack growth analysis of concrete on the macro scale.

This chapter first presents the fundamental concepts of LEFM. The original cohesive crack model developed for Mode-I dominated problems and an improved model for mixed-mode problems with their adaptation for automatic crack growth simulation are compared and discussed based on this description. Furthermore a stress-based and an energy-based crack criterion are presented and analyzed by means of several numerical examples. Finally the modeling of the bond between concrete and reinforcement is shown and verified.

The presented algorithm describes crack evolution in two dimensions, modeling only the tensile failure of concrete. Thus linear-elastic behavior was assumed for the base material by neglecting the nonlinear behavior of concrete under compression.

4.1 Introduction to Linear Elastic Fracture Mechanics

Linear elastic fracture mechanics (LEFM) is the basic theory of fracture, which was introduced by (Griffith 1921) and completed by (Irwin 1956) and (Rice 1968). LEFM is based on an ideal situation in which the material is elastic except in a vanishing region, which is the crack tip. This concept can be applied to describe the behavior of any material with cracks if the size of the inelastic zone is small compared to the dimension of the elastic domain. In the theory of LEFM the stress field contains a singularity directly at the crack tip no matter how small the external load is. Thus (Griffith 1921) proposed an energetic approach to decide upon growth of existing cracks since a strength criterion can not be applied. In this criterion the energy release rate $\mathcal{G}$, representing the energy available for fracture of a unit crack surface, and the specific fracture energy G_f, representing the energy required for fracture of a unit crack surface, are the basic quantities. By assuming that an existing crack in a plane structure of thickness t under quasi-static loading advances by an infinitesimal length δa, the balance of energy for quasi-static crack growth requires (Bažant and Planas 1998)

$$\mathcal{G}t\delta a = G_f t\delta a. \tag{4.1}$$

In a more general dynamic situation with the initial kinetic energy $\mathcal{K} = 0$ and the kinetic energy increase $\delta\mathcal{K} \geq 0$, Eq. (4.1) reads

$$\mathcal{G}t\delta a = G_f t\delta a + \delta\mathcal{K} \tag{4.2}$$

which leads to the following fracture criterion

$$
\begin{aligned}
&\text{if} \quad \mathcal{G} < G_f \quad \text{then} \quad \delta a = 0 \quad \text{and} \quad \delta\mathcal{K} = 0 \quad \text{No crack growth,} \\
&\text{if} \quad \mathcal{G} = G_f \quad \text{then} \quad \delta a \geq 0 \quad \text{and} \quad \delta\mathcal{K} = 0 \quad \text{Quasi-static crack growth,} \\
&\text{if} \quad \mathcal{G} > G_f \quad \text{then} \quad \delta a > 0 \quad \text{and} \quad \delta\mathcal{K} > 0 \quad \text{Dynamic crack growth.}
\end{aligned}
\tag{4.3}
$$

4.1.1 The concept of stress intensity factors

(Irwin 1956) introduced the stress intensity factors which can be used to describe the stress and displacement field around a crack tip. This concept is based on the decomposition of the crack configuration into three different crack opening modes, Mode-I, Mode-II and Mode-III. A Mode-I crack results from pure in-plane tension loading, Mode-II from in-plane shear loading, and Mode-III from anti-plane shear loading. All three opening modes are shown in Fig. 4.1. (Irwin 1956) defines the dependence of the three opening modes from only three scalar values, the stress intensity factors K_I, K_{II} and K_{III} which may be interpreted as a measure of the crack tip singularity.

In the following sections a two-dimensional stress state is assumed, thus the Mode-III
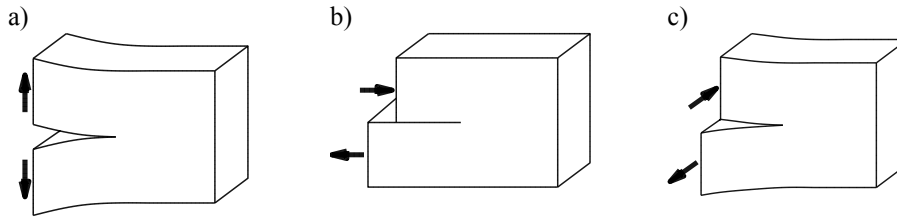
Figure 4.1. Crack opening modes: a) Mode-I, b) Mode-II and c) Mode-III

stress intensity factor vanishes. The stress and displacement field for a pure Mode-I crack are then given in local coordinates as (Anderson 1991)

$$
\begin{bmatrix} \sigma_{\bar{x}\bar{x}} \\ \sigma_{\bar{y}\bar{y}} \\ \sigma_{\bar{x}\bar{y}} \end{bmatrix} = \frac{K_I}{\sqrt{2\pi r}} \cos\frac{\theta}{2} \begin{bmatrix} 1 - \sin\frac{\theta}{2}\sin\frac{3\theta}{2} \\ 1 + \sin\frac{\theta}{2}\sin\frac{3\theta}{2} \\ \sin\frac{\theta}{2}\cos\frac{3\theta}{2} \end{bmatrix} \tag{4.4}
$$

and

$$
\begin{bmatrix} u_{\bar{x}} \\ u_{\bar{y}} \end{bmatrix} = \frac{K_I}{2\mu}\sqrt{\frac{r}{2\pi}} \begin{bmatrix} \cos\frac{\theta}{2}\left(\kappa - 1 + 2\sin^2\frac{\theta}{2}\right) \\ \sin\frac{\theta}{2}\left(\kappa + 1 - 2\cos^2\frac{\theta}{2}\right) \end{bmatrix} . \tag{4.5}
$$

The angle θ and the distance r from the crack tip and the local $\bar{x}, \bar{y}$ coordinate system are indicated in Fig. 4.2.
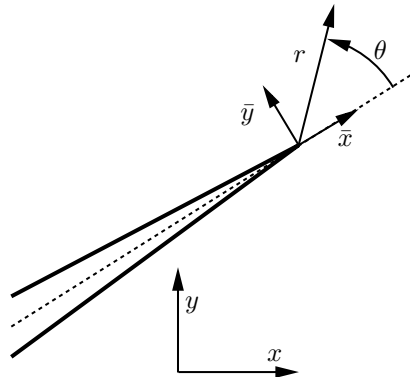

Figure 4.2. Global, local and polar coordinates at an existing crack tip

For a pure Mode-II crack the following formulation is valid

$$
\begin{bmatrix} \sigma_{\bar{x}\bar{x}} \\ \sigma_{\bar{y}\bar{y}} \\ \sigma_{\bar{x}\bar{y}} \end{bmatrix} = \frac{K_{II}}{\sqrt{2\pi r}} \begin{bmatrix} -\sin\frac{\theta}{2}\left(2 + \cos\frac{\theta}{2}\cos\frac{3\theta}{2}\right) \\ \sin\frac{\theta}{2}\cos\frac{\theta}{2}\cos\frac{3\theta}{2} \\ \cos\frac{\theta}{2}\left(1 - \sin\frac{\theta}{2}\sin\frac{3\theta}{2}\right) \end{bmatrix} \tag{4.6}
$$

and

$$\begin{bmatrix} u_{\bar{x}} \\ u_{\bar{y}} \end{bmatrix} = \frac{K_{II}}{2\mu} \sqrt{\frac{r}{2\pi}} \begin{bmatrix} \sin\frac{\theta}{2}\left(\kappa + 1 + 2\cos^2\frac{\theta}{2}\right) \\ -\cos\frac{\theta}{2}\left(\kappa - 1 - 2\sin^2\frac{\theta}{2}\right) \end{bmatrix}, \tag{4.7}$$

where μ is the shear modulus introduced in Eq. (2.29) and κ is the Kolosov constant

$$\kappa = \begin{cases} \dfrac{3-\nu}{1+\nu} & \text{for plane stress} \\[2ex] 3 - 4\nu & \text{for plane strain} \end{cases} \tag{4.8}$$

with the Poisson's ratio ν.

A transformation to polar coordinates leads to the well-known formulation for the stress field for mixed-mode cracking in a two-dimensional domain

$$\begin{bmatrix} \sigma_{rr} \\ \sigma_{\theta\theta} \\ \sigma_{r\theta} \end{bmatrix} = \frac{1}{\sqrt{2\pi r}} \cos\frac{\theta}{2} \begin{bmatrix} K_I\left(1 + \sin^2\frac{\theta}{2}\right) + K_{II}\left(\frac{3}{2}\sin\theta - 2\tan\frac{\theta}{2}\right) \\ K_I\cos^2\frac{\theta}{2} - \frac{3}{2}K_{II}\sin\theta \\ \frac{1}{2}K_I\sin\theta + \frac{1}{2}K_{II}\left(3\cos\theta - 1\right) \end{bmatrix}. \tag{4.9}$$

The energy release rate can be expressed for $\theta = 0$ in terms of the stress intensity factors as (Irwin 1956)

$$\mathcal{G} = \frac{1}{E'}\left(K_I^2 + K_{II}^2\right), \tag{4.10}$$

where

$$E' = \begin{cases} E & \text{for plane stress} \\[2ex] \dfrac{E}{1-\nu^2} & \text{for plane strain} \end{cases}. \tag{4.11}$$

Different methods have been developed for the determination of the stress intensity factors in a numerical analysis. The most common are the Displacement Correlation Method, the Virtual Crack Extension technique, the Crack Closure Integral method and the J-integral method. The Displacement Correlation Method is very simple and correlates the computed local displacements with their theoretical values in Eq. (4.5) and Eq. (4.7) with the stress intensity factors as scaling parameters. For this purpose single points can be evaluated or many displacement values can be used by averaging the obtained stress intensity factors. The Displacement Correlation Method relies on local displacement differences, thus it is very dependent on the local discretization. The Virtual Crack Extension technique is an energy based method and will be explained in detail in the next section. The Crack Closure Integral approach was first suggested by (Rybicki
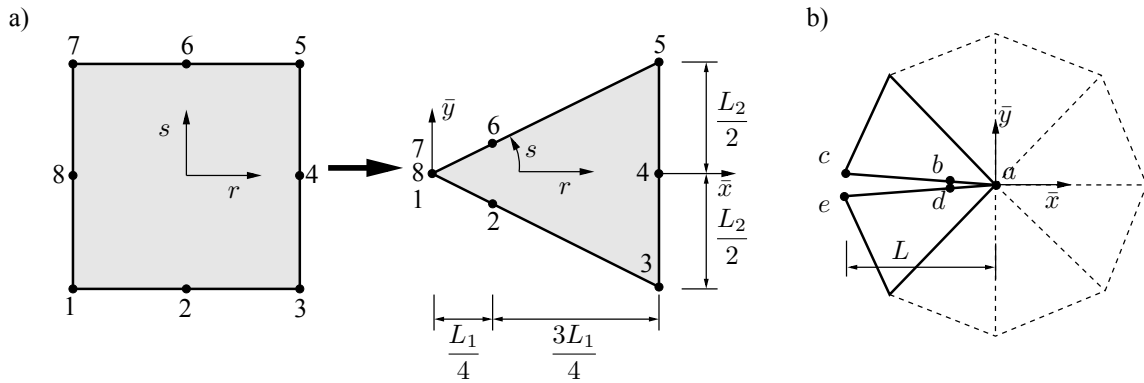
Figure 4.3. a) Transformation of an eight-node isoparametric finite element to a crack tip element with $1/\sqrt{r}$ singularity and b) symmetric discretization around the crack tip

and Kanninen 1977) and is based on the notion in (Irwin 1956) of reversing crack growth to compute the energy release rate. Early versions required two separate numerical calculations, the first with the current crack geometry and the second with a small crack extension. In the Modified Crack Closure Integral method (Singh et al. 1998) only one calculation is necessary by assuming, that the change of the local displacements is small. Another common method is the J-integral approach (Rice 1968), where a contour integral is obtained along the boundary of the crack tip domain, having the singularity inside. This integral is path independent if no body forces are inside the integration area, if no traction affects the crack surface and if the material is linear elastic. For the latter case the J-integral can be interpreted as being equivalent to the energy release rate. The Crack Closure Integral approach and the J-integral method have not been applied in this work, thus they will not be presented more detailed. In general the Virtual Crack Extension technique, the Crack Closure Integral approach and the J-integral method give more accurate results than the Displacement Correlation Method, since they use energy quantities, which are more independent of the discretization than displacement values.

The $1/\sqrt{r}$ stress singularity at the crack tip cannot be represented exactly with standard finite element or meshless interpolation functions. For this reason special approaches have been developed for both methods to overcome this problem and to obtain sufficient accurate results for LEFM problems even with coarse discretization levels. One possibility to introduce a crack tip singularity in a finite element mesh was presented by (Barsoum 1974). There isoparametric eight-node finite elements have been used around the crack tip by merging the three nodes of one edge and moving the middle nodes of the adjacent element edges into the quarter points as shown in Fig. 4.3a. The $1/\sqrt{r}$ singularity is obtained in the merged nodes throughout the Jacobi transformation (Bathe 1996). The stress intensity factors can be simply calculated for a symmetric configuration as shown in

Fig. 4.3b by using the Displacement correlation method according to (Wawrzynek 1991)

$$K_I = \frac{\mu}{1+\kappa}\sqrt{\frac{2\pi}{L}}\left[4(u_{b\bar{y}} - u_{d\bar{y}}) - (u_{c\bar{y}} - u_{e\bar{y}})\right],$$

$$K_{II} = \frac{\mu}{1+\kappa}\sqrt{\frac{2\pi}{L}}\left[4(u_{b\bar{x}} - u_{d\bar{x}}) - (u_{c\bar{x}} - u_{e\bar{x}})\right].$$

$$(4.12)$$

In the Element-free Galerkin Method two different approaches have been developed to enrich the interpolation functions (Fleming 1997). The first method introduces the stress intensity factors as global unknowns in the interpolation

$$u_i(\mathbf{x}) = \mathbf{p}^T(\mathbf{x})\mathbf{a}_i(\mathbf{x}) + K_I Q_{1i}(\mathbf{x}) + K_{II} Q_{2i}(\mathbf{x}),\tag{4.13}$$

where Q_{1i} and Q_{2i} characterize the displacement field as given in Eq. (4.5) and Eq. (4.7). This approach leads to good results, but the implementation is complicated and the number of global unknowns increase. More elegant is a second method, where the base polynomial is extended. The complete enrichment, which can represent the displacement field in Eq. (4.5) and Eq. (4.7) exactly, is given in (Fleming 1997) as

$$\mathbf{p}^T(\mathbf{x}) = \begin{bmatrix} 1 & x & y & ... & \sqrt{r}\cos\frac{\theta}{2} & \sqrt{r}\sin\frac{\theta}{2} & \sqrt{r}\sin\frac{\theta}{2}\sin\theta & \sqrt{r}\cos\frac{\theta}{2}\sin\theta \end{bmatrix}.$$

$$(4.14)$$

This method does not increase the number of global unknowns, but the higher number of base polynomial terms requires the enlargement of the influence radius, which leads to additional numerical effort. Thus in (Fleming 1997) a simplified enrichment is introduced

$$\mathbf{p}^T(\mathbf{x}) = \begin{bmatrix} 1 & x & y & ... & \sqrt{r} \end{bmatrix},\tag{4.15}$$

which can represent the crack tip singularity with much smaller additional effort. Outside of the crack tip domain the $\sqrt{r}$ extension is neglected, which leads to a discontinuous displacement field. In (Hegen 1997) this approach is improved by using a smooth blending of the additional term to obtain continuous displacements. Furthermore in (Hegen 1997) it is noted, that the integration of the crack tip area needs special attention to obtain accurate results. Therefor an integration scheme similar to this of the crack tip elements was applied, where triangle integration cells are mapped onto the unit square as shown in Fig. 4.3a.

In (Sukumar 1998) an enrichment for the Natural Neighbor Interpolation was proposed similar to Eq. (4.15) using only a $\sqrt{r}$ extension. The full enrichment shown in Eq. (4.14) was applied for the Extended Finite Element Method in (Belytschko and Black 1999), whereby only the crack tip element was enriched with crack tip functions. In the

adjacent elements the additional displacement field is blended out with linear functions. In (Fuhlrott 2004) it was found, that this enrichment does not converge to the exact solution for a Mode-I problem, which may be caused by the applied standard integration scheme, using a subdivision of the crack tip element into triangle cells. The application of the integration method proposed in (Hegen 1997) could lead to more accurate results.

In this work an enrichment of the meshless interpolation functions was not implemented, since the simulation of cohesive crack growth is of final interest, where no singularity exists at the cohesive crack tip. The singular crack tip elements have been used for comparison in section 4.5.1 and 4.5.2.

4.1.2 Virtual Crack Extension

The Virtual Crack Extension (VCE) method computes the rate of change of the total potential energy of a system for a virtual extension δa of the crack. It was first proposed by (Parks 1975) and (Hellen 1975) to calculate stress intensity factors.

The formulation of the total potential for the linear elastic case given in Eq. (2.45) can be rewritten as

$$\Pi = \frac{1}{2}\tilde{\mathbf{u}}^T \mathbf{K}\tilde{\mathbf{u}} - \tilde{\mathbf{u}}^T \mathbf{f}^{ext} \tag{4.16}$$

with

$$\begin{aligned} \mathbf{K} &= \int_\Omega \mathbf{B}^T \mathbf{C}\mathbf{B}d\Omega \\ \mathbf{f}^{ext} &= \int_\Omega \mathbf{\Phi}^T \mathbf{f}^B d\Omega + \int_{\Gamma^f} \mathbf{\Phi}^T \mathbf{f}^S d\Gamma, \end{aligned} \tag{4.17}$$

where $\tilde{\mathbf{u}}$ is the nodal displacement vector, $\mathbf{K}$ is the elastic stiffness matrix and $\mathbf{f}^{ext}$ is external nodal force vector of the system. The energy release rate can be expressed as the derivative of the total potential energy with respect to the change of the crack surface A, which is caused by a virtual extension δa (Parks 1975)

$$\mathcal{G} = \frac{\delta \Pi}{\delta A} = -\frac{1}{2}\tilde{\mathbf{u}}^T \frac{\delta \mathbf{K}}{\delta A}\tilde{\mathbf{u}} + \tilde{\mathbf{u}}^T \frac{\delta \mathbf{f}^{ext}}{\delta A}. \tag{4.18}$$

Different approaches are possible to define the virtual crack extension in a numerical discretization. The most common method is to extend only the crack tip by keeping the remaining discretization constant. For the use with standard finite elements, this approach assumes that only the position of the crack tip node is changed. This leads to the assumption, that the external loads keep constant for a change of the crack surface, which is valid if no body forces are applied in the domain influenced by the crack extension and if there
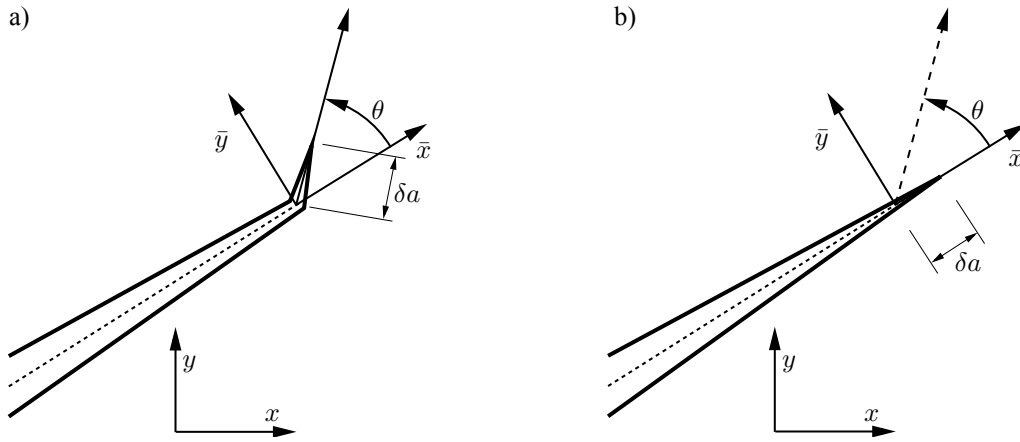
Figure 4.4. a) Noncoplanar VCE extension δa in the direction of the maximum energy release rate and b) simplified coplanar VCE extension in local crack direction

is no externally applied traction on the crack surface. Then Eq. (4.18) can be written as

$$\mathcal{G} = -\frac{1}{2}\tilde{\mathbf{u}}^T \frac{\delta \mathbf{K}}{\delta A}\tilde{\mathbf{u}}. \qquad (4.19)$$

This special type of the VCE technique is called Stiffness Derivative Method.

The crack extension is introduced in the most studies in the local crack direction. This approach is called the coplanar VCE technique (Fig. 4.4b). This local crack direction is only for Mode-I cracking the direction with the maximum energy release rate. Several studies have performed a noncoplanar technique (Hellen 1975), (Sha 1984) as shown in Fig. 4.4a, but indeed errors have been reported, when Mode-II condition is approached (Sha 1984). This technique requires additional numerical effort to determine the direction of the maximum energy release rate. In this study the coplanar VCE technique is used, since in (Xie 1995) it was shown, that this technique did not introduce significant errors. Furthermore in (Ingraffea 1989) it was indicated that mixed-mode crack propagation has always a tendency of approaching Mode-I condition, where the coplanar VCE assumption is valid.

For the general case Eq. (4.19) can be expressed by a finite difference approximation (Parks 1975)

$$\mathcal{G} = -\frac{1}{2\Delta A}\tilde{\mathbf{u}}^T \Delta \mathbf{K}\tilde{\mathbf{u}}, \qquad (4.20)$$

where ΔA is the increase of the crack surface after a crack extension Δa. For a two-dimensional structure with thickness t this value reads $\Delta A = t\Delta a$. An analytical solution for the stiffness derivative can be found for a symmetric discretization around the crack tip with the crack tip elements (Hwang et al. 1998), but this is not possible for an arbitrary asymmetric discretization. In (Yang et al. 2001) it was shown, that the finite difference approximation converges for small values of Δa. Thus in this work the presented finite

difference approach is used to calculate the stiffness derivative.

For the calculation of the stress intensity factors the mode decomposition method (Ishikawa 1980) can be applied. By substituting the Mode-I (symmetric) and Mode-II (anti-symmetric) displacements, $\tilde{\mathbf{u}}_I$ and $\tilde{\mathbf{u}}_{II}$, in Eq. (4.20) the following formulation is obtained

$$
\begin{aligned}
\mathcal{G} &= -\frac{1}{2\Delta A} \left(\tilde{\mathbf{u}}_I + \tilde{\mathbf{u}}_{II} \right)^T \Delta \mathbf{K} \left(\tilde{\mathbf{u}}_I + \tilde{\mathbf{u}}_{II} \right), \\
&= -\frac{1}{2\Delta A} \tilde{\mathbf{u}}_I^T \Delta \mathbf{K} \tilde{\mathbf{u}}_I - \frac{1}{2\Delta A} \tilde{\mathbf{u}}_{II}^T \Delta \mathbf{K} \tilde{\mathbf{u}}_{II} \\
&\quad - \frac{1}{2\Delta A} \tilde{\mathbf{u}}_I^T \Delta \mathbf{K} \tilde{\mathbf{u}}_{II} - \frac{1}{2\Delta A} \tilde{\mathbf{u}}_{II}^T \Delta \mathbf{K} \tilde{\mathbf{u}}_I.
\end{aligned}
\tag{4.21}
$$

The mode-coupling terms vanish, which was proved e.g. in (Hwang et al. 2005), thus the Mode-I and Mode-II energy release rates can be obtained as

$$
\begin{aligned}
\mathcal{G}_I &= -\frac{1}{2\Delta A} \tilde{\mathbf{u}}_I^T \Delta \mathbf{K} \tilde{\mathbf{u}}_I, \\
\mathcal{G}_{II} &= -\frac{1}{2\Delta A} \tilde{\mathbf{u}}_{II}^T \Delta \mathbf{K} \tilde{\mathbf{u}}_{II}.
\end{aligned}
\tag{4.22}
$$

This leads to the absolute values of the stress intensity factors

$$
\begin{aligned}
|K_I| &= \sqrt{E'\mathcal{G}_I}, \\
|K_{II}| &= \sqrt{E'\mathcal{G}_{II}},
\end{aligned}
\tag{4.23}
$$

where E' is defined in Eq. (4.11). To decide the sign of the stress intensity factors the relative displacements of two nodes located symmetrically at both crack surfaces as shown in Fig. 4.5 (node A and B) can be used (Hwang et al. 2005). The relative displacements are defined in local crack coordinates as

$$
\begin{aligned}
\Delta u_{\bar{x}} &= u_{A\bar{x}} - u_{B\bar{x}}, \\
\Delta u_{\bar{y}} &= u_{A\bar{y}} - u_{B\bar{y}}.
\end{aligned}
\tag{4.24}
$$

The sign of K_I is positive if $\Delta u_{\bar{y}}$ is positive and K_{II} is positive if $\Delta u_{\bar{x}}$ is positive.

The Mode-I and Mode-II displacements can be obtained by decomposing the total displacement values. This is realized in this work according to (Yang et al. 2001), where mirror images of the nodes are used. For the node C with belonging mirror node D as shown in Fig. 4.5 this decomposition reads in global coordinates

$$
\mathbf{u}_C = \begin{bmatrix} u_{Cx} \\ u_{Cy} \end{bmatrix} = \mathbf{u}_{C_I} + \mathbf{u}_{C_{II}} = \begin{bmatrix} u_{Cx_I} \\ u_{Cy_I} \end{bmatrix} + \begin{bmatrix} u_{Cx_{II}} \\ u_{Cy_{II}} \end{bmatrix},
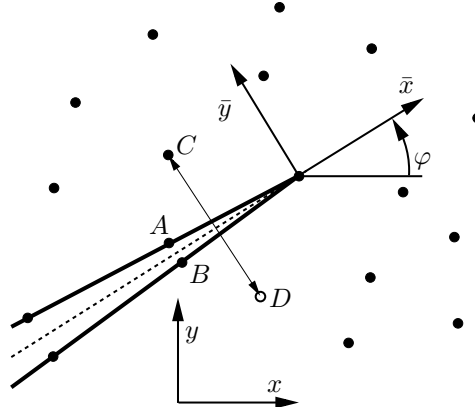\tag{4.25}
$$

Figure 4.5. Decomposition of the nodal displacements using mirror images of the nodes

with

$$
u_{Cx_I} = \frac{1}{2} \left[u_{Cx} + \left(\cos^2\varphi - \sin^2\varphi \right) u_{Dx} + 2\cos\varphi \, \sin\varphi \, u_{Dy} \right],
$$

$$
u_{Cy_I} = \frac{1}{2} \left[u_{Cy} + \left(\sin^2\varphi - \cos^2\varphi \right) u_{Dy} + 2\cos\varphi \, \sin\varphi \, u_{Dx} \right],
$$

$$
u_{Cx_{II}} = \frac{1}{2} \left[u_{Cx} + \left(\sin^2\varphi - \cos^2\varphi \right) u_{Dx} - 2\cos\varphi \, \sin\varphi \, u_{Dy} \right], \tag{4.26}
$$

$$
u_{Cy_{II}} = \frac{1}{2} \left[u_{Cy} + \left(\cos^2\varphi - \sin^2\varphi \right) u_{Dy} - 2\cos\varphi \, \sin\varphi \, u_{Dx} \right],
$$

where φ is the angle between the local and global axes. If the mirror image of a node coincides with an existing nodes, then simply the displacement values of this node are taken for the decomposition. If this is not the case, in this work the displacement values at the mirror node position are calculated using the nodal displacement values interpolated with the meshless shape functions. This procedure and the calculation of the energy release rate in Eq. (4.22) can be done by considering all nodes and the global stiffness change. More efficient is the way to consider only the crack tip domain Ω_{CT}, which is influenced by the shifted crack tip. Using finite elements this crack tip area contains all elements, which are spanned by the crack tip node. In this work the stiffness difference in Eq. (4.22) is computed for the meshless formulation from the integration points influenced by the crack tip node. In Fig. 4.6 this is shown for the Natural Neighbor Interpolation. There the circumcircles of the Delaunay triangles spanned by the crack tip node, which define this integration domain, are illustrated together with the crack tip area nodes. These nodes have to be considered for computing $\tilde{\mathbf{u}}_I$ and $\tilde{\mathbf{u}}_{II}$ if at least one of their belonging triangle circumcircles contains an integration point of the marked integration area.
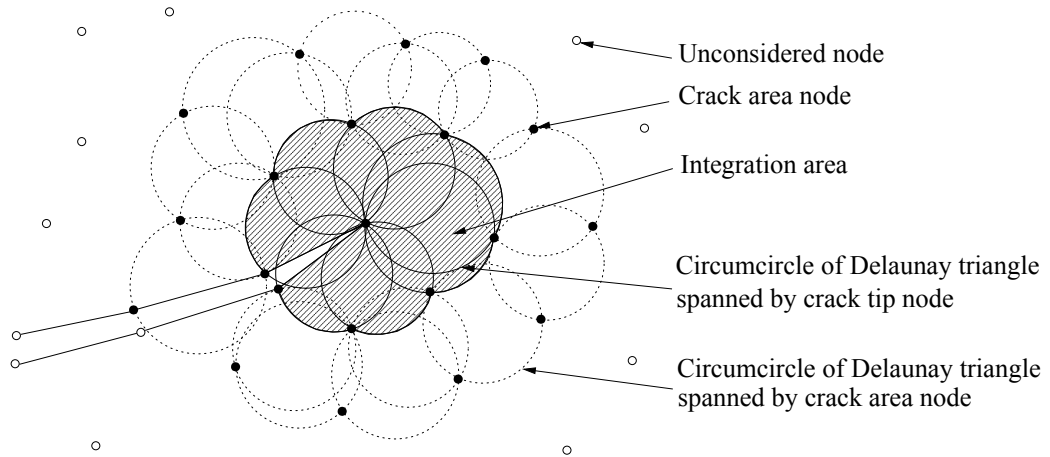
Figure 4.6. Observed nodes in the crack tip area Ω_{CT} and corresponding integration domain for the determination of the stiffness derivative using the Natural Neighbor Interpolation

4.1.3 Crack direction criteria

The most common criterion for predict the crack direction in LEFM is the criterion of maximum circumferential stress (Erdogan and Sih 1963). This criterion states that, for in-plane mixed-mode loading, the crack grows in this direction, where the normal stress across the crack path is tensile, principal and maximum. The traction over the new crack surface are $\sigma_{\theta\theta}$ as normal stress and $\sigma_{r\theta}$ as tangential stress. If the circumferential stress $\sigma_{\theta\theta}$ is maximum the shear stress $\sigma_{r\theta}$ is equal to zero. This leads to the following equation

$$K_I \sin\theta_c + K_{II}(3 \cos\theta_c - 1) = 0, \tag{4.27}$$

since the trivial solution $\cos \theta/2 = 0$ corresponds to $\theta = \pm 180°$, which is the existing crack surface with minimum circumferential stress. The solution of Eq. (4.27) leads to the well-known formulation for the new crack angle

$$\theta_c = 2\arctan\frac{1}{4}\left(\frac{K_I}{K_{II}} \pm \sqrt{\left(\frac{K_I}{K_{II}}\right)^2 + 8} \right), \tag{4.28}$$

where the sign is chosen to make the hoop stress $\sigma_{\theta\theta}$ positive. This is valid if Eq. (4.29) is fulfilled.

$$\sigma_{\theta\theta} = \frac{1}{\sqrt{2\pi r}} \cos\frac{\theta_c}{2} \left[K_I \cos^2\frac{\theta_c}{2} - \frac{3}{2}K_{II} \sin\theta_c \right] \geq 0 \tag{4.29}$$

In (Bažant and Planas 1998) it is noted, that the following criteria are equivalent: the circumferential stress is principal ($\sigma_{r\theta} = 0$), the circumferential stress $\sigma_{\theta\theta}$ is maximum with respect to θ and the magnitude $\sqrt{\sigma_{\theta\theta}^2 + \sigma_{r\theta}^2}$ of the traction vector is maximum with respect to θ.

Another well-known criterion is the maximum energy release rate criterion, which

defines the crack propagation angle in this direction, where the energy release rate is maximum. In LEFM the energy release rate is a function of the direction of propagation and the loading. For infinitesimal crack growth, the loading is completely defined by the near-tip field, which is characterized by K_I and K_{II}. The cracking direction θ_c can be obtained from the following equation

$$\mathcal{G}\left(K_I, K_{II}, \theta\right)|_{\theta=\theta_c} = \text{maximum.} \tag{4.30}$$

This angle can be determined e.g. with the noncoplanar Virtual Crack Extension technique. In (Nuismer 1975) it was shown, that this criterion leads for LEFM to a similar propagation angle as the criterion of maximum circumferential stress.

In (Hussain et al. 1974) an analytical solution for the direction of the maximum energy release rate was found. By assuming an infinitesimal kink at an existing crack analogous to Fig. 4.4a, the new stress intensity factors $K_I(\theta)$ and $K_{II}(\theta)$ have been formulated in terms of the stress intensity factors of the original crack as

$$\left\{ \begin{array}{c} K_I(\theta) \\ K_{II}(\theta) \end{array} \right\} = \frac{4}{3 + \cos^2\theta} \left(\frac{1 - \frac{\theta}{\pi}}{1 + \frac{\theta}{\pi}} \right)^{\frac{\theta}{\pi}} \left\{ \begin{array}{c} K_I \cos\theta - \frac{3}{2}K_{II}\sin\theta \\ K_{II}\cos\theta + \frac{1}{2}K_I\sin\theta \end{array} \right\}. \tag{4.31}$$

The energy release rate can be obtained by assuming coplanar crack growth using Eq. (4.10) as

$$\mathcal{G}(\theta) = \frac{1}{E'} \left(K_I^2(\theta) + K_{II}^2(\theta) \right). \tag{4.32}$$

Substituting Eq. (4.31) in Eq. (4.32) yields

$$\begin{aligned} \mathcal{G}(\theta) = & \frac{4}{E'} \left(\frac{1}{3 + \cos^2\theta} \right)^2 \left(\frac{1 - \frac{\theta}{\pi}}{1 + \frac{\theta}{\pi}} \right)^{\frac{\theta}{\pi}} \\ & \left[(1 + 3\cos^2\theta)K_I^2 - 8\sin\theta \cos\theta K_I K_{II} + (9 - 5\cos^2\theta)K_{II}^2 \right]. \end{aligned} \tag{4.33}$$

The angle of crack propagation θ_c is found by maximizing $\mathcal{G}(\theta)$

$$\begin{aligned} \frac{\partial \mathcal{G}(\theta)}{\partial \theta} &= 0, \\ \frac{\partial^2 \mathcal{G}(\theta)}{\partial \theta^2} &< 0. \end{aligned} \tag{4.34}$$

In Fig.4.7 the energy release rate is plotted depending on the assumed crack propagation angle for different ratios of the stress intensity factors. Fig. 4.8 shows the obtained crack angles, where the energy release rate is maximum, in comparison to the values obtained with the maximum circumferential stress criterion given in Eq. (4.28). The figure indicates, that both approaches give similar values. For pure Mode-II with $K_I = 0$ the crack
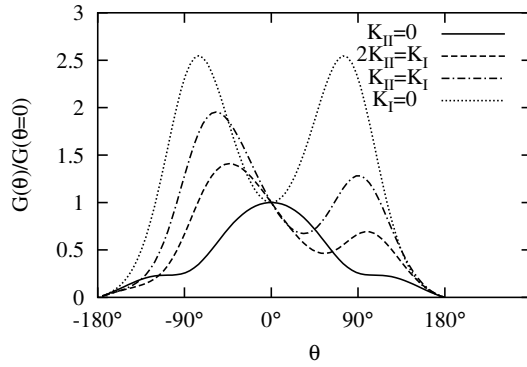
Figure 4.7. Energy release rate depending on the assumed crack propagation angle for different ratios K_I/K_{II}
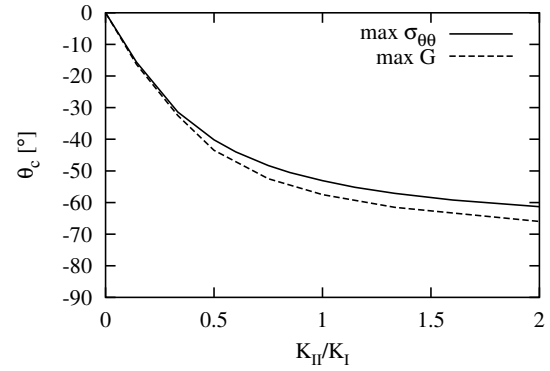
Figure 4.8. Prediction of θ_c using the direction of maximum circumferential stress and maximum energy release rate

propagation angle is $\theta_c = -75.2°$ using the maximum energy release rate direction and $\theta_c = -70.5°$ using the direction of maximum circumferential stress.
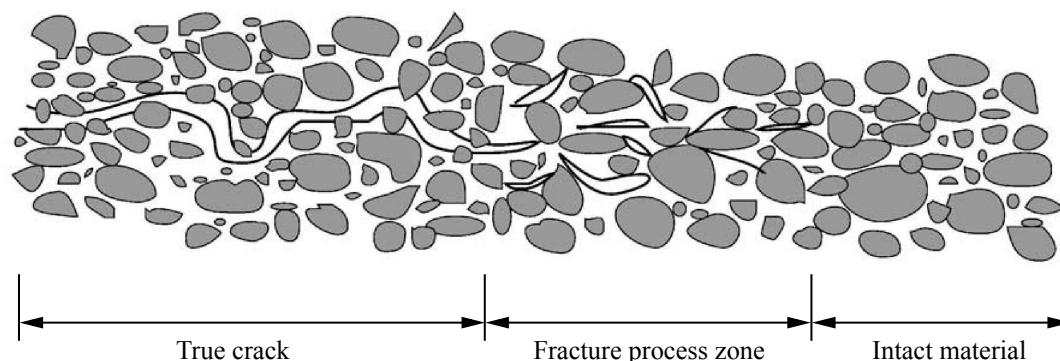
4.2   Cohesive Crack Model

Figure 4.9. Cracking process in concrete (Gálvez et al. 2002)

In LEFM the fracture process is considered to occur at the tip of a sharp crack, which is valid if the fracture process zone is small compared to the relevant dimensions of the specimen. For the description of cracking in concrete structures, this approach can not be applied since the crack length or other dimensions of the structure are small compared to a fully developed fracture process zone. In that case a detailed description of the process in the fracture process zone is necessary. Fig. 4.9 shows the principle of this process. In an intact material which has not been loaded up to its strength the fracture process zone develops when the material strength is reached. In this zone the material is partially broken by micro cracks, but with unbroken bridges, which are able to transmit stresses through the interface. If these bridges are destroyed, the micro cracks turn into a true crack without stresses transmission through the interface.

4.2.1   Mode-I cohesive crack model

(Hillerborg et al. 1976) proposed the so-called Cohesive or Fictitious Crack Model, which models the fracture process on the macroscopic level. In this model the fracture process zone ahead of a real crack tip is lumped into a fictitious crack line transferring surface stresses until the crack width reaches a critical value. This model has been successfully applied in a huge number of studies dealing with the crack propagation in concrete. Part of this success is due to its simplicity and physical meaning.

The stress σ_N normal to the crack surface is formulated in this model as a function of the crack opening Δu_N. Two properties of the softening curve are most important: the tensile strength f_t and the specific fracture energy for Mode-I G_f^I, which are introduced in the cohesive crack model as constant material parameters. Several types for this softening function have been developed. Some widely used are shown in Fig. 4.10. The rectangular and linear function are very simple, but can not reproduce the softening behavior sufficient accurate. In (Petersson 1981) a bilinear curve with fixed kink was presented. This type is very common, since in can be fitted very simple for different experimental curves. In
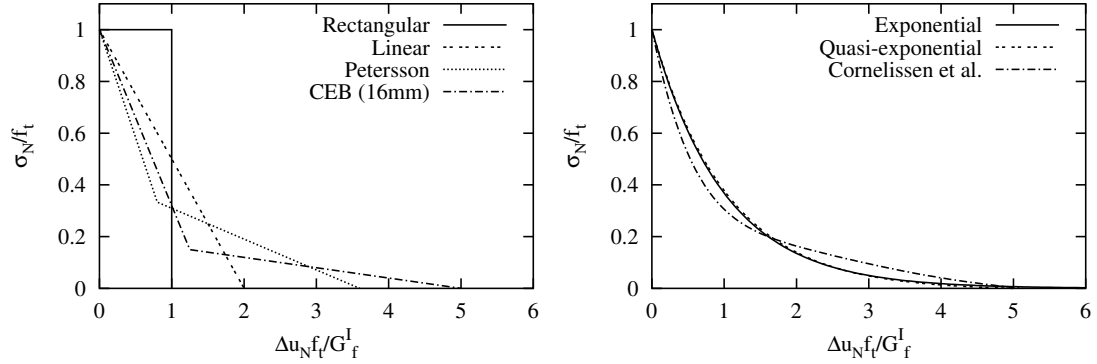
Figure 4.10. Softening functions of linear/bilinear and exponential type

the CEB-FIB Model Code (Telford 1993) several bilinear curves are given for different maximum aggregate sizes.

A huge number of softening laws have been derived from the exponential function type

$$\sigma_N = f_{ct} \cdot \exp\left[-\frac{f_{ct}\Delta u_N}{G_f^I}\right]. \tag{4.35}$$

One is the quasi-exponential softening law (Hillerborg et al. 1976)

$$\sigma_N = \begin{cases} f_t\left(1 + c_1\right) \cdot \exp\left[-c_2 \frac{f_t \Delta u_N}{G_f^I}\right] - f_t c_1 & \Delta u_N \leq \Delta u_{Nc} \\ 0 & \Delta u_N > \Delta u_{Nc} \end{cases} \tag{4.36}$$

where the dimensionless parameters c_1 and c_2 can be obtained from the following equations

$$c_2 = 1 - c_1 \frac{1 + c_1}{c_1}, \quad \frac{f_t}{G_f^I}\Delta u_{Nc} = \frac{1 - c_2}{c_1 c_2}. \tag{4.37}$$

The critical crack opening Δu_{Nc}, where the fictitious crack turns into a real crack without normal stresses is given for standard concrete in (Planas and Elices 1991) as $\Delta u_{Nc} = 5G_f^I/f_t$ which gives the required parameters using Eq. (4.37) as $c_1 = 8.2896 \cdot 10^{-3}$ and $c_2 = 0.9602016$. Another well-known softening curve of exponential type was proposed in (Cornelissen et al. 1986)

$$\sigma_N = \begin{cases} f_t\left[1 + 0.199\left(\frac{f_t \Delta u_N}{G_f^I}\right)^3\right] \cdot \exp\left[-1.35\frac{f_t \Delta u_N}{G_f^I}\right] \\ -0.00533\frac{f_t^2 \Delta u_N}{G_f^I} & \Delta u_N \leq \Delta u_{Nc} \\ 0 & \Delta u_N > \Delta u_{Nc} \end{cases} \tag{4.38}$$
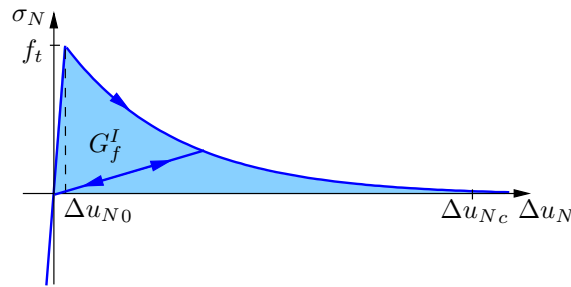
Figure 4.11. Modified normal stress function depending on crack opening displacement

where the critical crack width is given with $\Delta u_{Nc} = 5.14 G_f^I / f_t$. For the general case the function for the normal stress σ_N can be formulated as

$$
\sigma_N = \begin{cases} \sigma_N^{soft}\left(f_t, G_f^I, \Delta u_N\right) & \Delta u_N \le \Delta u_{Nc} \\ 0 & \Delta u_N > \Delta u_{Nc} \end{cases} \tag{4.39}
$$

with $\Delta u_{Nc} = \Delta u_{Nc}\left(f_t, G_f^I\right)$.

In order to minimize the penetration of existing crack surfaces caused by compressive loading and to activate the maximum tensile forces over a crack width $\Delta u_{N0} > 0$, which is necessary to obtain numerical stability, a linear penalty function with constant stiffness k_N is applied in this work for a crack width Δu_N below Δu_{N0}. This leads to the following modified normal stress function

$$
\sigma_N^{mod} = \begin{cases} k_N \Delta u_N & \Delta u_N \le \Delta u_{N0} \\ \sigma_N^{soft}\left(f_t, G_f^{Imod}, \Delta u_N - \Delta u_{N0}\right) & \Delta u_{N0} < \Delta u_N \le \Delta u_{Nc}^{mod} + \Delta u_{N0} \\ 0 & \Delta u_{Nc}^{mod} + \Delta u_{N0} < \Delta u_N \end{cases} \tag{4.40}
$$

with

$$
\Delta u_{N0} = \frac{f_t}{k_N}, \qquad k_N \gg \frac{f_t^2}{G_f^I},
$$
$$
\Delta u_{Nc}^{mod} = \Delta u_{Nc}\left(f_t, G_f^{Imod}\right), \qquad G_f^{Imod} = G_f^I - \frac{f_t \cdot \Delta u_{N0}}{2}. \tag{4.41}
$$

The modifications in the softening function in Eq. (4.40) are necessary to keep the integral of the whole function for positive values of Δu_N equal to the specific fracture energy G_f^I. The penalty stiffness k_N has to be chosen as large as possible to minimize the artifical activation crack width Δu_{N0} but avoiding numerical problems within the global iteration procedure. For un- and reloading a linear function back to the point of origin is assumed. In Fig. 4.11 the modified normal stress function depending on the crack width is visualized for a quasi-exponential softening type.

In the basic cohesive crack model the shear stress transmission in tangential direction is neglected. In some studies, e.g. (Häussler-Combe 2001), this model was enhanced by introducing shear stresses according to the Coulomb friction hypothesis. This extended model can still not represent the interaction between the normal traction and shear traction damage of the crack surfaces and the dilatancy caused by the saw-teeth effect of the irregularities along the crack surfaces. Thus it leads to sufficiently accurate results only for Mode-I dominated problems.

4.2.2 Improved mixed-mode cohesive crack model

Due to the limitation of the standard cohesive crack model for Mode-I dominated problems, in this work a coupled mixed-mode cohesive crack model proposed by (Carol et al. 1997) is adapted for the use in automatic crack growth simulation. This model represents the degradation of the fictitious crack surfaces under coupled normal and shear traction. Thus the destruction of the aggregate interlocking due to pure sliding of the crack surfaces or combined sliding and opening can be modeled. Furthermore this model is able to represent the dilatancy effect, which leads to crack opening under pure tangential loading.

This model was proposed for the three-dimensional case, but in this section the implemented two-dimensional formulation is presented for simplicity. The degradation of the crack surface is described by (Carol et al. 1997) in terms of the classical plasticity theory, where the well-known continuum formulation is transferred into an interface formulation, where relative displacements $\Delta \mathbf{u}$ in the crack surface are used instead of strains. Based on a decomposition of $\Delta \mathbf{u}$ into an elastic part $\Delta \mathbf{u}^{el}$ and a plastic part $\Delta \mathbf{u}^{cr}$ in the following form

$$\Delta \mathbf{u} = \begin{bmatrix} \Delta u_N \\ \Delta u_T \end{bmatrix} = \Delta \mathbf{u}^{el} + \Delta \mathbf{u}^{cr} = \begin{bmatrix} \Delta u_N^{el} + \Delta u_N^{cr} \\ \Delta u_T^{el} + \Delta u_T^{cr} \end{bmatrix}, \tag{4.42}$$

the stresses in the crack surface are defined as

$$\boldsymbol{\sigma} = \begin{bmatrix} \sigma_N \\ \sigma_T \end{bmatrix} = \mathbf{C} \left(\Delta \mathbf{u} - \Delta \mathbf{u}^{cr} \right) = \begin{bmatrix} k_N & 0 \\ 0 & k_T \end{bmatrix} \begin{bmatrix} \Delta u_N - \Delta u_N^{cr} \\ \Delta u_T - \Delta u_T^{cr} \end{bmatrix}, \tag{4.43}$$

where $\mathbf{C}$ is the elastic material stiffness matrix, which contains only decoupled terms, and Δu_T and σ_T are the relative displacement and the stress in tangential direction, respectively. The elastic stiffness values k_N and k_T are, similar to k_N in the standard cohesive model with the penalty approach in Eq. (4.40), numerical parameters for the activation of the normal and shear stresses without physical meaning.

The fracture process is described by a hyperbolic yield surface shown in Fig. 4.12a

$$F = \sigma_T^2 - (c - \sigma_N \tan\phi)^2 + (c - \chi \tan\phi)^2, \tag{4.44}$$
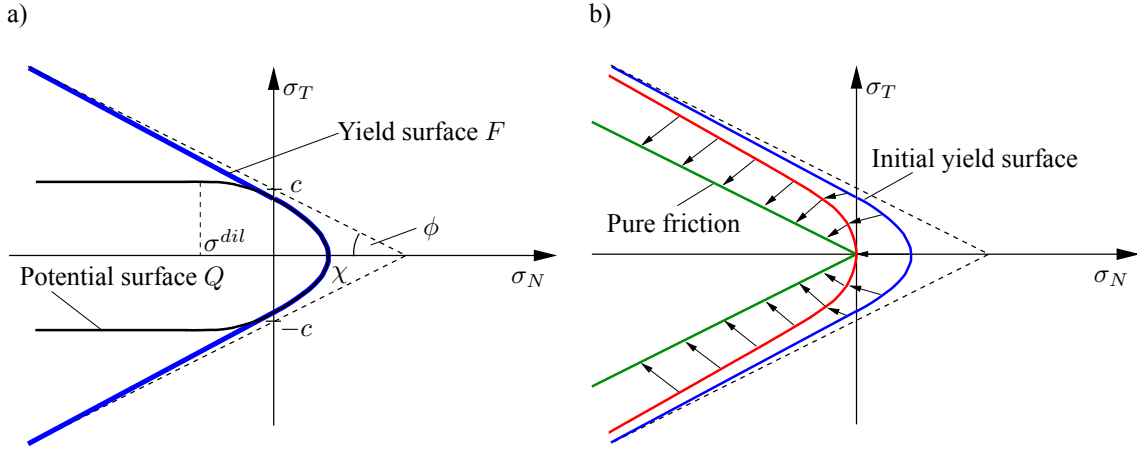
a)

b)

Figure 4.12. a) Hyperbolic yield surface and plastic potential, b) Development of yield surface

where $\tan\phi$ is the friction coefficient for Coulomb friction and c and χ are internal variables belonging to the actual shear and tensile strength, respectively. If the value of the yield criterion F is negative, the interface material is in an elastic state (initial or un-/reloading), and if F is equal to zero the material is in a plastic state, where the internal variables c and χ show a softening behavior with increasing plastic relative displacements $\Delta\mathbf{u}^{cr}$. In Fig. 4.12b the development from the initial yield surface to the state with completely destroyed interlocking of the crack surfaces is shown. This final state represents Coulomb's friction between two plain surfaces.

In (Carol et al. 1997) the softening behavior of χ and c is described in terms of the work W^{cr} spent on the fracture process during the formation of the crack. They are assumed to decrease from their initial values χ_0 and c_0, which are the initial tensile and shear strength taken as material parameters, to zero when $W^{cr} = G_f^I$ and $W^{cr} = G_f^{IIa}$, respectively. The initial tensile strength χ_0 is equivalent to f_t defined in the previous section. G_f^I is the Mode-I specific fracture energy, which is used in the standard cohesive model, and G_f^{IIa} is the Mode-IIa specific fracture energy. The latter case is also called asymptotic Mode-II, where the crack opening due to dilatancy effects is avoided by very high compression forces. The variation of c and χ is defined by a scaling function ψ as

$$
\begin{aligned}
\chi &= \chi_0 - \chi_0\,\psi\left(\frac{W^{cr}}{G_f^I}, \alpha_\chi\right), \\
c &= c_0 - c_0\,\psi\left(\frac{W^{cr}}{G_f^{IIa}}, \alpha_c\right),
\end{aligned}
\tag{4.45}
$$

with

$$
\psi(\xi, \alpha) = \frac{e^{-\alpha\xi}}{1 + (e^{-\alpha} - 1)\,\xi}.
\tag{4.46}
$$

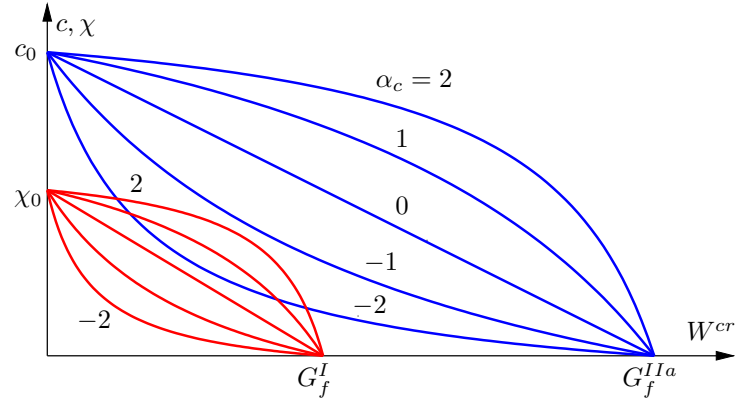In Fig. 4.13 the softening curves for c and χ depending on W^{cr} are shown for different

Figure 4.13. Softening functions for c and χ depending on the shape parameters α_c and α_χ

scaling parameters α_c and α_χ. Linear decreasing functions are obtained for $\alpha = 0$.

The change of the actual work W^{cr} is defined in (Carol et al. 1997) as

$$
dW^{cr} = \begin{cases} \sigma_N du_N^{cr} + \sigma_T du_T^{cr} & \sigma_N \geq 0 \\ \sigma_T du_T^{cr} \left(1 - \left| \dfrac{\sigma_N \tan\phi}{\sigma_T} \right| \right) & \sigma_N < 0 \end{cases} \tag{4.47}
$$

which implies, that in tension all dissipated work goes into the fracture process, while in compression only the shear work by subtracting the basic friction is considered.

The yield direction is defined in classical plasticity theory perpendicular to the plastic potential surface Q. In this model this potential surface is taken as the yield surface by introducing following two modifications: Initially the potential surface coincides with the yield surface in tension. For compression the dilatancy vanishes for a compressive stress higher than the dilatancy stress σ^{dil}, which is introduced as material parameter. Furthermore the amount of dilatancy has to decrease with increasing degradation of the crack surface. It vanishes completely for the pure friction state with $c = 0$. This leads to the following expressions for the derivatives of the plastic potential, which describe the yield direction

$$
\frac{\partial Q}{\partial \sigma_N} = 2 \tan\phi(c - \sigma_N \tan\phi) f_\sigma^{dil} f_c^{dil}, \quad \frac{\partial Q}{\partial \sigma_T} = 2\sigma_T, \tag{4.48}
$$

where f_σ^{dil} and f_c^{dil} are the factors introduced to represent the two mentioned effects. These factors are defined using the scaling function in Eq. (4.46) as follows

$$
\begin{aligned}
f_\sigma^{dil} &= 1 - \psi\left(\frac{|\sigma|}{\sigma^{dil}}, \alpha_\sigma^{dil} \right), \\
f_c^{dil} &= 1 - \psi\left(\frac{c_0 - c}{c_0}, \alpha_c^{dil} \right).
\end{aligned} \tag{4.49}
$$

The plastic potential is shown in Fig. 4.12a together with the yield surface for an initial material state. Altogether the presented model has twelve parameters, the elastic stiff-

nesses k_N and k_T, the initial tensile and shear strength χ_0 and c_0, the Mode-I and Mode-IIa specific fracture energy G_f^I and G_f^{IIa}, the friction coefficient $\tan\phi$, the dilatancy stress σ^{dil} and four shape parameters, α_χ, α_c, α_σ^{dil} and α_c^{dil}, where the elastic stiffnesses are pure numerical parameters, which have to be taken as large as possible without causing numerical problems.

In this work the implementation of the presented model clarified a significant problem of the formulation, which limits the application to very small incremental steps. This problem is caused by the quadratic formulation of the yield surface in Eq. (4.44) concerning σ_N, which has two independent functions fulfilling $F = 0$. This is shown in Fig. 4.14. If the elastic predictor in the stress update procedure is to large, caused by large increments or high elastic stiffnesses, the iteration converges to the second zero line, which has no physical meaning. In the worst case elastic behavior is indicated if the elastic predictor is in the second domain with $F < 0$.

This problem is solved here, by transforming the original surface with quadratic terms to the following formulation

$$F_{mod} = \sqrt{\sigma_T^2 + (c - \chi \tan\phi)^2} - c + \sigma_N \tan\phi, \qquad (4.50)$$

where no quadratic term concerning σ_N is included. Fig. 4.14 indicates, that the modified surface has only one function with $F = 0$, which coincides exactly with the first function of the original surface. The derivatives of the modified yield function lead to the following formulation of the yield direction

$$\frac{\partial Q}{\partial \sigma_N} = \tan\phi f_\sigma^{dil} f_c^{dil}, \quad \frac{\partial Q}{\partial \sigma_T} = \frac{\sigma_T}{\sqrt{\sigma_T^2 + (c - \chi \tan\phi)^2}}. \qquad (4.51)$$

The modified model has been implemented by using the General Closest Point Projection algorithm (Simo and Hughes 1998), which is an implicit method and leads to the fulfillment of the constitutive equations presented in this section with a given tolerance.
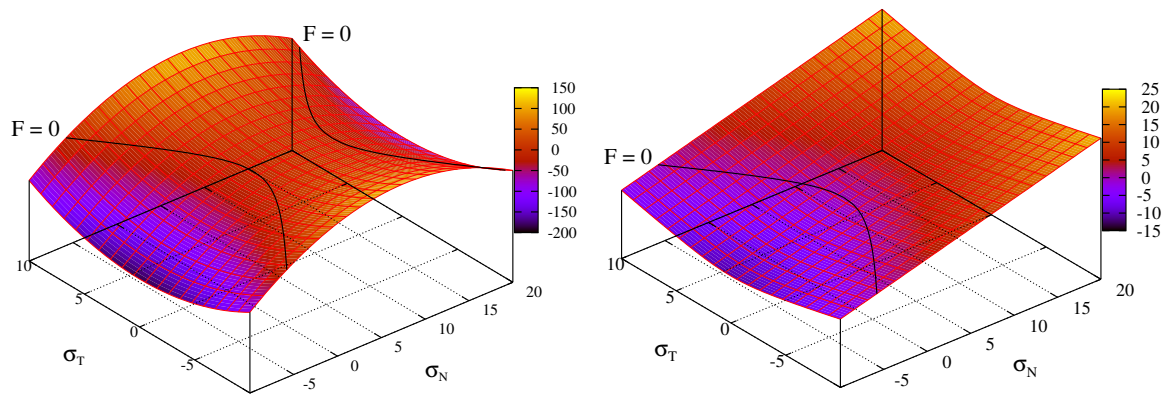

Figure 4.14. Original yield surface with two functions for $F = 0$ and modified surface with only one zero line

Thus it can be applied to larger increments, which enables a stable global iteration procedure. The algorithm and the tangential material stiffness matrix are derived in detail in the appendix.

Due to the formulation of the softening function of c and χ in terms of the work W^{cr} and the scaling function $\psi(\xi, \alpha)$, the direct fitting of experimental curves, e.g. from uniaxial tension tests, is not directly possible. For the case of uniaxial tension and $\alpha_\chi = 0$ the following relation has been derived in (Carol et al. 1997) for the total crack opening displacement

$$\Delta u_N = \frac{\sigma_N}{k_N} + \frac{G_f^I}{\chi_0} \ln \frac{\chi_0}{\sigma_N}, \tag{4.52}$$

which is valid for $\Delta u_N > \chi_0/k_N$, describing the softening part of the function. This equation can not be inverted in closed form to give σ_N in terms of Δu_N, but for a very high elastic stiffness k_N, this relation leads to the well-known exponential softening curve in Eq. (4.35). This means, that the exponential curve modified by the penalty approach in Eq. (4.40) and the result given in Eq. (4.52) agree exactly for $k_N = \infty$. For smaller values of k_N the curves differ as shown in Fig. 4.15. In this work the value for the normal
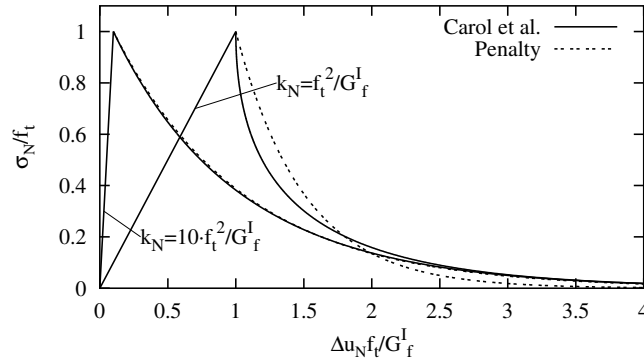

Figure 4.15. Comparison of the uniaxial softening function obtained by using the model of (Carol et al. 1997) and the penalty approach

stiffness is taken as $k_N > 1000 f_t^2/G_f^I$, thus both curves agree almost exactly. For linear or piecewise linear uniaxial softening curves, the function of c and χ in terms of W^{cr} can be derived analytically. This enables an easy fitting of experimental data, e.g. using a bilinear approximation. For linear softening the function of χ in terms of W^{cr} reads

$$\chi^{linear}(W^{cr}) = \begin{cases} \chi_0 \sqrt{1 - \dfrac{W^{cr}}{G_f^I}} & W^{cr} \leq G_f^I \\ \\ 0 & W^{cr} > G_f^I \end{cases} \tag{4.53}$$

which can be used analogous for c. For the general bilinear case, shown in Fig. 4.16, the
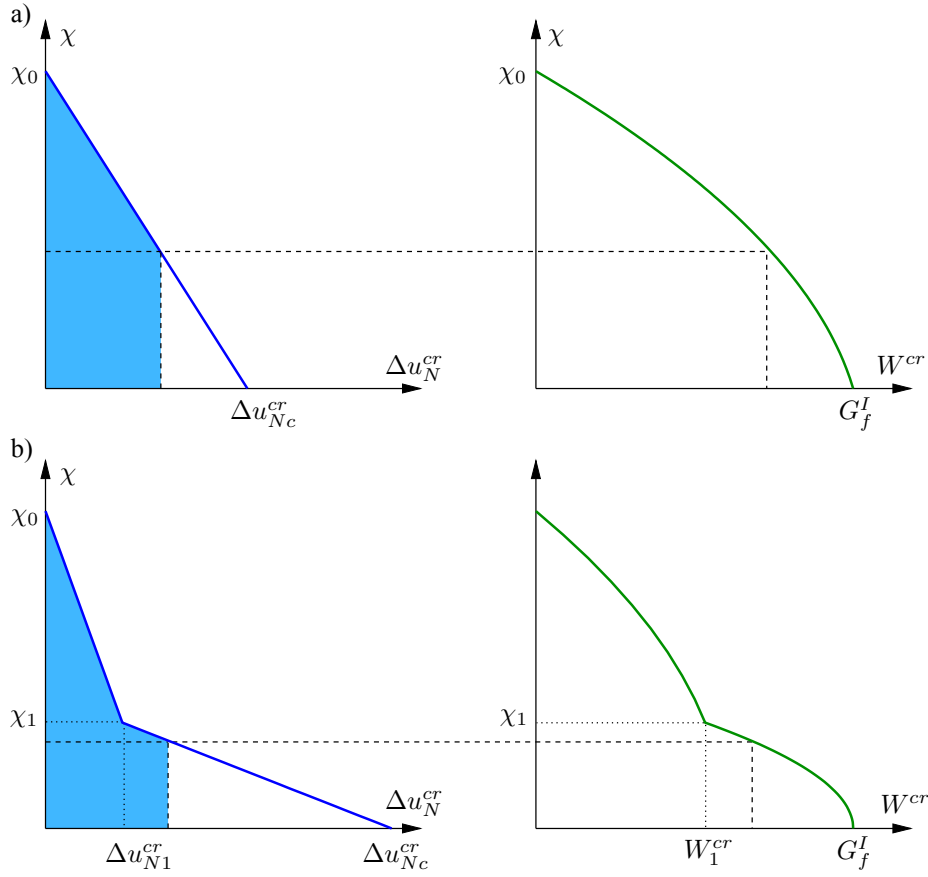
Figure 4.16. a) Linear and b) bilinear softening curves χ vs. Δu_N^{cr} and corresponding functions in terms of W^{cr}

following softening function of χ in terms of Δu_N^{cr} can be formulated

$$
\chi^{bilinear}(\Delta u_N^{cr}) = \begin{cases} \chi_0 - \dfrac{\chi_0 - \chi_1}{\Delta u_{N1}^{cr}} \Delta u_N^{cr} & \Delta u_N^{cr} \leq \Delta u_{N1}^{cr} \\[3mm] \chi_1 \dfrac{\Delta u_{Nc}^{cr} - \Delta u_N^{cr}}{\Delta u_{Nc}^{cr} - \Delta u_{N1}^{cr}} & \Delta u_{N1}^{cr} < \Delta u_N^{cr} \leq \Delta u_{Nc}^{cr} \\[3mm] 0 & \Delta u_N^{cr} > \Delta u_{Nc}^{cr} \end{cases} \quad (4.54)
$$

which leads to

$$
\chi^{bilinear}(W^{cr}) = \begin{cases} \chi_0 \sqrt{1 - 2W^{cr}\dfrac{\chi_0 - \chi_1}{\Delta u_{N1}^{cr}\chi_0^2}} & W^{cr} \leq W_1^{cr} \\[3mm] \chi_1 \sqrt{1 - \dfrac{2}{\chi_1}\dfrac{W^{cr} - W_1^{cr}}{\Delta u_{Nc}^{cr} - \Delta u_{N1}^{cr}}} & W_1^{cr} < W^{cr} \leq G_f^I \\[3mm] 0 & W^{cr} > G_f^I \end{cases}
$$

$$(4.55)$$

with

$$W_1^{cr} = \frac{1}{2}\chi_1(\Delta u_{Nc}^{cr} - \Delta u_{N1}^{cr}). \tag{4.56}$$

A detailed derivation of the formulation for the linear and the bilinear case can be found in the appendix. By using the linear softening relation for the χ-Δu_N^{cr} function in this model, the obtained stress-crack opening relation for uniaxial tension is exactly the same than using the penalty approach in Eq. (4.40), independently of k_N

$$\chi^{linear}(\Delta u_N) = \begin{cases} k_N \Delta u_N & \Delta u_N \leq \dfrac{\chi_0}{k_N} \\[2ex] \dfrac{\Delta u_{Nc} - \Delta u_N}{\dfrac{\Delta u_{Nc}}{\chi_0} - \dfrac{1}{k_N}} & \dfrac{\chi_0}{k_N} < \Delta u_N \leq \Delta u_{Nc} \\[2ex] 0 & \Delta u_N > \Delta u_{Nc} \end{cases} \tag{4.57}$$

with

$$\Delta u_{Nc} = \frac{2G_f^I}{\chi_0}. \tag{4.58}$$

For the bilinear case both approaches lead to exactly the same relation only for the asymptotic case $k_N = \infty$, similar to the exponential softening curve.

In (Gálvez et al. 2002) a simplified model, using the same yield function as the model in (Carol et al. 1997) was proposed. There the internal variables c and χ are formulated in terms of an effective plastic displacement Δu_{eff}^{cr}

$$\begin{aligned} c &= c(\Delta u_{eff}^{cr}), \\ \chi &= \chi(\Delta u_{eff}^{cr}), \end{aligned} \tag{4.59}$$

with

$$\begin{aligned} \Delta u_{eff}^{cr} &= \int \dot{\Delta u}_{eff}^{cr} dt, \\ \dot{\Delta u}_{eff}^{cr} &= \dot{\Delta u}_N^{cr} + \dot{\Delta u}_T^{cr}. \end{aligned} \tag{4.60}$$

This assumption enables the direct implementation of the determined uniaxial relations between χ and Δu_N^{cr} and c and Δu_T^{cr} and leads to the same softening curve for uniaxial tension as the formulation in (Carol et al. 1997). But for combined loading the assumption in Eq. (4.59) leads to a faster decrease of the dilatancy. This is caused, since for negative normal stresses the increase of Δu_N^{cr} contributes to the increase of Δu_{eff}^{cr}, where the increase of W^{cr} depends only on the change of Δu_T^{cr} if Δu_N^{cr} is negative. Furthermore the pure frictional part of the plastic displacements is included in Δu_{eff}^{cr}, which leads to an unrealistic softening. Thus the consistent formulation in (Carol et al. 1997) using W^{cr}

is preferred in this work. The assumption in Eq. (4.59) is used only for comparison.

4.2.3   Stress-based crack criterion

The well-known Rankine criterion is the one of the mostly used criteria for crack initiation
and crack growth in the context of the cohesive crack model. This criterion is fulfilled, if
the maximum principle stress exceeds the tensile strength

$$\max(\sigma_{1,2}) \geq f_t. \tag{4.61}$$

In this work this criterion is evaluated by means of an averaged stress tensor similar to
(Häussler-Combe 2001) and (Feist 2003). This averaging gives more stable results for
points close to stress singularities, caused by the geometrical shape of the domain or by
a point-wise coupling of continuum elements with elements of the reinforcement, which
is described in section 4.4. Furthermore it is necessary to obtain a representative stress
tensor directly at the crack tip, where generally no integration point is located. Here
a nonlocal approach is used according to (Jirásek and Zimmermann 1997), where the
nonlocal stress tensor is evaluated within a given interaction area as

$$\overline{\boldsymbol{\sigma}}(\mathbf{x}) = \int_{\Omega_E} \alpha(\mathbf{x}, \boldsymbol{\xi}) \boldsymbol{\sigma}(\boldsymbol{\xi}) d\boldsymbol{\xi}, \quad \alpha(\mathbf{x}, \boldsymbol{\xi}) = \frac{\alpha_\infty \left(\|\mathbf{x} - \boldsymbol{\xi}\| \right)}{\int_{\Omega_E} \alpha_\infty \left(\|\mathbf{x} - \boldsymbol{\zeta}\| \right) d\boldsymbol{\zeta}}, \tag{4.62}$$

where α, Ω_E and $\boldsymbol{\xi}$ are the nonlocal weighting function, the nonlocal interaction area and
the coordinate of the investigated point, respectively. The second part in this equation is
necessary to represent a constant stress field exactly. As weighting function a bell shaped
polynomial is chosen (Rolshoven and Jirásek 2003)

$$\alpha_\infty^{\text{bell}}(r) = \begin{cases} \dfrac{1}{c} \left(1 - \dfrac{r^2}{R^2} \right)^2 & |r| \leq R \\ \\ 0 & |r| > R \end{cases} \tag{4.63}$$

where the distance is given as $r = \|\mathbf{x} - \boldsymbol{\xi}\|$ and R indicates an interaction radius R, which
is assumed to be a material depending parameter. In (Feist 2003) this quantity is assumed
to be between three and five times of the maximum aggregate size. The scaling factor c
is defined for 2D problems as $c = \pi R^2/3$. Fig. 4.17 shows this averaging procedure for a
point $\mathbf{x}$ located in a set of integration points. The Rankine criterion is evaluated using the
nonlocal stress tensor for single integration points to decide upon crack initiation and for
the crack tips to decide upon crack growth. In order to neglect integration points located
on the opposite side of a crack the visibility criterion presented in section 3.1.3 is used as
shown in Fig. 4.17.

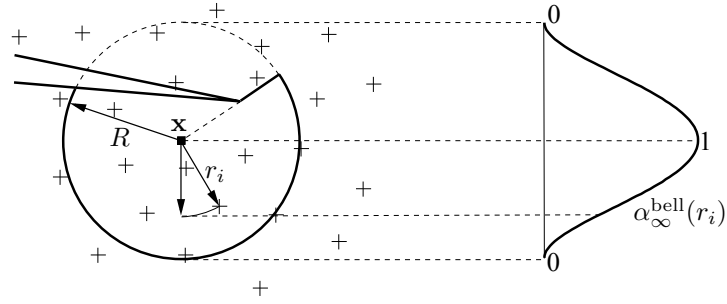   The nonlocal scheme gives good results, if the integration points considered for the

Figure 4.17. Nonlocal influence domain for a point $\mathbf{x}$ located close to an existing crack tip

averaging procedure are in a similar stress state. This is not valid, if the interaction radius is taken too large depending on the gradients in the surrounding stress field. As a consequence a delay of the crack initiation or propagation will be caused, which will be shown in the examples. If the interaction radius is taken too small or if the discretization is too coarse, the points in the influence domain are not enough to obtain a nonlocal information about the stress field.

4.2.4 Energy-based criterion using Virtual Crack Extension

The expression for the total potential in Eq. (4.16) formulated for LEFM can be extended for an elastic body with cohesive cracks as follows

$$\Pi^{coh} = \frac{1}{2}\tilde{\mathbf{u}}^T\mathbf{K}\tilde{\mathbf{u}} - \tilde{\mathbf{u}}^T\mathbf{f}^{ext} + \tilde{\mathbf{u}}^T\mathbf{f}^{coh}, \tag{4.64}$$

where $\mathbf{f}^{coh}$ are the cohesive forces acting on the fictitious crack surface. From this extended potential (Xie 1995) derived a criterion for cohesive crack propagation using the Virtual Crack Extension technique

$$0 = \frac{\delta\Pi^{coh}}{\delta A} = -\frac{1}{2}\tilde{\mathbf{u}}^T\frac{\delta\mathbf{K}}{\delta A}\tilde{\mathbf{u}} + \tilde{\mathbf{u}}^T\frac{\delta\mathbf{f}^{ext}}{\delta A} - \tilde{\mathbf{u}}^T\frac{\delta\mathbf{f}^{coh}}{\delta A}. \tag{4.65}$$

By assuming again that no external forces are applied on the crack surfaces and that the body forces are zero in the domain of the crack tip and using the definition in Eq. (4.19), the following relation is obtained

$$\mathcal{G} - \tilde{\mathbf{u}}^T\frac{\delta\mathbf{f}^{coh}}{\delta A} = 0, \tag{4.66}$$

with

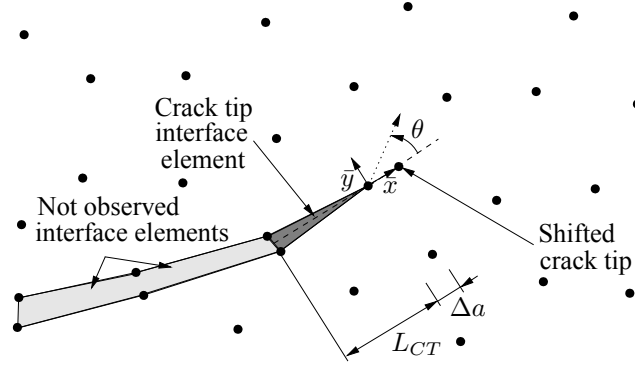$$\mathcal{G} = -\frac{1}{2}\tilde{\mathbf{u}}^T\frac{\delta\mathbf{K}}{\delta A}\tilde{\mathbf{u}}, \tag{4.67}$$

Figure 4.18. Virtual Crack Extension for a cohesive crack tip with finite interface elements

which implies, that an existing cohesive crack growths, if the elastic energy release rate $\mathcal{G}$ due to a virtual crack extension δA reaches the energy rate in the cohesive interface. No crack growth takes place for

$$\mathcal{G} - \tilde{\mathbf{u}}^T \frac{\delta \mathbf{f}^{coh}}{\delta A} < 0. \tag{4.68}$$

This criterion can be applied only to decide upon the extension of existing cracks but not for crack initiation. In (Xie 1995) and (Yang and Chen 2004) it was applied to cohesive crack growth simulation with adaptive finite elements. In these studies the derivative of the stiffness matrix in Eq. (4.67) was carried out by using the finite difference scheme as presented in section 4.1.2.

The cohesive energy rate can be obtained for the general case using finite differences in the same manner as for the elastic energy release rate

$$\frac{\partial \mathbf{f}^{coh}}{\partial A} \approx \frac{\Delta \mathbf{f}^{coh}}{\Delta A}. \tag{4.69}$$

In this work the coplanar VCE-technique (section 4.1.2) is applied to obtain the elastic energy release rate and the cohesive energy rate. If finite interface elements are used to transmit the cohesive forces, only the element at the crack tip has to be considered as shown in Fig. 4.18. By using two-dimensional linear interface elements the following simple relation is derived (see appendix C.3)

$$\frac{\partial \mathbf{f}^{coh}}{\partial A} = \frac{\mathbf{f}^{int}_{CT}}{L_{CT} \cdot t} \tag{4.70}$$

where $\mathbf{f}^{int}_{CT}$ is the internal force vector and L_{CT} is the length of the crack tip interface element.

In (Xie 1995) and (Yang and Chen 2004) the standard cohesive crack model was applied, which does not consider shear stresses across the cohesive crack surfaces of an

opened crack. This assumption results in the following decomposition

$$\mathbf{f}^{coh} = \mathbf{f}^{coh}_{I}; \quad \mathbf{f}^{coh}_{II} = 0. \tag{4.71}$$

Thus the implementation is limited to Mode-I dominated problems, since the Mode-II component is missing in the cohesive energy release rate but exists for the elastic energy release rate, if the Mode-II displacements are nonzero.

In this work the presented improved mixed-mode cohesive crack model is used in the framework of the energy-based criterion, where both, Mode-I and Mode-II, components of the cohesive forces are considered. Thus the presented completed approach can be applied to Mode-I and Mode-II dominated and mixed-mode problems in the same manner.

4.2.5 Crack direction criteria

If the criterion for crack initiation or crack growth is fulfilled for a point in the investigated domain, the direction of the new crack or crack increment has to be predicted. The quality of this prediction has a major influence on the global behavior, since the global inelastic energy needed for the fracture process is directly influenced by the cohesive crack geometry and the displacements of the crack surfaces. For cohesive crack propagation modeling no universal approach exists like in LEFM, which works accurately and efficiently for different geometries and loading situation. Thus this topic is still a field for many researchers. In this section several methods will be presented and discussed.

If the Rankine criterion is applied for crack initiation or crack growth the crack angle is assumed in general to be perpendicular to the maximum principle stress direction. In (Xie 1995), (Yang and Chen 2004) this approach is used in combination with the presented energy-based crack criterion. In order to obtain a stable direction prediction, mostly a nonlocal averaging scheme is used for the determination of the representative stress or strain tensor (Jirásek and Zimmermann 1997),(Häussler-Combe 2001),(Feist 2003). The prediction of the crack angle using this nonlocal stress tensor gives very good results for the most cases, which will be shown in the examples, but a similar stress state in the nonlocal domain is required, as already mentioned in section 4.2.3.

This is not the case, e.g. if the structure is almost completely cracked, as shown simplified in Fig. 4.19 for a Mode-I crack. the stress gradients in the nonlocal domain have large values, which lead to a significant sensitivity of the prediction with respect to the position of the averaged integration points. If for a Mode-I crack the integration point arrangement is asymmetric with respect to the theoretical crack line, the nonlocal stress tensor in crack tip coordinates shown in Fig. 4.2 has nonzero shear components $\bar{\sigma}_{\bar{x}\bar{y}}$. Thus the prediction of the crack angle reads $\theta_c \neq 0$. This error increases for higher stress gradients. The author has tried to solve this problem using stress points for the nonlocal averaging, which are located symmetrically with respect to the existing crack tip, but the
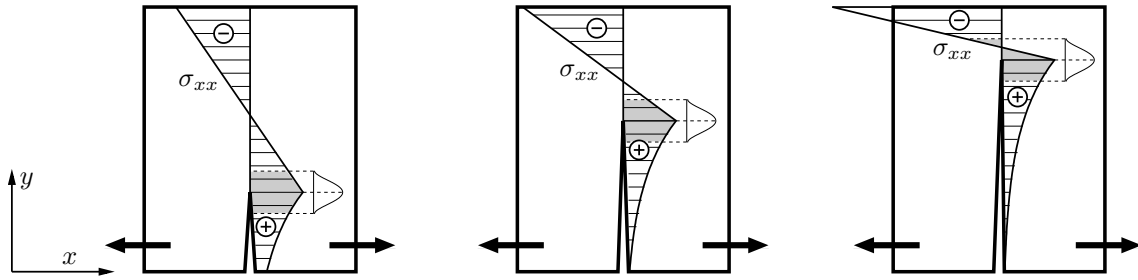
Figure 4.19. Stresses and belonging nonlocal influence domain for a growing Mode-I crack

crack angle prediction was not improved significantly for an asymmetric nodal discretization, since the stress field is still slightly asymmetric. Good results for the crack path of a Mode-I problem could only be obtained, if the nodal discretization keeps symmetric with respect to the theoretical crack during the simulation. But for the general case, using an arbitrary discretization to describe an arbitrary crack path, this cannot be assured.

In (Jirásek and Marfia 2005) a method was proposed, which determines the maximum circumferential stress on a semicircle around the crack tip. The radius has been taken smaller than the nonlocal influence radius. The angle of the maximum circumferential stress is assumed to be the angle of crack growth, similar to LEFM. Investigations by the author lead to similar results for the Mode-I problem as using the nonlocal stress tensor: for an asymmetric discretization, the stress field is asymmetric and the maximum circumferential stress (local or smoothed) will be found in the analysis not for all cases as $\theta_c \approx 0$. This clarifies the fact, that as long as the stress field is almost equal around the crack tip, the prediction of the crack angle gives good results with a stress-based approach. If this is not the case, these approaches are not adequate for a good prediction.

(Dumstorff and Meschke 2004) investigated several approaches and similar results have been obtained using a stress-based criterion. Furthermore the method using the direction of the maximum total energy release rate from LEFM described in section 4.1.3 was adapted in (Dumstorff and Meschke 2004) for cohesive cracks in the context of the Extended Finite Element Method. This direction was determined by an iterative process extending the existing crack in the investigated possible crack direction similar to the noncoplanar VCE technique. The problems of stress-based approaches did not occur with this method and good crack path predictions could be obtained, since the energy release rate is an integral quantity and is much more independent of the discretization than a stress-based method. This method is not applied in this work, because of the large numerical effort, which is necessary to extend the crack in several directions during the iteration process.

In this work the application of the criterion of the maximum circumferential stress introduced for LEFM in terms of the stress intensity factors was investigated for cohesive

crack growth simulation. By writing Eq. (4.27) in terms of the Mode-I and Mode-II components of the elastic energy release rate using Eq. (4.23) the following equation is obtained

$$\theta_c = 2\arctan\frac{1}{4}\left(\pm\sqrt{\frac{G_I}{G_{II}}} \pm \sqrt{\frac{G_I}{G_{II}} + 8}\right).$$

(4.72)

The choice of the signs is done according to section 4.1.2 and 4.1.3. Both components of the elastic energy release rate are obtained using the mode decomposition procedure described in section 4.1.2. The approach in Eq. (4.72) is based on the assumption of a singular stress field at the crack tip. This is not valid for the cohesive crack, thus this criterion can not be used in general in this context, but for Mode-I dominated problems, where G_{II} is very small, Eq. (4.72) predicts the crack angle with $\theta_c \approx 0$. In this work good results could be obtained with this approach for theoretical crack paths with small curvature. For stronger curved crack geometries the crack angle is overestimated. The nonlocal stress-based direction gives good results for the latter case. Thus in this work a combined direction criterion is formulated, which takes the angle for the crack extension from the criterion based on LEFM if the absolute value of the crack angle is smaller than with the nonlocal prediction. In the other case the nonlocal crack angle is taken.

$$\theta_c = \begin{cases} \theta_{LEFM} & \text{if} \quad |\theta_{LEFM}| \leq |\theta_{Nonlocal}| \\ \theta_{Nonlocal} & \text{if} \quad |\theta_{LEFM}| > |\theta_{Nonlocal}| \end{cases}$$

(4.73)

4.3   Crack growth algorithm

In fully automatic crack propagation the crack extension and the direction is predicted without user interaction. In this work a quasi-automatic algorithm is used where the new crack-length increment has to be provided by the user. This value has to be chosen as large as possible to reduce the numerical effort during the calculation, but as small as needed to represent the investigated crack geometry with sufficient accuracy. In (Wawrzynek 1991) the initial crack length increment was reduced with increasing crack angle θ_c. For simplicity, this length increment is assumed to be constant in this work and has to be chosen at the beginning of a calculation. In the algorithm only one crack increment is allowed in one iteration step, namely for the point (crack tip or integration point) where the crack criterion is most exceeded. When a new crack increment is introduced, the global nonlinear iteration is done again without increasing the external load or prescribed displacement values. This is repeated until the crack criterion is exceeded nowhere else and the new increment of the external load or prescribed displacement is applied.

4.3.1   Representation of moving discontinuities

After deciding, that an existing crack grows or a new crack begins to form and the determination of the new crack geometry, the crack has to be represented in the actual discretization. In the two-dimensional case the crack contour can be easily described by a sequence of line segments, which was realized by many researches, e.g. (Belytschko et al. 1994),(Hegen 1997),(Rao and Rahman 2000) and (Häussler-Combe 2001). The description in three dimensions is much more complicated, since the complete crack surface has to be represented. Several studies use triangles to span the surface (Feist 2003), (Oliver et al. 2004). Another approach is the level set method (Sethian 1999) which is widely used in the Extended Finite Element Method, e.g. in (Sukumar et al. 2001). There the crack surface is assumed to be the zero-level-set-curve of a function in the fourth-dimensional space. The moving of the surface is included in this function by means of a hyperbolic formulation. In this work only the two-dimensional case is investigated, thus the crack path is represented using line segments.

The representation of the crack as discontinuity line can be done directly in the Element-free Galerkin method due to the modification of the weighting function described in section 3.1.3. In (Belytschko et al. 1994) this was realized without modifying the background integration cells as shown in Fig. 4.20a. This assumption leads to a kind of smeared discontinuity in the belonging integration cells, due to the applied Gauss integration scheme assuming a polynomial function. In (Hegen 1997) an improvement of this approach was realized by subdividing the integration cells containing a discontinuity line in that way, that the sub-cell edges coincide exactly with discontinuity lines (Fig. 4.20b). This concept was adapted later for the Extended Finite Element Method in (Moës et al. 1999). For
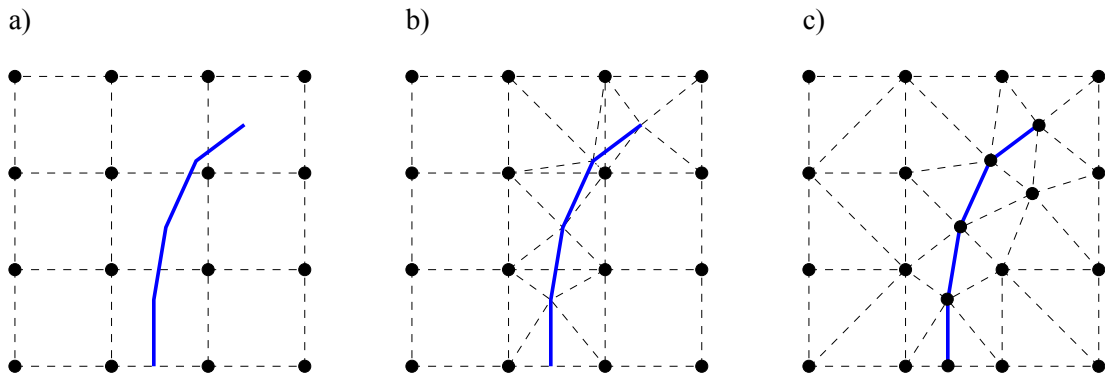
Figure 4.20. Representation of a crack a) without update of the discretization, b) with update of the integration cells and c) with adaptation of the nodal discretization and integration cells

both concepts the description of cohesive cracks can be done with an integration along the crack surface, in which the displacement differences, which are the input quantities for the cohesive crack model, are directly obtained from the meshless displacement interpolation. This was realized e.g. in (Häussler-Combe 2001).

Better results than using both presented concepts can be obtained, if the crack surface is discretized by node pairs at the end of the segments and a node directly at the crack tip as shown in Fig. 4.20c. In (Rao and Rahman 2000) this concept was applied and additional nodes are introduced to improve the discretization around the crack tip.

In this work the first concept is used for the EFG method only for comparison. For the general case the third concept was implemented for the EFG method and the Natural Neighbor Galerkin Method, because of the better results for the EFG approach, although the new nodes and the adaptation of the integration cells require additional effort. For the NEM only this concept can be used, since the discontinuity has to be modeled as external or internal boundary segments each spanned by two nodes.
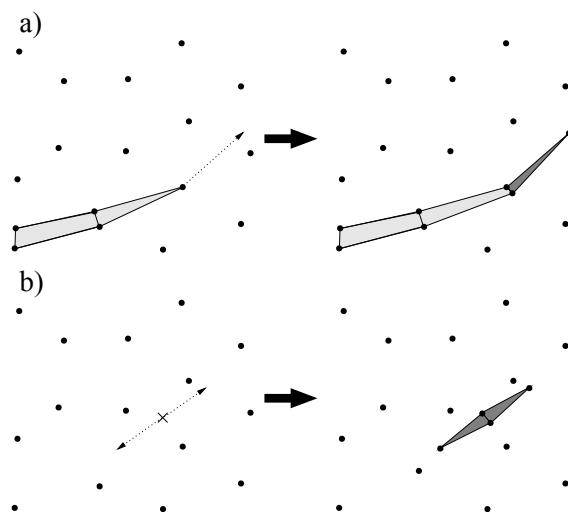

Figure 4.21. Generation of the crack surface nodes and belonging interface elements a) for an existing crack tip and b) for a new crack

If an existing crack grows the new crack increment is introduced into the meshless
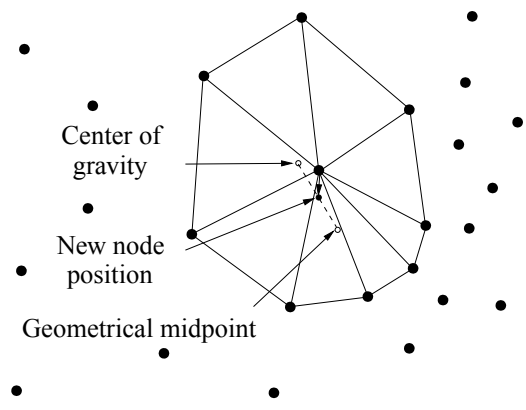
Figure 4.22. New node position from one single smoothing step

discretization by splitting the previous crack tip node and creating an additional node at the new crack tip. For crack initiation a node pair is created at the stress point, where the crack criterion is exceeded, and the two new crack tip nodes are generated along the predicted crack direction with a distance to this node pair equal to the half size of the specified crack increment length. For cohesive crack modeling the transmission of the surface forces is realized by integrating finite interface elements between the crack surface nodes. These procedures are shown in principle in Fig. 4.21 for an existing crack tip and an initial crack. Due to the obtained linear precision of the Natural Neighbor Interpolation and the blended MLS-interpolation along the domain boundary, the application of linear interface elements is to the best advantage. In the appendix a detailed description of this element type can be found.

Through the insertion of additional crack nodes the triangle integration cell configuration close to the crack tip, which is updated in this procedure, may contain some strongly distorted triangles, which still fulfill the Delaunay criterion but lead to remarkable errors in the integration procedure as shown in (Unger 2003) for the Natural Neighbor Interpolation. The author developed an algorithm to overcome this problem based on the Laplacian smoothing technique (Herrmann 1976). The original procedure in (Herrmann 1976) moves every node to the center of gravity of all triangles belonging to this node. After a small number of cycles over all movable nodes the algorithm converges and the nodes hold their new positions. But if the node density varies very much this can lead to some longish triangles. To overcome this problem the new nodal position is taken here as the midpoint between the center of gravity of the node-belonging triangles and the geometrical midpoint of their nodes. This is shown exemplarily in Fig. 4.22 for one single smoothing step. The smoothing for non-convex subregions is only executed if the new node position is not outside of the subregion. Nodes on the external and on the crack surface boundaries are not allowed to be moved. Furthermore additional nodes are included around the new crack increment if the increment length is smaller than the average node distance in the surrounding domain in order to avoid distorted triangles at the new crack
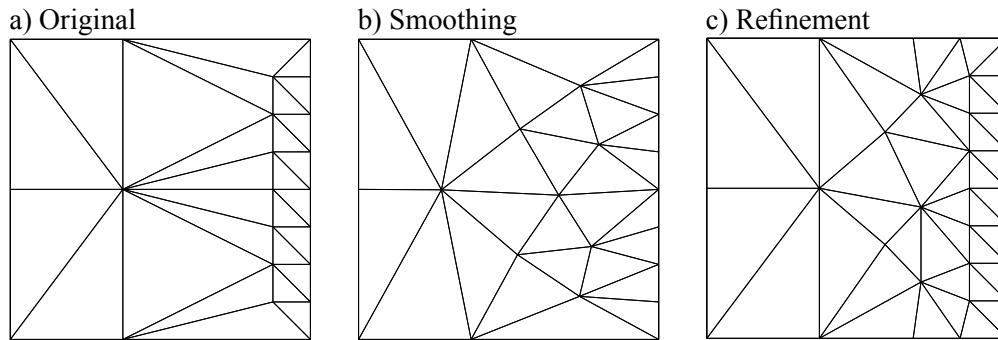
Figure 4.23. a) Initial triangulation improved by b) the smoothing and c) the refinement algorithm to reduce distorted triangles

tip. After the convergence of the algorithm the smoothed triangles in general do not fulfill the Delaunay criterion and a local re-triangulation is required. This algorithm is a local procedure, which is fast and simple in two dimensions. The extension for the 3D case seems to be more complicated.

In (Unger et al. 2004) another algorithm for the update of the triangulation procedure around an extended crack tip has been proposed. This method is based on Rupperts refinement algorithm (Ruppert 1995), which can produce grading triangle meshes and already existing nodes are kept in the final triangulation. Compared to the smoothing algorithm this procedure can guarantee that all triangles get small distortions, but on the other hand additional nodes will be created at the boundary. If a new node is inserted on a crack surface boundary within the refinement procedure some additional effort is necessary to adapt the interface elements. In (Most et al. 2005) both algorithms have been investigated in a crack growth algorithm and similar results have been obtained. Thus in this work the smoothing algorithm is used, since its implementation is much simpler and no additional nodes are necessary at the boundary. In Fig. 4.23 the result of the smoothing algorithm is shown compared to a refined discretization using an initial state containing strongly distorted triangles.

4.3.2 Adaptive coupling with finite elements

As already mentioned in the previous sections, the numerical effort for using the meshless interpolation is in general higher than using standard finite elements. For this reason an adaptive coupling of the meshless discretization with finite elements is an efficient way to reduce this effort. In this concept, which was applied e.g. in (Karutz 2000) for crack growth simulation in brittle materials, only this domain is discretized with meshless components, where the crack growth happens. In this work this is realized by starting from an initial finite element discretization and transforming these elements with corresponding neighbor elements to meshless zones, where the maximum principle stress reaches 95% of the tensile strength. In this procedure, the existing nodes are kept and only the critical elements are deleted. The meshless components are discretized with these existing nodes
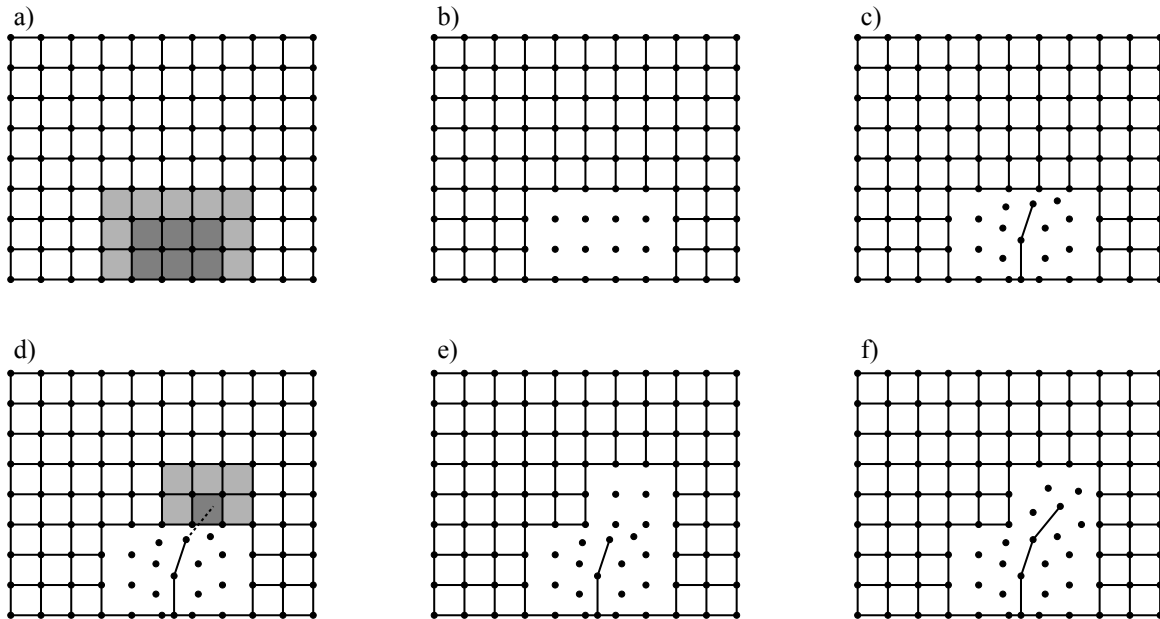
Figure 4.24. Crack growth algorithm with adaptive coupling with finite elements:
a) initial FE-mesh with determined critical and neighbor elements, b) transformation into meshless component, c) crack growth in meshless zone, d) element touched by new crack increment with neighbor elements, e) adapted meshless zone and f) further crack growth

and the coupling with the remaining elements is done directly. This is shown in principle in Fig. 4.24.

The direct coupling is possible, since the boundary conditions are fulfilled in the presented meshless interpolation. Due to the linear precision along the meshless boundary, linear finite elements are preferred in this work, which leads to a compatible displacement field along the coupling boundary. During this procedure an arbitrary number of meshless zones can be created, which will be merged if they share a common edge. The presented crack criterion will be checked in all meshless components and the new increment is introduced, where the criterion is mostly exceeded. If a new crack increment will end in an adjacent element, the crack increment is not used and this element with corresponding neighbor elements is transformed, as shown in Fig. 4.24. After doing the nonlinear iteration, the crack criterion is checked again and the new crack increment is included. The displacement values of the nodes, which are created or smoothed during the update around the crack tip, are interpolated from the old discretization state using the meshless shape function. Then the next nonlinear iteration will converge faster, since the start values are consistent to the last equilibrium state for all nodes. The transfer of history variables from the old integration points to the new arrangement is straight-forward, due to the continuous stress function, and can be done similar using the meshless interpolation function. In this work the base material is assumed to be linear elastic, thus such a transfer is not necessary. In Fig. 4.25 the applied algorithm of a single step for one global load or displacement increment is presented in principle.
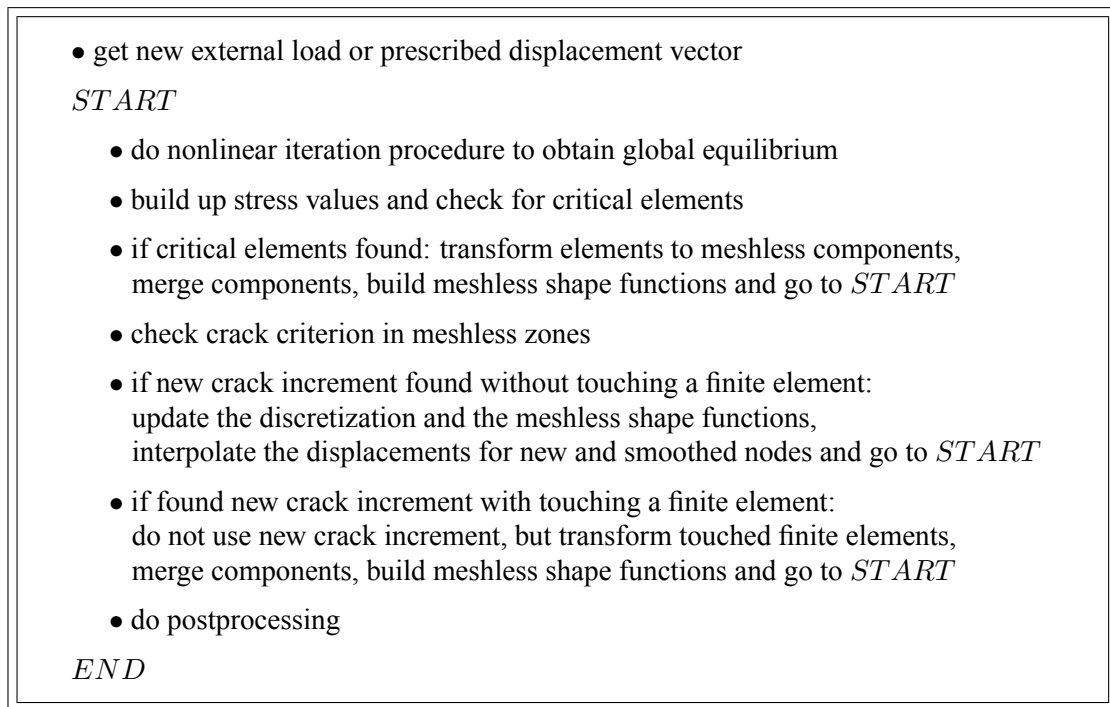
- get new external load or prescribed displacement vector

START

- do nonlinear iteration procedure to obtain global equilibrium
- build up stress values and check for critical elements
- if critical elements found: transform elements to meshless components, merge components, build meshless shape functions and go to *START*
- check crack criterion in meshless zones
- if new crack increment found without touching a finite element:
  update the discretization and the meshless shape functions,
  interpolate the displacements for new and smoothed nodes and go to *START*
- if found new crack increment with touching a finite element:
  do not use new crack increment, but transform touched finite elements,
  merge components, build meshless shape functions and go to *START*
- do postprocessing

END

Figure 4.25. Single step for one global load or displacement increment in the crack growth algorithm with adaptive coupling of finite elements and meshless components

4.4 Modeling of the bond behavior in reinforced concrete

The explicit description of the bond behavior between concrete and reinforcement is necessary for the modeling of discrete crack growth in reinforced concrete structures. In such analyses the reinforcement is generally modeled in two dimensions with bar elements which are coupled with the concrete discretization. This was done e.g. in (Mehlhorn and Kolleger 1995) and (Häussler-Combe 2001). If the bond behavior is assumed to be perfect, the reinforcement and the concrete discretization is directly coupled, which leads to the formation of a large number of cracks as shown in (Červenka 1998) without a realistic representation of the crack process. In this process a slip between the reinforcement and concrete causes shear stresses in the bond surface. Due to these shear stresses the tension forces, which are transmitted by the reinforcement over the surface of a macro crack, are transmitted back to the concrete over a certain length. There is still no unified description of this bond behavior by considering the important global and local influences as the reinforcement surface geometry or the lateral pressure. Thus this problem is still a field of active research.

For practical use the relation between the shear stress and the relative displacements between reinforcement and concrete, the slip, is assumed to be nonlinear. In this work this concept is applied by using the following relation proposed in (Doerr 1980) between

the bond shear stress σ_τ and the relative displacement in reinforcement direction Δu_τ,

$$
\frac{\sigma_\tau}{f_t} = \begin{cases} 83.2\Delta u_\tau - 1260\Delta u_\tau^2 + 6480\Delta u_\tau^3, & \Delta u_\tau \leq \Delta \bar{u}_\tau \\ 83.2\Delta \bar{u}_\tau - 1260\Delta \bar{u}_\tau^2 + 6480\Delta \bar{u}_\tau^3, & \Delta \bar{u}_\tau < \Delta u_\tau \leq \Delta \tilde{u}_\tau \\ 0 & \Delta u_\tau > \Delta \tilde{u}_\tau \end{cases} \quad (4.74)
$$

where Δu_τ has to be taken in mm. (Doerr 1980) gives the relative displacement value $\Delta \bar{u}_\tau$ where the shear stress is at its maximum depending on the lateral pressure σ_l as

$$
\Delta \bar{u}_\tau = \begin{cases} 0.06mm, & \sigma_l = 0N/mm^2 \\ 0.08mm, & \sigma_l = 5N/mm^2 \\ 0.13mm, & \sigma_l = 10N/mm^2 \\ 0.15mm, & \sigma_l = 15N/mm^2 \end{cases} \quad . \quad (4.75)
$$

The critical displacement value $\Delta \tilde{u}_\tau$ where the shear stress gets zero is taken in general as triple size of $\Delta \bar{u}_\tau$. Un- and reloading is assumed to be linear with a stiffness equivalent to the initial value. In Fig. 4.26 the nonlinear relation between shear stress and relative displacement is shown.

The coupling between the reinforcement and the concrete nodes is done in this work using so-called bond-link-elements (Mehlhorn and Kolleger 1995), which in 2D are two springs, one in axial reinforcement direction using the nonlinear bond model and the other in normal direction with a linear penalty law to avoid relative displacements between concrete and reinforcement in normal direction. The shear stress obtained from the bond model has to be multiplied by the surface area of the reinforcement segment belonging to the spring to obtain the internal force of the spring element.
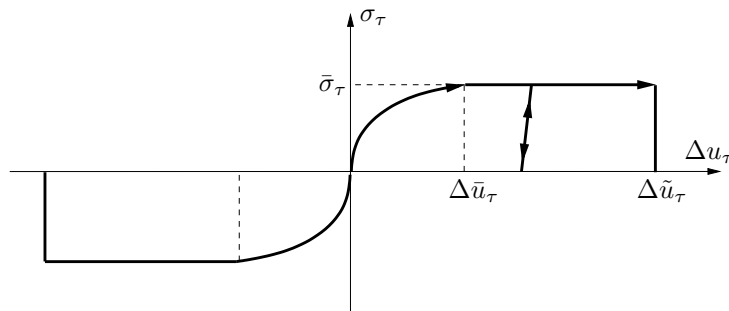

Figure 4.26. Nonlinear bond model according to (Doerr 1980)

4.5 Examples

The following examples will clarify the applicability of the presented algorithm to crack growth problems in plain and reinforced concrete structures. For this purpose a step-wise verification is done in the following sequence: First the Virtual Crack Extension procedure is applied to Mode-I and mixed-mode LEFM problems and the obtained meshless results are compared to those of finite element simulations and the analytical solutions. Then the improved mixed-mode cohesive crack model is verified independent of the crack growth algorithm by means of simple tests. In the following examples the developed model is applied to the Mode-I and mixed-mode evolution of a single crack in plain concrete and the influence of the crack criteria and the type of the cohesive crack model are investigated. The final example in this section investigates the propagation of multiple cracks in a reinforced concrete beam.

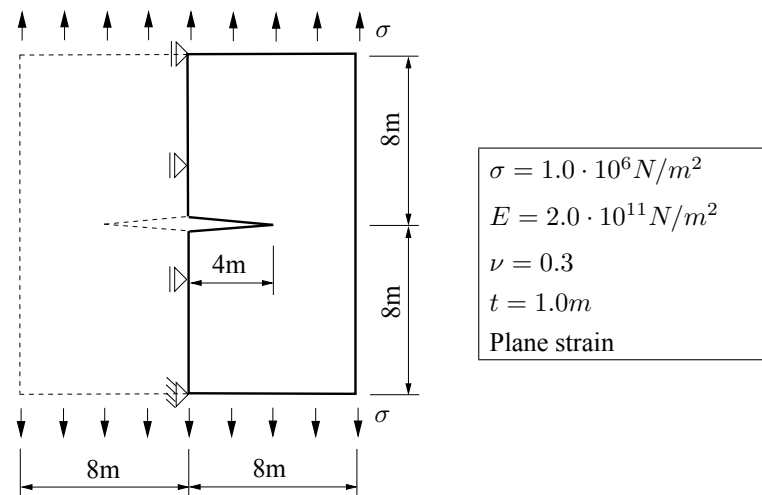### 4.5.1 Application of VCE technique for Mode-I cracking

Figure 4.27. Mode-I fracture: square plate with horizontal crack

This numerical example, corresponding to Mode-I Linear Elastic Fracture Mechanics has been carried out to verify the adaptation of the VCE for the meshless formulation. For this purpose a quadrilateral panel with a horizontal central crack was analyzed by calculating the Mode-I stress intensity factor according to (Yang et al. 2001). In Fig. 4.27 the material and geometrical properties are given. The analytical solution for this problem is $K_I = 4.72 \cdot 10^6 N/\sqrt{m}$ (Tada et al. 1993).

First the system was investigated using the eight-node singular crack tip elements. For the numerical analysis different nodal discretizations were investigated and only one half of the plate was modeled by considering the symmetry of the system. The coarsest finite element mesh is shown in Fig. 4.28a. The stress intensity factors have been calculated with these elements using the Displacement Correlation Method and the Virtual Crack
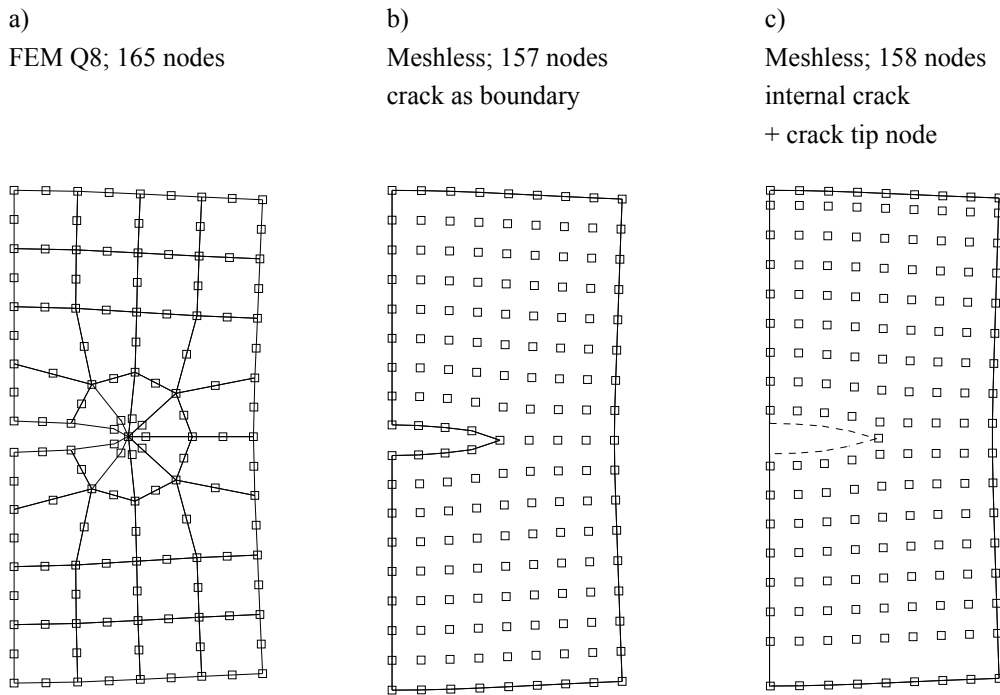
a)
FEM Q8; 165 nodes

b)
Meshless; 157 nodes
crack as boundary

c)
Meshless; 158 nodes
internal crack
+ crack tip node

Figure 4.28. Mode-I fracture: a) Deformed finite element mesh with singular crack tip elements, b) deformed meshless zone with crack modeled as boundary and c) modeled as internal discontinuity

Extension technique. In Table 4.1a the numerical errors in comparison to the analytical solution are shown. The table indicates, that the VCE method gives much better results for coarser meshes than the Displacement Correlation Method.

Investigations for the different meshless formulations were carried out with the standard interpolation functions for increasing discretization levels. For comparisson an analysis with standard four-node finite elements (Q4) was performed. In Fig. 4.28b the investigated regular discretization is shown where the crack was explicitly modeled as domain boundary. The numerical errors for these calculations are given in Table 4.1b in which the values for the Q4 elements show excellent agreement with these obtained by (Yang et al. 2001) (47 nodes: -18.6%, 157 nodes: -11.2%). The results using the Natural Neighbor Interpolation (NEM) and the MLS-interpolation with the regularized spline weighting (RS) agree very well with the finite element solution. The application of the Gaussian weighting function leads to similar results, but the rate of convergence is smaller. All MLS calculations have been carried out using a bilinear base polynomial with an influence radius of $D = 2d_{min}$, where d_{min} is the minimal nodal distance. The numerical integration was done for the MLS and the NEM using 25 Gauss integration points per integration cell. The virtual crack extension ratio was assumed with $R_i = 10^{-6}d_{min}$. This quantity is defined here as

$$R_i = \frac{\Delta a}{L} \tag{4.76}$$

where Δa and L are the virtual crack extension and the distance between the nodes on the

a) Singular Q8 crack tip elements

	Error of prediction K_I [%]	
No. of nodes	Virtual Crack Extension	Displacement Correlation
165	0.21	5.70
581	0.07	2.23
2177	0.03	0.81
8425	0.02	0.17

b) Virtual Crack Extension with standard interpolation functions

	Error of prediction K_I [%]				Internal crack + tip node
			Crack as domain boundary		
No. of nodes	FEM, Q4	NEM	MLS, G	MLS, RS	MLS, RS
47	-18.73	-16.25	-17.11	-17.41	-21.11
157	-11.30	-10.96	-13.40	-10.66	-16.78
569	-7.82	-8.44	-11.86	-7.44	-13.37
2161	-6.16	-7.22	-11.14	-5.88	-11.46
8417	-5.35	-6.62	-10.78	-5.11	-10.88

c) influence of the virtual crack ratio R_i

	Error of prediction K_I [%]				Internal crack + tip node
	Crack as domain boundary			Internal crack	
R_i	NEM	MLS, G	MLS, RS	MLS, RS	MLS, RS
$10^{-0.5}$	-20.27	-21.73	-23.57	-39.08	-18.98
$10^{-1.0}$	-17.48	-19.34	-19.38	-22.06	-14.11
$10^{-1.5}$	-16.64	-20.79	-17.59	-22.22	-21.75
$10^{-2.0}$	-16.38	-28.11	-16.07	35.01	-21.11
$10^{-3.0}$	-16.27	-17.13	-17.44	20.42	-23.35
$10^{-4.0}$	-16.25	-17.12	-17.42	404.2	-15.73
$10^{-6.0}$	-16.25	-17.11	-17.41	-	-

Table 4.1. Mode-I fracture: a) results from singular finite element simulations, b) from finite element and meshless simulations with standard shape functions and c) influence of the virtual crack extension ratio R_i using the discretization with 47 nodes

crack surface, which is equal to d_{min} for this example. In Table 4.1c it is shown, that the obtained numerical values converge for a decreasing size of R_i.

Furthermore the system was analyzed using the MLS interpolation where the crack was modeled as internal discontinuity as presented in Fig. 4.28c. The integration cells have not been adapted around the crack, but 100 equally weighted integration points per cell were used to reduce the integration error along the crack line. It was obtained, that the virtual crack extension ratio can not be chosen very small as shown in Table 4.1c. If an additional node is introduced directly at the crack tip this problem can be solved, if R_i is not too small, but the numerical errors, given in Table 4.1b and which are obtained using $R_i = 10^{-2}$, are larger than modeling the crack as external boundary.

For all MLS calculations the visibility criterion presented in section 3.1.3 was used to describe the crack as non-convex boundary or as internal discontinuity. This criterion gives in general better results for LEFM problems than the diffraction or the transparency method, which was shown in (Belytschko et al. 1996). By means of this example the

diffraction criterion was analyzed additionally and the obtained numerical errors were larger than the results presented in Table 4.1b (47 nodes using MLS interpolation with RS weighting: -17.41% error with visibility criterion; -21.68% error for $\lambda_D = 1$ and -18.83% error for $\lambda_D = 2$ with diffraction method).

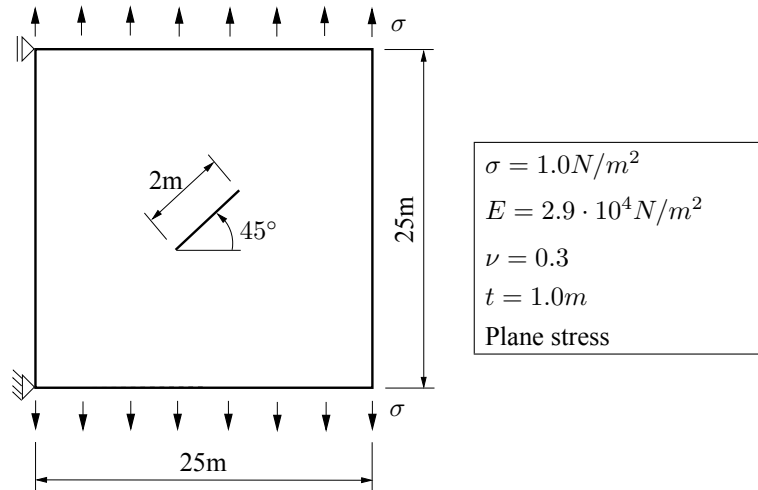## 4.5.2   Verification of coplanar VCE method for mixed-mode cracking

Figure 4.29. Mixed-mode fracture: square plate with $45°$ inclined crack

This example has been chosen to verify the coplanar VCE technique for mixed-mode Linear Elastic Fracture Mechanics. For this purpose a square panel having an inclined crack subjected to uniaxial tension was investigated. By assuming an infinite plate the analytical solution can be obtained according to (Tada et al. 1993) as

$$K_I = \sigma\sqrt{\frac{\pi a}{2}}\cos^2(\beta), \quad K_{II} = \sigma\sqrt{\frac{\pi a}{2}}\sin(\beta)\cos(\beta), \tag{4.77}$$

where β is the crack angle and a is the crack length. This leads to $K_I = K_{II} = 0.8862 N/\sqrt{m}$ for the parameters given in Fig. 4.29.

According to the previous example, the system was analyzed first with the singular Q8 elements around the crack tip. The coarsest finite element mesh is shown in Fig. 4.30a. The obtained numerical errors by applying the VCE technique are again much smaller than using the Displacement Correlation Method as shown in Table 4.2a. The remaining error for the VCE method does not converge to zero, caused by the coplanar crack extension, but the error values are quite small, thus this technique can be certainly applied to mixed-mode problems.

Meshless investigations have been carried out for different discretization levels by applying the Natural Neighbor Interpolation with standard shape functions in which a regular nodal grid was used around the crack tips. Fig. 4.30b shows one meshless discretization. The obtained numerical errors, which are presented in Table 4.2b have similar

convergency behavior for an increasing discretization level as in the previous example. A finite element simulation with Q4 elements was performed as well. The results of the finite element and NEM simulation are compared in Table 4.2b be means of the mixed mode energy release rate, which results from the analytical stress intensity factors as $G = 5.4165 \cdot 10^{-5} Nm$. These results show very good agreement.

The results of this and the previous example have shown, that the application of the Virtual Crack Extension technique leads to good results for Mode-I and mixed-mode LEFM problems, if the standard meshless shape functions are used.

a)

FEM; 1091 nodes

b)

Meshless; 601 nodes
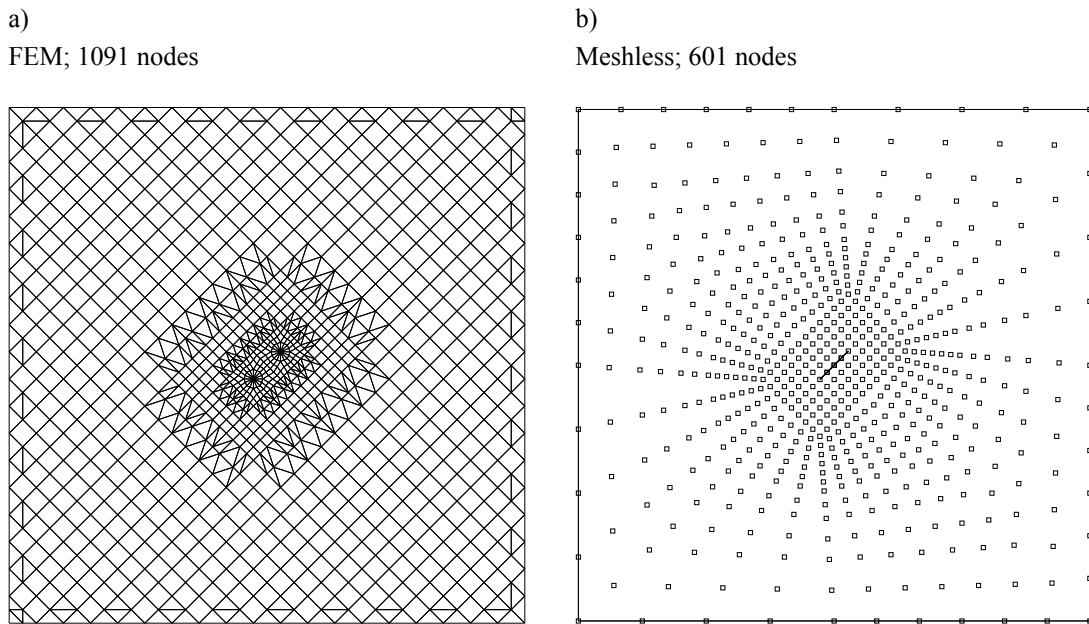
Figure 4.30. Mixed-mode fracture: a) Finite element mesh with singular crack tip elements and b) meshless discretization

a) Singular Q8 crack tip elements

| No. of nodes | Error of prediction [%] | | | |
| | Virtual Crack Extension | | Displacement correlation | |
	K_I	K_{II}	K_I	K_{II}
1091	0.69	0.18	6.91	7.19
1439	0.57	0.37	3.29	3.53

b) Virtual Crack Extension with standard interpolation functions

| No. of nodes | Error of prediction [%] | | | |
| | Meshless, NEM | | | FEM, Q4 |
	K_I	K_{II}	G	G
157	-19.47	-30.35	-43.30	-47.24
601	-11.85	-14.46	-24.44	-26.75
253	-8.58	-8.43	-16.73	-17.33
9313	-7.03	-6.65	-13.21	-12.84
37057	-6.28	-5.68	-11.60	-10.72

Table 4.2. Mixed-mode fracture: a) results from singular finite element simulations, b) from finite element and meshless simulations with standard shape functions

4.5.3 Verification of improved mixed-mode cohesive crack model

This example was carried out according to (Carol et al. 1997) to verify the mixed-mode cohesive crack model (CCM) for pure tension loading, for shear loading under constant compression and for combined loading. The first two artificial tests have been designed in (Carol et al. 1997) and the material parameters are given in Table 4.3, where for the pure tension test only the Mode-I parameters are necessary, the Mode-II parameters can be chosen arbitrarily. In the third calculation the experimental results of the test in (Hassanzadeh 1990) have been used for fitting the material parameters. The obtained parameters are given additionally in Table 4.3. During this test a prismatic concrete specimen of $7 \times 7cm$ cross section with a perimetral $1.5cm$ deep notch was subjected to pure tension, until the peak of normal stresses was reached and the tensile crack began to form through the notched cross section. From this point on, normal and shear displacements were applied simultaneously in a fixed proportion characterized by $\tan \theta = \Delta u_N / \Delta u_T$.

			Pure tension	Shear/compression	Hassanzadeh
Normal stiffness	k_N	$[10^9 N/m^3]$	1.0	25.0	200.0
Tangential stiffness	k_T	$[10^9 N/m^3]$	-	25.0	200.0
Tensile strength	χ_0	$[10^6 N/m^2]$	3.0	3.0	2.8
Shear strength	c_0	$[10^6 N/m^2]$	-	4.5	7.0
Mode-I fracture energy	G_f^I	$[Nm/m^2]$	10, 30, 100	30.0	100
Mode-IIa fracture energy	G_f^{IIa}	$[Nm/m^2]$	-	60.0	1000
Dilatancy stress	σ^{dil}	$[10^6 N/m^2]$	-	30.0	56.0
Friction coefficient	$\tan \phi$	[-]	-	0.8785	0.9
Shape parameter	α_χ	[-]	0.0	0.0	0.0
Shape parameter	α_c	[-]	-	0.0	1.5
Shape parameter	α_σ^{dil}	[-]	-	2.0	2.7
Shape parameter	α_c^{dil}	[-]	-	0.0	3.0

Table 4.3. Parameters for verification of mixed-mode CCM according to (Carol et al. 1997)

The calculations have been carried out here using a single interface element by performing a displacement controlled analysis. The improved mixed-mode CCM presented in section 4.2.2 was investigated for all three tests with the modifications of the yield and potential surface as shown in Eq. (4.14) and Eq. (4.51). The results displayed in Fig. 4.31, 4.32 and 4.33, where this improved mixed-mode CCM is marked as Model 1, show excellent agreement with these obtained in (Carol et al. 1997). The analytical solution for the pure tension problem can be obtained using Eq. (4.52). In Fig. 4.32 it can be seen, that the tangential stresses converge to the Coulomb friction values and that the dilatancy effect depends on the normal stress. Fig. 4.33 clarifies, that the model can represent the complex mixed-mode fracture process investigated in (Hassanzadeh 1990) very well.

In a further investigation the simplified approach for the softening description according to (Gálvez et al. 2002) was analyzed, which is given in Eq. (4.59). For pure tension

this Model 2 leads to the same results as Model 1, where the softening is formulated in terms of the fracture work. In Fig. 4.32 it can be seen, that the dilatancy effect is less significantly than with Model 1, caused by the reasons mentioned in section 4.2.2. Due to the consistent softening formulation in Model 1 in terms of the fracture work, where negative normal stresses and pure friction does not contribute to the softening process, this model gives more adequate results, which is shown in the Hassanzadeh test, where the dilatancy effect plays an important role.
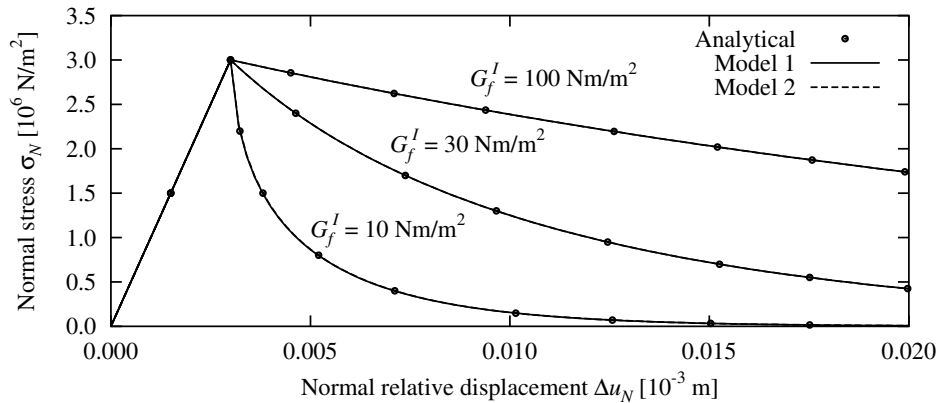
Figure 4.31. Pure tension: Normal stress vs. normal relative displacement for different values of Mode-I fracture energy
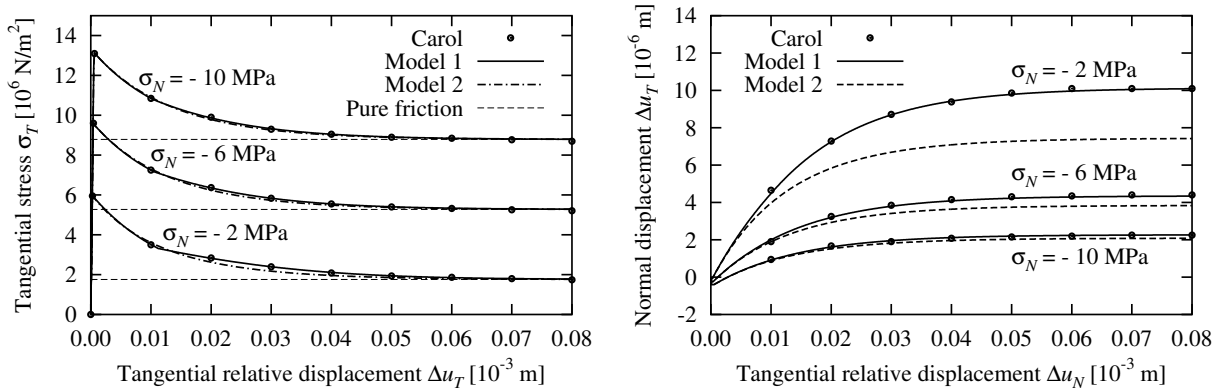
Figure 4.32. Shear under constant compression: Shear stress vs. tangential relative displacement and evolution of dilatancy for different values of compressive stress
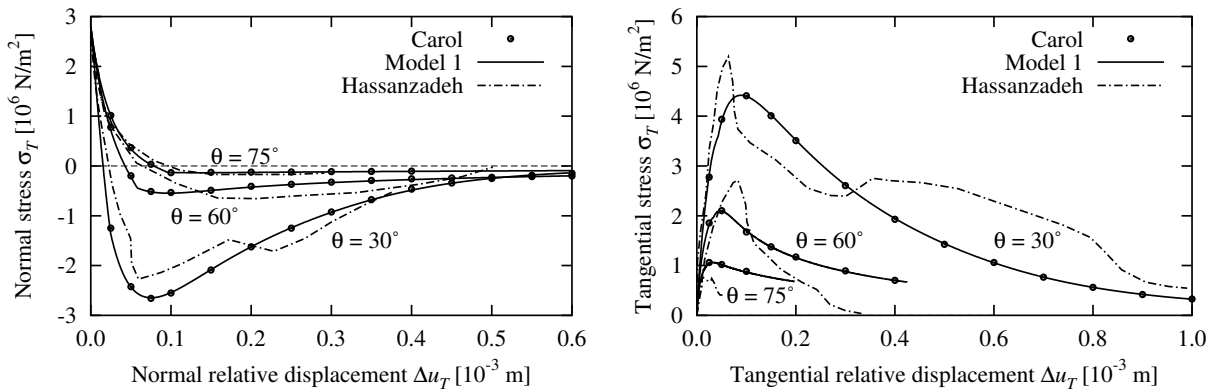
Figure 4.33. Hassanzadeh test: Normal stress vs. normal relative displacement and shear stress vs. tangential relative displacement

4.5.4   Mode-I problem: Three-point bending beam with initial crack
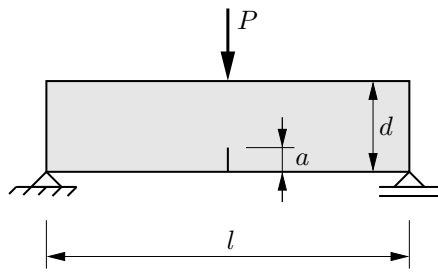
Young's modulus E	$3.65 \cdot 10^{10} \, N/m^2$
Poisson's ratio ν	0.1
Tensile strength f_t	$3.19 \cdot 10^6 \, N/m^2$
Spec. fracture energy G_f^I	$100 \, Nm/m^2$
Beam length l	$0.6 \, m$
Beam heigth d	$0.15 \, m$
Beam thickness t	$1.00 \, m$
Initial crack length a_0	$0.045 \, m$

Figure 4.34. Three point bending beam with initial crack (Carpinteri et.al. 1986)

Within this example the presented crack growth model is verified for a Mode-I problem by comparing the results with (Carpinteri et al. 1986), where a simply supported beam with an initial center crack was investigated by means of standard finite elements. Fig. 4.34 shows the system and the geometrical and material properties taken in (Carpinteri et al. 1986), where the softening behavior of concrete was assumed to be a linear function and the resulting cohesive forces were applied via nodal forces along the theoretical crack line. Here first a finite element calculation with the presented interface elements along the theoretical crack-line coupled with four-node 2D-solid elements was performed. The beam was discretized with 1721 nodes and 80×20 solid elements, the crack line with 15 node pairs and 14 linear interface elements, where the standard cohesive crack model was used due to the Mode-I situation with $k_N = 10^{14} N/m^3$. The Young's modulus was calibrated with respect to the linear part of the given load displacement curve as $E = 4.0 \cdot 10^{10} N/m^2$ to obtain the same stiffness of the finite element model as the model in (Carpinteri et al. 1986) (This calibration is caused by the coarser discretization which leads to a stiffer model in (Carpinteri et al. 1986)). The meshless calculation was done by using a coupled discretization between a Natural Neighbor meshless area in the middle of the beam and two 35×20 four-node 2D-solid FE regions to the left and to the right of it. The total node number was 1707 and 12 Gauss integration points per triangle were used for the computation of the system matrices and vectors. Simulations with the MLS-interpolation lead to similar results as the Natural Neighbor Interpolation. Due to the faster shape function computation the latter method is generally used in this and in the following examples.

Investigation of crack growth criteria

First the system was investigated using the energy-based approach with the VCE technique to decide upon crack growth and the direction of the maximum principle nonlocal stress to determine the crack direction. As shown in Fig. 4.35a the problems mentioned in section 4.2.5 occured, where the crack geometry deviates from the theoretical line caused
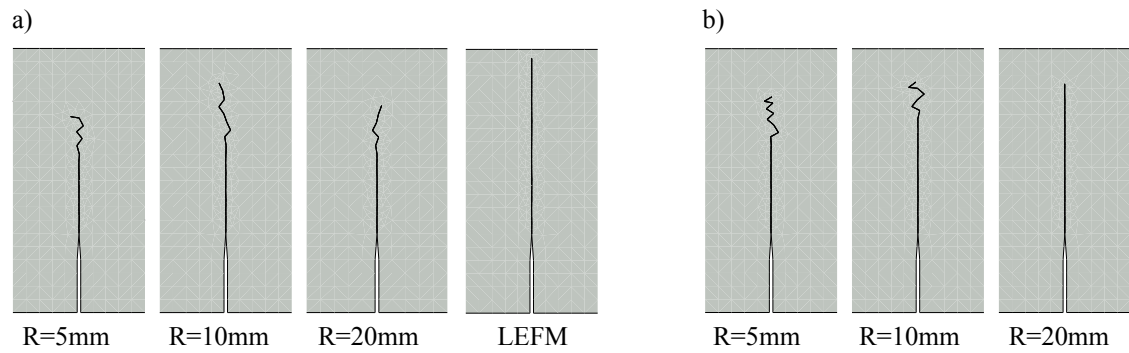
a)

R=5mm R=10mm R=20mm LEFM

b)

R=5mm R=10mm R=20mm

Figure 4.35. Crack geometries obtained with meshless simulations using a) the VCE technique for crack growth and the nonlocal stress tensor and LEFM for the crack direction and b) the nonlocal stress tensor for crack growth and the crack direction
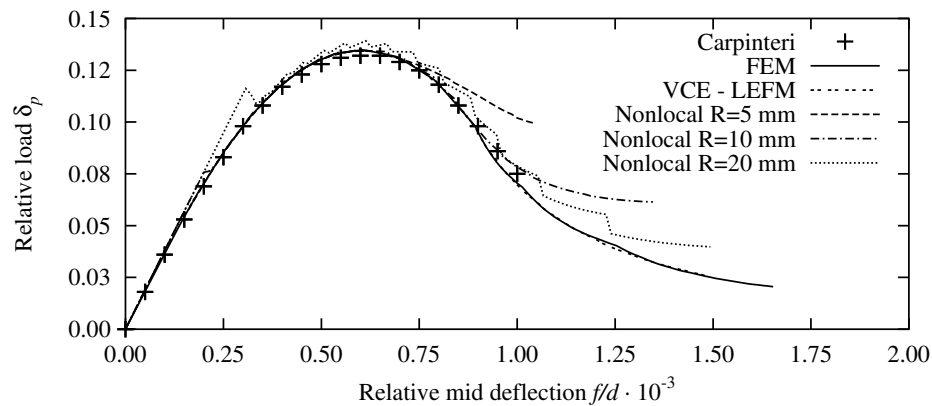

Figure 4.36. Calculated load displacement curves of three point bending beam using Natural Neighbor Galerkin Method and FEM compared to the results in Carpenteri et.al. 1986

by the sensitivity of the direction criterion subjected to small perturbations. After a certain crack length the deviation becomes so large that a strong oscillation of the crack line can be observed. Investigations with the maximum hoop stress criterion from LEFM in Eq. (4.28) for the crack direction gives a very good prediction of the crack line. The obtained load displacement curves are plotted in comparison to the results in (Carpinteri et al. 1986) in Fig. 4.36, where the relative load is defined as the following term

$$\delta_p = \frac{P}{t \cdot d \cdot f_t} \tag{4.78}$$

and the relative mid deflection is given as the quotient of the mid deflection and the beam height. The numerical results obtained with the VCE criterion and the LEFM direction show an excellent agreement with the finite element results and with those in (Carpinteri et al. 1986). All meshless calculations have been carried out with a constant crack increment length of $l_I = 5mm$.

If the nonlocal maximum principle stress is used to decide upon crack growth, similar problems in the crack path prediction can be seen. This leads to an artificial stiffening effect in the load displacement curve. The increasing of the interaction radius R can eliminate the oscillation, as shown in Fig. 4.35b, but then the crack criterion is overestimated and we obtain a choppy curve which deviates considerably from the desired relation.

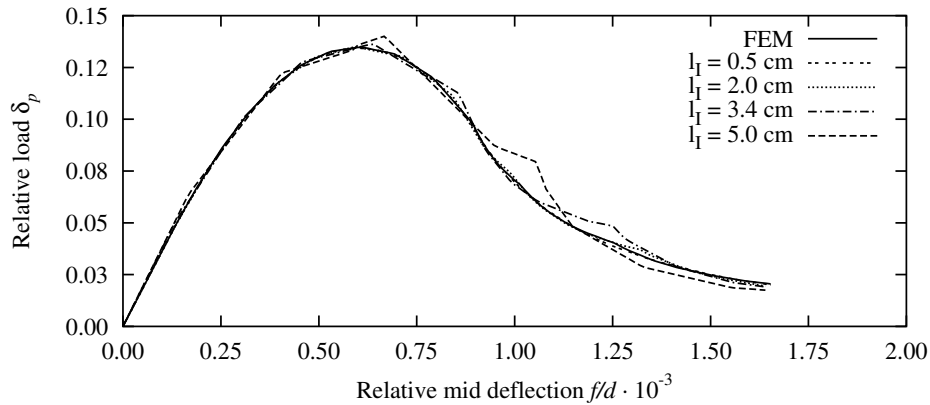**Influence of crack increment length and system size**

Figure 4.37. Load displacement curves of three point bending beam obtained by using NEM with different crack increment lengths in comparison to FEM results

Different crack increment lengths between $l_I = 0.5cm$ and $l_I = 5.0cm$ have been investigated by using the energy-based criterion. The obtained load displacement curves are shown in Fig. 4.37. The figure indicates, that all calculations show a good agreement with the finite element solution. If the crack increment is taken very large, the resulting crack surface is discretized with only a few interface elements ($l_I = 3.4cm$: 3 interface elements; $l_I = 5cm$: 2 interface elements) and the obtained curves are not smooth but represent the global behavior in general. This shows the independence of the results from the crack increment length for smaller values if problems with theoretical straight crack lines are investigated. For the investigation of mixed-mode crack propagation, the increment length has to be chosen small enough to represent the curved crack line sufficiently accurate.

In (Häussler-Combe 2001) the developed crack growth algorithm was verified by means of this numerical example using different system sizes. This verification will be done here analogous by defining an initial crack brittleness

$$s_0 = \frac{a_0 \cdot f_t}{G_f^I} \tag{4.79}$$

The investigations in (Häussler-Combe 2001) have shown, that different system sizes with equal crack brittleness, which should lead to exactly the same load displacement curves, show good agreement. Here different configurations have been investigated, which are given in Table 4.4. The structure size is modified depending on the scaling factor by

Brittleness s_0	718			1436			2871			14355		
G_f^I $[Nm/m^2]$	100	200	400	50	100	200	25	50	100	5	10	20
Scaling factor	0.5	1.0	2.0	0.5	1.0	2.0	0.5	1.0	2.0	0.5	1.0	2.0

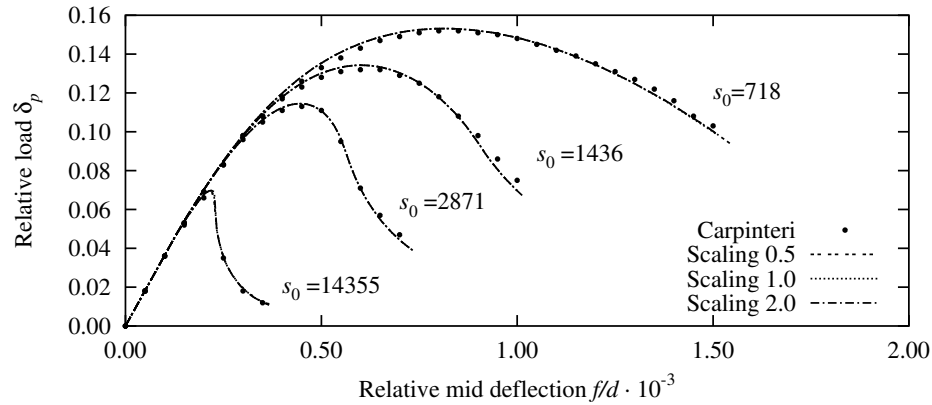**Table 4.4.** Investigated configurations of specific fracture energy and scaling factors

Figure 4.38. Load displacement curves for varying crack brittleness using different scaling factors

keeping the geometry relations a_0/d and d/l constant. In Fig. 4.38 the obtained load displacement curves for the investigated configurations are shown. It can be seen, that the calculated curves for the same brittleness agree exactly and a very good comparison with the curves obtained by (Carpinteri et al. 1986) was found. This shows that the developed crack growth algorithm works, as expected, independently of the system size.

Cohesive Crack Model vs. Linear Elastic Fracture Mechanics
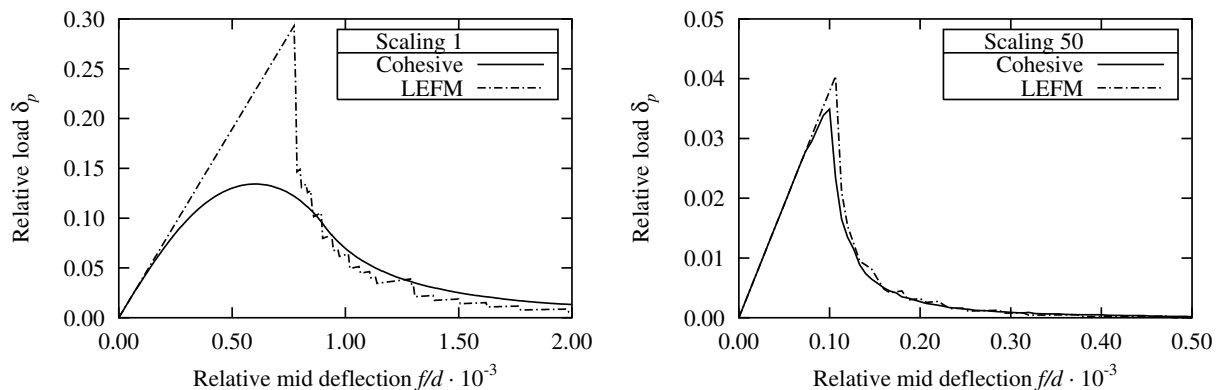
Figure 4.39. Obtained load-displacement curves by using the Cohesive Crack Model and Linear Elastic Fracture Mechanics (LEFM) for different scaling factors

A further investigation using this beam was carried out to demonstrate the fact, that with increasing system size compared to the fracture process zone the assumptions of Linear Elastic Fracture Mechanics become suitable. For this purpose first the load displacement curves obtained by using the crack criterion according to LEFM given in Eq. (4.3) and the Cohesive Crack Model (CCM) with the energy-based crack criterion are compared for the beam in Fig. 4.34 scaled with factor 1 and then for a scaling factor 50. Fig. 4.39 shows the calculated curves. The figure clearly indicates, that for a concrete structure with standard size the application of LEFM instead of CCM leads to a strong overestimation of the maximum load. If the structure is very large (scaling 50 corresponds to $d = 7.5m$) the load displacement curves show good agreement. In Fig. 4.40 the convergence of both methods for increasing system size is displayed. The length of the fracture process zone
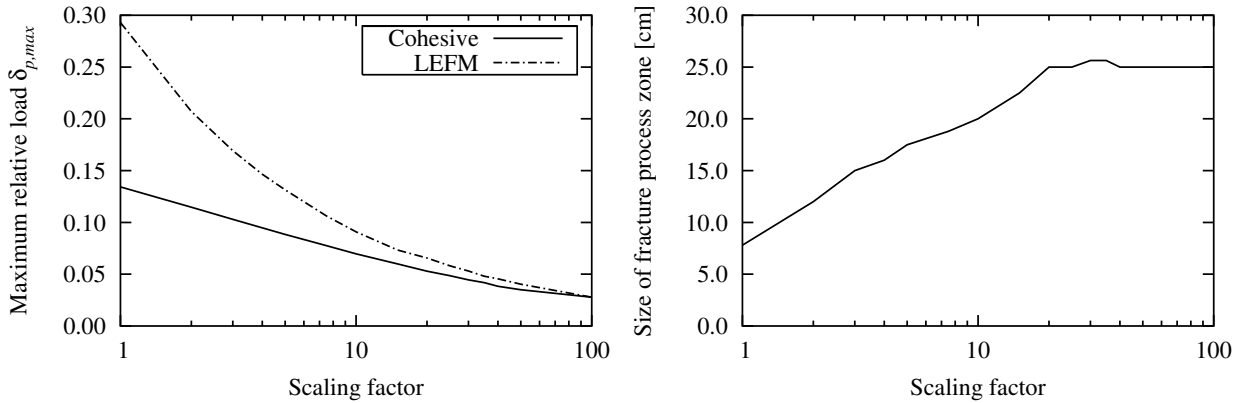
Figure 4.40. Convergence of Cohesive Crack Model and LEFM for increasing specimen size and corresponding convergence of the length of the cohesive fracture process zone

in the cohesive model was simply estimated from the number of interface elements, which still transmit normal forces if the normal stress at the crack mouth becomes zero.

Efficiency of crack growth algorithm

By means of this example the efficiency of the developed crack growth algorithm was investigated. For this purpose the computational time for calculating 75 displacement increments of $0.002mm$ at the loading point was determined for using the finite element discretization with predefined crack (FEM + crack), using a coupled meshless and FEM discretization with predefined crack (FEM + meshless + crack) and a coupled meshless and FEM discretization with the automatic crack growth algorithm (FEM + meshless + algorithm). For each displacement increment five steps for the nonlinear iteration have been used for every method. The displacement error norm given in Eq. (2.85) of the nonlinear iteration in the meshless calculations is after the five steps always below 10^{-14}, which is in the range of the machine precision. The obtained computational time for the whole calculation on a Pentium 4 with 2.4 GHz is given in Table 4.5.

	FEM + crack	FEM + meshless + crack	FEM + meshless + algorithm
NEM	160 s	186 s	190 s
MLS	160 s	234 s	239 s

Table 4.5. Computational time for 75 displacement increments

The crack increment length has been taken as $l_I = 0.75cm$, which is equivalent to the interface element length in the calculation with predefined crack. All meshless calculations have been carried out using 12 Gauss integration points per triangle cell. For the MLS simulations a linear base polynomial with 6 nodes in the influence domain and the regularized spline weighting type was taken. The table clearly indicates, that the developed algorithm for checking the crack criterion and updating the discretization works very efficient, since the additional time compared to the coupled simulation with predefined crack is about 2%. The MLS calculations are more time consuming than the NEM

caused by the complex shape function computation. Compared to the finite element simulation the additional effort of the meshless calculations using 5 steps for the nonlinear iteration is not increased very much (about 19% for the NEM and 50% for the MLS).
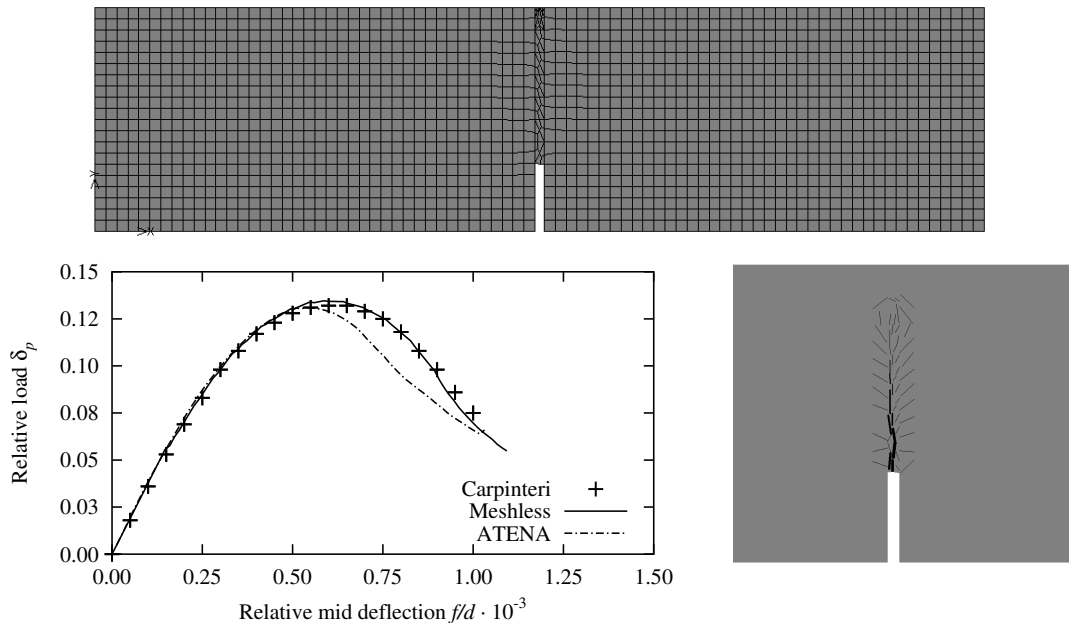

Figure 4.41. ATENA discretization, obtained load displacement curve and crack geometry

In order to compare the implemented algorithm with existing implementations of other crack models the beam shown in Fig. 4.34 was investigated with the program ATENA (Červenka and Pukl 2003). Several smeared crack models with a local formulation are available in this program, here the rotating crack model was used, since it gives in general better results as e.g. the fixed crack model. The structure was discretized with the same element size using 80×20 solid elements and some additional elements along the theoretical crack line as shown in Fig. 4.41. The obtained load displacement curve show significant deviations from the reference and the meshless solution, which is mainly caused by the calculated crack pattern shown in Fig. 4.41. Through the local formulation, this crack geometry is not a straight line and several adjacent elements are cracked perpendicular to the theoretical line. Due to this mesh sensitivity the smeared approach could not be applied without special improvements to obtain accurate results. This was shown for other implementations of smeared crack models in several studies e.g. in (Feist et al. 2004). Aside from the accuracy problems, the numerical effort is much higher than using discrete approaches. The presented investigation with ATENA needed 56 minutes instead of about three minutes for the meshless calculation on the same computer for the same number of displacement increments.

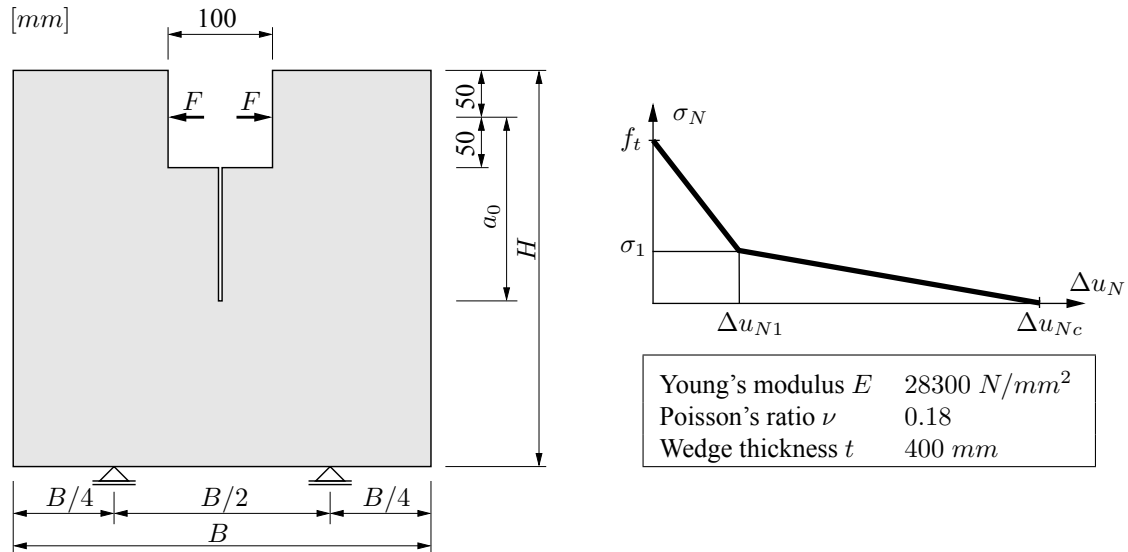### 4.5.5   Mode-I problem: Wedge splitting tests on dam concrete

Figure 4.42. Wedge splitting test setup and assumed softening curve (Trunk 1999)

By means of this example the developed crack growth algorithm will be verified for a Mode-I crack by experimental data. For this purpose the wedge splitting tests performed by (Trunk 1999) for different specimen sizes were analyzed numerically. The system and the elastic material properties are given in Fig. 4.42. The fracture parameters given in Table 4.6 have been determined in (Trunk 1999) for the different specimen sizes by assuming linear softening as shown in Fig. 4.42. The numerical simulation has been carried

$H[mm]$	$B[mm]$	$a_0[mm]$	$G_f^I[N/mm]$	$f_t[N/mm^2]$	$\sigma_1[N/mm^2]$	$\Delta u_{N1}[mm]$	$\Delta u_{Nc}[mm]$
400	400	175	0.300	2.27	0.37	0.15	0.62
800	800	375	0.373	2.12	0.27	0.20	1.24
1600	1600	775	0.482	2.11	0.38	0.20	1.40
3200	3200	1575	0.480	2.27	0.29	0.25	1.42

Table 4.6. Dimension of wedge splitting specimens with identified fracture parameters

out by using again a coupled finite element - meshless discretization, where the energy-based criterion for crack growth and the maximum hoop stress criterion from LEFM for the crack direction were taken. Bilinear and quasi-exponential softening behavior was investigated using the standard cohesive crack model with $k_N = 10^{14} N/m^3$. The obtained numerical crack geometries are shown in Fig. 4.43 together with the discretizations for the different specimen sizes. Additionally the used crack increment length l_I is indicated in the figure. It can be seen, that all crack geometries agree very well with theoretical straight crack line. In Fig. 4.44 the calculated load displacement curves are presented. The curves using the bilinear softening model show good agreement with the experimental curves. If the quasi-exponential softening is used, some deviations can be remarked, but the general behavior can be represented.
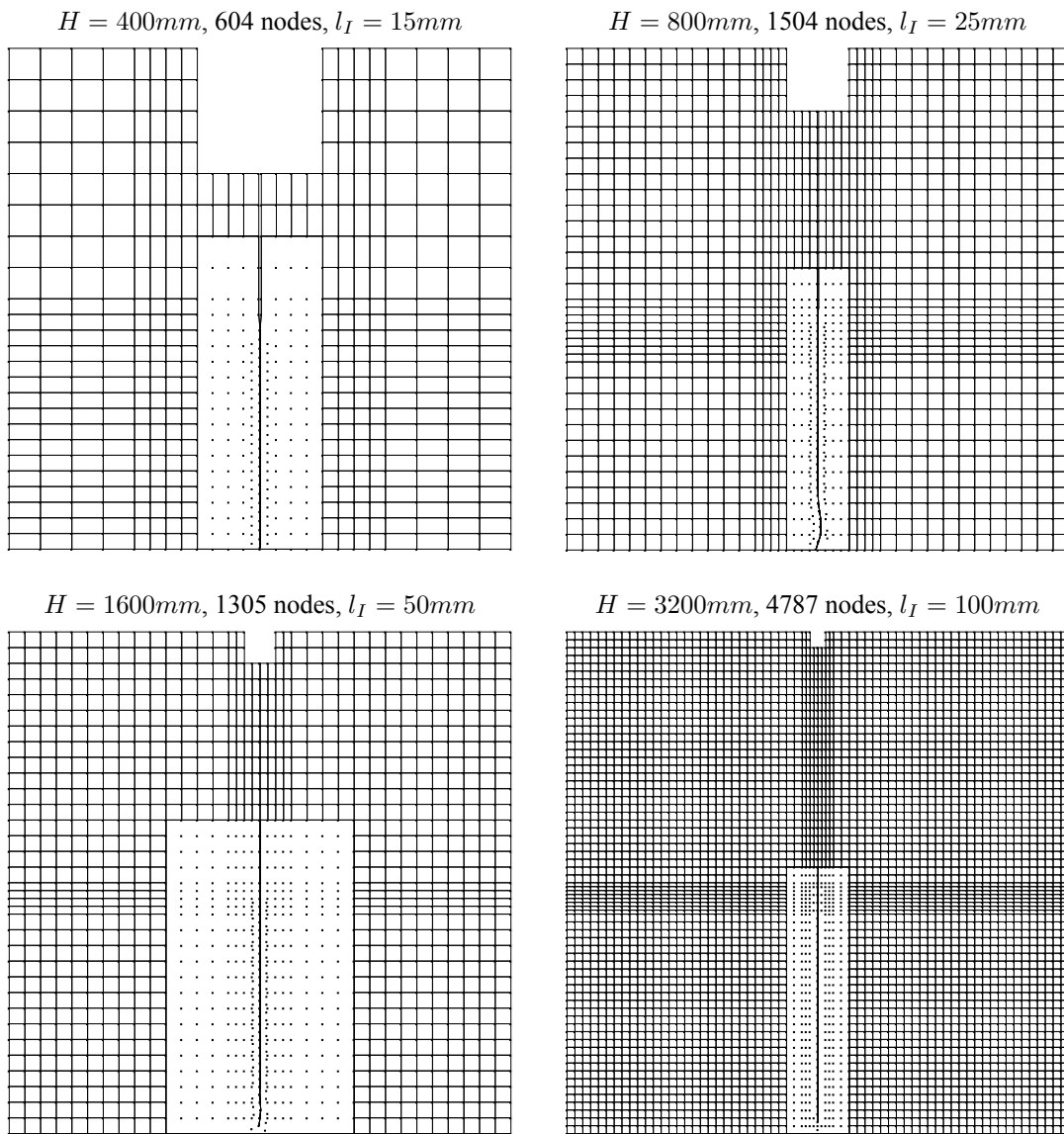
$H = 400mm$, 604 nodes, $l_I = 15mm$ $H = 800mm$, 1504 nodes, $l_I = 25mm$

$H = 1600mm$, 1305 nodes, $l_I = 50mm$ $H = 3200mm$, 4787 nodes, $l_I = 100mm$

Figure 4.43. Calculated crack geometries for the different specimen sizes

Beside the good agreement of numerical and experiment results, this examples shows the limitation of the cohesive crack model: The specific fracture energy G_f^I, which is assumed as a material constant in the CCM, depends on the size of the specimen as shown in Table 4.6, although the same concrete type was used. Thus the assumption of the CCM are not correct, if the fracture process zone is not fully developed due to limited specimen sizes or if two or more cracks have theoretical overlapping fracture process zones.
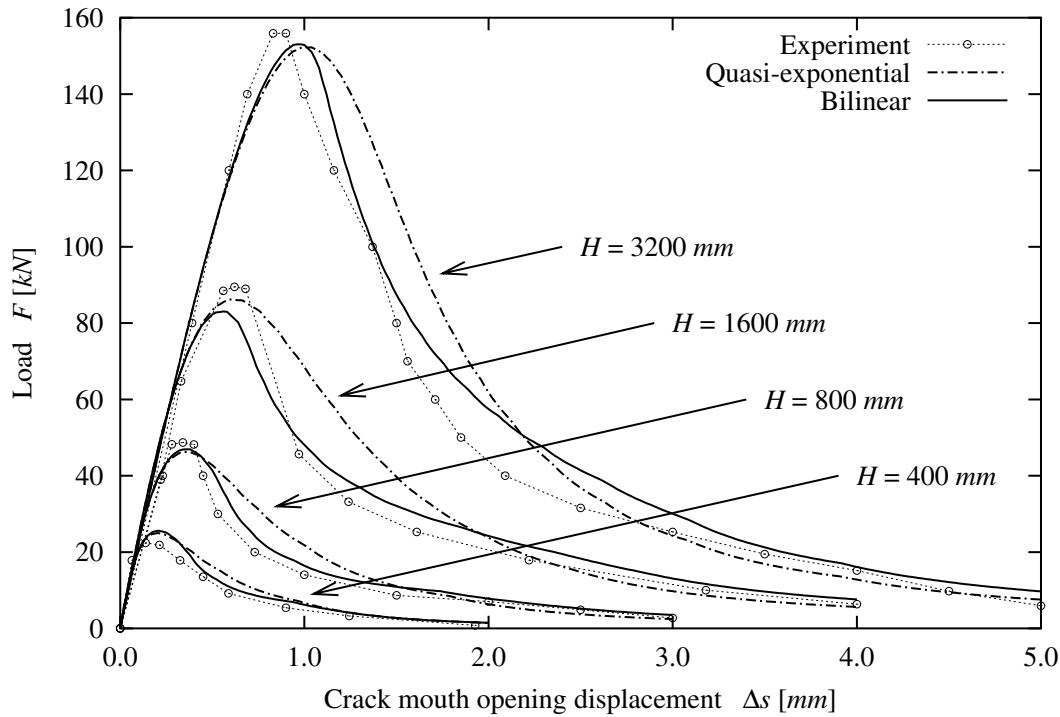
Figure 4.44. Experimental and numerical load displacement curves for different specimen sizes using quasi-exponential and bilinear softening laws

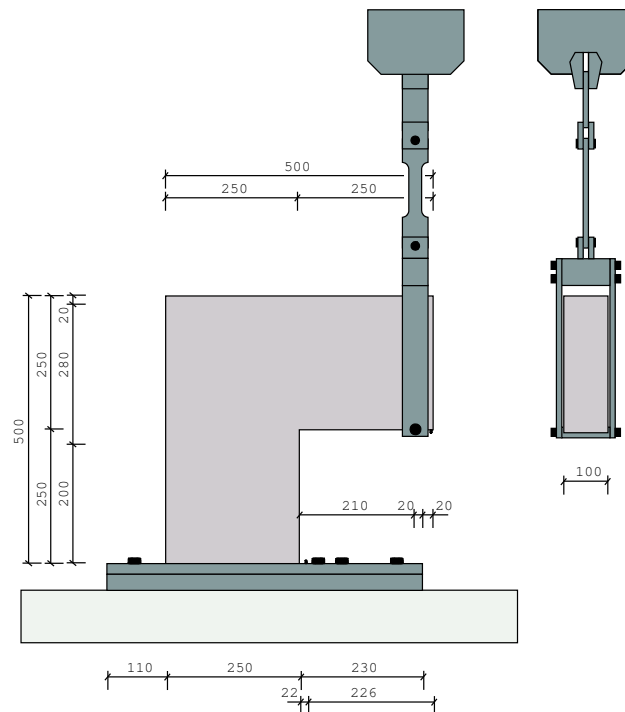## 4.5.6   Investigation of L-shaped panel

Figure 4.45. Test setup of investigated L-shaped panel (Winkler 2001, dimensions in mm)

Within this example the presented algorithm was used to predict curved crack patterns. For this purpose a L-shaped concrete panel, which was investigated experimentally in (Winkler 2001), was analyzed by using the standard and the improved cohesive crack

model. The experiments have been carried out with three displacement controlled tests. The test setup of the panel is shown in Fig. 4.45. In Table 4.7 the parameters, which have been determined in (Winkler 2001) are given. For the numerical investigations the Young's modulus was calibrated on the linear part of the load displacement curve by using an initial uniform finite element discretization with 1200 four-node elements and 1281 nodes. The Mode-I specific fracture energy was modified analogous to the contribution of Oliver et. al. to (NW-Ialad 2003) which was determined by integrating the experimental load displacement curves. The additional parameters for the improved cohesive crack model were estimated from the given quantities and are given in Table 4.7

Parameters determined in (Winkler 2001)		Estimated parameters	
Young's modulus E	$2.6 \cdot 10^{10} N/m^2$	Young's modulus E	$1.8 \cdot 10^{10} N/m^2$
Poisson's ratio ν	0.18	Shear strength c_0	$4.0 \cdot 10^6 N/m^2$
Tensile strength f_t, χ_0	$2.7 \cdot 10^6 N/m^2$	Mode-I fracture energy G_f^I	$95\ Nm/m^2$
Mode-I fracture energy G_f^I	$65 - 90\ Nm/m^2$	Mode-IIa fracture energy G_f^{IIa}	$200\ Nm/m^2$
Panel thickness t	$100\ mm$	Dilatancy stress σ^{dil}	$30.0 \cdot 10^6 N/m^2$
		Friction coefficient $\tan \phi$	0.55
		Shape par. $\alpha_\chi, \alpha_c, \alpha_\sigma^{dil}, \alpha_c^{dil}$	0

Table 4.7. Determined and estimated parameters for the L-shaped panel test

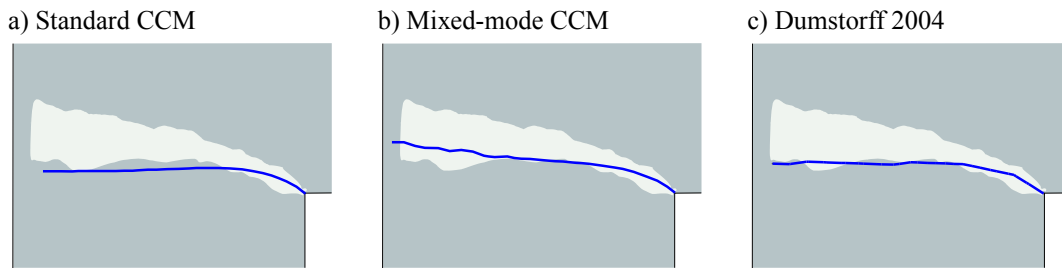a) Standard CCM   b) Mixed-mode CCM   c) Dumstorff 2004

Figure 4.46. Crack patterns of L-panel obtained using a) the standard cohesive crack model (CCM), b) the improved mixed-mode CCM and c) the direction of maximum energy release rate in comparison to the experimental spectrum

Exponential softening behavior was assumed by using the standard cohesive crack model and the improved mixed-mode crack model, where the interface stiffnesses were taken with $k_N = 10^{13} N/m^3$ and $k_T = 10^{12} N/m^3$. All meshless calculations were done by using the initial finite element discretization and transforming the critical elements during the calculation as described in section 4.3.2. In the created meshless zone 12 Gauss points per triangle cell were used. The energy-based criterion was taken for crack growth and the combined criterion for the crack direction. The nonlocal influence radius for combined direction was assumed to be $R = 20mm$. In Fig. 4.46 the obtained crack geometries are shown compared to the experimental scatter. In can be seen, that if the standard cohesive crack model is used, the crack turns early into a Mode-I crack due to the missing shear resistance. For the improved model, the crack cannot change its direction so early and the obtained crack path is more realistic. In Fig. 4.46c the crack path obtained

in (Dumstorff and Meschke 2004) using the direction of the maximum energy release rate with the standard cohesive crack model is shown. This path shows good comparison to the crack geometry in 4.46a. Thus the developed simple combined crack direction can give similar results as the much more complex approach using the direction of the maximum energy release rate.

In Fig. 4.47 the numerical results for both cohesive models are displayed compared to the experimental values. Both simulations lead to good results. The deviation for the improved model is less than using the standard model. The remaining deviation from the experimental values may be caused by the inaccurate determination of the fracture energy.
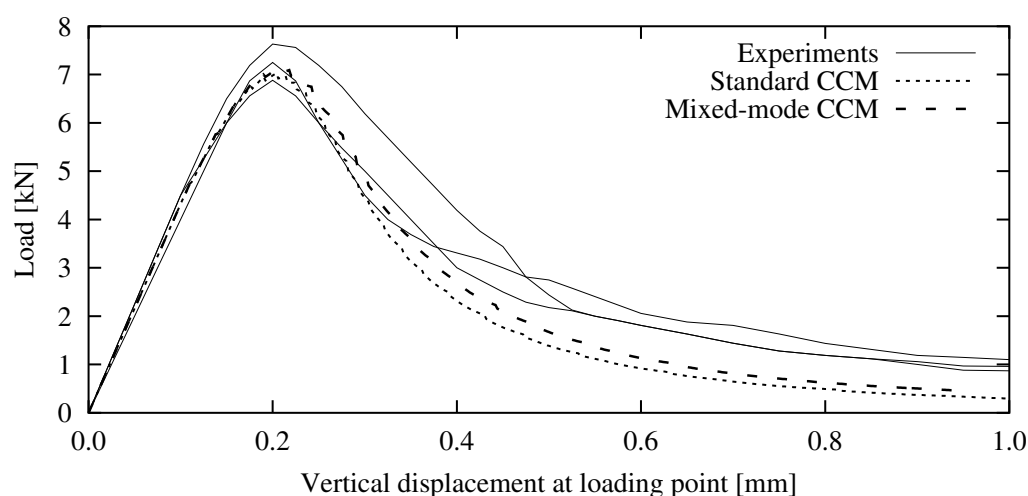
Figure 4.47. Experimental and numerical load displacement curves

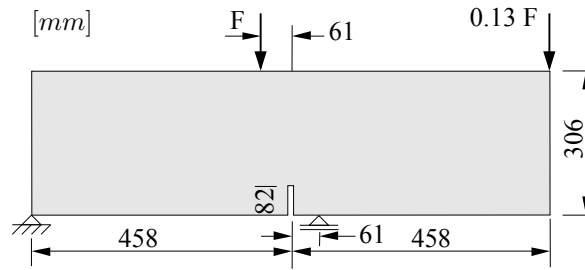### 4.5.7   Four-point single edge-notched shear beam

Figure 4.48. Four-point single edge-notched shear beam (Arrea and Ingraffea 1982)

As another example a four-point single-edge notched shear beam (SENS) was investigated. This beam has been analyzed experimentally by (Arrea and Ingraffea 1982) and has become a standard benchmark for the verification of mixed-mode crack simulations. The geometrical properties are shown in Fig. 4.48 and the thickness is assumed to be $152mm$. In Table 4.8 the material parameters determined in (Arrea and Ingraffea 1982) are given. Different estimations of the fracture parameters, which have not been identified in the experiments, can be found for this example as given in Table 4.8. In (Xie et al. 1995) the standard cohesive crack model was applied, thus the Mode-II parameters were not needed. In (Gálvez et al. 2002) a simplified mixed-mode model was used, but the dependence of the yield direction from compressive normal stresses, described in (Carol et al. 1997) by the dilatancy stress σ^{dil}, was neglected. The parameters, which were finally used in this work for the presented standard and improved mixed-mode cohesive crack model are given in the last column of Table 4.8.

			Arrea 1982	Xie 1995	Gálvez 2002	Estimated
Young's modulus	E	$[10^9 N/m^2]$	24.8	24.8	24.8	24.8
Poisson's ratio	ν	$[-]$	0.18	0.18	0.18	0.18
Compressive strength	f_c	$[10^6 N/m^2]$	45.5	-	-	-
Tensile strength	f_t, χ_0	$[10^6 N/m^2]$	-	4.0	3.7	4.0
Mode-I fracture energy	G_f^I	$[Nm/m^2]$	-	150	107	120
Shear strength	c_0	$[10^6 N/m^2]$	-	-	5.0	4.0
Mode-IIa fracture energy	G_f^{IIa}	$[Nm/m^2]$	-	-	143	200
Dilatancy stress	σ^{dil}	$[10^6 N/m^2]$	-	-	-	30.0
Friction coefficient	$\tan \phi$	$[-]$	-	-	0.55	0.55
Shape parameter	$\alpha_\chi, \alpha_c, \alpha_\sigma^{dil}, \alpha_c^{dil}$		-	-	-	0

Table 4.8. Determined and estimated parameters for four-point single edge-notched shear beam

For the numerical analysis the beam was modeled initially with 24×8 four-node solid elements and 227 nodes, where 8×8 elements of the middle part of the beam have been transformed to a meshless zone coupled with the remaining finite elements. The calculations have been carried out by using the energy based criterion for crack growth and the combined criterion for the crack direction. The nonlocal interaction radius R, used for the combined direction criterion, was assumed to be $10mm$ and the crack increment

length $l_I = 10mm$. The interface stiffnesses were taken again with $k_N = 10^{13}N/m^3$ and $k_T = 10^{12}N/m^3$. In Fig. 4.49 the obtained numerical relations between load and crack mouth sliding displacement (CMSD) and the calculated crack geometries are compared to the experimental spectrum. The figures indicate, that if the mixed-mode cohesive crack
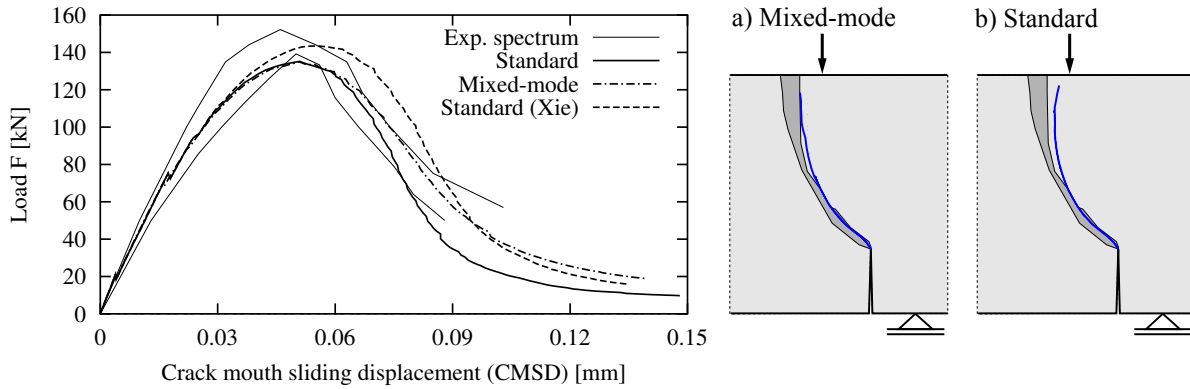

Figure 4.49. Experimental and numerical load-crack mouth sliding displacement curves with belonging crack geometries

model is used, the numerical curve agrees very well with the experimental data. By using the standard CCM, the numerical curve has a large deviation in the post-peak part. For this reason in (Xie et al. 1995) an increased value of the Mode-I fracture energy was used, which leads to the third numerical curve in Fig. 4.49, which still does not completely fit in the experimental envelope. The obtained crack geometries agree well with the experimental results. The mixed-mode model gives slightly better results.
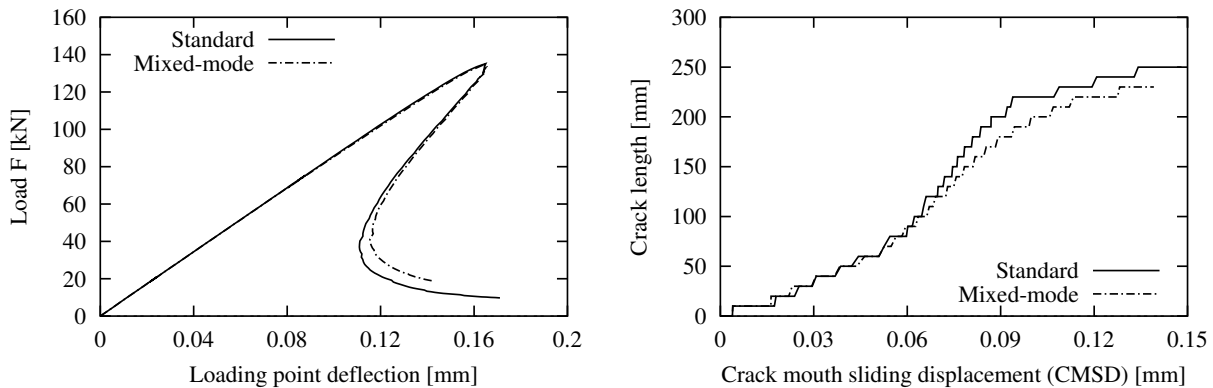

Figure 4.50. Sharp snap-back in load-displacement curve and relation between crack length and crack mouth sliding displacement

Fig. 4.50 gives the determined relation between load and load point deflection for both simulations. In can be remarked in the figure, that the curves show a sharp snap-back behavior, thus the presented modified arc-length method according to (Hellweg and Crisfield 1998) was applied. Furthermore the figure shows the calculated crack increment length depending of the CMSD. It can be seen, that the crack using the standard model growths for $CMSD > 0.06mm$, which corresponds to the post-peak part in Fig. 4.49, faster than using the improved mixed-mode model caused by the missing shear resistance.
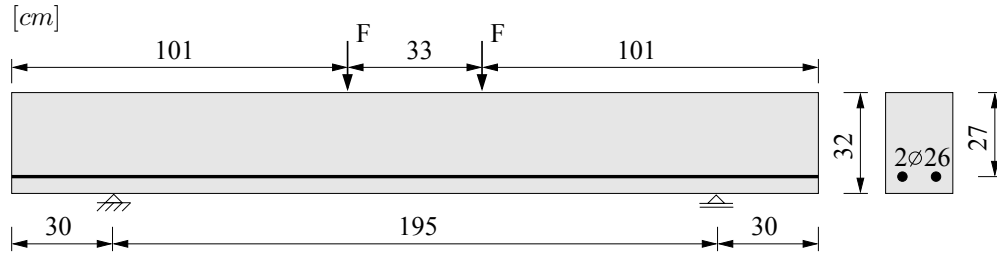
4.5.8 Reinforced four-point bending beam

Figure 4.51. Reinforced four-point bending beam (Leonard and Walther 1962)

Within this example the developed crack growth algorithm is used for describing multiple cracking in reinforced concrete. For this purpose the test beam shown in Fig. 4.51 was analyzed. In (Leonhardt and Walther 1962) two load-controlled experiments with this beam have been carried out and the maximum loads were measured with $F = 60kN$ and $F = 78kN$. The beam was reinforced by two longitudinal bars without vertical reinforcement. The standard material parameters for this beam have been calculated in (Červenka 1998) from the concrete cube strength of $35 \cdot 10^6 N/m^2$ according to the CEB-FIB Model Code (Telford 1993). In Table 4.9 the parameters from (Červenka 1998) and the estimated missing values are given.

Parameters taken from (Červenka 1998)		Estimated parameters	
Concrete			
Young's modulus E	$3.17 \cdot 10^{10} N/m^2$	Shear strength c_0	$3.0 \cdot 10^6 N/m^2$
Poisson's ratio ν	0.2	Mode-IIa fracture energy G_f^{IIa}	$200\ Nm/m^2$
Tensile strength f_t, χ_0	$1.64 \cdot 10^6 N/m^2$	Dilatancy stress σ^{dil}	$30.0 \cdot 10^6 N/m^2$
Mode-I fracture energy G_f^I	$100\ Nm/m^2$	Friction coefficient $\tan\phi$	0.55
		Shape par. $\alpha_\chi, \alpha_c, \alpha_\sigma^{dil}, \alpha_c^{dil}$	0
Reinforcement			
Young's modulus E	$2.08 \cdot 10^{11} N/m^2$		
Poisson's ratio ν	0.3		
Yield stress σ_y	$250 \cdot 10^6 N/m^2$		

Table 4.9. Material parameters for the four-point bending beam

For the numerical analysis one half of the beam was modeled initially with 56×12 four-node solid elements. During the simulation the critical elements were transformed to meshless zones. Exponential softening was assumed by using the improved mixed-mode CCM. The energy based criterion for crack growth and the combined criterion for the corresponding crack direction and the nonlocal criterion for crack initiation were applied where the nonlocal interaction radius R was taken as $30mm$ and the crack increment length as $l_I = 50mm$. As interface stiffnesses $k_N = 10^{13}N/m^3$ and $k_T = 10^{12}N/m^3$ were used. The material behavior of the reinforcement was modeled linear elastic until the yield stress was reached. After this point ideal plasticity was assumed. The description of the bond behavior was done using the nonlinear shear-stress-slip-relation presented

in section 4.4 according to (Doerr 1980). The lateral pressure in the bond surface was assumed to be zero, thus the required model parameters were taken from Eq. (4.74) as $\Delta \bar{u}_\tau = 0.06mm$ and $\Delta \tilde{u}_\tau = 0.18mm$.
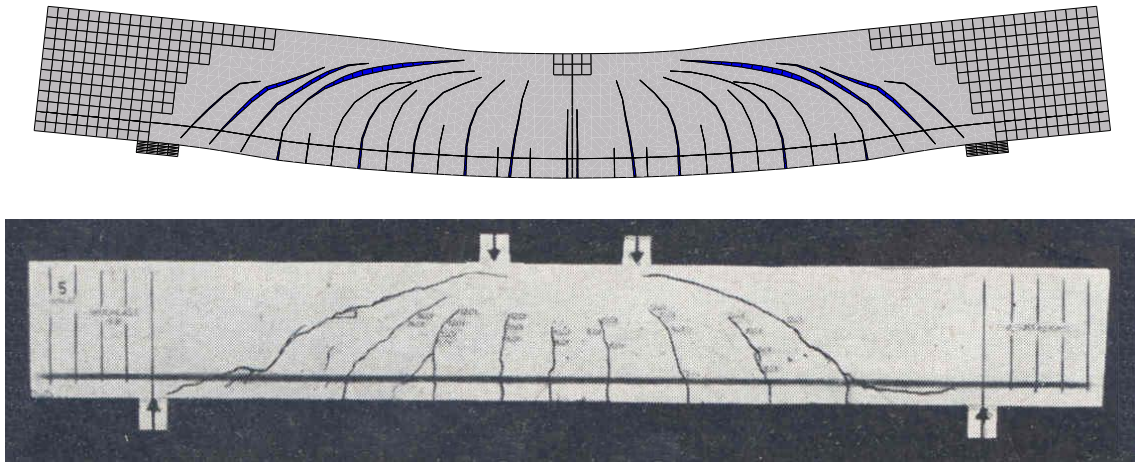

Figure 4.52. Numerical (deformation scaled with 30) and experimental crack patterns

The ultimate load of the beam was calculated as $F = 76kN$. At this point the reinforcement has reached the yield stress at several integration points. In Fig. 4.52 the obtained numerical crack pattern is shown at the ultimate load, where the deformation is scaled with factor 30 to visualize the crack opening. The cracks with significant opening correspond very well to the experimentally observed macro cracks. In the numerical crack pattern several cracks with small opening can be seen, which arise due to the stress concentration around coupling points between concrete and reinforcement. The normal traction for the crack state at the ultimate load is shown in Fig. 4.53 for the simulated half of the beam. The final dominant shear cracks obtained in the experimental analysis are represented in the numerical results due to four curved cracks, where each almost intersects the neighbor crack. The calculated load displacement curve is displayed in Fig. 4.54 and agrees very well with the experimental curve.
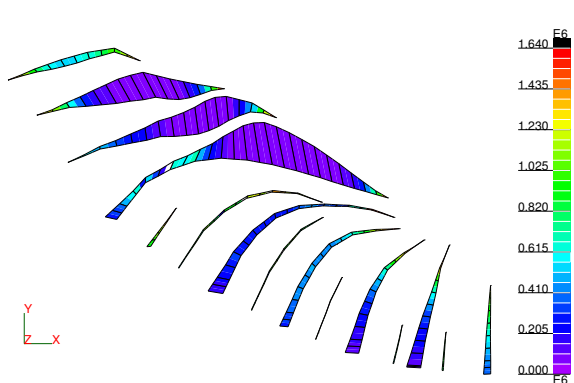

Figure 4.53. Normal stresses in the cohesive crack surfaces (deformation scaled with 200)
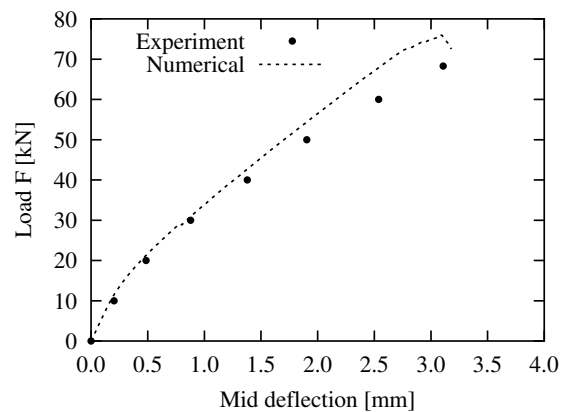
Figure 4.54. Experimental and numerical load displacement curves

Chapter 5

Modeling of uncertainties

Estimating uncertainties is an important task in the design process of engineering structures. While the standard way using safety factors according to the valid design code is applied in most practical cases, a newer development using an explicit stochastic modeling of the uncertainties in the loading, geometrical, and material properties becomes more and more attractive as it designs more efficient structures.

Several procedures have been developed for a stochastic analysis. A simple method is the description of such uncertainties by a set of correlated random variables, where each variable represents a material parameter, load factor, or geometrical property. Such an approach is used for example in (Pukl et al. 2003) and (Teplý et al. 2003) for the analysis of concrete bridges.

A more detailed method assumes a spatial distribution of geometrical or material properties and models this random distribution by a continuous field called a random field. In combination with the Finite Element Method this approach is generally called Stochastic Finite Elements (Brenner 1995), (Matthies et al. 1997). Applications of this procedure to geometrical uncertainties can be found for example in (Schorling 1997) and (Most et al. 2004), where the dynamic stability behavior of randomly imperfect shell structures was analyzed, and in (Bucher and Ebert 2000), where geometrical imperfections of steel flanges were modeled. Fluctuations of material properties of steel structures were investigated for example in (Brenner 1995) and (Rahman and Rao 2001), the latter study simulates discrete crack growth using the Element-free Galerkin Method. Similar analyses have been carried out for concrete structures in (Ebert 2002), where the cracking of the material was considered by means of predefined cohesive interfaces. Further applications can be found in the research activities of the Collaborative Research Center 532 "Textile Reinforced Concrete - Foundation of a new technology" at the RWTH Aachen University, where the material properties of multi-filament yarns are represented by random fields.

Stochastic modeling of a structure is generally performed in order to determine the probabilistic response or to assess reliability. Different procedures are usually applied in the two cases. In this work only the probabilistic response is calculated for the investi-

gated systems, which can be done using a sampling strategy, that covers the probability space very well. The plain Monte Carlo Simulation (MCS) is a very robust and simple approach for this purpose, but the number of random realizations required to obtain good estimations of the statistical characteristics of a response quantity is very high. A more efficient tool is Latin Hypercube Sampling (McKay et al. 1979), which will be described in this chapter. This sampling type enables a good estimation of statistical properties from a small number of samples.

In the reliability analyses of engineering structures, generally very small failure probabilities have to be estimated. In principle plain MCS is suitable for this task, but a large number of samples is required. Several much more efficient methods have been developed, which are only briefly mentioned here. Some of these sampling strategies are Importance Sampling (Bourgund and Bucher 1986) or Adaptive Sampling (Bucher 1988), which are improved Monte Carlo Simulations modifying the original distribution. Thus during the stochastic simulation a large fraction of realizations will be obtained in the failure domain and the probability of failure can be estimated very well with a much smaller number of samples. Other methods are the First and Second Order Reliability Method, where the limit state function is approximated by a linear or quadratic expression. For the investigation of complex nonlinear systems the reduction of the required evaluation points could be necessary. This is achieved by using an approximation of either the structural characteristics or the limit state function between the evaluation points. A powerful and widely used approach to such an approximation is the Response Surface Method (Bucher and Bourgund 1990), (Bucher and Macke 2004), where mostly a polynomial regression of the evaluated values is used for the reliability analysis. In recent years neural networks have been applied in some studies for this purpose, e.g. in (Hurtado and Alvarez 2001). Within these networks the structural response is approximated by means of a complex set of nonlinear functions.

This chapter describes the random field concept and its application and adaptation for use in the developed crack growth algorithm. An introduction to random variables and vectors is given. The basic ideas of Monte Carlo Simulation and Latin Hypercube Sampling will be presented. These sampling methods will be applied in the numerical examples to determine the probabilistic response of plain and reinforced concrete structures. In the simulation carried out in this chapter the stochastic modeling is limited to the important concrete material parameters. The presented concept can be extended directly to model the material parameters of the reinforcement or the geometrical properties as the covering of the reinforcement as random fields.

5.1 Introduction to random variables

5.1.1 Random variables

Let X be a single real valued random variable. The probability P, that this random variable is smaller than a deterministic value x is defined by the cumulative distribution function

$$F_X(x) = P[X < x]. \tag{5.1}$$

The probability density function is obtained by differentiating the distribution function with respect to x

$$f_X(x) = \frac{\partial F_X(x)}{\partial x}. \tag{5.2}$$

Random variables are often described by their mean value, standard deviation and distribution type. The mean value $\bar{X}$ of a random variable X is defined as

$$\bar{X} = E[X] = \int_{-\infty}^{\infty} x f_X(x) dx. \tag{5.3}$$

The standard deviation σ_X is the square root of the variance of X, defined as

$$\sigma_X^2 = E[(X - \bar{X})^2] = \int_{-\infty}^{\infty} (x - \bar{X})^2 f_X(x) dx. \tag{5.4}$$

The normalized standard deviation is called coefficient of variation

$$V_X = \frac{\sigma_X}{\bar{X}}. \tag{5.5}$$

In Table 5.1 some common distribution types are listed with their distribution and probability density function and a graphical representation. As indicated in the table, the exponential and Rayleigh distribution types are a special case of the Weibull distribution. The normal distribution with zero mean and unit standard deviation is called standard normal distribution and its cumulative distribution function is denoted as $\Phi(.)$ as indicated in Table 5.1.
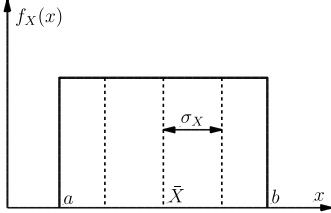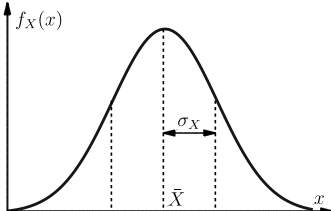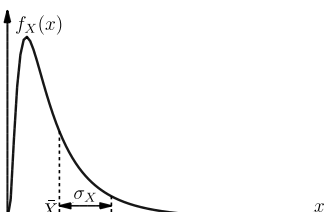
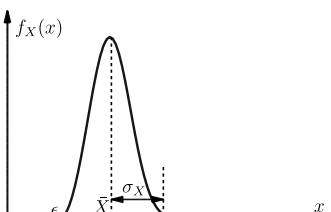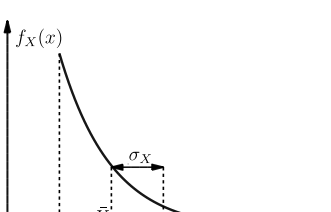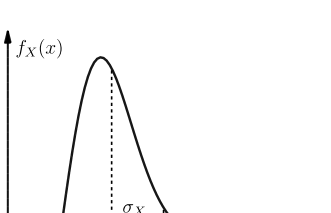|		
Uniform $a \le x \le b$	$f_X(x) = \frac{1}{b-a}$ $F_X(x) = \frac{x-a}{b-a}$ $\bar{X} = \frac{a+b}{2}$ $\sigma_X = \frac{b-a}{\sqrt{12}}$	
Normal (Gauss) $-\infty \le x \le \infty$	$f_X(x) = \frac{1}{\sigma_X\sqrt{2\pi}} \exp\left(-\frac{(x-\bar{X})^2}{2\sigma_X^2}\right)$ $F_X(x) = \Phi\left(\frac{x-\bar{X}}{\sigma_X}\right)$ $\Phi(z) = \frac{1}{\sqrt{2\pi}} \int_{-\infty}^{z} \exp\left(-\frac{u^2}{2}\right) du$	
Lognormal $0 < x \le \infty$	$f_X(x) = \frac{1}{xs\sqrt{2\pi}} \exp\left(-\frac{(\ln(x/\mu))^2}{2s^2}\right)$ $F_X(x) = \Phi\left(\frac{\ln(x/\mu)}{s}\right)$ $s = \sqrt{\ln\left(\frac{\sigma_X^2}{\bar{X}^2} + 1\right)}$ $\mu = \bar{X} \exp\left(-\frac{s^2}{2}\right)$	
Weibull $\epsilon \le x \le \infty$	$f_X(x) = \frac{k}{w-\epsilon} \left(\frac{x-\epsilon}{w-\epsilon}\right)^{k-1} \exp\left(-\left(\frac{x-\epsilon}{w-\epsilon}\right)^k\right)$ $F_X(x) = 1 - \exp\left(-\left(\frac{x-\epsilon}{w-\epsilon}\right)^k\right)$ $\bar{X} = \epsilon + (w-\epsilon)\Gamma\left(1+\frac{1}{k}\right)$ $\sigma_X = (w-\epsilon)\sqrt{\Gamma\left(1+\frac{2}{k}\right) - \Gamma^2\left(1+\frac{1}{k}\right)}$	
Exponential (Weibull, $k=1$) $\epsilon \le x \le \infty$	$f_X(x) = \frac{1}{\lambda} \exp\left(-\frac{x-\epsilon}{\lambda}\right)$ $F_X(x) = 1 - \exp\left(-\frac{x-\epsilon}{\lambda}\right)$ $\bar{X} = \epsilon + \lambda$ $\sigma_X = \lambda$ $\lambda = w - \epsilon$	
Rayleigh (Weibull, $k=2$) $\epsilon \le x \le \infty$	$f_X(x) = \frac{x-\epsilon}{\alpha^2} \exp\left(-\frac{(x-\epsilon)^2}{2\alpha^2}\right)$ $F_X(x) = 1 - \exp\left(-\frac{(x-\epsilon)^2}{2\alpha^2}\right)$ $\bar{X} = \epsilon + \alpha\sqrt{\pi/2}$ $\sigma_X = \alpha\sqrt{2 - \pi/2}$ $\alpha = (w-\epsilon)/\sqrt{2}$	

Table 5.1. Common distribution types with corresponding distribution function $F_X(x)$, probability density function $f_X(x)$, mean value $\bar{X}$, standard deviation σ_X and specific parameters

5.1.2 Random vectors

For multi-dimensional stochastic problems the covariance function between two random variables X_1 and X_2 gives information about the correlation between both variables

$$C_{XX}(X_1, X_2) = E\left[\left(X_1 - \bar{X}_1\right)\left(X_2 - \bar{X}_2\right)\right].$$ (5.6)

The coefficient of correlation reads

$$\rho_{12} = \frac{E\left[\left(X_1 - \bar{X}_1\right)\left(X_2 - \bar{X}_2\right)\right]}{\sigma_{X_1}\sigma_{X_2}} = \frac{C_{XX}(X_1, X_2)}{\sigma_{X_1}\sigma_{X_2}}$$ (5.7)

and is defined between -1 and 1. If ρ_{12} is one, both variables are fully correlated, and if ρ_{12} is zero, they are uncorrelated. This is the case, e.g. if X_1 is independent of X_2. An arbitrary number of random variables can be arranged in a random vector

$$\mathbf{X} = [X_1, X_2, \ldots, X_n]^T,$$ (5.8)

with the mean value vector

$$\bar{\mathbf{X}} = \left[\bar{X}_1, \bar{X}_2, \ldots, \bar{X}_n\right]^T.$$ (5.9)

The corresponding covariance matrix, containing the pairwise values of the covariance function, is defined as

$$\mathbf{C_{XX}} = E\left[\left(\mathbf{X} - \bar{\mathbf{X}}\right)\left(\mathbf{X} - \bar{\mathbf{X}}\right)^T\right].$$ (5.10)

For the description of multi-dimensional distributions two models with prescribed individual (marginal) distributions and covariances are usually applied. These are the Morgenstern model (Morgenstern 1956) and the Nataf model (Nataf 1962), (Liu and Der Kiureghian 1986). The Morgenstern model is valid only for small coefficients of correlation but the Nataf model is applicable to a rather wide range of correlation coefficients. In this work the Nataf concept is used, since strongly correlated random variables have to be described as well as weakly correlated variables. In the Nataf model a vector of standard normal distributed random variables

$$\mathbf{Z} = [Z_1, Z_2, \ldots, Z_n]^T, \quad i = 1, \ldots, n$$ (5.11)

is obtained by the marginal transformation of the original random vector $\mathbf{X}$ as

$$Z_i = \Phi^{-1}[F_{X_i}(X_i)], \quad i = 1, \ldots, n.$$ (5.12)

By assuming that $\mathbf{Z}$ is jointly normal distributed, the joint probability density function of

X reads

$$f_\mathbf{X}(\mathbf{x}) = f_{X_1}(x_1)f_{X_2}(x_2)\ldots f_{X_n}(x_n)\frac{\phi_n(\mathbf{z}, \mathbf{C_{ZZ}})}{\phi(z_1)\phi(z_2)\ldots\phi(z_n)}, \qquad (5.13)$$

where $z_i = \Phi^{-1}[F_{X_i}(x_i)]$, $\phi(.)$ is the standard normal probability density function and $\phi_n(\mathbf{z}, \mathbf{C_{ZZ}})$ is the n-dimensional standard normal density depending on the covariance matrix of **Z**. The elements of this covariance matrix are the correlation coefficients of **Z**

$$C_{ZZ}(Z_i, Z_j) = \tilde{\rho}_{ij}, \qquad (5.14)$$

which are defined in terms of the correlation coefficients ρ_{ij} of the original random vector **X** as

$$\rho_{ij} = \int\limits_{-\infty}^{\infty}\int\limits_{-\infty}^{\infty}\left(\frac{x_i - \bar{X}_i}{\sigma_{X_i}}\right)\left(\frac{x_j - \bar{X}_j}{\sigma_{X_j}}\right)f_{X_i}(x_i)f_{X_j}(x_j)\frac{\phi_2(z_i, z_j, \tilde{\rho}_{ij})}{\phi(z_i)\phi(z_j)}\,dx_i\,dx_j,$$

$$= \int\limits_{-\infty}^{\infty}\int\limits_{-\infty}^{\infty}\left(\frac{x_i - \bar{X}_i}{\sigma_{X_i}}\right)\left(\frac{x_j - \bar{X}_j}{\sigma_{X_j}}\right)\phi_2(z_i, z_j, \tilde{\rho}_{ij})\,dz_i\,dz_j.$$

$$(5.15)$$

The Nataf model can be applied if the covariance matrix $\mathbf{C_{ZZ}}$ is positive definite and if the distribution functions $F_{X_i}(x_i)$ are continuous and strictly increasing. Eq. (5.15) can be solved iteratively to obtain $\tilde{\rho}_{ij}$ for each pair of marginal distributions with known coefficient of correlation ρ_{ij}. In (Liu and Der Kiureghian 1986) regression formulas for the modified correlation coefficients $\tilde{\rho}_{ij}$ have been derived, which were introduced as

$$\tilde{\rho}_{ij} = \rho_{ij}F, \quad F \geq 1, \qquad (5.16)$$

where F is the Nataf coefficient depending on ρ_{ij} and the original marginal distributions. In Table 5.2 some of these coefficients with corresponding bounds are given for random variable pairs X_i and X_j with the same marginal distribution type. The formula for the exponential distribution is taken from (Brenner 1995), where it was improved for coefficient of correlation close to one. The regression formulas in Table 5.2 are independent of the parameters of the distribution, except for the lognormal distribution, which depends on the coefficients of variation $V_{X_i} = \sigma_{X_i}/\bar{X}_i$ and $V_{X_j} = \sigma_{X_j}/\bar{X}_j$.

In (Brenner 1995) it was mentioned, that this transformation concept cannot be applied to strongly correlated random variables of all distribution types, e.g. for variables with Weibull distribution.

Marginal distribution	Nataf coefficient F	Lower/upper bounds on ρ_{ij}
Uniform	$1.047 - 0.047\rho_{ij}$	-0.999/0.999
Rayleigh	$1.028 - 0.029\rho_{ij}$	-0.947/1.000
Exponential	$1 + 0.19004(1 - \rho_{ij})$ $-0.047098(1 - \rho_{ij})^2$ $+0.0797(1 - \rho_{ij})^3$	-0.645/1.000
Lognormal	$\dfrac{\ln(1 + \rho_{ij} V_{X_i} V_{X_j})}{\sqrt{\ln(1 + V_{X_i}^2)\ln(1 + V_{X_j}^2)}}$	-1.000/1.000 $(V_{X_i} = V_{X_j} < 1)$

Table 5.2. Selected Nataf coefficients F and their area of validity for two random variables of the same distribution type according to (Liu and Der Kiureghian 1986) and (Brenner 1995)

5.2 Random fields

5.2.1 Properties

A random field H can be interpreted as a geometrical multi-dimensional stochastic process, which can be described as

$$\{H(\mathbf{x}); \quad \mathbf{x} \in D \subseteq R^n\}, \tag{5.17}$$

where D defines the domain containing the possible positions $\mathbf{x}$. The dimension n of the geometrical space can be arbitrary. For the application in stochastic finite element simulations, one-, two- or three-dimensional spaces are usual.

A random field is characterized by its distribution type and its statistical parameters, e.g. the mean value

$$\bar{H}(\mathbf{x}) = E\left[H(\mathbf{x})\right] \tag{5.18}$$

and the variance

$$\sigma_H^2(\mathbf{x}) = E\left[\left(H(\mathbf{x}) - \bar{H}(\mathbf{x})\right)^2\right]. \tag{5.19}$$

The correlation of a random field can be formulated by the auto correlation function R_{HH}, which is influenced by further random field properties as isotropy and homogeneity. A random field is called weakly homogenous, if the mean value and the covariance function are independent of the position vectors. Then Eq. (5.20) is valid.

$$R_{HH}(\mathbf{x}_1, \mathbf{x}_2) = R_{HH}(\mathbf{x}_1, \mathbf{x}_1 + \boldsymbol{\xi}) = R_{HH}(\boldsymbol{\xi}), \tag{5.20}$$

where

$$\boldsymbol{\xi} = \mathbf{x}_2 - \mathbf{x}_1. \tag{5.21}$$

For isotropic random fields the correlation function fulfills

$$R_{HH}(\mathbf{x}_1, \mathbf{x}_1 + \boldsymbol{\xi}) = R_{HH}(\|\boldsymbol{\xi}\|), \tag{5.22}$$

which means, that the correlation depends only on the distance between the two points and no direction dependency exists.

The correlation function is often described by the correlation length l_H. For isotropic random fields this quantity is unique for every direction. For the anisotropic case different values for each direction are taken, e.g. for three dimensions l_{Hx}, l_{Hy} and l_{Hz}. A very common function type is the exponential correlation function defined for the isotropic case as

$$R_{HH}(\|\boldsymbol{\xi}\|) = \sigma_H^2 \exp\left(-\frac{\|\boldsymbol{\xi}\|}{l_H}\right), \tag{5.23}$$

which is based on the assumption, that the correlation between two points of the random field decreases with increasing distance. If the correlation length tends to infinity, the random field is fully correlated and if the correlation length is zero, the field is completely uncorrelated. Thus the coefficients of correlation of a random field with such correlation function are between zero and one and negative values are not possible.

5.2.2 Discretization

For the numerical representation in a finite element analysis a random field has to be discretized. Several methods have been developed for this purpose, most of them are described and discussed in (Matthies et al. 1997). One class of discretization schemes are point discretization methods. These methods represent the uncertainties of a random field at several points. The number of these points is equivalent to the number of random variables. The discretized value at a point i is directly given as

$$H_i = H(\mathbf{x}_i). \tag{5.24}$$

The covariance between two points reads

$$C_{H_i H_j} = C_{HH}(\mathbf{x}_i, \mathbf{x}_j). \tag{5.25}$$

In (Matthies et al. 1997) several advantages and disadvantages of this class of methods are mentioned. These advantages are the simple computation of the covariance matrix,

the always positive definite covariance matrix and the same distribution function in the discretized and in the continuous case, which enables the application to different distribution types. The disadvantages are the limitation of the mesh size compared to the correlation length and a required almost regular discretization. For very short correlation lengths the random field discretization has to be very fine, which increases the numerical effort dramatically. Thus these methods are only useful for medium and long correlation lengths. Two common point discretization methods are the midpoint method (Liu and Der Kiureghian 1989), where the random field is discretized only at the centroids of the finite elements, and the integration point method (Brenner 1995), where the Gaussian integration points are used for the random field representation.

Another class of discretization methods are schemes based on an averaging procedure, as the local averaging method (Zhu et al. 1992) and the interpolation method (Liu et al. 1986). The local averaging method determines discrete values as

$$H_i = \frac{1}{V_i} \int_{\Omega_i} H(\mathbf{x}) d\mathbf{x}, \tag{5.26}$$

where Ω_i is the local averaging domain and V_i is the corresponding volume of Ω_i. This method yields to accurate results even for coarse meshes, but the determination of the distribution function of H_i is difficult or even impossible, except for random fields with normal (Gaussian) distribution, which limits these methods for this case. The interpolation method uses an additional grid to discretize the random field independently of the finite element mesh. The required random field values are obtained by using an interpolation scheme similar to the finite element interpolation. This method can give good results even for coarse or irregular finite element meshes, but the disadvantage is the need of an additional discretization.

The third class are series expansion methods, where the random field is represented by series with deterministic functions and random coefficients. Such an expansion can be done by Taylor series, where the number of considered terms depends on the size of the coefficients of variation. For small coefficients a first order approximation gives good results, but for larger coefficients the high number of required terms complicates the application of this method.

Due to the presented advantages of point discretization methods compared to other approaches and its applicability for non-Gaussian distribution types, these methods have been applied in several practical analyses, e.g. in (Brenner 1995), (Ebert 2002) and (Bucher and Ebert 2000). In this work the integration point method was preferred for the use with the presented coupled meshless and finite element discretization. The meshless integrations points are handled in the same manner as these of the finite elements and the computation of the covariance matrix is done without modifications.

5.2.3   Simulation of random field samples

The number of random variables $H_i = H(\mathbf{x}_i)$ of the discretized random field can be written in a random vector

$$\mathbf{H} = [H(\mathbf{x}_1), H(\mathbf{x}_2), \dots, H(\mathbf{x}_i), \dots, H(\mathbf{x}_n)]^T, \quad i = 1, \dots, n. \tag{5.27}$$

The covariance matrix in the original space is then defined as

$$\mathbf{C_{HH}} = E\left[\left(\mathbf{H} - \bar{\mathbf{H}}\right)\left(\mathbf{H} - \bar{\mathbf{H}}\right)^T\right]. \tag{5.28}$$

This matrix is directly computed from the integration point positions using the pre-defined auto correlation function as

$$C_{H_i H_j} = R_{HH}(\mathbf{x}_i, \mathbf{x}_j, l_H). \tag{5.29}$$

If the exponential auto correlation function is used, the entries of this matrix are between zero and one depending on the distance between two random field points. Thus a random field vector contains strongly and weakly correlated random variables.

In order to simulate discrete samples of the random field, it is necessary to decouple the random variables. This can be realized for normal distributed random field variables by a transformation to the uncorrelated Gaussian space. If the distribution type is non-Gaussian a transformation into the Gaussian space is required. In (Brenner 1995) this was realized by using the Nataf model described in section 5.1.2. The obtained covariance matrix $\mathbf{C_{ZZ}}$ in the correlated Gaussian space is then transformed to the uncorrelated Gaussian space by solving the standard eigenvalue problem

$$\mathbf{C_{ZZ}} = \mathbf{\Psi} \mathbf{C_{YY}} \mathbf{\Psi}^T, \tag{5.30}$$

where $\mathbf{C_{YY}} = \text{diag}(\sigma_{Y_i}^2)$ is a diagonal matrix containing the sorted variances of the uncorrelated Gaussian random variables and the matrix $\mathbf{\Psi}$ consists of the corresponding deterministic eigenvectors

$$\mathbf{\Psi} = [\mathbf{\Psi}_1, \mathbf{\Psi}_2, \dots, \mathbf{\Psi}_n]. \tag{5.31}$$

This spectral representation has the advantage, that in the most cases only a small number k of the largest eigenvalues with corresponding eigenvectors $\mathbf{\Psi}_1, ..., \mathbf{\Psi}_k$ are necessary to represent the properties of a random field with a sufficient quality. This quality Q has been estimated in (Brenner 1995) as follows

$$Q = \frac{\sum_{i=1}^{k} \mathbf{C_{YY}}(i,i)}{\text{tr}(\mathbf{C_{YY}})} = \frac{\sum_{i=1}^{k} \mathbf{C_{YY}}(i,i)}{\text{tr}(\mathbf{C_{ZZ}})}. \tag{5.32}$$

With decreasing size of the correlation length the number of required eigenvalues and -vectors has to be increased to obtain a certain Q.

A discrete sample of a random field is obtained by simulating first the reduced uncorrelated random variable vector

$$\tilde{\mathbf{y}} = [\tilde{y}_1, \tilde{y}_2, ..., \tilde{y}_k]^T .$$ (5.33)

Then a backward transformation to the correlated Gaussian space has to be performed as follows

$$\tilde{\mathbf{z}} = \sum_{i=1}^{k} \mathbf{\Psi}_i \tilde{y}_i.$$ (5.34)

For non-Gaussian distribution types finally the inverse Nataf transformation has to be applied, which can be done element-wise

$$\tilde{H}(\mathbf{x}_i) = F_{H_i}^{-1}[\Phi(\tilde{z}_i)], \quad i = 1, \dots, n.$$ (5.35)

The described assembling of the original covariance matrix, its transformation to the Gaussian space and its spectral decomposition has to be done only once. The following simulation of discrete samples requires only the execution of the operations in Eq. (5.34) and Eq. (5.35) for each sample.

5.2.4   Modeling of multiple correlated random parameters

The presented random field concept was applied in (Brenner 1995), (Ebert 2002) and (Bucher and Ebert 2000) in that way, that a random parameter, e.g. the Young's modulus E, was modeled at an integration point i as follows

$$E(\mathbf{x}_i) = E_0 \, H_E(\mathbf{x}_i),$$ (5.36)

where E_0 is the deterministic mean value and $H_E(\mathbf{x})$ is a homogenous, isotropic random field with unit mean. The standard deviation of the random field σ_{H_E} is equivalent to the coefficient of variation and the resulting standard deviation of the Young's modulus is $\sigma_E = E_0 \, \sigma_{H_E}$. With this concept only uncorrelated material and geometrical parameters can be modeled, which was done in (Brenner 1995) for the Young's modulus, the mass density and the thickness in a linear elastic example and for the Young's modulus and the yield stress in another example describing a steel structure with an linear-elastic ideal-plastic material law. In (Ebert 2002) the same approach was used to model a random

Young's modulus and a random tensile strength of a concrete beam independently

$$
\begin{aligned}
E(\mathbf{x}_i) &= E_0 H_E(\mathbf{x}_i), \\
f_t(\mathbf{x}_i) &= f_{t_0} H_{f_t}(\mathbf{x}_i).
\end{aligned}
\tag{5.37}
$$

This means, that in these applications a random field for every parameter was defined, spectral decomposed and simulated separately.

For the modeling of material uncertainties in concrete structures the consideration of correlations between the different material parameters might be necessary. For this reason the concept of single-parameter random fields was extended in this work to a multi-parameter approach, which will be described as follows. The members of a single-parameter covariance matrix of random field read in terms of the coefficients of correlation

$$
\mathbf{C_{HH}}(i,j) = \sigma_H^2 \rho_{ij}.
\tag{5.38}
$$

This matrix has the size $n \times n$, where n is number of random variables, which is equivalent to the number of points, where the random field is discretized. The entries of this matrix are computed with the auto correlation function and depend only on the geometry of the investigated system. Thus this matrix is called in the following description geometric covariance matrix. In order to describe multi-parameter random fields here a constant predefined matrix is introduced, which describes the correlation between the several parameters at a certain point

$$
\mathbf{C_{PP}}(i,j) = \hat{\rho}_{ij}.
\tag{5.39}
$$

The size of $\mathbf{C_{PP}}$ is $m \times m$, with m as the number of correlated material parameters. The extended covariance matrix $\mathbf{C_{HH}^*}$ with size $m \cdot n \times m \cdot n$ is then obtained by multiplying the geometrical covariance matrix element-wise with the parameter correlation matrix

$$
\begin{aligned}
\mathbf{C_{HH}^*}((i-1)m + r, (j-1)m + s) &= \mathbf{C_{HH}}(i,j)\,\mathbf{C_{PP}}(r,s); \\
i,j &= 1, \ldots, n; \quad r,s = 1, \ldots, m,
\end{aligned}
\tag{5.40}
$$

which reads in terms of the coefficients of correlation

$$
\mathbf{C_{HH}^*}((i-1)m + r, (j-1)m + s) = \sigma_{Hr}\,\sigma_{Hs}\,\rho_{ij}\,\hat{\rho}_{rs}.
\tag{5.41}
$$

The total number of random variables of the extended random field is $m \cdot n$. In Eq. (5.41) varying standard deviations for the different parameters are assumed, which have to be considered in the Nataf transformation and the simulation of the uncorrelated random variables. This is similar for different distribution types of the parameters. Here a unique

standard deviation and distribution type for all parameters is taken for simplicity. Then the procedure presented in section 5.2.3 can be applied to the extended covariance matrix $\mathbf{C}^*_{\mathbf{HH}}$ in the same manner as for a single-parameter random field. The final correlated set of material parameters P_r of the extended random field H^* at an integration point i reads

$$
\begin{aligned}
P_1(\mathbf{x}_i) &= P_{1_0} H^*(\mathbf{x}_i, 1), \\
P_2(\mathbf{x}_i) &= P_{2_0} H^*(\mathbf{x}_i, 2), \\
&\vdots \\
P_m(\mathbf{x}_i) &= P_{m_0} H^*(\mathbf{x}_i, m).
\end{aligned}
\tag{5.42}
$$

In Table 5.3 the covariance matrix of simple random field with one and two parameters is assembled exemplarily and the corresponding eigenvalues and eigenvectors in the uncorrelated Gaussian space are displayed. The table indicates, that each eigenvector of the single-parameter field belongs to a symmetric and anti-symmetric eigenvector of the two-parameter field. The sum of the corresponding variances is twice the variance of the single-parameter eigenvector.

5.2.5 Adaptive transfer of random field data

During the crack growth algorithm the discretization, which is in general a regular finite element mesh, is adaptively changed by transforming finite elements to meshless zones and introducing new nodes during the crack growth procedure. Both, the transformation and the crack growth, need a rearrangement of the integration points. This requires an update of the initial random field data of the current sample. Here this is realized using an interpolation of a continuous field. The developing discontinuities in the investigated structure are neglected for this interpolation.

The random field data for new meshless zones are interpolated using the shape functions of the transformed finite elements. For the interpolation only this element is used, in which the new integration point is located. First the nodal values will be calculated from the element integration points. The values of the new point will be computed by using the natural coordinates r and s, which can be determined analytically for linear elements (Rehle 1996). If distorted higher order elements are used, which was not done in this work, an iterative method according to (Werkle and Gong 1993) can be applied.

Another possibility to obtain the random field data from the transformed elements, using the MLS interpolation scheme, was investigated only exemplarily for this case. This led to similar results as with the finite element shape functions, which will be shown in section 5.4.1, but with higher numerical effort, due to the more complex shape function computation.

For the integration point arrangement during the crack growth procedure, the random field data of the new points are obtained directly from the old integration points using
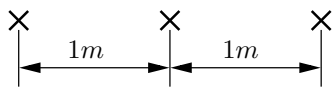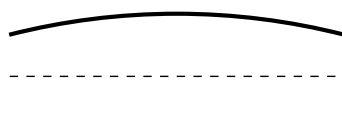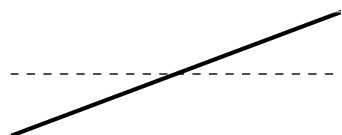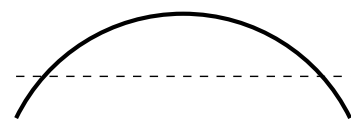
System

$l_H = 1m; \quad \sigma_H = 1; \quad R_{HH}(\|\boldsymbol{\xi}\|) = \exp\left(-\|\boldsymbol{\xi}\|\right)$

Random field with one parameter

$$\mathbf{C_{HH}} = \begin{bmatrix} 1.000 & 0.368 & 0.135 \\ 0.368 & 1.000 & 0.368 \\ 0.135 & 0.368 & 1.000 \end{bmatrix} = \boldsymbol{\Psi}\mathbf{C_{YY}}\boldsymbol{\Psi}^T$$

$\sigma_{Y_1}^2 = 1.593$ $\qquad\qquad \sigma_{Y_2}^2 = 0.865$ $\qquad\qquad \sigma_{Y_3}^2 = 0.543$

Random field with two parameters

$$\mathbf{C_{HH}^*} = \mathbf{C_{HH}^*}(\mathbf{C_{HH}}, \mathbf{C_{PP}}) = \boldsymbol{\Psi}^*\mathbf{C_{YY}^*}\boldsymbol{\Psi}^{*T}; \quad \mathbf{C_{PP}} = \begin{bmatrix} 1.000 & 0.500 \\ 0.500 & 1.000 \end{bmatrix}$$

$$\mathbf{C_{HH}^*} = \begin{bmatrix} 1.000 & 0.500 & 0.368 & 0.184 & 0.135 & 0.068 \\ 0.500 & 1.000 & 0.184 & 0.368 & 0.068 & 0.135 \\ 0.368 & 0.184 & 1.000 & 0.500 & 0.368 & 0.184 \\ 0.184 & 0.368 & 0.500 & 1.000 & 0.184 & 0.368 \\ 0.135 & 0.068 & 0.368 & 0.184 & 1.000 & 0.500 \\ 0.068 & 0.135 & 0.184 & 0.368 & 0.500 & 1.000 \end{bmatrix}$$

$\sigma_{Y_1}^{*2} = 2.388$ $\qquad\qquad \sigma_{Y_2}^{*2} = 1.297$ $\qquad\qquad \sigma_{Y_3}^{*2} = 0.815$

$\sigma_{Y_4}^{*2} = 0.796$ $\qquad\qquad \sigma_{Y_5}^{*2} = 0.432$ $\qquad\qquad \sigma_{Y_6}^{*2} = 0.271$

Table 5.3. Simple three-point Gaussian random field with one and two parameters and belonging covariance matrices and variances and eigenshapes in the uncorrelated space

the MLS interpolation with the regularized weighting type and linear polynomial basis independently of the applied interpolation scheme in the mechanical model. This was done by considering all integration points in the deleted triangle cells as supporting points of the interpolation.

5.3 Sampling strategies

5.3.1 Plain Monte Carlo Simulation

The standard Monte Carlo Simulation is a very simple and robust sampling strategy to estimate statistical properties of an investigated stochastic problem. The expected value $E[.]$ of a function $u(\mathbf{X})$ of a random vector $\mathbf{X}$ is defined as

$$v = \int_{-\infty}^{\infty} \ldots \int_{-\infty}^{\infty} u(\mathbf{X}) f_{X_1 \ldots X_K}(\mathbf{x}) dx_1 \ldots dx_K = E[u(\mathbf{X})], \tag{5.43}$$

where K is the number of members of $\mathbf{X}$. This expected value of $u(\mathbf{X})$ can be estimated using the mean value of the sample results

$$\hat{v} = \hat{E}[u(\mathbf{X})] = \frac{1}{N} \sum_{i=1}^{N} u(\mathbf{X}_i), \tag{5.44}$$

where $\mathbf{X}_i$ is the i-th sample of $\mathbf{X}$ and N is the number of samples, respectively. Eq. (5.44) is the basis principle of the Monte Carlo Simulation. This means, that N samples of the random vector $\mathbf{X}$ are computed using the joint density function $f_{X_1 \ldots X_K}(\mathbf{x})$, the function $u(\mathbf{X})$ is calculated for each sample separately and finally the estimated expected value is obtained. The estimator $\hat{v}$ is unbiased

$$E[\hat{v}] = E[u(\mathbf{X})] \tag{5.45}$$

and its variance is defined as

$$\sigma_{\hat{v}}^2 = \frac{1}{N} \sigma_{u(\mathbf{X})}^2, \tag{5.46}$$

where

$$\sigma_{u(\mathbf{X})}^2 = E[(u(\mathbf{X}))^2] - (E[u(\mathbf{X})])^2. \tag{5.47}$$

The statistical error e is a measure of the estimators accuracy

$$e = \frac{1}{\sqrt{N}} \frac{\sigma_{u(\mathbf{X})}}{E[u(\mathbf{X})]}. \tag{5.48}$$

The disadvantage of MCS is the large number of samples, which are necessary to obtain a sufficient accuracy of the estimation.

Monte Carlo samples are often obtained using a random generator, which computes uniformly distributed samples between zero and one. These samples can be transformed into the desired distribution type using the inverse distribution function.

5.3.2   Latin Hypercube Sampling

In this section the basic theory of Latin Hypercube Sampling is presented according to (Olsson et al. 2003) and (Ebert 2002). Latin Hypercube Sampling (LHS) has been first proposed by (McKay et al. 1979) and further developed in many studies, e.g. in (Florian 1992). LHS is a Monte Carlo Simulation with class stratification, a so-called Stratified Sampling Method. These methods can reach a sufficient accuracy by estimating statistical properties with only a few samples compared to plain MCS.

In this method the theoretical probability distribution of the independent base variables x_i is stratified in N classes D_j with uniform probability

$$P\left[x_i \in D_j\right] = \frac{1}{N}; \quad i = 1, ..., K; \quad j = 1, ..., N, \tag{5.49}$$

where K and N are equivalent to the number of base variables and to the number of computed LHS samples, respectively. For each class a representative value $\hat{x}_{ij}$ is simulated as follows:

First an $N \times K$ matrix $\mathbf{P}$ is assembled, where each of the K columns is a random permutation of $1, \ldots, N$. Then an $N \times K$ matrix $\mathbf{R}$ containing independent uniformly distributed random values between zero and one is simulated. The final sampling matrix $\mathbf{S}$ is then obtained as

$$\mathbf{S} = \frac{1}{N}(\mathbf{P} - \mathbf{R}). \tag{5.50}$$

The final values $\hat{x}_{ij}$ with the target marginal distribution are obtained by mapping the elements of $\mathbf{S}$ as

$$\hat{x}_{ij} = F_{x_j}^{-1}(s_{ij}). \tag{5.51}$$

A single sample of the random vector reads

$$\hat{\mathbf{x}}_i = [\hat{x}_{i1}, \hat{x}_{i2}, \ldots, \hat{x}_{ik}]^T. \tag{5.52}$$

In Fig. 5.1 a possible sampling for two random variables and five realization is shown according to (Olsson et al. 2003).

Between the columns of the permutation matrix $\mathbf{P}$ unrequested correlations can arise.

$$\mathbf{P} = \begin{bmatrix} 1 & 2 \\ 2 & 4 \\ 3 & 3 \\ 4 & 1 \\ 5 & 5 \end{bmatrix} \quad \mathbf{R} = \begin{bmatrix} 0.60 & 0.83 \\ 0.42 & 0.11 \\ 0.69 & 0.51 \\ 0.32 & 0.58 \\ 0.83 & 0.32 \end{bmatrix}$$

$$\Rightarrow \mathbf{S} = \begin{bmatrix} 0.08 & 0.23 \\ 0.32 & 0.78 \\ 0.46 & 0.50 \\ 0.74 & 0.08 \\ 0.83 & 0.94 \end{bmatrix}$$
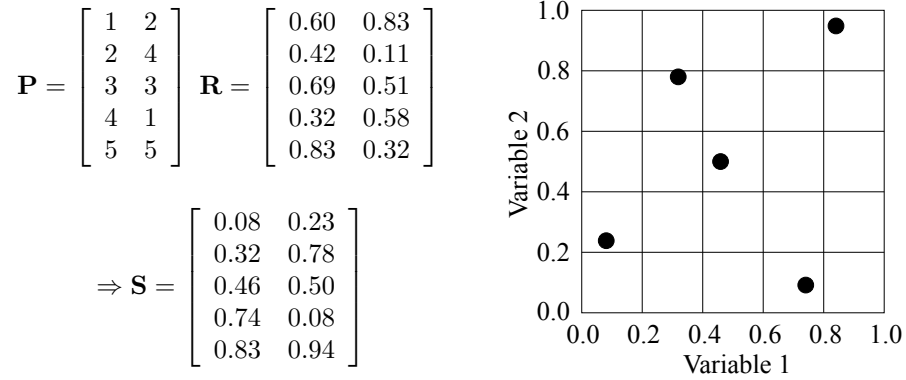
Figure 5.1. LHS sampling plan for two random variables with five realizations

In (Iman and Conover 1982) and (Novák and Shiraishi 1993) a method was proposed which reduces the correlations by reordering the permutation matrix as follows:

First the members of the permutation matrix p_{ij} are mapped on a standard normal distribution

$$y_{ij} = \Phi^{-1}\left(\frac{p_{ij}}{N+1}\right). \tag{5.53}$$

Then the covariance matrix of the obtained matrix $\mathbf{Y}$ is estimated and decomposed using Cholesky factorization

$$\bar{\mathbf{L}}\bar{\mathbf{L}}^T = \mathbf{C}_{\mathbf{YY}}. \tag{5.54}$$

A new matrix $\mathbf{Y}^*$ is obtained

$$\mathbf{Y}^* = \mathbf{Y}\bar{\mathbf{L}}^{-T}, \tag{5.55}$$

where the ranks of the elements of the columns of $\mathbf{Y}^*$ become the elements in the columns of the modified permutation matrix $\mathbf{P}^*$. The Cholesky factorization requires a positive definite matrix $\mathbf{C}_{\mathbf{YY}}$, which implies that the number of realization is higher than the number of random variables.

5.4   Examples

In this section three examples will be presented, where the first very simple example analyzes the quality of the random transformation. In the second one the probabilistic model is verified by means of a simple plain concrete beam with single crack growth, and in the final example multiple crack propagation in a reinforced concrete beam is analyzed.

5.4.1   Random field transformation

This example was chosen to investigate the quality of the random field data interpolation. The disc shown in Fig.5.2, which was discretized with 12×20 nine-node 2D solid-elements, was assumed to be the initial system. In the analysis the elements in the marked area were transformed to a meshless zone. The material data uncertainties were
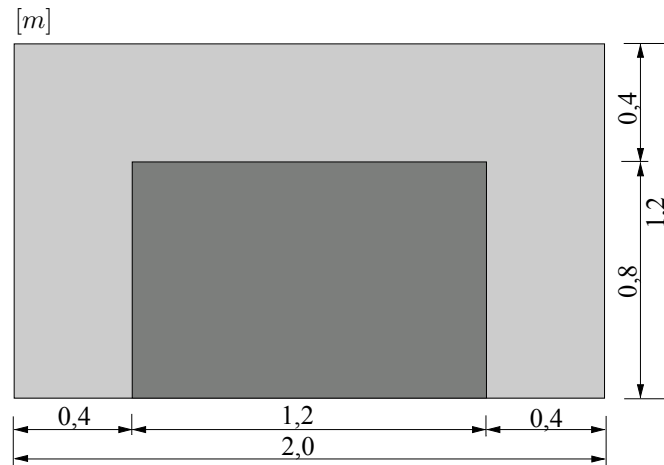

Figure 5.2. Simple plate with included transformation area

described by an isotropic random field with two log-normally distributed parameters, the Young's modulus and the mass density. By using the exponential correlation function, the correlation length was taken with $2m$, which is equivalent to the system length. The coefficients of variation were defined as $V_E = V_\rho = 0.2$ and the mean values were taken with $\bar{E} = 3.4 \cdot 10^{10} N/m^2$ for the Young's modulus and $\bar{\rho} = 3400 kg/m^2$ for mass density. The correlation coefficient between the two parameters was assumed to be $\hat{\rho}_{12} = 0.8$. The first 20 eigenvectors were used for the simulation of the random field, which represent the 4320 random variables with a quality of 93.1%. The transformed random field data obtained by using the FE-interpolation and the MLS-interpolation did not show visible differences among each other. In Fig.5.3 the original and the FE-transformed Young's modulus and mass density distributions for one sample are displayed. The figure indicates good agreement between the initial and the transformed distribution. The visible smoothing is caused by the higher integration point density in the new meshless component (four integration points per triangle integration cell).
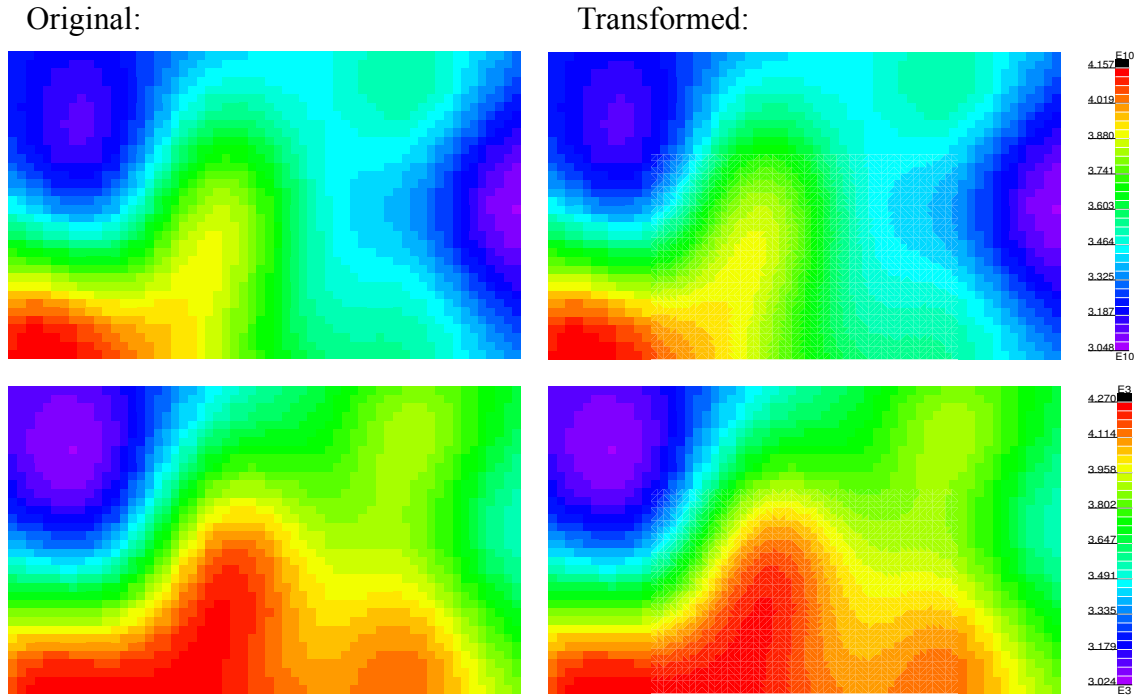
Original: Transformed:

Figure 5.3. Transformation of single random field sample describing the Young's modulus and mass density distribution

A statistical analysis was applied in order to quantify the errors due to the transformation procedure. Therefore the system was discretized with 3×5 nine-node and 6×10 four-node elements. By using a representation of 100% of the random field, the results of transformed random field discretization could be directly compared to an initial coupled FE-meshless random field. The statistical properties were evaluated by simulating 10^6 Monte Carlo samples. The elements of the transformed geometric correlation matrix $\mathbf{C}_{\mathbf{HH}}^{trans}$, which was computed from all MCS samples using Eq. (5.7), the coefficient of variation and the mean value of the random field and the correlation coefficient between the parameters are compared to the given values. The maximal absolute deviations for each investigated quantity are shown in Table 5.4. The results show, that both transfor-

	max $\Delta\mathbf{C}_{\mathbf{HH}}(i,j)$	max ΔV_H	max $\Delta\bar{H}$	max $\Delta\hat{\rho}_{12}$
FEM nine-node	0.04339	0.00377	0.00114	0.00320
MLS nine-node	0.05162	0.00703	0.00108	0.00118
FEM four-node	0.02827	0.00420	0.00173	0.00303
MLS four-node	0.02807	0.00405	0.00173	0.00304

Table 5.4. Maximum deviations of the statistical properties of the transformed random field

mation methods lead nearly to the same deviations. The interpolation errors in the statistical values, which have been computed at each integration point (coefficient of variation, mean value and parameter correlation coefficient), are one order of magnitude smaller than the errors in the elements of the correlation matrix, since the interpolation function can not reproduce the auto correlation function exactly. If more integration points are in the original random field, which are used for the interpolation, the correlation errors in

the transformed random field are reduced.

5.4.2   Three-point plain concrete beam

In this example the three-point bending beam with initial crack according to (Carpinteri et al. 1986), which was analyzed deterministically in section 4.5.4, was investigated by assuming random material properties. For this purpose a three parameter lognormally distributed random field with exponential correlation function was used to model the Young's modulus, the tensile strength and the Mode-I fracture energy as correlated parameters. The mean values of these three quantities have been taken as the deterministic values given in Fig. 4.34. The other material and geometrical parameters are assumed to be deterministic as the values given in section 4.5.4. The correlation length, the coefficients of variation and the parameter correlation coefficients have been taken with $l_H = 0.6m$, $V_E = V_{f_t} = V_{G_f^I} = 0.2$ and $\hat{\rho}_{12} = \hat{\rho}_{13} = \hat{\rho}_{23} = 0.8$, respectively.

The initial random field, which contains 4800 random variables (40×10 four-node finite elements, each having 4 integration points with 3 random parameters) was modeled with the largest 30 eigenvalues and belonging eigenvectors, which is equivalent to a representation of 95.84%. In Fig. 5.4 one realization of the random field is shown.
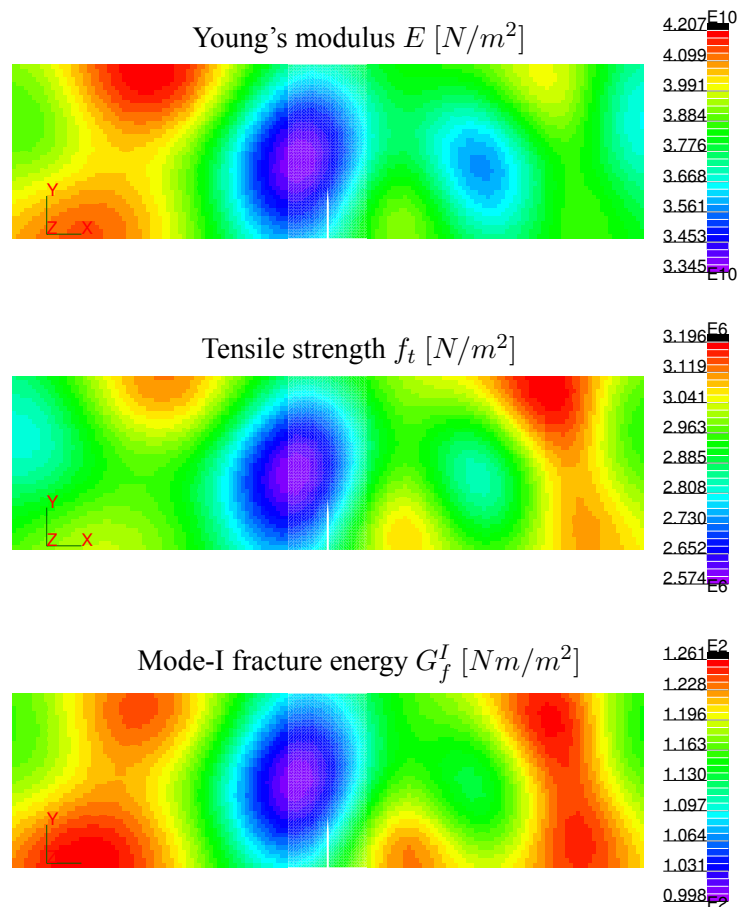

Figure 5.4. Single three parameter random field sample for the three-point bending beam

The stochastic analysis has been carried out by calculating the load displacement

curves of 10000 plain Monte Carlo Simulations of the 30 uncorrelated random variables. In Fig. 5.5 the statistical curves (mean value and standard deviation) are shown in comparison to the deterministic curve.
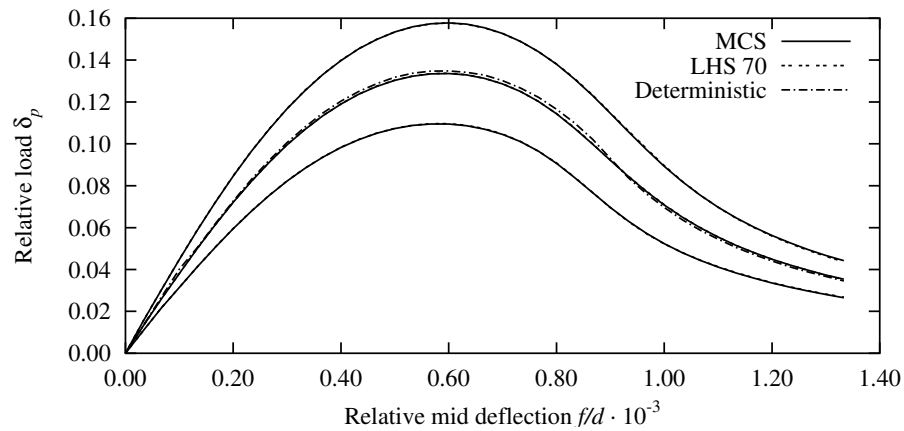

Figure 5.5. Statistical load displacement curves (mean values and mean values $\pm$ standard errors) of three point bending beam using Monte Carlo Simulation and Latin Hypercube Sampling

In a next step the analysis was performed by using Latin Hypercube Sampling with different numbers of samples. In Table 5.5 the investigated number of samples with the corresponding undesired maximum correlations between the 30 random variables are given. The table indicates, that for 10, 20 and 30 samples these correlations are very large and for 50 and more samples the errors are small enough to represent the statistical behavior sufficient accurate. In Fig. 5.5 the statistical curves obtained with 70 LHS samples are shown, which agree excellent with the MCS curves. This shows, that LHS can be successfully applied to crack propagation problems to obtain the statistical characteristics of the complete structural response with only a small number of samples.

Number of LHS samples	10	20	30	50	70	100	200
Maximum undesired correlation	0.8667	0.7023	0.4852	0.0262	0.0151	0.0118	0.0052

Table 5.5. Investigated number of Latin Hypercube Samples with corresponding maximum undesired correlation between the 30 independent random variables

In further investigations the histograms of the relative load have been determined for the MCS results for the relative mid deflections of 0.0001, 0.0007 and 0.0013, which belongs to the elastic part, to the middle and to the end of the load displacement curves and for the maximum relative load. These histograms are shown in Fig. 5.6. Additionally the probability density functions (PDFs) by assuming a lognormal distribution are shown using the indicated mean values and standard deviations obtained from the 10000 samples. The histograms and the PDFs agree very well, thus the distribution type of the relative load is nearly lognormal. Furthermore the PDFs obtained using the mean values and standard deviations of 70 LHS samples are shown, which almost exactly agree with the PDFs of the MCS.

Finally the mean value and the standard deviation of the peak load have been calculated for all LHS simulations and for the MCS samples by using an increasing number of samples. The obtained values are displayed in Fig. 5.7 depending on the number of samples. As indicated in the figure, Latin Hypercube Sampling gives very good results for the mean value with a much smaller number of samples (more than 20) as the MCS. For a well approximated standard deviation more than 50 samples are necessary, which is still a small number compared to the required number of MCS samples.
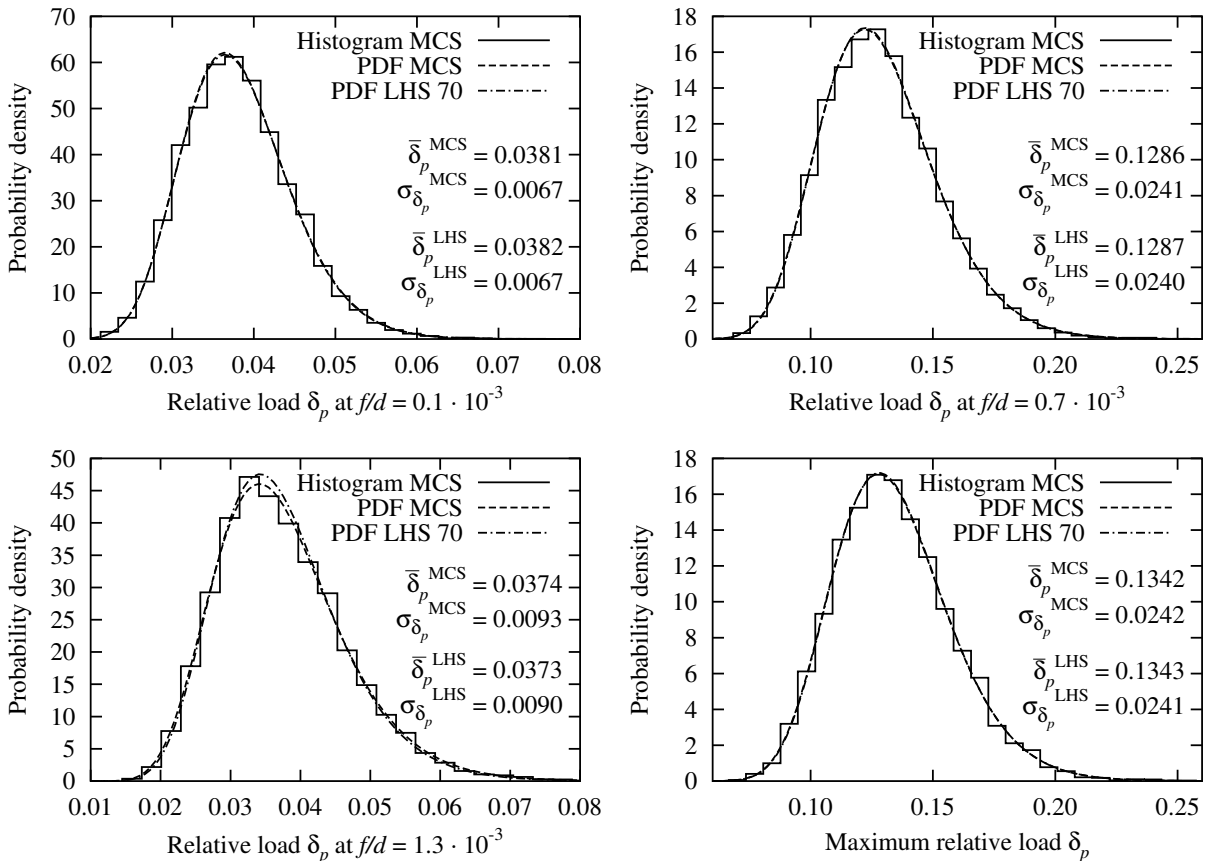

Figure 5.6. Histograms of the MCS samples and probability density functions of the MCS and LHS samples using the indicated statistical values and a lognormal distribution
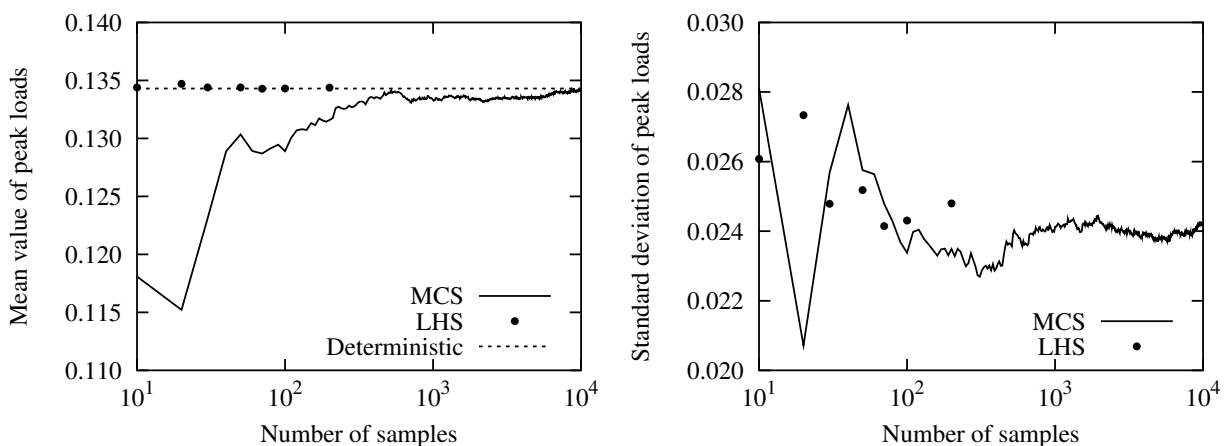

Figure 5.7. Calculated mean values and standard errors of the peak load depending on the number of samples for Monte Carlo Simulation and Latin Hypercube Sampling

5.4.3 Four-point reinforced concrete beam

In this final example the applicability of the presented stochastic model to multiple crack growth will be shown. For this purpose an experimentally investigated reinforced concrete beam (Ebert and Bucher 2002) was analyzed numerically in order to represent the statistical behavior of the structural response. Fig. 5.8 shows the test setup with loading and boundary conditions. The indicated material parameters have been estimated in (Ebert and Bucher 2002) according to the CEB-FIB Model Code (Telford 1993).
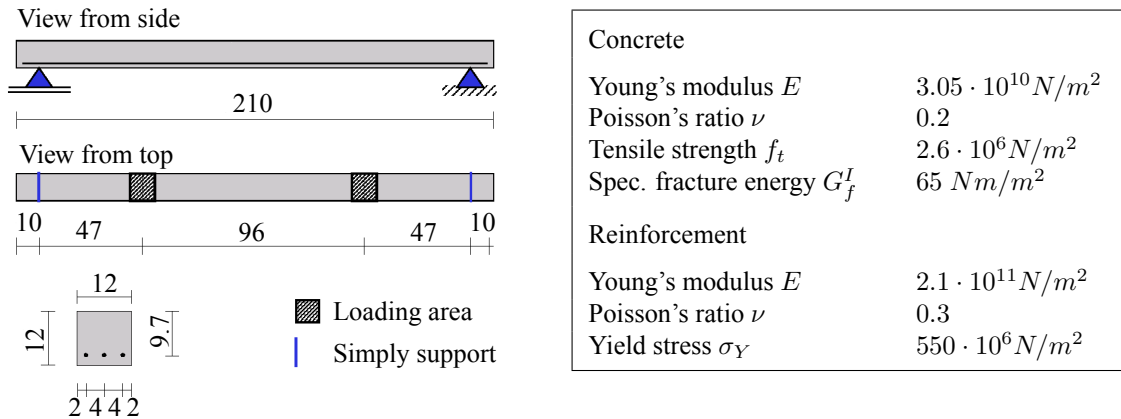

Figure 5.8. Simply supported reinforced concrete beam (Ebert and Bucher 2002, dimensions in *cm*), system properties and mean and deterministic values of the material parameters

In the experimental tests 20 beams reinforced with 3 bars with a diameter of $10mm$ have been analyzed load controlled and their mid deflection was measured depending on the applied external load F. In Fig. 5.9 the obtained histogram of the mid deflection for the first load step with $F = 2500N$ is shown. In order to define a distribution type for the numerical analysis different common types have been investigated. Their probability density functions obtained with the experimental mean value and standard deviation are given additionally in Fig. 5.9. The lognormal PDF shows the best agreement with the experimental histogram. Thus a lognormally distributed random field was used in the numerical analysis. Within this analysis the Young's modulus, the tensile strength and the specific fracture energy of the concrete were assumed to be the three correlated random field parameters. The parameter correlation coefficients were taken as $\hat{\rho}_{12} = \hat{\rho}_{13} = 0.8; \hat{\rho}_{23} = 1.0$, which means, that the tensile strength and the specific fracture energy are fully correlated. All other material parameters of the concrete and the properties of the reinforcement were assumed to be deterministic. The initial discretization of the concrete was done by using 10×168 four-node finite elements and the reinforcement was modeled with 168 bar elements. Thus the initial random field consists of 13440 random variables. The crack growth simulation was carried out using the Mode-I cohesive crack model with exponential softening, since the middle part of the beam is subjected to an almost constant moment, which led to mainly Mode-I cracks in the experiments. The parameters for the bond model were taken from Eq. (4.74) as $\Delta \bar{u}_\tau = 0.06mm$ and

$\Delta \tilde{u}_\tau = 0.18 mm$.

Different values for the correlation length l_H and the coeffcient of variation have been used for the investigations, which are given in Table 5.6. The coeffcient of variation for the case with $l_H = 0.5m$ has been taken in order to obtain almost the same standard deviation at $F = 2500N$ as with $l_H = 2.1m$ and $V_E = V_{f_t} = V_{G_f^I} = 0.25$. The number of random variables has been reduced as presented in section 5.2.3 and Latin Hypercube Sampling was applied to simulate the random field. The number of considered eigenvectors of the random field and the used number of LHS samples are given in Table 5.6. In Fig. 5.9 the

	Experimental	Numerical		
Correlation length l_H	-	$0.5\,m$	$2.1\,m$	$2.1\,m$
Coeffcents of variation $V_E = V_{f_t} = V_{G_f^I}$	-	0.30	0.25	0.35
Number of used random variables	-	50	20	20
Representation quality	-	0.9434	0.9748	0.9748
Number of LHS samples	-	70	30	30
Maximum undesired correlation	-	0.0325	0.0519	0.0519
Mean mid deflection at $F = 2500N$	$0.8459\,mm$	$0.5862\,mm$	$0.5692\,mm$	$0.6087\,mm$
Standard deviation at $F = 2500N$	$0.1809\,mm$	$0.1237\,mm$	$0.1179\,mm$	$0.1878\,mm$

Table 5.6. Investigated sets of correlation length and coefficient of variation and calculated corresponding quantities

obtained numerical histogram for $l_H = 0.5m$ is displayed for the first load step, which shows good agreement with the equivalent lognormal probability density function.
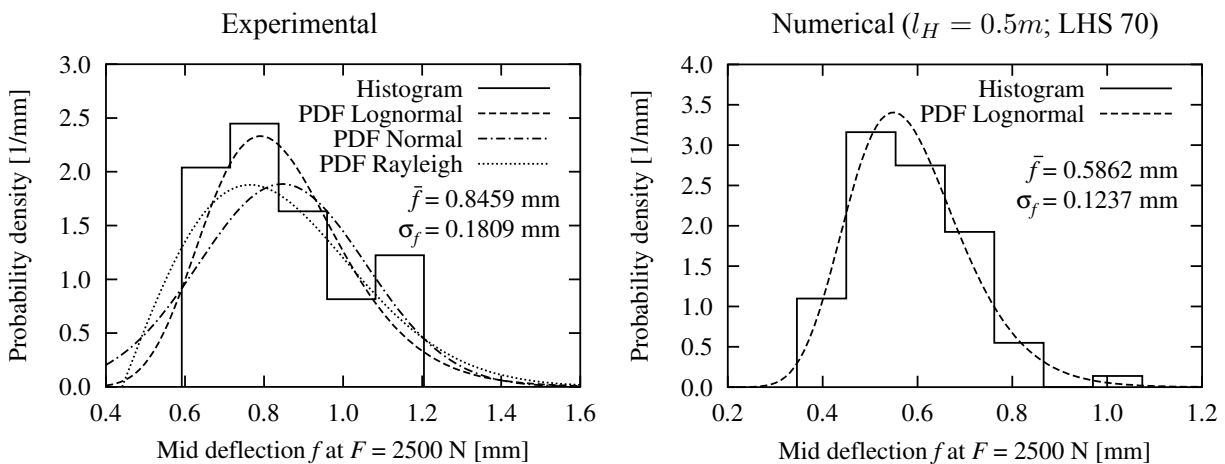
Figure 5.9. Histogram of experimental mid deflections and assumed probability density functions for different distribution types and of numerical mid deflections with lognormal PDF

The crack development in the numerical simulation is shown for several load steps in Fig. 5.10 for one random field sample. The figure indicates, that in two weak zones the first cracks occur and with further increasing load the middle part of the beam is cracked almost uniformely. In the final state at $F = 21000N$ the numerical crack pattern shows good agreement with the experimental crack geometries but the detailed crack branching

and intersection observed in the experiments, which is caused by the local inhomogenity, is not represented in the numerical model. An explicit representation of the cement matrix and aggregates could model such a crack development, but this was not the aim of this work, since the global cracking behavior can be represented sufficient accurate with a homogenized concrete model. In Fig. 5.10 the initial and transformed random fields are compared, which agree very well.

Young's modulus distribution
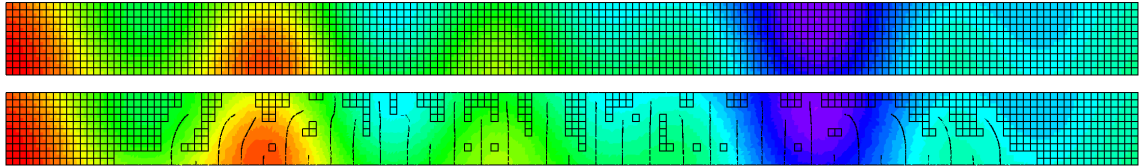
Tensile strength and fracture energy distribution
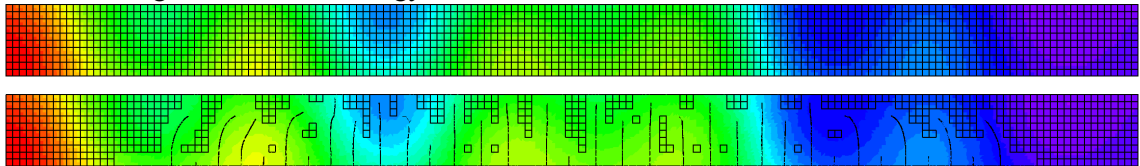
$F = 4000N$
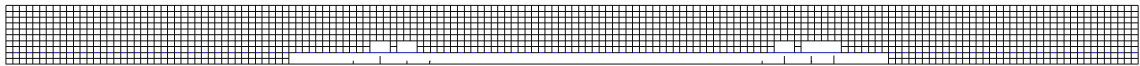
$F = 5000N$
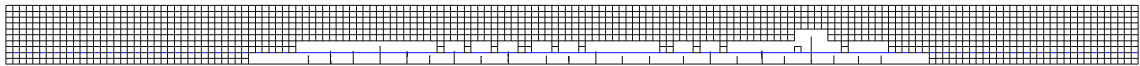
$F = 6000N$
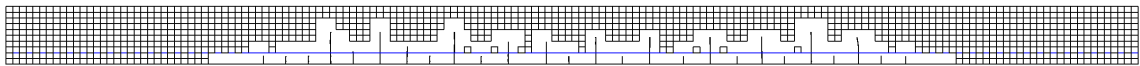
$F = 9000N$
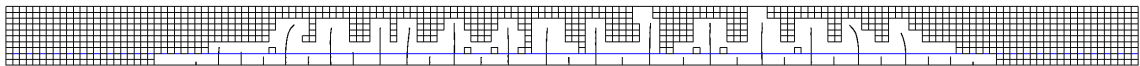
$F = 14000N$
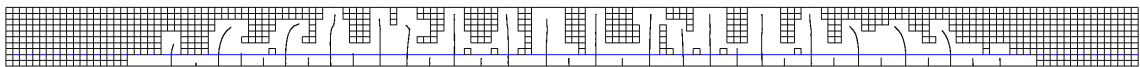
$F = 21000N$
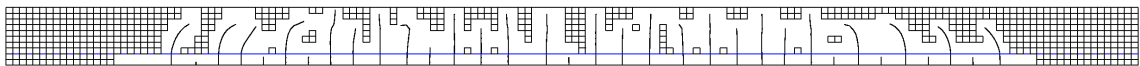
Experiment ($F = 18000N$)
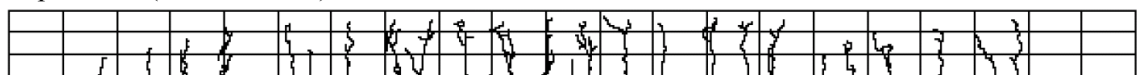
Figure 5.10. Initial and final random field sample and crack development with increasing load compared to experimental crack patterns

Finally the experimental and numerical load displacement curves have been statistically analyzed and the obtained mean values and standard deviations of the mid deflection depending on the external load are given in Fig. 5.11. The calculated curves of the mean values of all numerical simulations are almost similar and show good agreement with the

experimental mean deflections. The experimental standard deviations are in between the numerical values, but the hump in the numerical curves between 4 and $8 kN$ was not obtained in the experimental function. The numerical cases with $l_H = 0.5m$ and $V_H = 0.3$ and with $l_H = 2.1m$ and $V_H = 0.25$ led to almost the same curves for the standard deviation, which is a very interesting result.

The deviation of the numerical results from the experimental curve may be caused by the fact, that the fracture parameters and/or the standard deviations of these quantities have been overestimated. Another possibility may be, that the fluctuation inside of a single random field sample is smaller than assumed. In this case the crack development, which is asymmetric at the beginning of the numerical simulations, would be almost symmetric and the standard deviation would be decreased. Nevertheless the numerical results show, that the developed stochastic crack growth algorithm is an useful method for the modeling of such problems.

Figure 5.11. Experimental and numerical mean value and standard deviation of the mid deflection using different correlation lengths l_H and coefficients of variation (COV)

Chapter 6

Conclusions

The research activities in the frame work of this dissertation attempted to develop an automatic algorithm for the numerical simulation of multiple cracking in reinforced concrete structures. It was intended that this method be applicable to systems in the dimension of structural members. For this purpose three main points had to be solved in this work. The firs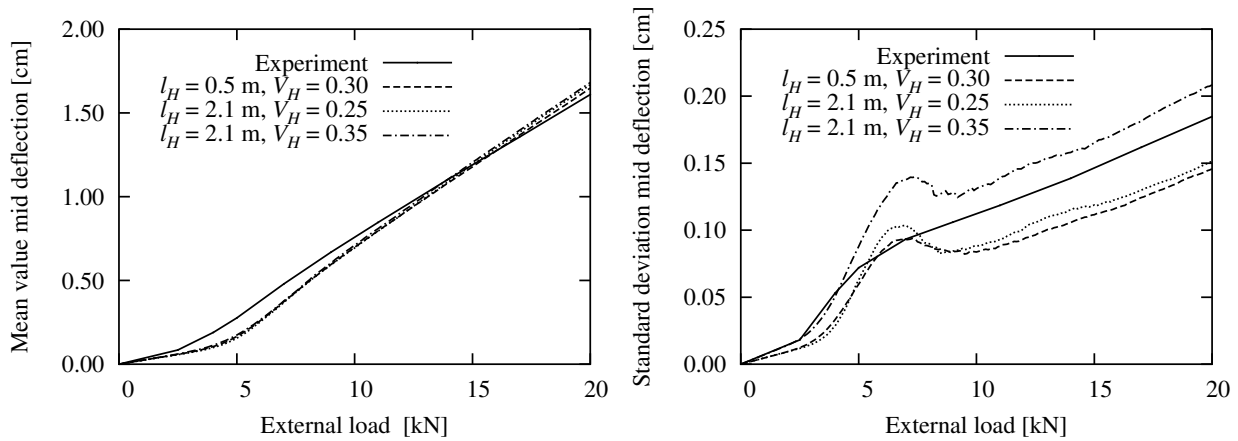t problem was the flexible representation of crack discontinuities. The second one was the stable modeling of the concrete fracture process which should be almost independent of the discretization. The consideration of fluctuations in the material properties, which are higher for concrete than for other materials, was the third point.

The representation of the growing crack discontinuities was achieved by using an adaptively coupled discretization, where the regions without crack growth were modeled by standard finite elements and the regions where cracks develop were discretized using meshless interpolation schemes. For this purpose two different meshless methods were improved and adapted. The first method is the Element-free Galerkin Method, which uses the Moving Least Squares approach. The MLS method is not a true interpolation and the imposition of the essential boundary conditions and the coupling with finite elements could be realized in existing studies only with additional effort. In this work a new weighting function type was introduced, which leads to an interpolation with fulfillment of the interpolation property at very high accuracy. In the numerical examples it could by shown that by using this weighting type, the results are relatively independent of the choice of the nodal influence domain and of an applied distortion of discretization in strong contrast to the standard weighting types. The interpolation was further improved by a special boundary blending, which leads to a linear precision along the boundaries. Thus a compatible coupling with finite elements could by achieved.

The second meshless interpolation scheme was the Natural Neighbor Interpolation, which is based on a Voronoi diagram of the nodal domain. This method was adapted to non-convex domains in order to enable its application in crack growth simulations. In the implemented two-dimensional algorithm this interpolation method was more efficient than the MLS scheme, due to the smaller number of influencing nodes and the

simpler shape function computation. But on the other hand this method requires an adaptation of the nodal configuration with corresponding Voronoi diagram in a crack growth simulation. In the realized 2D algorithm this did not lead to any remarkable efficiency decrease, but the extension for the three-dimensional case is much more complex than using the improved MLS interpolation where the moving discontinuity does not require such an adaptation. Nevertheless the developed improvements for both interpolation schemes present an important step in the research dealing with meshless methods.

For the representation of the cracking behavior of concrete on the macro scale an existing improved cohesive crack model was adapted for use in an automatic simulation. This model can reproduce the fracture process under mixed-mode loading very well, which leads to significantly better predictions in the numerical examples than the standard model. In this work the integration of the improved model in an energy-based criterion for crack growth was achieved for the first time. This criterion gives very stable results for coarse discretization levels due to the evaluation of energy quantities. For the determination of the crack direction a combined criterion using nonlocal stress and energy quantities was developed. It could be shown that this criterion leads to good results, but due to the used stress values the discretization has some requirements. The development of an efficient pure energy-based criterion for the crack direction is a field for further research.

The application of the developed crack growth algorithm in combination with a standard macroscopic law, describing the bond behavior between reinforcement and concrete, led to very good results for reinforced concrete systems, which was shown in the numerical examples. Thus an improvement of this model was not intended.

The random field concept was used in order to model the fluctuations of the concrete properties. Thus an application to the coupled finite element-meshless discretization could by realized directly using the interpolation point method for an isotropic homogenous random field. The standard single parameter concept was extended to an arbitrary number of correlated material parameters assuming the pointwise correlation to be constant. The modeling of spatial fluctuating correlation coefficients was not necessary in the opinion of the author. For the implementation of the probabilistic model the distribution types and the coefficients of variation of these parameters were assumed to be uniform. This assumption allowed for a simple extension of the single parameter concept. The consideration of varying distribution types and coefficients of variation was discussed. For the material parameters a lognormal distribution type was assumed, which led to good agreement with the measured data in the final example. However, the stochastic random field parameters such as the coefficient of variation and the correlation length were chosen without experimental background due to missing data. For this reason an experimental program was initialized in the final period of the Collaborative Research Center at the Bauhaus-University, where the initial distribution of Young's modulus and the cor-

responding crack development shall be measured. These data might lead to an improved estimation of the stochastic parameters.

The presented algorithm gives a good basis for the reliability analysis of reinforced concrete structures. Due to the applied reduction of the number of random variables, it is possible to apply approximation techniques such as the response surface method or neural networks. For systems of larger size such an approximation seems to be essential. Viscous effects in the constitutive laws and crack models might be considered in order to use dynamic measurements as advance information in such an analysis. Furthermore the modeling of lifetime influencing phenomena such as corrosion of the reinforcement could be an important enhancement of the numerical analysis. This might be achieved with minor effort, since the discrete crack simulation can provide the crack openings and other required information directly.

References

Amestoy, P. R., I. J. Duff, J.-Y. L'Excellent, and J. Kloster (2003). *MUltifrontal Massively Parallel Solver* (4.3 ed.). Toulouse, France: ENSEEIHT-IRIT.

Anderson, T. L. (1991). *Fracture Mechanics*. CRC Press, Boca Raton.

Anderson, E. et al. (1995). *LAPACK Users' Guide* (second ed.). Philadelphia, PA: Society for Industrial and Applied Mathematics.

Argyris, J. H. and S. Kelsey (1954). Energy theorems and structural analysis. *Aircraft Engineering 26, 27*, 347–356, 383–387.

Arrea, M. and A. R. Ingraffea (1982). Mixed-mode crack propagation in mortar and concrete. Report 81-13, Department of Structural Engineering, Cornell University.

Atluri, S. N. and T. Zhu (1998). A new Meshless Local Petrov- Galerkin (MLPG) approach in computational mechanics. *Computational Mechanics 22*, 117–127.

Babuška, I., U. Banerjee, and J. E. Osborn (2002). Survey of meshless and generalized finite element methods: A unified approach. Technical Report 02-40, TICAM, The University of Texas at Austin.

Barnand, S. T., A. Pothen, and H. D. Simon (1993). A spectral algorithm for envelope reduction of sparse matrices. In *Proceedings Supercomputing 1993*.

Barsoum, R. S. (1974). Application of quadratic isoparametric finite elements in linear elastic fracture mechanics. *International Journal of Fracture 10*, 603–605.

Bathe, K.-J. (1996). *Finite Element Procedures*. Englewood Cliffs: Prentice Hall.

Bažant, Z. P. and G. Pijaudier-Cabot (1988). Nonlocal continuum damage, localization, stability and convergence. *Journal of Applied Mechanics 55*, 287–293.

Bažant, Z. P. and J. Planas (1998). *Fracture and Size Effect in Concrete and other Quasibrittle Materials*. New York: CRC Press.

Beissel, S. and T. Belytschko (1996). Nodal integration of the element-free Galerkin method. *Computer Methods in Applied Mechanics and Engineering 139*, 49–74.

Belikov, V. V., V. D. Ivanov, V. K. Kontorovich, S. A. Korytnik, and A. Y. Semenov (1997). The non-sibsonian interpolation: a new method of interpolation of the values of a function on an arbitrary set of points. *Computational Mathematics and Mathematical Physics 37*, 9–15.

Belytschko, T. and T. Black (1999). Elastic crack growth in finite elements with minimal remeshing. *International Journal for Numerical Methods in Engineering 45*, 601–620.

Belytschko, T., J. Fish, and B. E. Engelmann (1988). A finite element with embedded localization zones. *Computer Methods in Applied Mechanics and Engineering 70*, 59–89.

Belytschko, T., L. Gu, and Y. Y. Lu (1994). Fracture and crack growth by element-free Galerkin methods. *Modelling and Simulation in Material Science and Engineering 2*, 519–534.

Belytschko, T., Y. Krongauz, M. Fleming, D. Organ, and W. K. Liu (1996). Smoothing and accelerated computations in the Element-free Galerkin Method. *Journal of Computational and Applied Mathematics 74*, 111–126.

Belytschko, T., Y. Krongauz, D. Organ, M. Fleming, and P. Krysl (1996). Meshless methods: an overview and recent developments. *Computer Methods in Applied Mechanics and Engineering 139*, 3–48.

Belytschko, T., Y. Y. Lu, and L. Gu (1994). Element-free Galerkin methods. *International Journal for Numerical Methods in Engineering 37*, 229–256.

Blackford, L. S. et al. (1997). *ScaLAPACK User's Guide*. SIAM Press.

Bourgund, U. and C. Bucher (1986). Importance sampling procedure using design points - ISPUD - a user's manual. Report 8-86, Institute of Engineering Mechanics, University of Innsbruck, Austria.

Brenner, C. E. (1995). *Ein Beitrag zur Zuverlässigkeitsanalyse von Strukturen unter Berücksichtigung von Systemuntersuchungen mit Hilfe der Methode der Stochastischen Finite Elemente*. Ph. D. thesis, University of Innsbruck, Austria.

Bronstein, I. N. and K. A. Semendjajew (1979). *Taschenbuch der Mathematik*. Leipzig und Moskau: BSB B.G. Teubner Verlagsgesellschaft und Verlag Nauka.

Bucher, C. and U. Bourgund (1990). A fast and efficient response surface approach for structural reliability problems. *Structural Safety 7*, 57–66.

Bucher, C. and M. Ebert (2000). Load carrying behavior of prestressed bolted steel flanges considering random geometrical imperfections. In Kareem et al. (Eds.), *Proc. 8th ASCE Specialty Conf. on Prob. Mech. and Struct. Rel., Notre Dame, Indiana, USA; July 24-26*. Rotterdam: Balkema.

Bucher, C. and M. Macke (2004). Response surface for reliability assessment. In E. Nikolaidis and D. Ghiocel (Eds.), *Structural Reliability Handbook*, Chapter 19. CRC Press.

Bucher, C. G. (1988). Adaptive sampling - an iterative fast Monte Carlo procedure. *Structural Safety 5*, 119–126.

Bucher, C. et al. (2002). SLang -*The Structural Language* (5.0 ed.). Institute of Structural Mechanics, Bauhaus-University of Weimar, Germany.

Carol, I., P. C. Prat, and C. M. López (1997). Normal/shear cracking model: Application to discrete crack analysis. *Journal of Engineering Mechanics ASCE 123*, 765–773.

Carpinteri, A., A. Di Tommaso, and M. Fanelli (1986). Influence of material parameters and geometry on cohesive crack propagation. In F. Wittmann (Ed.), *Fracture Toughness and Fracture Energy of Concrete - Proc. Int. Conf. on Fracture Mechanics of Concrete, Lausanne, Switzerland, October 1-3, 1985*. Amsterdam: Elsevier.

Červenka, V. (1998). Simulation of shear failure modes of R/C structures. In R. de Borst, N. Bićanić, H. Mang, and G. Meschke (Eds.), *Computational Modelling of Concrete Structures - Proc. Europ. Conf. EURO-C 1998, Bad Gastein, Austria, 31 March - 3 April, 1998*. Rotterdam: Balkema.

Červenka, V. and R. Pukl (2003). *ATENA Program documentation*. Prague, Czech Republic: Červenka consulting.

Chen, J.-S., C.-T. Wu, S. Yoon, and Y. You (2001). A stabilized conforming nodal integration for galerkin mesh-free methods. *International Journal for Numerical Methods in Engineering 50*, 435–466.

Cornelissen, H. A. W., D. A. Hordijk, and H. W. Reinhardt (1986). Experimental determination of crack softening characteristics of normal and lightweight concrete. *HERON 31*, 45–56.

Crisfield, M. A. (1981). A fast incremental iterative solution procedure that handles snapthrough. *Computers and Structures 13*, 55–62.

Crisfield, M. A. (1983). An arc-length method including line searches and accelerations. *International Journal for Numerical Methods in Engineering 19*, 1269–1289.

Cueto, E., M. Doblare, and L. Gracia (2000). Imposing essential boundary conditions in the natural element method by means of density-scaled alpha-shapes. *International Journal for Numerical Methods in Engineering 49*, 519–546.

Cuthill, E. and J. McKee (1969). Reducing the bandwidth of sparse symmetric matrices. In *24th Nat. Conf. Assoc. Comp. Mech. - ACM*, pp. 157–172.

Davis, T. A., P. Amestoy, and I. S. Duff (1994). An approximate minimum degree ordering algorithm. Technical report TR-94-039, Comp. Inform. Sciences Dept., University of Florida.

De, S. and K. J. Bathe (2000). The method of finite spheres. *Computational Mechanics 25*, 329–345.

De, S. and K. J. Bathe (2001a). The method of finite spheres with improved numerical integration. *Computers and Structures 79*, 2183–2196.

De, S. and K. J. Bathe (2001b). Towards an efficient meshless computational technique: the method of finite spheres. *Engineering Computations 18*, 170–192.

Doerr, K. (1980). *Ein Beitrag zur Berechnung von Stahlbetonscheiben unter besonderer Berücksichtigung des Verbundverhaltens*. Ph. D. thesis, TH Darmstadt.

Dolbow, J. and T. Belytschko (1999). Numerical integration of the galerkin weak form in meshfree methods. *Computational Mechanics 23*, 219–230.

Dongarra, J. and R. van de Geijn (1991). Two dimensional basic linear algebra communication subprograms. Technical Report CS-91-138, Computer Science Dept., University of Tennessee, Knoxville.

Duarte, C. A. (1995). A review of some meshless methods to solve partial differential equations. Technical Report 95-06, TICAM, The University of Texas at Austin.

Duarte, C. A. and J. T. Oden (1996). An h-p adaptive method using clouds. *Computer Methods in Applied Mechanics and Engineering 139*, 237–262.

Dumstorff, P. and G. Meschke (2004). Investigation of crack growth criteria in the context of the Extended Finite Element Method. In P. Neittaanmäki et al. (Eds.), *Proc. 4th European Congress on Computational Mechanics in Applied Sciences and Engineering (ECCOMAS), Jyväskylä, Finland, July 24-28, 2004*. University of Jyväskylä.

Dunavant, D. A. (1985). High degree efficient symmetrical gaussian quadrature rules for the triangle. *International Journal for Numerical Methods in Engineering 21*, 1129–1148.

Ebert, M. (2002). *Experimentelle und numerische Untersuchung des dynamischen Tragverhaltens von Stahlbetontragwerken unter Berücksichtigung stochastischer Eigenschaften*. Ph. D. thesis, Bauhaus-University Weimar, Germany.

Ebert, M. and C. Bucher (2002). Damage effects on the dynamic properties of R/C beams - experimental and numerical investigations. In H. Grundmann and G. Schuëller (Eds.), *Proc. 5th European. Conf. on Structural Dynamics (EURODYN), Munich, Germany, September 2-5, 2002*. Rotterdam: Balkema.

Erdogan, F. and G. C. Sih (1963). On the crack extension in plate under in plane loading and transverse shear. *Journal of Basic Engineering 85(4)*, 519–527.

Feist, C. (2003). *Numerical Simulations of Localization Effects in Plain Concrete*. Ph. D. thesis, University of Innsbruck, Austria.

Feist, C., W. Kerber, H. Lehar, and G. Hofstetter (2004). A comparative study of numerical models for concrete cracking. In P. Neittaanmäki et al. (Eds.), *Proc. 4th European Congress on Computational Mechanics in Applied Sciences and Engineering (ECCOMAS), Jyväskylä, Finland, July 24-28, 2004*. University of Jyväskylä.

Fleming, M. A. (1997). *The Element-free Galerkin Method for fatique and quasi-static fracture*. Ph. D. thesis, Northwestern University, Evanston, Illinois.

Florian, A. (1992). An efficient sampling scheme: Updated Latin Hypercube Sampling. *Probabilistic Engineering Mechnics 7*, 123–130.

Fortune, S. (1995). *Computing in Euclidean Geometry*, Volume 1 of *Lecture Notes Series on Computing*, pp. 193–233. Du, D.-Z. and Hwang, F.K.

Fries, T. P. and H. G. Matthies (2003). Classification and overview of meshfree methods. Informatikbericht 2003-3, Technical University Braunschweig, Brunswick, Germany.

Fuhlrott, A. (2004). Implementierung der X-FEM in SLang und Verifizierung der Anwendbarkeit für Rissberechnungen. Master's thesis, Bauhaus-University, Weimar, Germany.

Galerkin, B. G. (1915). Reihenentwicklung für einige Fälle des Gleichgewichtes von Platten und Balken. *Wjestnik Ingenerow Petrograd 10*.

Gálvez, J., J. Červenka, D. A. Cendón, and V. Saouma (2002). A discrete crack approach to normal/shear cracking of concrete. *Cement and Concrete Research 32*, 1567–1587.

Geist, A. et al. (1994). *PVM: Parallel Virtual Machine. A Users' Guide and Tutorial for Networked Parallel Computing*. Cambridge, MA: MIT Press.

Gonzáles, D., E. Cueto, M. A. Martínez, and M. Doblaré (2004). Numerical integration in natural neighbour galerkin methods. *International Journal for Numerical Methods in Engineering 60*, 2077–2104.

Green, P. J. and R. R. Sibson (1978). Computing dirichlet tessellations in the plane. *The Computer Journal 21*, 168–173.

Griffith, A. A. (1921). The phenomena of rupture and flows in solids. *Philos. T. Roy. Soc. A 221*, 163–197.

Gupta, A. and H. Akbar (1984). Cracking in reinforced concrete analysis. *Journal of Structural Engineering ASCE 110*, 1735–1746.

Hanson, R., F. Krogh, and C. Lawson (1973). A proposal for standard linear algebra subprograms. ACM SIGNUM Newsletter 8.

Hao, S., H. S. Park, and W. K. Liu (2002). Moving particle finite element method. *International Journal for Numerical Methods in Engineering 53*, 1937–1958.

Hassanzadeh, M. (1990). Determination of fracture zone properties in mixed mode I and mode II. *Engineering Fracture Mechanics 35*, 845–853.

Häussler-Combe, U. (2001). *Elementfreie Galerkin-Verfahren: Grundlagen und Einsatzmöglichkeiten zur Berechnung von Stahlbetontragwerken*. Habilitationthesis, University of Karlsruhe, Germany.

Hegen, D. (1997). *Element-free Galerkin Method for crack propagation in brittle materials*. Ph. D. thesis, Technische Universiteit, Eindhoven.

Hellen, T. K. (1975). On the method of virtual crack extensions. *International Journal for Numerical Methods in Engineering 9*, 187–207.

Hellweg, H.-B. and M. A. Crisfield (1998). A new arc-length method for handling sharp snap-backs. *Computers and Structures 66*, 705–709.

Herrmann, L. R. (1976). Laplacian-isoparametric grid generation scheme. *J. Eng. Mech. Division, ASCE 102*, 749–756.

Hillerborg, M., M. Modeer, and P. E. Peterson (1976). Analysis of crack formation and crack growth in concrete by means of fracture mechanics and finite elements. *Cement and Concrete Research 6*, 773–782.

Hurtado, J. E. and D. A. Alvarez (2001). Neural-network-based reliability analysis: a comparative study. *Computer Methods in Applied Mechanics and Engineering 191*, 113–132.

Hussain, M., S. Pu, and J. Underwood (1974). Strain energy release rate for a crack under combined mode I and mode II. *ASTM, STP 560*, 2–28.

Hwang, C. G., P. A. Wawrzynek, and A. R. Ingraffea (2005). On the calculation of derivatives of stress intensity factors for multiple cracks. *Engineering Fracture Mechanics 72*, 1171–1196.

Hwang, C. G., P. A. Wawrzynek, A. K. Tayebi, and A. R. Ingraffea (1998). On the Virtual Crack Extension method for calculation of the rates of energy release rate. *Engineering Fracture Mechanics 59*, 521–542.

Idelsohn, S. R., E. Oñate, N. Calvo, and F. Del Pin (2002). Meshless finite element ideas. In H. Mang, F. Rammerstorfer, and J. Eberhardsteiner (Eds.), *Proc. 5th World Congress on Computational Mechanics, Vienna, Austria, July 7-12, 2002*.

Iman, R. L. and W. J. Conover (1982). A distribution-free approach to inducing rank correlation among input variables. *Communications in Statistics - Simulation and Computation 11*, 311–334.

Ingraffea, A. R. (1989). Shear cracks. In L. Elfgren (Ed.), *Fracture mechanics of concrete structures*. London: Chapman and Hall.

Intel Corporation (2004). *Intel Math Kernel Library Reference Manual* (7.0 ed.).

Irwin, G. R. (1956). Analysis of stresses and strains near the end of a crack traversing a plate. *Journal of Applied Mechanics - Trans. ASME 24*, 361–364.

Ishikawa, H. (1980). A finite element analysis of stress intensity factors for combined tensile and shear loading by only a virtual crack extension. *International Journal of Fracture 16*, 243–246.

Jirásek, M. and Z. P. Bažant (2002). *Inelastic analysis of structures*. London, New York: J. Wiley & Sons.

Jirásek, M. and T. Belytschko (2002). Computational resolution of strong discontinuities. In H. Mang, F. Rammerstorfer, and J. Eberhardsteiner (Eds.), *Proc. 5th World Congress on Computational Mechanics, Vienna, Austria, July 7-12, 2002*.

Jirásek, M. and S. Marfia (2005). From localized damage to discrete cracks. In G. Hofstetter and G. Meschke (Eds.), *Book of Abstracts, EUROMECH Colloquium 460: Numerical Modelling of Concrete Cracking, Innsbruck, Austria, February 21-23, 2005*.

Jirásek, M. and T. Zimmermann (1997). Rotating crack model with transition to scalar damage: I. local formulation, II. nonlocal formulation and adaptivity. LSC Internal Report 97/01, Swiss Federal Institute of Technology, Lausanne, Switzerland.

Kaljevic, I. and S. Saigal (1997). An improved element free Galerkin formulation. *International Journal for Numerical Methods in Engineering 40*, 2953–2974.

Karutz, H. (2000). *Adaptive Kopplung der Elementfreien Galerkin-Methode mit der Methode der Finiten Elemente bei Rissfortschrittsproblemen*. Ph. D. thesis, Ruhr-Universität Bochum, Germany.

Karypis, G. and V. Kumar (1998). *METIS - A software package for partitioning unstructured graphs, partitioning messhes and computing fill-reducing orderings of sparse matrices* (4.0 ed.). University of Minnesota.

Krongauz, Y. (1996). *Application of Meshless methods to solid mechanics*. Ph. D. thesis, Northwestern University, Evanston, Illinois.

Lancaster, P. and K. Salkauskas (1981). Surface generated by moving least squares methods. *Mathematics of Computation 37*, 141–158.

Lasserre, J. B. (1983). An analytical expression and an algorithm for the volume of a convex polyhedron in r^n. *International Journal for Optimization Theory and Applications 39*, 1655–1679.

Lawson, C. L. (1977). Software for C^1 surface interpolation. In J. Rice (Ed.), *Mathematical Software III*, Volume 3. New York: N.Y. Academic Press.

Leonhardt, F. and R. Walther (1962). Schubversuche an einfeldrigen Stahlbetonbalken mit und ohne Schubbewehrung. *Deutscher Ausschuss für Stahlbeton 151*.

Levin, D. (1998). The approximation power of moving least-squares. *Mathematics of Computation 67*(224), 1517–1531.

Li, S. and W. K. Liu (2002). Meshfree and particle methods and their applications. *Applied Mechanics Review 55*, 1–34.

Liu, P.-L. and A. Der Kiureghian (1986). Multivariate distribution models with prescribed marginals and covariances. *Probabilistic Engineering Mechanics 1*, 105–112.

Liu, P.-L. and A. Der Kiureghian (1989). Finite element reliability methods for geometrically nonlinear stochastic structures. Report UCB/SEMM-89/05, Structural Engineering, Mechanics and Materials, Department of Civil Engineering, University of California, Berkeley, CA.

Liu, W. K., T. Belytschko, and A. Mani (1986). Random field finite elements. *International Journal for Numerical Methods in Engineering 23*, 1831–1845.

Liu, W. K., W. Han, H. Lu, S. Li, and J. Cao (2004). Reproducing kernel element method. *Computer Methods in Applied Mechanics and Engineering 193*, 993–951.

Liu, W. K., S. Jun, and Y. Zhang (1995). Reproducing kernel particle methods. *International Journal for Numerical Methods in Fluids 20*, 1081–1106.

Lo, S. H. (1989). Delaunay triangulation of non-convex planar domains. *International Journal for Numerical Methods in Engineering 28*, 2695–2707.

Lu, Y. Y., T. Belytschko, and L. Gu (1994). A new implementation of the Element-free Galerkin Method. *Computer Methods in Applied Mechanics and Engineering 113*, 397–414.

Lucy, L. B. (1977). A numerical approach to the testing of fission hypothesis. *The Astronomical Journal 82*, 1013–1024.

Matthies, H. G., C. E. Brenner, C. G. Bucher, and C. G. Soares (1997). Uncertainties in probabilistic numerical analysis of structures and solids - Stochastic finite elements. *Structural Safety 19*, 283–336.

McKay, M. D., W. J. Conover, and R. J. Beckmann (1979). A comparison of three methods for selecting values of input variables in the analysis of output from a computer code. *Technometrics 21*, 239–245.

Mehlhorn, G. and J. Kolleger (1995). Anwendung der Finiten Elemente Methode im Stahlbetonbau. In *Der Ingenieurbau: Grundwissen Band 6: Rechnerorientierte Baumechanik*, pp. 293 – 425. Berlin: Ernst & Sohn.

Melenk, J. M. and I. Babuška (1996). The Partition of Unity Finite Element Method: Basic theory and applications. *Computer Methods in Applied Mechanics and Engineering 139*, 289–314.

Moës, N. and T. Belytschko (2002). Extended finite element method for cohesive crack growth. *Engineering Fracture Mechanics 69*, 813–833.

Moës, N., J. Dolbow, and T. Belytschko (1999). A Finite Element Method for crack growth without remeshing. *International Journal for Numerical Methods in Engineering 46*, 131–150.

Morgenstern, D. (1956). Einfache Beispiele zweidimensionaler Verteilungen. *Mitteilungsblatt für Mathematische Statistik 8*, 234–235.

Most, T. and C. Bucher (2003). Moving Least Squares-elements for stochastic crack propagation simulations coupled with stochastic finite elements. In A. Der Kiureghian et al. (Eds.), *Proc. 9th Int. Conf. Applications of Statistics and Probability in Civil Engineering (ICASP), San Francisco, California, July 6-9, 2003*. Rotterdam: Balkema.

Most, T., C. Bucher, and Y. Schorling (2004). Dynamic stability analysis of nonlinear structures with geometrical imperfections under random loading. *Journal of Sound and Vibration 276*, 381–400.

Most, T. and S. Eckardt (2004). Application of a hybrid parallelisation technique to accelerate the numerical simulation of nonlinear mechanical problems. In K. Beuke et al. (Eds.), *Proc. 10th Int. Conf. on Computing in Civil and Building Engineering (ICCCBE-X), Weimar, Germany, June 2-4, 2004*. Bauhaus-University Weimar.

Most, T., J. F. Unger, and C. Bucher (2005). Cohesive discrete crack modeling using Virtual Crack Extension technique within the Natural Neighbor Galerkin Method. *Computers and Structures*. submitted for publication.

M.P.I. Forum (1994). MPI: A message passing interface standard. *International Journal of Supercomputer Applications and High Performance Computing 8*, 3–4.

Nataf, A. (1962). Détermination des distributions de probabilités dont les marges sont données. *Comptes Rendus de l'Academie des Sciences 225*, 42–43.

Nayroles, B., G. Touzot, and P. Villon (1992). Generalizing the FEM: diffuse approximations and diffuse elements. *Computational Mechanics 10*, 307–318.

Novák, D. and N. Shiraishi (1993). Latin hypercube response approximation and sensitivity analysis for reliability problems. Research Report 93-ST-01, School of Civil Engineering, Kyoto-University, Japan.

Nuismer, R. J. (1975). An energy release rate criterion for mixed mode fracture. *International Journal of Fracture 11*.

NW-Ialad (2003). Integrity assessment of large dams, http://nw-iald.uibk.ac.at.

Oliver, J., A. E. Huespe, M. D. G. Pulido, S. Blanco, and D. Linero (2004). Recent advances in computational modeling of material failure. In P. Neittaanmäki et al. (Eds.), *Proc. 4th European Congress on Computational Mechanics in Applied Sciences and Engineering (ECCOMAS), Jyväskylä, Finland, July 24-28, 2004*. University of Jyväskylä.

Olsson, A., G. Sandberg, and O. Dahlblom (2003). On Latin hypercube sampling for structural reliability analysis. *Structural Safety 25*, 47–68.

OpenMP Architecture Review Board (2002). *OpenMP C and C++ application program interface* (2.0 ed.).

Park, S. H. and S. K. Youn (2001). The least-squares meshfree method. *International Journal for Numerical Methods in Engineering 52*, 997–1012.

Parks, D. M. (1975). A stiffness derivative finite element technique for determination of crack tip stress intensity factors. *International Journal of Fracture 10*, 487–502.

Peraire, J., M. Vahdati, K. Morgan, and O. Z. Zienkiewicz (1987). Adaptive remeshing for compressible flow computations. *J. Comp. Phys. 72*, 449–466.

Petersson, P.-E. (1981). Crack growth and development of fracture process zone in plain concrete and similar materials. Report TVBM-1006, Division of Building Materials, Lund Institute of Technology, Lund, Sweden.

Planas, J. and M. Elices (1991). Nonlinear fracture of cohesive materials. *International Journal of Fracture 51*, 139–157.

Pukl, R., D. Novák, and K. Bergmeister (2003). Reliability assessment of concrete structures. In N. Bićanić, R. de Borst, H. Mang, and G. Meschke (Eds.), *Computational Modelling of Concrete Structures - Proc. Europ. Conf. EURO-C 2003, St. Johann, Austria, March 17-20, 2003*. Lisse: Swets & Zeitlinger.

Rahman, S. and B. N. Rao (2001). An element-free Galerkin method for probabilistic mechanics and reliability. *International Journal of Solids and Structures 38*, 9313–9330.

Rao, B. N. and S. Rahman (2000). An efficient meshless method for fracture analysis of cracks. *Computational Mechanics 26*, 398–408.

Rehle, N. (1996). *Adaptive Finite Element Verfahren bei der Analyse von Flächentragwerken*. Ph. D. thesis, University of Stuttgart, Germany.

Reich, R. (1993). *On the marriage of mixed Finite Element Methods and fracture mechanics: An application on concrete dams*. Ph. D. thesis, University of Colorado, Boulder, Colorado.

Rice, J. R. (1968). A path independent integral and the approximate analysis of strain concentrations by notches and cracks. *Journal of Applied Mechanics - Trans. ASME 35*, 379–386.

Rolshoven, S. and M. Jirásek (2003). Numerical aspects of nonlocal plasticity with strain softening. In N. Bićanić, R. de Borst, H. Mang, and G. Meschke (Eds.), *Computational Modelling of Concrete Structures - Proc. Europ. Conf. EURO-C 2003, St. Johann, Austria, March 17-20, 2003*. Lisse: Swets & Zeitlinger.

Ruppert, J. (1995). A delaunay refinement algorithm for quality two-dimensional mesh generation. *Journal of Algorithms 18*, 548–585.

Rybicki, E. F. and M. F. Kanninen (1977). A finite element calculation of stress intensity factors by Modified Crack Closure Integral. *Eng. Fracture Mechanics 9*, 931–938.

Saouma, V. E. (1981). *Interactive finite element analysis of reinforced concrete: a fracture mechanics approach*. Ph. D. thesis, Cornell University.

Schenk, O. and K. Gärtner (2004). Solving unsymmetric sparse systems of linear equations with PAR-DISO. *Journal of Future Generation Computer Systems 20*, 475–487.

Schorling, Y. (1997). *Beitrag zur Stabilitätsuntersuchung von Strukturen mit räumlich korrelierten geometrischen Imperfektionen*. Ph. D. thesis, Bauhaus-University Weimar, Germany.

Schrader, K. (2004a). Implementation des MUltifrontal Massively Parallel Solver über ein C-Interface in SLang zur Lösung großer linearer Gleichungssysteme mit schwachbesetzten Matrizen. Student research project, Bauhaus-University Weimar, Germany.

Schrader, K. (2004b). Parallelisierung des Nested-Dissection-Vorkonditionierers METIS für den MPI-basierten MUMPS-Solver in SLang zur Strukturoptimierung schwachbesetzter Matrizen. Student research project, Bauhaus-University Weimar, Germany.

Schrader, K. (2005). Algorithmische Umsetzung eines elasto-plastischen Kontakt-Materialgesetzes zur Abbildung der Rissflächen-Degradation bei kohäsiven Rissen. Diploma thesis, Bauhaus-University Weimar, Germany.

Schulze, J. (2001). Towards a tighter coupling of bottom-up and top-down sparse matrix ordering methods. *BIT 41*, 800–841.

Sethian, J. A. (1999). *Level Set Methods and Fast Marching Methods*. Cambridge University Press.

Sha, G. (1984). On the Virtual Crack Extenion technique for stress intensity factors and energy release rate calculations for mixed fracture mode. *International Journal of Fracture 25*, R33–R42.

Shepard, D. (1968). A two-dimensional interpolation function for irregular spaced data. In *Proc. 23rd Nat. Conf. ACM*, pp. 517–24.

Shewchuk, J. R. (1996). Triangle: A two-dimensional quality mesh generator and delaunay triangulator. Technical report, School of Computer Science, Carnegie Mellon University. download: http://www.cs.cmu.edu/ quake/triangle.html.

Sibson, R. (1980). A vector identity for the dirichlet tesselation. In *Mathematical Proceedings of the Cambridge Philosophical Society 87*, pp. 151–155.

Simo, J. C. and T. J. R. Hughes (1986). On variational foundations of assumed strain methods. *Journal of Applied Mechanics 53*, 51–54.

Simo, J. C. and M. S. Rifai (1990). A class of mixed assumed strain methods and the method of incompatible modes. *International Journal for Numerical Methods in Engineering 29*, 1595–1638.

Simo, J. R. and T. J. R. Hughes (1998). *Computational Inelasticity*. New York: Springer.

Singh, R., B. Carter, P. Wawrzynek, and A. Ingraffea (1998). Universal crack closure integral for SIF estimation. *Engineering Fracture Mechanics 60*, 133–146.

Snir, M., S. W. Otto, S. Huss-Lederman, D. W. Walker, and J. J. Dongarra (1996). *MPI: The Complete Reference*. Cambridge, MA: MIT Press.

Sukumar, N. (1998). *Natural Element Method in Solid Mechanics*. Ph. D. thesis, Nortwestern University, Illinois.

Sukumar, N., L. Chopp, N. Moës, and T. Belytschko (2001). Modeling holes and inclusion by Level Sets in the Extended Finite Element Method. *Computer Methods in Applied Mechanics and Engineering 190*, 6183–6200.

Sukumar, N., B. Moran, and T. Belytschko (1998). The Natural Element Method in solid mechanics. *International Journal for Numerical Methods in Engineering 43*, 839–887.

Sukumar, N., B. Moran, A. Y. Semenov, and V. V. Belikov (2001). Natural neighbour galerkin methods. *International Journal for Numerical Methods in Engineering 50*, 1–27.

Tada, H., P. Paris, and G. Irwin (1993). *The stress analysis of cracks handbook*. Hellertown, Pennsylvania: Del Research Corporation.

Telford, T. (1993). *CEB-FIP Modelcode 1990*. London.

Teplý, B., D. Lehký, D. Novák, E. M. Eichinger, J. Kollegger, R. Pukl, V. Červenka, and M. G. Stewart (2003). Prestressed bridges under corrosion attack. In N. Bićanić, R. de Borst, H. Mang, and G. Meschke (Eds.), *Computational Modelling of Concrete Structures - Proc. Europ. Conf. EURO-C 2003, St. Johann, Austria, March 17-20, 2003*. Lisse: Swets & Zeitlinger.

Trunk, B. (1999). *Einfluss der Bauteilgrösse auf die Bruchenergie von Beton*. Ph. D. thesis, Eidgenössische Technische Hochschule, Zürich, Switzerland.

Unger, J. F. (2003). Development of an efficient algorithm for the application of the Natural Neighbor Interpolation for crack growth simulations. Diploma thesis, Bauhaus-University Weimar, Germany.

Unger, J. F., T. Most, C. Bucher, and C. Könke (2004). Adaptation of the Natural Element Method for crack growth simulations. In P. Neittaanmäki et al. (Eds.), *Proc. 4th European Congress on Computational Mechanics in Applied Sciences and Engineering (ECCOMAS), Jyväskylä, Finland, July 24-28, 2004*. University of Jyväskylä.

Červenka, V. (1970). *Inelastic finite element analysis of reinforced concrete panels under in-plane loads*. Ph. D. thesis, University of Colorado.

Vondráček, R. (2003). Application of sparse direct solver on large systems of linear equations. In J. Vrba et al. (Ed.), *Book of Abstracts, 2nd PhD Workshop, Brno University of Technology, November, 20-22*.

Watson, D. F. (1994). NNGRIDR: An implementation of natural neighbor interpolation. Technical report.

Wawrzynek, P. A. (1991). *Discrete Modeling of Crack Propagation: Theoretical Aspects and Implementation Issues in Two and Three Dimensions*. Ph. D. thesis, Cornell University.

Werkle, H. and D. Gong (1993). CAD-unterstützte Generierung ebener Finiter-Elemente-Netze auf der Grundlage von Makroelementen. *Bauingenieur 68*, 351–358.

Winkler, B. J. (2001). *Traglastuntersuchungen von unbewehrten und bew. Betonstrukturen auf der Grundlage eines objektiven Werkstoffgesetzes für Beton*. Ph. D. thesis, University of Innsbruck, Austria.

Xie, M. (1995). *Finite element modelling of discrete crack propagation*. Ph. D. thesis, University of New Mexico, USA.

Xie, M., W. H. Gerstle, and P. Rahulkumar (1995). Energy-based automatic mixed-mode crack propagation modelling. *Journal of Engineering Mechanics ASCE 121*, 914–923.

Yang, Z. and J. Chen (2004). Fully automatic modelling of cohesive discrete crack propagation in concrete beams using local arc-length methods. *International Journal of Solids and Structures 41*, 801–826.

Yang, Z. J., J. F. Chen, and G. D. Holt (2001). Efficient calculation of stress intensity factors using virtual crack extension technique. *Computers and Structures 79*, 2705–2715.

Zhu, W. Q., Y. J. Ren, and W. Q. Wu (1992). Stochastic FEM based on local averages of random vector fields. *Journal of Engineering Mechanics 118*, 496–511.

Appendix A

A.1 Parallel computing using OpenMP

OpenMP (OpenMP Architecture Review Board 2002) is a parallelization environment for shared memory systems with a very easy application. It can be used for Fortran, C and C++. In this work several time consuming loops were accelerated with this tool. If the operation for one loop member works completely independent of each other, which means, that only corresponding variables or arrays are modified during the calculation, the parallel construct given in Fig. A.1 needs to be placed in front of the loop. This principle is used in this work for the assembling of the finite element stiffness matrices and internal force vectors, which are stored in the element structure, and the calculation of the meshless shape functions at the integration points. The loop counter, an error identifier and other controlling variables are defined as shared variables for all processors. Private variables are these, which have to be a local copy for each processor. The dynamic schedule type enables OpenMP to choose the optimal processor usage.

During the meshless calculations the domain is discretized with a few meshless zones, each containing a large number of nodes and integration cells. The resulting objects are stored in compact form for each meshless zone. This means that the parallelization of the loop over the integration cells can not be done independently as for finite elements. The problem can be solved by defining a critical region as shown in Fig. A.2, where the local stiffness matrix of one integration cell is transferred onto the stiffness matrix of the meshless zone, so that only one processor executes this part in a given time.

```
#pragma omp parallel shared(counter, error, ...) private(...)
#pragma omp for schedule(dynamic,1) nowait
    for(counter = 0; counter < number; counter ++)
    {
        /* do computation for single loop member */
        ...
    }
```

Figure A.1. OpenMP parallelized simple loop

```
#pragma omp parallel shared(counter, error, ...) private(...)
#pragma omp for schedule(dynamic,1) nowait
    for(counter = 0; counter < number; counter ++)
    {
        /* do computation for single loop member */
        ...
        #pragma omp critical
        {
            /* transfer computed data to global array */
            ...
        }
    }
```

Figure A.2. OpenMP parallelized loop with critical region

A.2   Isoparametric finite interface elements

In (Mehlhorn and Kolleger 1995) the concept of isoparametric finite interface elements is described for the general three-dimensional case for elements of arbitrary order. In this work only linear two-dimensional elements have been used, which will be presented here. In Fig. A.3 the implemented four-node element is shown. As input values for the interface
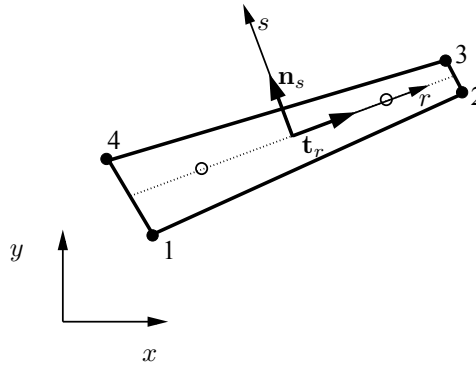
Figure A.3. Four-node isoparametric interface element with global and local coordinates and two Gaussian integration points

traction-separation law the relative displacements in local coordinates are calculated as follows

$$\mathbf{\Delta u}^{local} = \tilde{\mathbf{T}} \mathbf{B}_e^{global} \tilde{\mathbf{u}}_e, \tag{A.1}$$

where $\tilde{\mathbf{u}}_e$ is the nodal displacement vector and $\tilde{\mathbf{T}}$ is the transformation matrix from global to local coordinates

$$\tilde{\mathbf{T}} = \left[\begin{array}{cc} \mathbf{t}_r & \mathbf{n}_s \end{array} \right]^T. \tag{A.2}$$

The vector $\mathbf{n}_s$ is the normal on the interface surface and $\mathbf{t}_r$ is the tangential vector indicated in Fig. A.3. The matrix $\mathbf{B}_e^{global}$ characterizes the correlation between relative displacements in global coordinates and nodal displacements

$$\Delta\mathbf{u}^{global} = \mathbf{B}_e^{global}\tilde{\mathbf{u}}_e, \tag{A.3}$$

and is given for the presented element as

$$\mathbf{B}_e^{global} = \frac{1}{2}\begin{bmatrix} -1+r & 0 & -1-r & 0 & 1+r & 0 & 1-r & 0 \\ 0 & -1+r & 0 & -1-r & 0 & 1+r & 0 & 1-r \end{bmatrix}. \tag{A.4}$$

The stresses in the interface surface are defined as a function of the relative displacements

$$\boldsymbol{\sigma}^{local} = \boldsymbol{\sigma}^{local}\left(\Delta\mathbf{u}^{local}\right) = \begin{bmatrix} \sigma_T & \sigma_N \end{bmatrix}^T,$$
$$\dot{\boldsymbol{\sigma}}^{local} = \mathbf{D}\left(\Delta\mathbf{u}^{local}\right)\Delta\dot{\mathbf{u}}^{local}, \tag{A.5}$$

where $\mathbf{D}$ is tangential material stiffness matrix. In global coordinates we obtain

$$\boldsymbol{\sigma}^{global} = \tilde{\mathbf{T}}^T\boldsymbol{\sigma}^{local}\left(\Delta\mathbf{u}^{local}\right) = \begin{bmatrix} \sigma_x & \sigma_y \end{bmatrix}^T. \tag{A.6}$$

This leads to the following equations for the element stiffness matrix and internal force vector in global coordinates

$$\mathbf{K}_e^{global}(\tilde{\mathbf{u}}_e) = \int_A \left[\tilde{\mathbf{T}}\mathbf{B}_e^{global}\right]^T \mathbf{D}(\Delta\mathbf{u}^{local})\tilde{\mathbf{T}}\mathbf{B}_e^{global}dA,$$
$$\mathbf{f}_e^{int,global}(\tilde{\mathbf{u}}_e) = \int_A \left[\tilde{\mathbf{T}}\mathbf{B}_e^{global}\right]^T \boldsymbol{\sigma}^{local}(\Delta\mathbf{u}^{local})dA. \tag{A.7}$$

The numerical integration is carried out similarly to standard finite elements as presented in section 2.2.4 by using two Gauss integration points on the interface surface.

Appendix B

B.1 MLS weighting function derivatives

B.1.1 Gaussian weighting function

The weighting function is given as

$$
w_G(s) = \begin{cases} \dfrac{e^{-\frac{s^2}{\alpha^2}} - e^{-\frac{1}{\alpha^2}}}{1 - e^{-\frac{1}{\alpha^2}}} & s \leq 1 \\ 0 & s > 1 \end{cases} .
\tag{B.1}
$$

The first and second derivative for $s \leq 1$ can be obtained as

$$
\frac{\partial w_G(s)}{\partial s} = -\frac{e^{-\frac{s^2}{\alpha^2}}}{1 - e^{-\frac{1}{\alpha^2}}} \cdot \frac{2s}{\alpha^2},
$$

$$
\frac{\partial^2 w_G(s)}{\partial^2 s} = -\frac{e^{-\frac{s^2}{\alpha^2}}}{1 - e^{-\frac{1}{\alpha^2}}} \cdot \left(\frac{2}{\alpha^2} - \frac{4s^2}{\alpha^4} \right),
\tag{B.2}
$$

which leads to the following values of the derivatives at the boundary of the influence domain

$$
\frac{\partial w_G(s = 1; \alpha = 0.4)}{\partial s} \approx -0.024,
$$

$$
\frac{\partial^2 w_G(s = 1; \alpha = 0.4)}{\partial^2 s} \approx 0.278.
\tag{B.3}
$$

B.1.2 Cubic weighting function

The cubic weighting function reads

$$
w_C(s) = \begin{cases} 1 - 3s^2 + 2s^3 & s \leq 1 \\ 0 & s > 1 \end{cases} .
\tag{B.4}
$$

The derivatives for $s \leq 1$ can be determined easily as

$$\frac{\partial w_C(s)}{\partial s} = -6s + 6s^2,$$

$$\frac{\partial^2 w_C(s)}{\partial^2 s} = -6 + 12s,$$

(B.5)

which results in the values on the influence boundary given in Eq. (B.6)

$$\frac{\partial w_C(s = 1)}{\partial s} = 0,$$

$$\frac{\partial^2 w_C(s = 1)}{\partial^2 s} = 6.$$

(B.6)

B.1.3   Cubic spline weighting function

The derivatives of the cubic spline weighting function

$$w_S(s) = \begin{cases} 1 - 6s^2 + 6s^3 & s \leq \frac{1}{2} \\ 2 - 6s + 6s^2 - 2s^3 & \frac{1}{2} < s \leq 1 \\ 0 & s > 1 \end{cases}$$

(B.7)

can be given for $s \leq 1$ as

$$\frac{\partial w_S(s)}{\partial s} = \begin{cases} -12s + 18s^2 & s \leq \frac{1}{2} \\ -6 + 12s - 6s^2 & \frac{1}{2} < s \leq 1 \end{cases},$$

$$\frac{\partial^2 w_S(s)}{\partial^2 s} = \begin{cases} -12 + 36s & s \leq \frac{1}{2} \\ 12 - 12s & \frac{1}{2} < s \leq 1 \end{cases}.$$

(B.8)

The values for $s = 1$ and $s = 0.5$ can be derived as

$$\frac{\partial w_S(s = 1)}{\partial s} = 0, \qquad \frac{\partial^2 w_S(s = 1)}{\partial^2 s} = 0,$$

$$\frac{\partial w_S(s = 0.5)}{\partial s} = -1.5, \qquad \frac{\partial^2 w_S(s = 0.5)}{\partial^2 s} = 6.$$

(B.9)

B.1.4   Regularized weighting function

The regularized weighting function is defined as

$$\tilde{w}_R(s) = \frac{(s^2 + \epsilon)^{-2} - (1 + \epsilon)^{-2}}{\epsilon^{-2} - (1 + \epsilon)^{-2}}; \quad \epsilon \ll 1.$$

(B.10)

The first and second derivatives for $s \leq 1$ can be derived as

$$\frac{\partial \tilde{w}_R(s)}{\partial s} = \frac{-4s \left(s^2 + \epsilon\right)^{-3}}{\epsilon^{-2} - (1 + \epsilon)^{-2}},$$

$$\frac{\partial^2 \tilde{w}_R(s)}{\partial^2 d} = \frac{24s^2 \left(s^2 + \epsilon\right)^{-4} - 4 \left(s^2 + \epsilon\right)^{-3}}{\epsilon^{-2} - (1 + \epsilon)^{-2}},$$

(B.11)

and the values on the influence boundary can be approximated as

$$\frac{\partial \tilde{w}_R(s = 1)}{\partial s} \approx -4\epsilon^2,$$

$$\frac{\partial^2 \tilde{w}_R(s = 1)}{\partial^2 s} \approx 20\epsilon^2.$$

(B.12)

B.2   Interpolation error of regularized weighting function

Eq. (3.24) and Eq. (3.25) lead to the following formulation

$$w_R(s_i) = \frac{\left(s_i^2 + \epsilon\right)^{-2} - (1 + \epsilon)^{-2}}{\sum\limits_{j=1}^{m} \left[\left(s_j^2 + \epsilon\right)^{-2} - (1 + \epsilon)^{-2}\right]} \tag{B.13}$$

If we assume

$$\epsilon \ll 1; \quad s_{min}^2 \gg \epsilon \tag{B.14}$$

we can approximate

$$\sum_{j=1}^{m} \left[\left(s_j^2 + \epsilon\right)^{-2} - (1 + \epsilon)^{-2}\right] \approx \epsilon^{-2} - 1 + \sum_{j=1; j \neq i}^{m} \left[s_j^{-4} - 1\right] \tag{B.15}$$

$$\approx \epsilon^{-2}$$

by considering the fact, that the distance s_i for the support point itself is equal to zero. Under consideration of

$$\left(s_i^2 + \epsilon\right)^{-2} \leq \left(s_{min}^2 + \epsilon\right)^{-2}, \tag{B.16}$$

and of Eq. (B.15) we obtain for the maximum error of the weighting function

$$\left|w_i\left(\mathbf{x}_j\right) - \delta_{ij}\right|_{max} \approx \left[\left(s_{min}^2 + \epsilon\right)^{-2} - (1 + \epsilon)^{-2}\right] \cdot \epsilon^2 \tag{B.17}$$

$$\approx \left(s_{min}^{-4} - 1\right) \cdot \epsilon^2$$

Using the simpler formulation from Eq. (3.25) we obtain under considering Eq. (B.15) and Eq. (B.16) the same expression as given in Eq. (B.17)

$$\left|\tilde{w}_i\left(\mathbf{x}_j\right) - \delta_{ij}\right|_{max} \approx \left(s_{min}^{-4} - 1\right) \cdot \epsilon^2 \tag{B.18}$$

Appendix C

C.1 Implementation of mixed-mode cohesive crack model

C.1.1 Closest Point Projection Algorithm

In this section the adaptation of the General Closest Point Projection algorithm (Simo and Hughes 1998) for the improved mixed-mode cohesive crack model presented in section 4.2.2 is derived according to (Schrader 2005).

Based on the decomposition of the relative displacements in the crack surface in elastic and plastic quantities the following incremental formulation can be made

$$\mathbf{\Delta u}_{n+1}^{cr} = \mathbf{\Delta u}_n^{cr} + \delta\mathbf{\Delta u}_{n+1}^{cr}. \tag{C.1}$$

The increment of the plastic displacement difference can be formulated by means of the flow direction, specified by the derivatives of the plastic potential, and the plastic multiplier γ

$$\delta\mathbf{\Delta u}_{n+1}^{cr} = \delta\gamma \frac{\partial Q_{n+1}}{\partial \boldsymbol{\sigma}_{n+1}}. \tag{C.2}$$

The global residue can be defined as

$$\mathbf{R}_{n+1} = -\mathbf{\Delta u}_{n+1}^{cr} + \mathbf{\Delta u}_n^{cr} + \delta\gamma \frac{\partial Q_{n+1}}{\partial \boldsymbol{\sigma}_{n+1}} = 0, \tag{C.3}$$

and the yield criterion is given as

$$F_{n+1} = F(\boldsymbol{\sigma}_{n+1}) = 0, \tag{C.4}$$

with

$$\boldsymbol{\sigma}_{n+1} = \mathbf{C} : \left[\mathbf{\Delta u}_{n+1} - \mathbf{\Delta u}_{n+1}^{cr}\right]. \tag{C.5}$$

During the local iteration $\mathbf{\Delta u}_{n+1}$ remains constant, thus in the k-th iteration step the

following relation is valid

$$\delta\mathbf{\Delta u}_{n+1}^{cr\,(k)} = -\mathbf{C}^{-1} : \delta\boldsymbol{\sigma}_{n+1}^{(k)}.$$ (C.6)

This can be used to linearize Eq. (C.3) and Eq. (C.4)

$$\mathbf{R}_{n+1}^{(k)} + \left[\mathbf{\Xi}_{n+1}^{(k)}\right]^{-1} : \delta\boldsymbol{\sigma}_{n+1}^{(k)} + \delta^2\gamma_{n+1}^{(k)}\frac{\partial Q_{n+1}^{(k)}}{\partial\boldsymbol{\sigma}_{n+1}} = 0,$$

$$F_{n+1}^{(k)} + \frac{\partial F_{n+1}^{(k)}}{\partial\boldsymbol{\sigma}_{n+1}} : \delta\boldsymbol{\sigma}_{n+1}^{(k)} = 0,$$ (C.7)

where the Hessian matrix can be obtained as

$$\mathbf{\Xi}_{n+1}^{(k)} = \left[\mathbf{C}^{-1} + \delta\gamma\frac{\partial^2 Q_{n+1}^{(k)}}{(\partial\boldsymbol{\sigma}_{n+1})^2}\right]^{-1}.$$ (C.8)

Substitution of $\delta\boldsymbol{\sigma}_{n+1}^{(k)}$ in the second part of Eq. (C.7) reads

$$F_{n+1}^{(k)} + \frac{\partial F_{n+1}^{(k)}}{\partial\boldsymbol{\sigma}_{n+1}} : \mathbf{\Xi}_{n+1}^{(k)} : \left[-\mathbf{R}_{n+1}^{(k)} - \delta^2\gamma_{n+1}^{(k)}\frac{\partial Q_{n+1}^{(k)}}{\partial\boldsymbol{\sigma}_{n+1}}\right] = 0.$$ (C.9)

Solving Eq. (C.9) with respect to $\delta^2\gamma_{n+1}^{(k)}$ leads to the following relation

$$\delta^2\gamma_{n+1}^{(k)} := \frac{F_{n+1}^{(k)} - \dfrac{\partial F_{n+1}^{(k)}}{\partial\boldsymbol{\sigma}_{n+1}} : \mathbf{\Xi}_{n+1}^{(k)} : \mathbf{R}_{n+1}^{(k)}}{\dfrac{\partial F_{n+1}^{(k)}}{\partial\boldsymbol{\sigma}_{n+1}} : \mathbf{\Xi}_{n+1}^{(k)} : \dfrac{\partial Q_{n+1}^{(k)}}{\partial\boldsymbol{\sigma}_{n+1}}}.$$ (C.10)

Eq. (C.10) can be used for the update of the plastic relative displacements, which are the iteration variables

$$\delta\mathbf{\Delta u}_{n+1}^{cr\,(k)} = \mathbf{C}^{-1} : \mathbf{\Xi}_{n+1}^{(k)} : \left[\mathbf{R}_{n+1}^{(k)} + \delta^2\gamma_{n+1}^{(k)}\frac{\partial Q_{n+1}^{(k)}}{\partial\boldsymbol{\sigma}_{n+1}}\right].$$ (C.11)

Then the complete algorithm can be formulated, which is given in Table C.1.1. The required derivatives of the yield criterion and the plastic potential can be simply derived and are given in (Schrader 2005).

1. Initialize: $\quad \mathbf{\Delta u}_{n+1}^{cr(0)} = \mathbf{\Delta u}_n^{cr} \qquad W_{n+1}^{cr(0)} = W_n^{cr} \qquad \delta\gamma_{n+1}^{(0)} = 0$

2. Calculate actual stresses, fracture work, internal parameters and yield criterion:

$$\boldsymbol{\sigma}_{n+1}^{(k)} = \mathbf{C} : [\mathbf{\Delta u}_{n+1} - \mathbf{\Delta u}_{n+1}^{cr(k)}]$$

$$\delta W_{n+1}^{cr(k)} = \begin{cases} \boldsymbol{\sigma}_{n+1}^{(k)} : \left[\mathbf{\Delta u}_{n+1}^{cr(k)} - \mathbf{\Delta u}_n^{cr}\right] & \sigma_{N,n+1}^{(k)} \geq 0 \\[3mm] \sigma_{T,n+1}^{(k)} \left(\Delta u_{T,n+1}^{cr(k)} - \Delta u_{T,n}^{cr}\right) \left(1 - \left|\dfrac{\sigma_{N,n+1}^{(k)} \tan\phi}{\sigma_{T,n+1}^{(k)}}\right|\right) & \sigma_{N,n+1}^{(k)} < 0 \end{cases}$$

$$W_{n+1}^{cr(k)} = W_n^{cr} + \delta W_{n+1}^{cr(k)}$$

$$\chi_{n+1}^{(k)} = \chi(\chi_0, W_{n+1}^{cr(k)}) \qquad c_{n+1}^{(k)} = c(c_0, W_{n+1}^{cr(k)})$$

$$F_{n+1}^{(k)} = F(\sigma_{n+1}^{(k)}, \chi_{n+1}^{(k)}, c_{n+1}^{(k)})$$

IF $\dfrac{F}{F_{\text{norm}}} < TOL$ AND $k < 1$ THEN: GOTO 6.

$$\mathbf{R}_{n+1}^{(k)} = \mathbf{\Delta u}_n^{cr} - \mathbf{\Delta u}_{n+1}^{cr(k)} + \delta\gamma_{n+1}^{(k)}\partial_{\boldsymbol{\sigma}} Q_{n+1}^{(k)}$$

IF $\sqrt{\left(\dfrac{F}{F_{\text{norm}}}\right)^2 + \left(\dfrac{||\mathbf{R}||}{R_{\text{norm}}}\right)^2} < TOL$ THEN: GOTO 6.

3. Calculate increment of plastic multiplier:

$$\delta^2\gamma_{n+1}^{(k)} = \frac{F_{n+1}^{(k)} - \partial_{\boldsymbol{\sigma}} F_{n+1}^{(k)} : \mathbf{\Xi}_{n+1}^{(k)} : \mathbf{R}_{n+1}^{(k)}}{\partial_{\boldsymbol{\sigma}} F_{n+1}^{(k)} : \mathbf{\Xi}_{n+1}^{(k)} : \partial_{\boldsymbol{\sigma}} Q_{n+1}^{(k)}}$$

$$\mathbf{\Xi}_{n+1}^{(k)} = \left[\mathbf{C}^{-1} + \delta\gamma_{n+1}^{(k)} \partial_{\boldsymbol{\sigma}}^2 Q_{n+1}^{(k)}\right]^{-1}$$

4. Calculate increments of plastic relative displacement:

$$\delta\mathbf{\Delta u}_{n+1}^{cr(k)} = \mathbf{C}^{-1} : \mathbf{\Xi}_{n+1}^{(k)} : \left[\mathbf{R} + \delta^2\gamma_{n+1}^{(k)}\partial_{\boldsymbol{\sigma}} Q_{n+1}^{(k)}\right]$$

5. Actualize the iteration unknowns:

$$\mathbf{\Delta u}_{n+1}^{cr(k+1)} = \mathbf{\Delta u}_{n+1}^{cr(k)} + \delta\mathbf{\Delta u}_{n+1}^{cr(k)}$$

$$\delta\gamma_{n+1}^{(k+1)} = \delta\gamma_{n+1}^{(k)} + \delta^2\gamma_{n+1}^{(k)}$$

SET $k = k + 1$ GOTO 2.

6. End: $\quad \mathbf{\Delta u}_{n+1}^{cr} = \mathbf{\Delta u}_{n+1}^{cr(k+1)} \qquad W_{n+1}^{cr} = W_{n+1}^{cr(k+1)}$

Table C.1. General Closest Point Projection algorithm for mixed-mode cohesive crack model

Due to the different dimensions of the yield criterion F and the residues $\mathbf{R}$, which are for practical material parameters about $10^6 N/m^2$ for F and about $10^{-4}m$ for $\mathbf{R}$, the normalization terms F_{norm} and R_{norm} have been introduced in (Schrader 2005) as

$$F_{\text{norm}} = \sqrt{c_0^2 + \chi_0^2 \tan^2 \phi} \tag{C.12}$$

and

$$R_{\text{norm}} = \min \begin{cases} \dfrac{2G_f^I}{\chi_0} \\[2ex] \dfrac{2G_f^{IIa}}{c_0} \end{cases}, \tag{C.13}$$

and a dimensionless iteration criterion is obtained

$$\sqrt{\left(\frac{F}{F_{\text{norm}}}\right)^2 + \left(\frac{||\mathbf{R}||}{R_{\text{norm}}}\right)^2} < TOL. \tag{C.14}$$

C.1.2   Elasto-plastic tangent modulus

By using a rate formulation and index notation $(i, j, k, l, r, s = 1, 2)$ the following equations can be written for the elastic law

$$\dot{\sigma}_i = C_{ij} \left[\Delta \dot{u}_j - \Delta \dot{u}_j^{cr} \right], \tag{C.15}$$

and for the flow rule

$$\Delta \dot{u}_j^{cr} = \dot{\gamma} \frac{\partial Q}{\partial \sigma_j}. \tag{C.16}$$

The rate of the yield criterion can be formulated according to (Carol et al. 1997) as

$$\dot{F} = \frac{\partial F}{\partial \sigma_k} \dot{\sigma}_k - H \dot{\gamma}, \tag{C.17}$$

where H was introduced as softening parameter, which reads

$$H = -\frac{\partial F}{\partial \gamma} = \frac{\partial F}{\partial p_i} \frac{\partial p_i}{\partial W^{cr}} \frac{\partial W^{cr}}{\partial \Delta u_j^{cr}} \frac{\partial Q}{\partial \sigma_j}, \qquad \mathbf{p}^T = \begin{bmatrix} \chi & c \end{bmatrix}^T. \tag{C.18}$$

The rate of the plastic multiplier γ can by expressed using Eq. (C.17) as

$$\dot{\gamma} = \frac{1}{H} \left[\frac{\partial F}{\partial \sigma_k} \dot{\sigma}_k - \dot{F} \right], \tag{C.19}$$

where $\dot{F} = 0$ is valid for the plastic state of the material. By substituting this relation and Eq. (C.15) in Eq. (C.19) we obtain

$$\dot{\gamma} = \frac{1}{H}\frac{\partial F}{\partial \sigma_i}C_{ij}\left[\Delta \dot{u}_j - \Delta \ddot{u}_j^{cr}\right].$$ (C.20)

This can be further modified using Eq. (C.16) for the rate of the plastic relative displacements as follows

$$\dot{\gamma} = \frac{\dfrac{\partial F}{\partial \sigma_i}C_{ij}\Delta \dot{u}_j}{H + \dfrac{\partial F}{\partial \sigma_k}C_{kl}\dfrac{\partial Q}{\partial \sigma_l}}.$$ (C.21)

By substituting Eq. (C.21) and Eq. (C.16) in Eq. (C.15) the stresses can be expressed in terms of the total relative displacements

$$\dot{\sigma}_i = C_{ij}\Delta \dot{u}_j - \frac{C_{is}\dfrac{\partial Q}{\partial \sigma_s}\dfrac{\partial F}{\partial \sigma_r}C_{rj}}{H + \dfrac{\partial F}{\partial \sigma_k}C_{kl}\dfrac{\partial Q}{\partial \sigma_l}}\Delta \dot{u}_j,$$ (C.22)

which leads to the elasto-plastic material stiffness matrix

$$D_{ij} = C_{ij} - \frac{C_{is}\dfrac{\partial Q}{\partial \sigma_s}\dfrac{\partial F}{\partial \sigma_r}C_{rj}}{H + \dfrac{\partial F}{\partial \sigma_k}C_{kl}\dfrac{\partial Q}{\partial \sigma_l}}.$$ (C.23)

Due to the non-associated flow rule the obtained material stiffness matrix is asymmetric. In order to obtain a symmetric global stiffness matrix the material stiffness matrix is symmetrized in this work in the following form

$$D_{ij}^{sym} = \frac{1}{2}\left(D_{ij} + D_{ji}\right).$$ (C.24)

This leads to a slower convergence, due to the inconsistent linearization. But the application of the line search method increases the convergence for this case. Due to the fact, that the material stiffness matrix is only inconsistent for the interface elements of the cohesive cracks, while the base material remains linear elastic with consistently linearized stiffness, the overall global convergence is still fast enough for the investigated examples.

Another possibility is to use the asymmetric but consistent matrix and a special sparse matrix solver. The MUMPS solver (Amestoy et al. 2003) mentioned in section 2.3.1 can be used for this purpose, but the disadvantage of this proceeding is the necessity to assemble and store the complete global stiffness matrix, which needs more computational time and memory than using only one half of the symmetric matrix.

C.2 Formulation of softening curves in terms of W^{cr}

C.2.1 Linear softening curve

The linear uniaxial softening curve for the actual tensile strength χ in terms of the plastic crack opening displacement Δu_N^{cr} can be formulated for $\Delta u_N^{cr} \leq \Delta u_{Nc}^{cr}$ according to Fig. 4.16 as

$$\chi(\Delta u_N^{cr}) = \chi_0 \left(1 - \frac{\Delta u_N^{cr}}{\Delta u_{Nc}^{cr}} \right), \tag{C.25}$$

with $\Delta u_{Nc}^{cr} = 2G_f^I/\chi_0$. This leads to the following formulation for W^{cr}

$$W^{cr}(\Delta u_N^{cr}) = \int_0^{\Delta u_N^{cr}} \chi(\Delta u_N^{cr}) du = \chi_0 \Delta u_N^{cr} \left(1 - \frac{\Delta u_N^{cr} \chi_0}{4G_f^I} \right). \tag{C.26}$$

The inverse function of this formulation reads

$$\Delta u_N^{cr}(W^{cr}) = \frac{2G_f^I}{\chi_0} \left(1 \pm \sqrt{1 - \frac{W^{cr}}{G_f^I}} \right), \tag{C.27}$$

where the sign can only be negative since $\Delta u_N^{cr} \leq 2G_f^I/\chi_0$. Insertion of Eq. (C.27) in Eq. (C.25) leads to the final expression

$$\chi(W^{cr}) = \chi_0 \sqrt{1 - \frac{W^{cr}}{G_f^I}}. \tag{C.28}$$

C.2.2 General bilinear softening curve

For the general bilinear case, shown in Fig. 4.16, and for $\Delta u_N^{cr} \leq \Delta u_{Nc}^{cr}$ the uniaxial softening curve in terms of Δu_N^{cr} reads

$$\chi(\Delta u_N^{cr}) = \begin{cases} \chi_0 - \dfrac{\chi_0 - \chi_1}{\Delta u_{N1}^{cr}} \Delta u_N^{cr} & \Delta u_N^{cr} \leq \Delta u_{N1}^{cr} \\[2ex] \chi_1 \dfrac{\Delta u_{Nc}^{cr} - \Delta u_N^{cr}}{\Delta u_{Nc}^{cr} - \Delta u_{N1}^{cr}} & \Delta u_N^{cr} > \Delta u_{N1}^{cr} \end{cases} \tag{C.29}$$

The work spent on the fracture process is than given as

$$
W^{cr}(\Delta u_N^{cr}) = \begin{cases} \displaystyle\int_0^{\Delta u_N^{cr}} \chi(\Delta u_N^{cr})du & \Delta u_N^{cr} \leq \Delta u_{N1}^{cr} \\[2ex] \displaystyle W_1^{cr} + \int_{\Delta u_{N1}^{cr}}^{\Delta u_N^{cr}} \chi(\Delta u_N^{cr})du & \Delta u_N^{cr} > \Delta u_{N1}^{cr} \end{cases}
$$
$$
= \begin{cases} \Delta u_N^{cr}\left(\chi_0 - \dfrac{\chi_0 - \chi_1}{2\Delta u_{N1}^{cr}}\Delta u_N^{cr}\right) & \Delta u_N^{cr} \leq \Delta u_{N1}^{cr} \\[2ex] W_1^{cr} + \Delta u_N^{cr}\chi_1 \dfrac{\Delta u_{Nc}^{cr} - \Delta u_N^{cr}/2}{\Delta u_{Nc}^{cr} - \Delta u_{N1}^{cr}} & \\[2ex] \quad -\Delta u_{N1}^{cr}\chi_1 \dfrac{\Delta u_{Nc}^{cr} - \Delta u_{N1}^{cr}/2}{\Delta u_{Nc}^{cr} - \Delta u_{N1}^{cr}} & \Delta u_N^{cr} > \Delta u_{N1}^{cr} \end{cases} \tag{C.30}
$$

with

$$
W_1^{cr} = \int_0^{\Delta u_{N1}^{cr}} \chi(\Delta u_N^{cr})du = \frac{\chi_1}{2}(\Delta u_{Nc}^{cr} - \Delta u_{N1}^{cr}). \tag{C.31}
$$

The inverse function for $W^{cr} \leq W_1^{cr}$ reads

$$
\Delta u_N^{cr}(W^{cr}) = \frac{\chi_0 \Delta u_{N1}^{cr}}{\chi_0 - \chi_1}\left(1 \pm \sqrt{1 - 2W^{cr}\frac{\chi_0 - \chi_1}{\chi_0^2 \Delta u_{N1}^{cr}}}\right), \tag{C.32}
$$

and for $W_1^{cr} < W^{cr} \leq G_f^I$ we obtain

$$
\Delta u_N^{cr}(W^{cr}) = \Delta u_{Nc}^{cr} \pm (\Delta u_{Nc}^{cr} - \Delta u_{N1}^{cr})\sqrt{1 - \frac{2}{\chi_1}\frac{W^{cr} - W_1^{cr}}{\Delta u_{Nc}^{cr} - \Delta u_{N1}^{cr}}}. \tag{C.33}
$$

Again negative signs lead together with Eq. (C.29) to the final formulation

$$
\chi(W^{cr}) = \begin{cases} \chi_0 \sqrt{1 - 2W^{cr}\dfrac{\chi_0 - \chi_1}{\Delta u_{N1}^{cr}\chi_0^2}} & W^{cr} \leq W_1^{cr} \\[3ex] \chi_1 \sqrt{1 - \dfrac{2}{\chi_1}\dfrac{W^{cr} - W_1^{cr}}{\Delta u_{Nc}^{cr} - \Delta u_{N1}^{cr}}} & W_1^{cr} < W^{cr} \leq G_f^I \end{cases} \tag{C.34}
$$

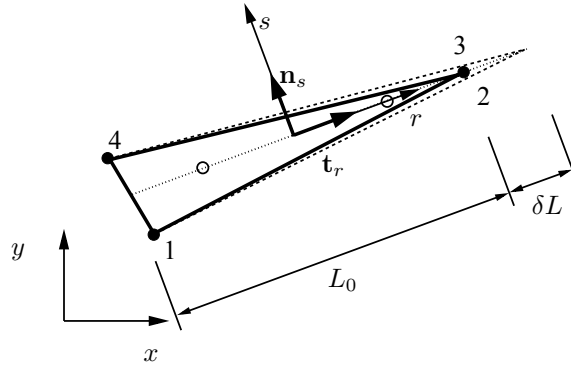## C.3   Cohesive energy rate for linear interface elements

Figure C.1. Coplanar Virtual Crack Extension for a linear isoparametric interface element with two Gaussian integration points

The interface at a cohesive crack tip has two merged nodes (2 and 3 in Fig. C.1). In appendix A.2 it was defined, that the displacement differences in the interface surface given in local r, s-coordinates read

$$\mathbf{\Delta u}^{local} = \mathbf{\tilde{T}B}_e^{global}\mathbf{\tilde{u}}_e. \tag{C.35}$$

The internal forces in global coordinates are obtained as

$$\mathbf{f}_e^{int,global}(\mathbf{\tilde{u}}_e) = \int_A \left[\mathbf{\tilde{T}B}_e^{global}\right]^T \boldsymbol{\sigma}^{local}(\mathbf{\Delta u}^{local})dA, \tag{C.36}$$

which leads to the following formulation using two Gauss integration points

$$\mathbf{f}_e^{int,global}(\mathbf{\tilde{u}}_e) = \sum_{i=1}^{2} \left[\mathbf{\tilde{T}B}_e^{global}\right]_i^T \boldsymbol{\sigma}^{local}(\mathbf{\Delta u}_i^{local})w_i\frac{L \cdot t}{2}, \tag{C.37}$$

where w_i is the weighting factor of the integration points and t is the thickness of the element. The actual length of the element can be defined as the sum of initial length and element extension

$$L = L_0 + \delta L, \tag{C.38}$$

where

$$\begin{aligned} A &= L \cdot t \\ &= L_0 \cdot t + \delta L \cdot t \\ &= A_0 + \delta A. \end{aligned} \tag{C.39}$$

If the length of the element is changed by keeping the local coordinate axis in r-

direction constant, which is valid if the merged node in Fig. C.1 is shifted in local tangential direction equivalent to the coplanar VCE-technique, the transformation matrix $\tilde{\mathbf{T}}$ remains unchanged. Thus the local displacement differences $\boldsymbol{\Delta}\mathbf{u}^{local}$ and even the local stresses $\boldsymbol{\sigma}^{local}(\boldsymbol{\Delta}\mathbf{u}_i^{local})$ are unchanged as well, if the nodal displacement values are kept constant, since $\mathbf{B}_e^{global}$ depends only on the local r coordinate, which is taken with fixed values for the Gauss integration points.

Insertion of Eq. (C.39) in Eq. (C.37) leads to the change of the internal forces for a element extension of δL

$$\delta\mathbf{f}_e^{int,global}(\tilde{\mathbf{u}}_e) = \frac{\delta A}{2} \sum_{i=1}^{2} \left[\tilde{\mathbf{T}}\mathbf{B}_e^{global}\right]_i^T \boldsymbol{\sigma}^{local}(\boldsymbol{\Delta}\mathbf{u}_i^{local})w_i. \tag{C.40}$$

The required derivative reads

$$\frac{\partial\mathbf{f}_e^{int,global}(\tilde{\mathbf{u}}_e)}{\partial A} = \frac{1}{2} \sum_{i=1}^{2} \left[\tilde{\mathbf{T}}\mathbf{B}_e^{global}\right]_i^T \boldsymbol{\sigma}^{local}(\boldsymbol{\Delta}\mathbf{u}_i^{local})w_i$$

$$= \frac{\mathbf{f}_e^{int,global}(\tilde{\mathbf{u}}_e)}{L \cdot t} \tag{C.41}$$

Zusammenfassung

Einführung

Numerische Simulationen haben sich in den letzten Jahrzehnten zu einer wichtigen Alternative zu experimentellen Untersuchungen entwickelt. Die Finite Elemente Methode stellt heutzutage ein etabliertes Werkzeug auf dem Gebiet des Bauingenieurwesens und des Maschinenbaus dar. Dabei wird die Entwicklung numerischer Modelle zur Beschreibung des Schädigungsverhaltens in mechanischen Systemen hauptsächlich im akademischen Umfeld vorangetrieben.

In den vergangenen Jahren wurden eine Vielzahl von Verfahren zur expliziten Abbildung lokalisierter Schädigung entwickelt. Diese Verfahren erlauben eine deutliche Verbesserung der Aussagefähigkeit insbesondere in Bereichen, in denen Rissbildung die Tragfähigkeit negativ beeinflusst. Als wichtige Vertreter solcher Risssimulationsverfahren sind erweiterte Finite Elemente Konzepte sowie netzfreie Verfahren zu nennen. Netzfreie Ansätze erlauben eine einfache Anpassung der Diskretisierung an wachsende Rissgeometrien und können im Gegensatz zur Finite Elemente Methode kontinuierliche Spannungsbilder reproduzieren. Dies erlaubt in der Regel relativ grobe Diskretisierungsstufen um gute numerische Ergebnisse zu erzielen. Jedoch besitzen bestehende netzfreie Verfahren verschiedene Nachteile, wie die Nichteinhaltung der Randbedingungen sowie den erhöhten numerischen Aufwand, die die Anwendung erschweren.

Die Zielsetzung dieser Arbeit bestand darin, einen automatischen Algorithmus zur effizienten Simulation der Rissentwicklung in Beton- und Stahlbetontragwerksteilen zu entwickeln. Zu diesem Zweck sollten netzfreie Verfahren in Kopplung mit finiten Elementen zum Einsatz kommen, um die Vorteile beider Verfahren auszunutzen. Der Versagensmechanismus des Betons sollte unter Berücksichtigung des komplexen Versagens bei kombinierter Rissöffnung und -gleitung auf der Makroebene modelliert werden. Dieser gemischte Zustand sollte weiterhin in einem Risskriterium abgebildet werden, das es erlaubt, mit relativ geringer Knotendichte im Bereich des Risses zu arbeiten. Als weiterer Punkt der Arbeit sollten die Schwankungen der Betoneigenschaften hervorgerufen durch die Inhomogenität des Materials sowie variierende Einbaubedingungen innerhalb eines probabilistischen Modells abgebildet werden.

Mechanische Grundlagen

Ausgehend von den kinematischen Formulierungen des Kontinuums werden die starke Form des Gleichgewichts sowie die konstitutiven Zusammenhänge eingeführt. Darauf aufbauend wird die Finite Elemente Methode als diskretisierte Form des schwachen Gleichgewichts sowie deren Erweiterung für nichtlineare Materialformulierungen vorgestellt.

Zur Lösung des globalen Gleichungssystems unter Berücksichtigung linearen bzw. nichtlinearen Materialverhaltens sind eine Vielzahl von Verfahren entwickelt worden. In dieser Arbeit werden wichtige Vertreter, die im Rahmen des vorgestellten Algorithmus angewendet werden, detailiert erläutert. Dabei werden anhand eines Beispiels die deutlichen Effizienzunterschiede verschiedener Gleichungslöser aufgezeigt.

Netzfreie Verfahren

Netzfreie Verfahren weisen entscheidende Vorteile gegenüber herkömmlichen Finite Elemente Formulierungen auf. Dazu zählen hauptsächlich eine Interpolation, die zu kontinuierlichen Spannungen führt, sowie eine einfache Abbildung veränderlicher Strukturränder, wie z.B. Risse. Jedoch ist der Einsatz netzfreier Verfahren aufgrund signifikanter Probleme deutlich erschwert. Zu diesen Problemen zählen der erhöhte numerische Aufwand zur Berechnung der Formfunktionen sowie die meist nicht eingehaltene Interpolationsbedingung, was das Aufbringen der Randbedingungen verkompliziert.

In der vorliegenden Arbeit wird aufgrund des erhöhten numerischen Aufwandes netzfreier Verfahren ein adaptives Vorgehen angewendet, bei dem nur die Bereiche mit Rissbildung mittels netzfreier Zonen diskretisiert werden und intakte Bereiche weiterhin mit Standardelementen vernetzt bleiben. Dieses Vorgehen erfordert jedoch eine kompatible Kopplung beider Diskretisierungsverfahren, was mit verfügbaren netzfreien Ansätzen nur durch erhöhten numerischen Aufwand zu bewältigen ist. Als ein Schwerpunkt dieser Arbeit werden zwei netzfreie Verfahren für diesen Zweck so verbessert, dass eine direkte Kopplung ohne erheblichen Mehraufwand ermöglicht wird. Für das gebräuchliche Elementfreie Galerkinverfahren, das die Moving Least Squares Interpolation verwendet, wird eine neue Wichtungsfunktion vorgestellt, die im Gegensatz zu bisher verfügbaren Funktionstypen zur Einhaltung der Interpolationseigenschaften mit sehr hoher Genauigkeit führt. Somit können Randbedingungen direkt und ohne zusätzlichen Aufwand aufgebracht werden. Weiterhin führt diese neue Wichtungsfunktion zu einer verbesserten Stabilität der Interpolation, d.h. die Größe des Knoteneinflussbereichs, der als künstlicher Parameter eingeführt wird, hat nun einen relativ geringen Einfluss auf die numerischen Ergebnisse.

Als zweites netzfreies Verfahren wird die Natural Neighbor Interpolation für nichtkonvexe Bereiche, die zwangsläufig durch Risswachstum entstehen, erweitert. Dieses

Verfahren erfüllt die Interpolationsbedingungen automatisch und kann somit direkt in einer gekoppelten Diskretisierung angewendet werden. Die Berechnung der Formfunktionen ist für die untersuchten Fälle deutlich weniger aufwendig als bei der Moving Least Squares Interpolation, allerdings beruht die Natural Neighbor Interpolation auf einer Voronoizerlegung des Knotengebietes, welche bei einem wachsenden Riss aktualisiert werden muss. Diese Aktualisierung ist bei der Moving Least Squares Interpolation nicht notwendig. Für zweidimensionale Simulationen, wie sie in dieser Arbeit vorgenommen werden, wird diese Aktualisierung durch einen schnellen, lokal begrenzten Algorithmus durchgeführt, der kaum Einfluß auf die globale Rechenzeit besitzt. Für die Erweiterung auf dreidimensionale Berechnungen scheint jedoch die Moving Least Squares Interpolation besser geeignet.

Diskrete Risssimulation

Zur Abbildung des Rissverhaltens in Beton hat sich innerhalb einer Beschreibung auf der Makroebene das fiktive Rissmodell weitgehend durchgesetzt. Dabei werden die entstehenden Mikrorisse einer sogenannten Prozesszone in einem fiktiven Riss mit Spannungsübertragung über die Rissufer zusammengefasst. In diesem Modell geht man jedoch nur von einer Kraftübertragung senkrecht zur Rissfläche aus. Anteile infolge Rissgleitung, die durch die Verzahnung der Rissufer hervorgerufen werden, können in diesem Modell nicht abgebildet werden. Aus diesem Grund wird in dieser Arbeit ein bestehendes, verbessertes Modell an die Anforderungen der automatischen Risssimulation angepasst. Dieses Modell kann die Degradation der Rissoberfläche durch kombinierte Rissöffnung und -gleitung wiedergeben. Infolge der erweiterten Modellierung der Vorgänge in der fiktiven Rissfläche können Rissgeometrien sowie globale Größen wie Last-Verschiebungsbeziehungen für solche kombinierten Fälle deutlich besser abgebildet werden als mit dem Standardmodell. Dies wird anhand verschiedener Beispiele verifiziert.

Um über Rissentstehung und -wachstum zu entscheiden, ist die Auswertung eines Risskriteriums notwendig. Dabei wird in der Regel das Rankinekriterium auf Basis der Hauptspannungen verwendet. Aufgrund der verwendeten lokalen Spannungsgrößen sind die berechneten Ergebnisse relativ stark von der verwendeten Diskretisierung abhängig. Daher wird in dieser Arbeit ein Energiekriterium mit virtueller Risserweiterung angewendet. Das Prinzip der virtuellen Risserweiterung wurde ursprünglich im Zusammenhang mit der linearen Bruchmechanik zur Simulation von Risswachstum in Metallen vorgestellt. Aus diesem Grund werden in dieser Arbeit die grundlegenden Formulierungen der linearen Bruchmechanik aufgeführt. Die Erweiterung des Konzepts der virtuellen Risserweiterung für kohäsive Risse in Beton wurde bisher nur für das standardmäßige fiktive Rissmodell umgesetzt, wodurch bei der Berechnung gemischten Versagens den äußeren Energieanteilen, die zu einer Schubverformung der Rissoberflächen führen, keine kohä-

siven Energieanteile gegenüberstehen. Dies kann bei kombinierter Beanspruchung zu unkontrolliertem Risswachstum führen. In dieser Arbeit wird erstmals ein vollständiger Ansatz für dieses Konzept vorgestellt, der durch Kombination des verbesserten fiktiven Rissmodells mit dem energiebasierten Risskriterium Normal- und Schubanteile auf der Einwirkungs- wie auf der Widerstandsseite berücksichtigt.

Um die Richtung des wachsenden Risses festzulegen, wird hier ein kombiniertes Kriterium verwendet. Dabei wird die Rissrichtung unter Verwendung der linearen Bruchmechanik aus den Anteilen der Energiefreisetzungsrate und aus der Richtung der maximalen Hauptspannung der Rissspitze bestimmt. Dieses Richtungskriterium führt zu realistischen Rissgeometrien, was anhand mehrerer numerischer Beispiele gezeigt wird.

Modellierung von Unsicherheiten

In dieser Arbeit werden die Schwankungen der Betoneigenschaften in einem stochastischen Modell unter Verwendung von Zufallsfeldern modelliert. Diese Zufallsfelder repräsentieren die räumliche Verteilung einer stochastischen Größe. Dabei geht man in der Regel davon aus, dass diese Verteilung nur durch geometrische Eigenschaften beeinflusst wird. Um eine Verteilung mehrerer Materialparameter abzubilden, bei der eine Korrelation dieser Größen untereinander modelliert werden kann, wird hier das gebräuchliche Ein-Parameter Konzept des Zufallsfeldes durch Definition einer konstanten Parameterkorrelationsmatrix erweitert. Somit läßt sich eine beliebige Anzahl von korrelierten Materialparametern modellieren.

Das probabilistische Modell wird im Rahmen dieser Arbeit für die statistische Bewertung der Strukturantwort unter Verwendung des entwickelten Algorithmus zur Risssimulation verwendet. Eine Anwendung im Rahmen einer Zuverlässigkeitsanalyse wird nicht vorgenommen ist jedoch direkt möglich. Zur Ermittlung der probabilistischen Strukturantwort kommen hier das Monte Carlo Simulationsverfahren sowie die Latin Hypercube Methode zu Einsatz. Das Latin Hypercube Simulationsverfahren ist in der Lage die statistischen Eigenschaften einer Antwortgröße mit relativ wenig Realisationen zu bestimmen, wodurch der numerische Aufwand einer stochastischen Analyse erheblich reduziert wird. Dies wird anhand verschiedener Beispiele gezeigt.

Zusammmmenfassung

In dieser Arbeit wurde ein automatischer Algorithmus zur Simulation diskreten Risswachstums in Beton- und Stahlbetonkonstruktionen vorgestellt. Dieser Algorithmus kann aufgrund der effizienten Gestaltung für stochastische Analysen auf der Bauteilebene angewendet werden. Die dabei umgesetzte adaptive Kopplung netzfreier Verfahren mit der Methode der Finiten Elemente stellt eine sinnvolle Vorgehensweise speziell für die Simulation

von Systemen mit mehrfacher Rissausbildung dar. Einige Probleme der verwendeten netzfreien Verfahren konnten im Rahmen dieser Arbeit gelöst werden, wodurch die Anwendbarkeit deutlich verbessert wurde.

Die Kopplung eines kombinierten fiktiven Rissmodells und eines energiebasierten Kriteriums für Rissfortschritt führte zu einer erheblichen Steigerung der Qualität der prognostizierten Rissgeometrien und globalen Größen bei gemischter Beanspruchung. Dabei konnte nachgewiesen werden, dass auch mit relativ groben Diskretisierungsstufen eine gute Aussagefähigkeit möglich ist.

Durch das vorgestellte Konzept zur Modellierung einer beliebigen Anzahl von korellierten Materialparameter wurde eine flexible Möglichkeit zur stochastischen Analyse geschaffen. Infolge der reduzierten Anzahl der verwendeten Zufallsvariablen kann die Anwendung von Approximationsverfahren im Rahmen einer Zuverlässigkeitsanalyse unkompliziert erfolgen. Die stochastischen Kennwerte wurden jedoch innerhalb der durchgeführten Analysen relativ willkürlich bestimmt. Eine experimentelle Ermittlung der Parameterverteilungen und die Identifikation zugehöriger Versagensverläufe stellen eine notwendige Aufgabe für weitere Forschungsaktivitäten dar.